Semiconductors, Vol. 36, No. 2, 2002, pp. 121–125. Translated from Fizika i Tekhnika Poluprovodnikov, Vol. 36, No. 2, 2002, pp. 129–133.
Original Russian Text Copyright © 2002 by Petukhov.

ATOMIC STRUCTURE AND NONELECTRONIC PROPERTIES OF SEMICONDUCTORS

Effect of Dynamic Aging of Dislocations on the Deformation Behavior of Extrinsic Semiconductors

B. V. Petukhov

Shubnikov Institute of Crystallography, Russian Academy of Sciences, Leninskiĭ pr. 59, Moscow, 117333 Russia

e-mail: petukhov@ns.crys.ras.ru

Submitted February 28, 2001; accepted for publication June 14, 2001

Abstract—The Alexander–Haasen theory of deformation in semiconductor crystals with low dislocation density was generalized by taking into account the effect of dynamic aging of dislocation caused by the impurity drag. The generalized theory explains some qualitative distinctions of the elastic–plastic transition in Czochralski-grown Si crystals from that in crystals of higher purity. Particularly, this concerns the dependence of the height of the yield-point peak on the initial dislocation density and the weakening of the strain-rate sensitivity of the yield stress. © *2002 MAIK "Nauka/Interperiodica".*

INTRODUCTION

Dislocations, being the extended defects of a crystal lattice, profoundly affect the electrical and mechanical properties of semiconductors. Interaction with dopants changes the dynamics of dislocations and provides the possibility of producing semiconductor materials with desirable characteristics. For example, Czochralski-grown Si crystals containing an appreciable amount of oxygen atoms and other impurities prove to be more suitable for obtaining integrated circuits than purer crystals grown by the floating zone method [1, 2] because of the formation of immobilizing impurity atmospheres, that is, so-called aging of dislocations.

The process of aging may involve both the diffusion of impurity atoms to dislocations and the drag of impurities by moving dislocations (dynamic aging). In the first case, as a consequence of the interaction with an impurity atmosphere, certain starting stresses occur which must be overcome in order to enable a dislocation to move [3–5]. In the second case, this interaction creates an additional retardation which renormalizes the driving force. Under certain conditions, dynamic aging leads to the unstable jump-like motion of dislocations because of the detachments from their atmospheres [6].

Experiments are aimed at studying both the mobility of individual dislocations, as well as the macroscopic plastic deformation of semiconductor crystals [1–5, 7–10]. Hereafter, we discuss the mechanical active-loading testing (at a constant strain rate $\dot{\varepsilon}$ = const). The plastic deformation of crystals with low dislocation density is characterized by the peculiar nonmonotonic behavior of kinetic curves at the transition from the elastic stage to a developed plastic flow. After attaining the highest stress at the end of elastic deformation (the so-called upper yield point τ_u) and at a sufficiently large density of mobile dislocations, the intense plastic flow progresses (a drop in loading to the so-called lower yield point τ_l). This part of a stress-strain curve is known as a yield-point peak. After passing the yield point, the stress τ increases relatively slowly owing to hardening by internal stresses partially caused by the fields of generated dislocations $\tau_{i1} = \alpha\sqrt{N}$, where α is Taylor's hardening coefficient. The qualitative shape of stress–strain curves $\tau(t)$ for intrinsic and extrinsic crystals is shown in Fig. 1.

For the description of the initial stage of plastic deformation of low-dislocation crystals, Alexander and Haasen suggested a model which accounts for the yield-point peak and makes it possible to evaluate the magnitudes of the upper and lower yield points [10].

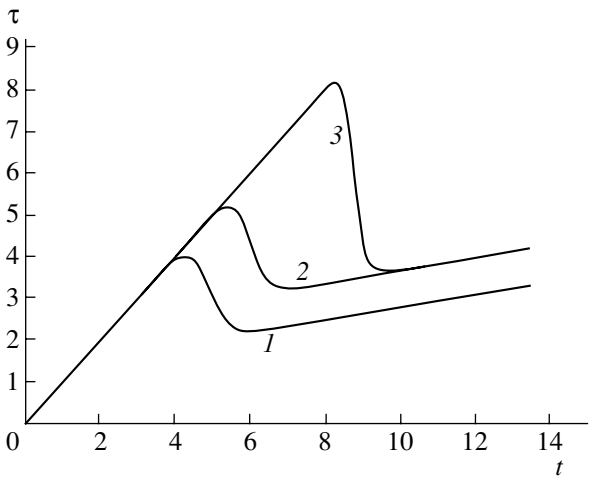

Fig. 1. The stress–strain curve, $\alpha_* = 1$. (*1*) Intrinsic crystal, $c_s = c_2 = 0$; (*2*) illustration of dynamic aging effect, $\beta c_s = \beta c_2 = 1$; (*3*) predominance of static aging, $\beta c_s = 6$, $\beta c_2 = 1$.

However, extrinsic semiconductors exhibit a number of features that cannot be explained within the context of the Alexander–Haasen model. Apart from the appreciable increase of deforming stress, the height of the yield-point peak is found to be almost independent of the initial dislocation density, contrary to the conclusions of the theory suggested by Alexander and Haasen [10] for intrinsic semiconductors. There is also a discordance in behavior of sensitivity to the rate of deforming stress, amongst other disagreements. In this study, the Alexander–Haasen model has been modified and generalized to extrinsic semiconductors, taking into account the dynamic aging of dislocations. First, we shall consider a model assumed for the description of intrinsic crystals with an initially low dislocation density.

ALEXANDER–HAASEN MODEL

The kinetics of dislocation multiplication is described by the equation [10, 11]

$$\frac{dN}{dt} = wNV. \tag{1}$$

Here, N is the dislocation density with initial value N_0, $V = \tau_e B$ is the dislocation velocity, and τ_e is the effective stress obtained from the external stress τ by subtracting the internal counteracting stresses. According to [1–5, 7–10], B contains the Arrhenius factor $B = V_0\exp(-E/kT)$. In the original Alexander–Haasen model, the multiplication coefficient w is chosen proportional to τ_e. However, as was found later, for a better description of the experimental data, the quantity w should be taken as a constant [1]. This type of model is used in our study.

The change of stress is described by the expression which represents the rate of total strain $\dot{\varepsilon}$ as a sum of elastic and plastic contributions:

$$\frac{1}{S}\frac{d\tau}{dt} = \dot{\varepsilon} - NbV, \tag{2}$$

where S is the combined elastic modulus of the sample and test machine, and b is the magnitude of the Burgers vector of dislocations.

We shall measure stress, the dislocation density, and time in units of τ_*, N_*, and t_*, respectively, and also introduce the dimensionless coefficient of hardening α_*:

$$\tau_* = \sqrt{\frac{S\dot{\varepsilon}}{wB}}, \quad t_* = \frac{1}{\sqrt{Sw\dot{\varepsilon}B}}, \quad N_* = \frac{1}{b}\sqrt{\frac{w\dot{\varepsilon}}{SB}},$$

$$\alpha_* = \frac{\alpha}{\sqrt{b}}\left(\frac{B}{\dot{\varepsilon}}\right)^{1/4}\left(\frac{w}{S}\right)^{3/4}.$$

Equations (1) and (2) are reduced to

$$\dot{N} = N\tau_e, \tag{3}$$

$$\dot{\tau} = 1 - N\tau_e. \tag{4}$$

The solution of Eqs. (3) and (4) yields the following results. The upper yield point is expressed as

$$\tau_u \approx \sqrt{2\ln(1/N_0)} - \frac{\ln\sqrt{2\ln(1/N_0)} + 1}{\sqrt{2\ln(1/N_0)}}. \tag{5}$$

The lower yield point is described by the formulas

$$\tau_l = \begin{cases} 3(\alpha_*/2)^{2/3}, & \alpha_* < 2/[2\ln(1/N_0)]^{3/4} \\ \alpha_*\sqrt{t_a + \alpha_*^2/4} - \alpha_*^2/2 + (1/t_a + \alpha_*^2/4) & \\ \alpha_* > 2/[2\ln(1/N_0)]^{3/4}. & \end{cases} \tag{6}$$

Here, t_a is the position of a minimum in the stress–strain curve,

$$t_a = \sqrt{2\ln(1/N_0)} + [2/\sqrt{2\ln(1/N_0)}]$$
$$\times \ln\{[\sqrt{2\ln(1/N_0)} + \alpha_*^2/4]^{1/2} - \alpha_*/2\}.$$

With an increase in the hardening coefficient α_*, the lower yield point rises, and, after exceeding a critical value α_{*c}, the yield-point peak disappears and the stress–strain curve becomes monotonic. This critical value of hardening is determined by the relation

$$\ln(1/N_0) \approx \frac{9}{2}\left(\frac{\alpha_{*c}}{2}\right)^{4/3} + \frac{2}{3}\ln(\alpha_{*c}/54) + 3. \tag{7}$$

Let us pass on to the generalization of these results considering the dynamic aging of dislocations.

MODEL OF DYNAMIC AGING OF DISLOCATIONS

We shall describe the drag of impurities by the equation

$$\frac{dc}{dt} = c_0\frac{rVt_*}{a^2} = c_2\tau_e, \tag{8}$$

where c is the concentration of impurity atoms at a dislocation (the fraction of atoms per single lattice parameter); c_0 is the concentration of impurities in the bulk; r is the impurity capture radius, the smallest value of which is the lattice parameter a; and $c_2 = c_0 r/a^2 w$. Equation (8) implies that the process of impurity capture per unit time involves all impurities in a layer with dimensions V in length and r in width. The velocity of dislocations is supposed to be moderate to allow the impurities to be dragged.

After the displacement of a dislocation over several lattice periods, the concentration of impurities at a dislocation begins to exceed appreciably the bulk concentration c_0. In the theories of dislocation aging, it is commonly accepted to associate the excess of atoms in a dislocation core with the retarding stress $\tau_{i2} = \beta c$ [6], where the proportionality factor β is on the order of

$E_b/a^2\tau_*$ and E_b is the energy of the binding of an impurity to a dislocation. This contribution also reduces the effective stress τ_e, which drives the dislocation; therefore, $\tau_e = \tau - \tau_{i1} - \tau_{i2}$. It is suggested that the change in the driving force is the main factor in the impurity effect, even more important than the modification of parameters.

The amount of impurities collected by a dislocation is determined by its path length, which depends on the time of generation of this dislocation. Correspondingly, the dislocations generated at different times are differently sensitive to the effective stresses. The dislocation generated at the moment t_1 will collect by the time t the concentration $c(t, t_1)$, which is determined, according to Eq. (8), by the relation

$$c(t, t_1) = c_2\int_{t_1}^{t}[\tau(t') - \alpha_*\sqrt{N(t')} - \beta c(t', t_1)]dt'. \quad (9)$$

The initial dislocations with the density N_0 that exist in a crystal have time to collect an impurity concentration c_s prior to the onset of the diffusion process due to the static aging. This impurity atmosphere is associated with the starting stress βc_s, which must be overcome in order to activate the process of dislocation motion. Thus, in the beginning, only elastic strain takes place, and stresses linearly increase until the moment $t_s = \beta c_s$. Then, the dislocations begin to move, their multiplication begins, and the process of elastic flow sets in.

The production of new dislocations will be different at the dislocations with different histories. In order to take this into account, we introduce the quantity $\rho(t)$, which is the density of dislocations generated within the time interval between t and $t + dt$. Then, the increment of total density of dislocations ΔN in time dt is $\Delta N = \rho(t)dt$. This value is the sum of contributions of all dislocations: the initial and newly generated ones at various moments between t_s and t. As a result, we have

$$\begin{aligned}\rho(t) &= N_0[\tau(t) - \alpha_*\sqrt{N(t)} - \beta c_i(t)] \\ &+ \int_{t_s}^{t}\rho(t_1)[\tau(t) - \alpha_*\sqrt{N(t)} - \beta c(t, t_1)]dt_1.\end{aligned} \quad (10)$$

Here, $c_i(t)$ is the impurity concentration at initial dislocations.

The dislocations generated at various instants of time t_1 are moving at a moment t with various velocities $V(t, t_1)$ and, consequently, contribute differently to the rate of plastic flow $\dot{\varepsilon}_p$. Summing up all contributions, we obtain the generalized Orowan's relation

$$\dot{\varepsilon}_p = N_0 bV_i(t) + \int_{t_s}^{t}\rho(t, t_1)bV(t, t_1)dt_1. \quad (11)$$

Here, $V_i(t)$ is the velocity of initial dislocations. In dimensionless variables, the equation for the change of deforming stress takes the form

$$\begin{aligned}\dot{\tau} &= 1 - N_0[\tau(t) - \alpha_*\sqrt{N(t)} - \beta c_i(t)] \\ &- \int_{t_s}^{t}\rho(t_1)[\tau(t) - \alpha_*\sqrt{N(t)} - \beta_s(t, t_1)]dt_1.\end{aligned} \quad (12)$$

Some special features in the influence of dynamic aging of dislocations on the plastic strain in crystals should be noted. While the fluctuations of internal stress are generally disregarded and assumed to be uniform for all dislocations, in the model considered here they should be taken into account because of the occurrence of a variety of internal stresses to which the dislocations generated at different times and having various path lengths are sensitive. Generally speaking, the existence of such "time-nonlocal" internal stresses complicates the detailed description of many of the characteristics of the deformation process. However, in the context of our simple model, it becomes possible to describe relatively easily the temporal changes in total deforming stress and total dislocation density.

The relation describing the total increment of dislocation density at a moment t, obtained by the integration of Eq. (10) and taking Eq. (8) into account, is

$$\begin{aligned}\Delta N(t) &= \int_{t_s}^{t}\rho(t')dt' = N_0[c_i(t) - c_s]/c_2 \\ &+ (1/c_2)\int_{t_s}^{t}\rho(t_1)c(t, t_1)dt_1.\end{aligned} \quad (13)$$

Using this relation, which contains the averaged internal stress created by impurities at all generated dislocations, the integral Eq. (10) can be reduced to the differential equation

$$\begin{aligned}\Delta\dot{N} &= \Delta N[\tau(t) - \alpha_*\sqrt{N(t)} - \beta c_2] \\ &+ N_0[\tau(t) - \alpha_*\sqrt{N(t)} - \beta c_s].\end{aligned} \quad (14)$$

Furthermore, comparison of Eqs. (10) and (12) leads to the relation $\dot{\tau} = 1 - \rho(t)$, which, after integration, yields

$$\tau(t) = t - \Delta N(t). \quad (15)$$

This relation makes it possible to exclude the variable τ from Eq. (14) and to finally obtain a closed-type equation for $\Delta N(t)$.

Let us analyze the initial stage of the process when the dislocation density is still low and the nonlinear terms in Eq. (14) can be disregarded. Equation (14) is then reduced to

$$\Delta\dot{N} \approx (t - \beta c_2)\Delta N + N_0(t - \beta c_s). \quad (16)$$

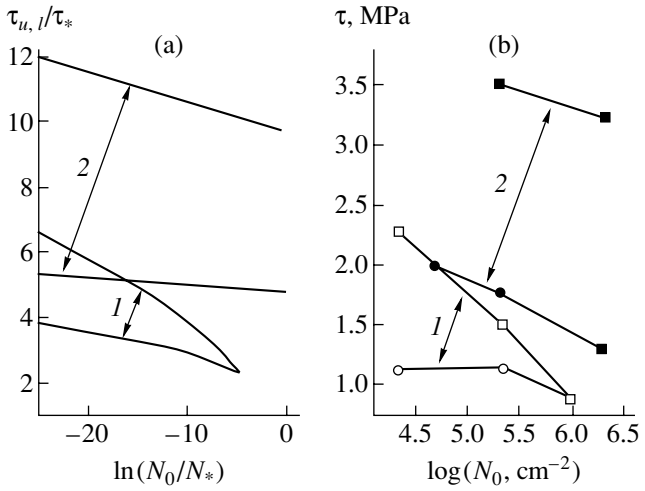

Fig. 2. Illustration of the dependence of the upper and lower yield points on the initial dislocation density. (a) Calculation, $\alpha_* = 1$: (*1*) Intrinsic crystal, $c_s = c_2 = 0$; (*2*) extrinsic crystal, $\beta(c_s - c_2) = 10$. (b) Experimental data [12] for silicon grown (*1*) by floating zone method and (*2*) by Czochralski method.

The solution of this simplified equation is given by

$$\Delta N(t) = N_0 \exp(t^2/2 - \beta c_2 t) \times \int_{t_s}^{t} (t' - \beta c_s) \exp(-t'^2/2 + \beta c_2) dt'. \quad (17)$$

The integral in (17) converges rapidly. The upper limit at large t can be taken equal to infinity. Then, we have

$$\Delta N(t) = N_0' \exp\{(t - \beta c_2)^2/2\}, \quad (18)$$

where

$$N_0' = N_0 \int_0^\infty t \exp\{-(1/2)[t + \beta(c_s - c_2)]^2\} dt. \quad (19)$$

It can easily be seen that the above derivation allows generalization to the case of the spectrum of starting stresses $\tau_s = \beta c_s$. For doing this, because of the linearity of the initial Eq. (16), the final expression (19) can be averaged relatively easily over the spectrum.

From Eq. (18) it follows that the density of newly generated dislocations at $t > \beta c_2$ abruptly increases with time and soon becomes higher than the initial density N_0. As a result, we may disregard the term containing N_0 in Eq.(14). The resulting equation differs from that for impurity-free crystals (3) only by the shift in time βc_2. As can be seen from expression (18), the quantity N_0' plays the role of initial dislocation density. Thus, the problem is reduced to that solved previously, and we can use the results (5)–(7) with corresponding renormalization of their parameters such as the shift of stress by βc_2 and substitution of N_0 by N_0'. If we denote the yield points for an intrinsic crystal as $\tau_{u,l}^0(N_0)$, these quantities for an extrinsic crystal will be expressed as $\tau_{u,l} = \beta c_2 + \tau_{u,l}^0(N_0')$ with N_0' defined by (19). Returning to dimensional values, the upper yield point is determined by

$$\tau_u \approx \frac{\beta c_0 r}{wa^2} + \tau_* \left\{ \sqrt{2\ln(N_*/N_0)} - \frac{\ln\sqrt{2\ln(N_*/N_0)} + 1}{\sqrt{2\ln(N_*/N_0)}} \right\}. \quad (20)$$

The lower yield point is equal to

$$\tau_l = \frac{\beta c_0 r}{wa^2} + \tau_* \begin{cases} 3(\alpha_*/2)^{2/3}, & \alpha_* < 2/[2\ln(N_*/N_0')]^{3/4} \\ \alpha_* \sqrt{t_a + \alpha_*^2/4} - \alpha_*^2/2 + 1/(t_a + \alpha_*^2/4) \\ \alpha_* > 2/[2\ln(N_*/N_0')]^{3/4}. \end{cases} \quad (21)$$

As can be seen from formula (19), for highly aged initial dislocations ($\beta c_s \longrightarrow \infty$)$\ln(1/N_0') \approx \ln(1/N_0) + \beta^2(c_s - c_2)^2/2$ and, according to formula (5), $\tau_u \longrightarrow \tau_* \beta c_s$. In this case, the height of the peak in the stress–strain curve is governed primarily by the starting stress τ_s. It should be noted that the occurrence of impurity contributions results in the weakening of the dependence of the deforming stress on the strain rate. In the opposite limit, when $c_s \longrightarrow 0$, $c_0 \longrightarrow 0$ we have $N_0' \longrightarrow N_0$, and τ_u changes to its value for an intrinsic crystal.

Figure 2a shows the calculated dependence of the upper and lower yield points on the initial dislocation density N_0 for intrinsic and extrinsic crystals. As can be seen, the interaction with impurities results in the rise of the yield point. Furthermore, the height of the yield-point peak ($\tau_u - \tau_l$) decreases more weakly with an increase of the initial dislocation density, which results in the widening of the range of the yield-point peak existence. This feature agrees qualitatively with the experimental data presented in Fig. 2b.

CONCLUSION

The interaction of moving dislocations with impurity atoms results in a change in the dynamic properties of dislocations. In order to quantitatively describe this effect of the dynamic aging of dislocations, we generalized the Alexander–Haasen model, which successfully explains many features of elastic-to-plastic transi-

tions in intrinsic semiconductors. The generalization includes, among other factors, the idea of a "nonlocal" (in time) internal stress, which is different for dislocations with different histories.

The formulas obtained in this study yield the dependences of the characteristics of the yield-point peak on temperature, strain rate, concentration of impurities, initial dislocation density, and other parameters. The generalization of the model showed that the effect of aging may be responsible not only for an increase in the deforming stress of extrinsic semiconductors, in comparison with intrinsic semiconductors, but also for the radical changes in various relationships inherent in intrinsic semiconductors. For example, the height of the yield-point peak decreases much more slowly with increasing initial dislocation density; this phenomenon is actually observed in the experiments with doped silicon [1, 12]. This results in the widening of the range of the yield-point peak existence. In addition, this leads to the weakening of the rate dependence of the deforming stress, which is also in accordance with the experimental data [1, 13].

Thus, we may conclude that the suggested model satisfactorily explains a number of distinctions of the deformation behavior of intrinsic and extrinsic semiconductor materials. In conclusion, we must state that this study is concerned with the initial stage of the dynamic aging of dislocations, disregarding various possible effects at a subsequent stage. For example, the saturation of a dislocation core by impurities may result in the stabilization of the impurity content. On the other hand, the detachments of dislocations from their atmospheres may result in the possibility of the repetition of the process described and in the instability of plastic strain (the Portevin–Le Shatelier effect, see review in [6, 14]).

REFERENCES

1. H. Alexander, *Dislocations in Solids*, Ed. by F. R. N. Nabarro (North-Holland, Amsterdam, 1986), Vol. 7, Chap. 35, p. 113.
2. M. G. Mil'vidskiĭ and V. V. Osvenskiĭ, *Structural Defects in Single Crystals of Semiconductors* (Metallurgiya, Moscow, 1984).
3. V. I. Nikitenko, in *Dynamics of Dislocations* (Naukova Dumka, Kiev, 1975), p. 7.
4. V. A. Makara, Preprint IPM-86-2 (IÉS im. E. O. Patona, Kiev, 1986).
5. K. Sumino and M. Imai, Philos. Mag. A **47**, 753 (1983).
6. Y. Estrin and L. P. Kubin, in *Continuum Models for Materials with Micro-Structure*, Ed. by H.-B. Mulhaus (Wiley, New York, 1995), p. 395.
7. Yu. L. Iunin, V. I. Nikitenko, V. I. Orlov, and B. Ya. Farber, Zh. Éksp. Teor. Fiz. **100**, 1951 (1991) [Sov. Phys. JETP **73**, 1079 (1991)].
8. A. George and J. Rabier, Rev. Phys. Appl. **22**, 941 (1987).
9. J. Rabier and A. George, Rev. Phys. Appl. **22**, 1327 (1987).
10. H. Alexander and P. Haasen, Solid State Phys. **22**, 27 (1968).
11. W. G. Johnston and J. J. Gilman, J. Appl. Phys. **30**, 129 (1959).
12. K. Sumino, I. Yonenaga, and H. Harada, Jpn. J. Appl. Phys. **51** (1), 217 (1980).
13. H. Siethoff and P. Haasen, *Lattice Defects in Semiconductors*, Ed. by R. Hasiguti (Tokyo Univ. Press, Tokyo, 1968), p. 491.
14. M. Zaiser and P. Hahner, Phys. Status Solidi B **199**, 267 (1997).

Translated by A. Zalesskiĭ

Semiconductors, Vol. 36, No. 2, 2002, pp. 126–129. Translated from Fizika i Tekhnika Poluprovodnikov, Vol. 36, No. 2, 2002, pp. 134–137.
Original Russian Text Copyright © 2002 by Aleksandrov, Zakhar'in, Sobolev.

ELECTRONIC AND OPTICAL PROPERTIES OF SEMICONDUCTORS

Electrical Properties of Silicon Layers Implanted with Ytterbium Ions

O. V. Aleksandrov*, A. O. Zakhar'in*, and N. A. Sobolev**

** St. Petersburg State Electrotechnical University, St. Petersburg, 197376 Russia*
e-mail: zaharium@online.ru
*** Ioffe Physicotechnical Institute, Russian Academy of Sciences, Politekhnicheskaya ul. 26, St. Petersburg, 194021 Russia*
Submitted June 27, 2001; accepted for publication July 11, 2001

Abstract—It is ascertained that implantation of 1-MeV ytterbium ions with a dose of 10^{13} cm^{-2} into silicon with subsequent annealing at temperatures of 600–1100°C gives rise to donor centers. The donor-center concentration is higher in the samples implanted additionally with oxygen ions. The results show that at least two types of donor centers are formed; these centers contain either ytterbium or oxygen impurity atoms. The dependence of electron mobility on the concentration of electrically active centers in the silicon layers implanted with the ytterbium rare-earth ions is determined in the concentration range of 7×10^{15}–10^{17} cm^{-3}. © *2002 MAIK "Nauka/Interperiodica".*

Recently, interest has been aroused in the properties of silicon doped with the rare-earth elements (REs) [1]. This interest is caused by the prospect of using the structures doped with REs in silicon-based optoelectronics as light-emitting sources. Specifically, the most extensively studied RE erbium emits at a wavelength of 1.54 μm, which corresponds to the lowest losses and dispersion in the fiber links; this circumstance makes the Si:Er system promising for silicon-based optoelectronics. Photoluminescence and electroluminescence at a wavelength of 1.96 μm have been observed in silicon doped with holmium [2, 3]. The luminescence efficiency depends on the characteristics of the optically and electrically active centers that contain REs. However, at present, there is no clear insight into the process of formation of these centers. From this standpoint, studying the electrical properties of silicon doped with various REs is topical for ascertaining the general laws in the processes of formation of electrically and optically active centers in such systems. So far, in addition to the electrical properties of Si:Er layers [4–6], those of Ho- and Dy-doped Si layers [7] and of the Si layers implanted with ytterbium ions and annealed at temperatures of 700 and 900°C [8] have been studied. In this paper, we report the results of studying the electrical properties of Si layers implanted with RE ytterbium ions and then annealed in a wide range of temperatures.

For substrates, we used the polished wafers of float-zone *n*-Si (*n*-FZ-Si) with a resistivity of 80–140 Ω cm and of Czochralski-grown *p*-Si (*p*-Cz-Si) with a resistivity of 20 Ω cm. The oxygen concentration in the original samples was $< 2 \times 10^{16}$ (in *n*-FZ-Si) and 1.1×10^{18} cm^{-3} (in *p*-Cz-Si). The 1-MeV ytterbium ions were implanted at a dose of $Q = 1 \times 10^{13}$ cm^{-2} using a High Voltage Engineering Europa 2MV heavy-ion accelerator. A fraction of the wafers were additionally implanted with 135-keV oxygen ions; the dose was 1×10^{14} cm^{-2}. The ions were implanted at an angle of 7° to the normal of the surface in order to avoid channeling; the substrate temperature during implantation was no higher than 50°C. Implantation did not result in amorphization of the material. Isochronous annealings for 30 min were performed in the temperature range T = 600–1100°C in a chlorine-containing atmosphere. Concentration profiles of electrically active centers $n(x)$ were determined from the capacitance–voltage (C–V) characteristics of the Hg–Si Schottky barrier using a mercury probe. The sheet resistance R_s was measured using the four-point probe method. The charge-carrier mobility was determined from the Hall effect measurements at room temperature with sequential removal of thin (~0.02 μm) layers. The effective activation coefficient for electrically active centers, k, was determined using the following two methods. In one of these, the coefficient k was defined as the ratio of the number of donor centers contained in the *n*-type layer and determined by integrating the profile $n(x)$ to the overall ytterbium-implantation dose. In the second method, k was determined by dividing the number of donor centers contained in the *n*-type layer according to the measurements of the sheet resistance by the total implantation dose using the relation $k = (e\mu R_s)^{-1}/Q$, where e is the elementary charge and μ is the electron mobility (μ = 1350 cm^2 V^{-1} s^{-1}); this method was used for calculating the coefficient k after annealing at temperatures of 600 and 1100°C.

Postimplantation annealing of the Si:Yb layers in the temperature range of 600–1100°C gives rise to donor centers; in *p*-Cz-Si, the *p*–*n* conversion of the conduction type is observed in the implanted layer. Previously [8], the Hall effect was used to evaluate the formation of donor centers in the Si:Yb layers as a result of annealing at 700 and 900°C. The concentration profiles of electrically active centers $n(x)$ in the layers under investigation have the shape of peaked curves (Figs. 1a, 1b). The highest concentration is observed after annealing at $T = 700$°C. An increase in the annealing temperature is accompanied with a decrease in the concentration of introduced centers at its maximum n_{max} and with a shift of the position of the peak x_{max} deeper into the sample. In the samples implanted additionally with oxygen, the value of n_{max} is larger and x_{max} is closer to the surface in the entire range of annealing temperatures under consideration.

The method of differential Hall effect was used to measure the concentration profiles of electrically active centers $n(x)$ and the electron-mobility profiles $\mu(x)$. By comparing these data, we plotted the dependences of electron mobility on the concentration of electrically active centers in the silicon layers implanted with 1-MeV Yb ions with a dose of 10^{14} cm^{-2} (Fig. 2, points *1*, *2*) and implanted additionally with oxygen ions with different doses (Fig. 2, points *3*, *4*). The concentration dependence of mobility $\mu(n)$ can be adequately approximated by the formula used to describe the similar dependence in silicon layers doped with conventional doping impurities [9]; i.e.,

$$\mu(n) = \mu_{min} + \frac{\mu_{max} - \mu_{min}}{1 + (n/N_{ref})^{\alpha}}.$$

The parameters μ_{max}, μ_{min}, N_{ref}, and α were determined using the least-squares method. The determined values of the parameters in the dependence for the Yb impurity and the parameters of this dependence for the majority donor impurities (P, As, and Sb) determined previously [9] are listed in the table. It can be seen from the data shown in Fig. 2 and listed in the table that the concentration dependence of the electron mobility (dashed line) in the concentration range under consideration (7×10^{15}–10^{17} cm^{-3}) is close to the corresponding dependence for the majority donor impurities (the solid line). An analysis of experimental data shows that electron mobility is nearly independent of the energy spectrum of the electrically active centers; this spectrum changes as a result of additional implantation with oxygen ions and variation of the annealing-temperature. This fact suggests that, as in the case of the conventional donor impurities, the electron mobility at room temperature in the Si:Yb samples is controlled by scattering at isolated electrically active centers and at the thermal lattice vibrations.

Dependences of the activation coefficient k for electrically active centers in Si:Yb and (Si:Yb):O layers on the temperature of isochronous annealing T are shown in Fig. 3. Concentration of electrically active centers in *p*-Cz-Si is higher than in *n*-FZ-Si (see Fig. 3, curves *1*, *3*). The largest values of k are observed at $T = 700$°C and amount to ~14% in Si:Yb and ~18% in (Si:Yb):O in relation to the total concentration of implanted ytterbium. Additional implantation of oxygen ions enhances

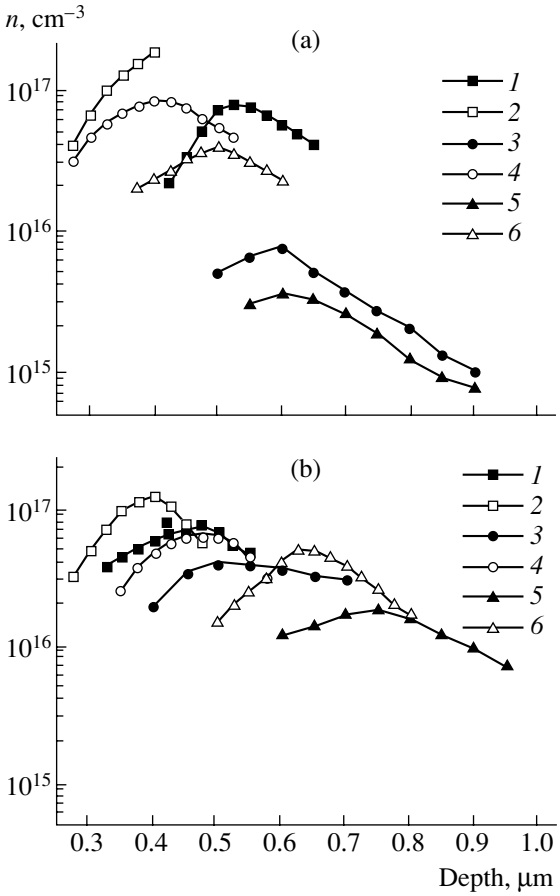

Fig. 1. Concentration profiles of electrically active centers determined from the measurements of the *C*–*V* characteristics after (*1*, *3*, and *5*) implantation of ytterbium ions and (*2*, *4*, and *6*) coimplantation of the ytterbium and oxygen ions into (a) *n*-FZ-Si and (b) *p*-Cz-Si with subsequent isochronous annealing for 0.5 h at temperatures of (*1*, *2*) 700, (*3*, *4*) 800, and (*5*, *6*) 900°C.

The values of parameters in the concentration dependence of electron mobility

Parameter	Si:Yb	The majority donor impurities in silicon [9]
μ_{min}, cm^2 V^{-1} s^{-1}	60	65
μ_{max}, cm^2 V^{-1} s^{-1}	1350	1330
N_{ref}, cm^{-3}	1.1×10^{17}	8.5×10^{16}
α	0.72	0.72

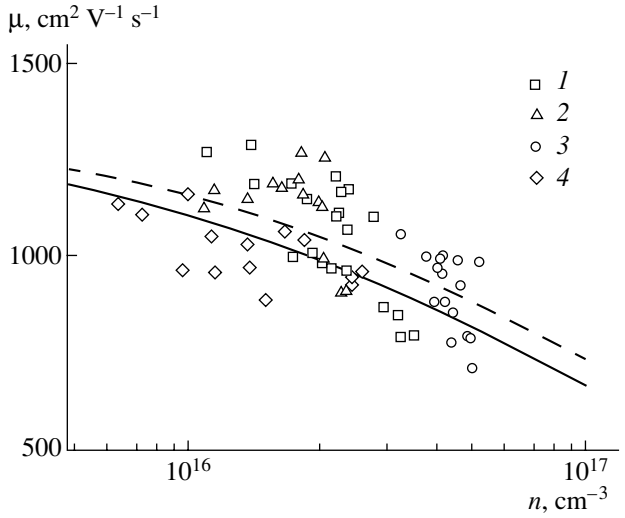

Fig. 2. Dependences of electron mobility on the concentration of electrically active centers in the silicon layers implanted with ytterbium ions with a dose of 10^{13} cm^{-2} and with oxygen ions with a dose of (*1*, *2*) 0 and (*3*, *4*) 10^{14} cm^{-2}. The annealing temperature T was equal to (*1*, *3*) 700, (*2*) 800, and (*4*) 900°C. The dashed line corresponds to Si:Yb, the solid line is for silicon doped with typical donor impurities [9].

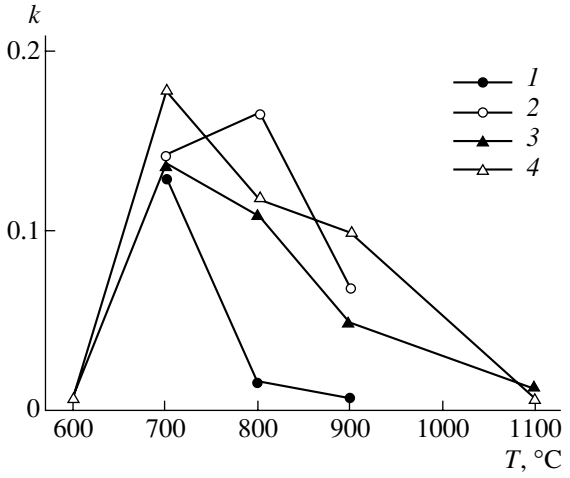

Fig. 3. Dependences of the activation coefficient for electrically active centers on the annealing temperature in (*1*, *2*) *n*-FZ-Si and (*3*, *4*) *p*-Cz-Si after (*1*, *3*) implantation of ytterbium ions and (*2*, *4*) coimplantation of the ytterbium and oxygen ions.

the concentration of the electrically active centers introduced (see Fig. 3, curves *2*, *4*).

After an annealing at T = 700°C, the concentration of donor centers in *n*-FZ-Si is several times higher than the oxygen concentration in the original material (see Fig. 1a, curve *1*). This finding suggests that the dominant donor centers do not contain oxygen atoms but contain the RE atoms. It has been ascertained previously [8] that annealing of the implanted Si layers at 700 and 900°C results in formation of two types of centers; these are the oxygen-containing quenched-in donors and the donor centers containing the RE atoms. It has been assumed that, along with oxygen atoms, intrinsic point lattice defects (vacancies and/or silicon interstitial atoms), produced in the course of annealing the implantation-induced defects, are involved in the formation of oxygen-containing quenched-in donors. The data represented in Figs. 1 and 3 favor this assumption. A higher concentration of electrically active centers in *p*-Cz-Si compared to that in *n*-FZ-Si (Fig. 3, curves *1*, *3*) is indicative of the involvement of oxygen in the formation of electrically active centers. The annealing of the Si:Yb and (Si:Yb):O samples at the same temperature is accompanied with an increase in the concentration of the introduced electrically active centers and with a shift in their concentration profile towards the surface as a result of the additional implantation of oxygen; this fact also indicates that oxygen atoms are involved in the formation of donor centers. The involvement of intrinsic point defects in the formation of donor centers is indicated by a decrease in the concentration of introduced centers and the shift of their concentration profile away from the surface as the annealing temperature for the same sample increases [5]. Since diffusion of RE atoms has not been observed in the annealing-temperature range under consideration [5, 7] and the energy distribution of oxygen-related quenched-in donors is nearly independent of the type of implanted RE ions (Dy, Ho, Er, and Yb) [8], we may assume that the atoms of RE impurities are not contained in the oxygen quenched-in donors.

Thus, we studied the effects of annealing temperature and oxygen impurity on electrical properties of silicon layers implanted with ytterbium. Introduction of Yb, as well as other RE elements (Er, Ho, and Dy) is accompanied with the formation of donor centers. It is ascertained that the electron mobility is virtually independent of the types of electrically active centers that formed; rather, the mobility is controlled by the total concentration of these centers. The concentration dependence of mobility $\mu(n)$ in the silicon layers doped with ytterbium is close to the corresponding dependence observed in the silicon layers doped with the majority donor impurities.

ACKNOWLEDGMENTS

We thank E.O. Parshin, R.V. Tarakanova, and E.I. Shek for their help in preparing the samples.

This study was supported in part by the Russian Foundation for Basic Research (project no. 99-02-17750), INTAS (grant no. 99-01872), and the joint project of the Russian Foundation for Research and the Austrian Agency for Scientific Cooperation (grant no. 01-02-02000).

REFERENCES

1. N. A. Sobolev, Fiz. Tekh. Poluprovodn. (St. Petersburg) **29**, 1153 (1995) [Semiconductors **29**, 595 (1995)].
2. B. A. Andreev, N. A. Sobolev, D. I. Kuritsyn, *et al.*, Fiz. Tekh. Poluprovodn. (St. Petersburg) **33**, 420 (1999) [Semiconductors **33**, 407 (1999)].
3. N. A. Sobolev, A. M. Emel'yanov, and Yu. A. Nikolaev, Fiz. Tekh. Poluprovodn. (St. Petersburg) **33**, 931 (1999) [Semiconductors **33**, 850 (1999)].
4. F. Priolo, S. Coffa, G. Franzo, *et al.*, J. Appl. Phys. **74**, 4936 (1993).
5. O. V. Aleksandrov, N. A. Sobolev, E. I. Shek, and A. V. Merkulov, Fiz. Tekh. Poluprovodn. (St. Petersburg) **30**, 876 (1996) [Semiconductors **30**, 468 (1996)].
6. N. A. Sobolev, O. V. Alexandrov, and E. I. Shek, Mater. Res. Soc. Symp. Proc. **442**, 237 (1997).
7. O. V. Aleksandrov, A. O. Zakhar'in, N. A. Sobolev, *et al.*, Fiz. Tekh. Poluprovodn. (St. Petersburg) **32**, 1029 (1998) [Semiconductors **32**, 921 (1998)].
8. V. V. Emtsev, V. V. Emtsev, Jr., D. S. Poloskin, *et al.*, Fiz. Tekh. Poluprovodn. (St. Petersburg) **33**, 649 (1999) [Semiconductors **33**, 603 (1999)].
9. D. M. Caughey and R. E. Thomas, Proc. IEEE **55**, 2192 (1967).

Translated by A. Spitsyn

Semiconductors, Vol. 36, No. 2, 2002, pp. 130–135. Translated from Fizika i Tekhnika Poluprovodnikov, Vol. 36, No. 2, 2002, pp. 138–143.
Original Russian Text Copyright © 2002 by Mitrokhin, Rembeza, Sviridov, Yaroslavtsev.

ELECTRONIC AND OPTICAL PROPERTIES OF SEMICONDUCTORS

Effect of Optical Radiation on Internal Friction in Piezoelectric Semiconductors with Deep-Level Centers

V. I. Mitrokhin*, S. I. Rembeza*, V. V. Sviridov, and N. P. Yaroslavtsev***

** Voronezh State Technical University, Moskovskiĭ pr. 14, Voronezh, 394026 Russia*

e-mail: imakarova@vmail.ru

*** Voronezh State Pedagogical University, ul. Lenina 86, Voronezh, 394043 Russia*

Submitted March 30, 2001; accepted for publication April 3, 2001

Abstract—The effect of optical radiation on internal friction in piezoelectric semiconductors was studied; this effect is related to electronic–mechanical relaxation at deep-level centers. It is ascertained that the behavior of internal friction depends heavily on the intensity and wavelength of radiation and on the sample temperature. An anomalous peak is observed in the spectral dependence of internal friction; this peak is located in the fundamental-absorption region and is associated with a shift of the optical-absorption zone to the irradiated surface. The effect of the internal-friction slow relaxation after the illumination was switched off was observed. A model relating the slow relaxation to thermal depletion of attachment levels is suggested. © *2002 MAIK "Nauka/Interperiodica".*

1. INTRODUCTION

The phenomenon of electronic–mechanical relaxation related to deep levels was first described by Mitrokhin *et al*. [1, 2]; this phenomenon consists in the emergence of relaxation maxima in the bending vibrations in the samples of high-resistivity piezoelectric semiconductors (GaAs, GaP, InP, and CdS). In this situation, the parameters of peaks in the temperature dependence of internal friction depend on the parameters of the deep-level centers, which govern the electrical properties of the sample. Mechanical energy of vibrations is spent on the Joule heat release as a result of a flow of charge-relaxation current in the piezoelectric field induced by the sample deformation.

A model of electronic–mechanical charge relaxation via deep levels [1, 2] accounts for the contributions of the following interrelated processes: thermal ionization and reverse capture of charge carriers by deep-level centers and the Maxwell relaxation of free charge carriers and their drift through the sample in a piezoelectric field. The relaxation time is expressed in terms of the intricate combination of characteristic times for the aforementioned processes.

Further experiments demonstrated a high sensitivity of the measured acoustic attenuation to optical radiation, which gives rise to the internal photoeffect in the semiconductor under investigation. Depending on the wavelength and intensity of radiation, the photogenerated nonequilibrium charge carriers screen the piezoelectric field and can radically modify the relation between the quantitative parameters of the aforementioned components of the relaxation time of charge carriers involved in electronic–mechanical relaxation via the deep levels. Photoelectric phenomena in semiconductors include such features as depth-nonuniform optical absorption, which gives rise to the nonuniform concentration of charge carriers; variation in the occupancy of deep levels in the course of illumination; an intricate kinetics of photoconductivity; and so on. Therefore, optical radiation can profoundly affect the processes of relaxation of the piezoelectric-polarization space charge in the sample bulk and, consequently, the magnitude and parameters of the peaks in the acoustic attenuation.

This study is concerned with gaining insight into the effect of optical radiation on the charge-carrier electronic–mechanical relaxation via deep levels under conditions when the equilibrium process of thermal activation of nonequilibrium charge carriers from deep-level centers is accompanied by the photogeneration of nonequilibrium charge carriers and the emergence of an alternating-sign piezoelectric field in the semiconductor bulk. These studies made it possible to gain new information about the photoelectric properties of piezoelectric semiconductors using contactless acoustic methods.

2. EXPERIMENTAL

We determined internal friction by measuring the damping of free bending vibrations of a rectangular plate [3, 4] at frequencies ranging from 5 to 20 kHz in the range of temperatures T from –120 to +180°C; we estimated the number of vibrations between two fixed amplitude thresholds. The samples were installed horizontally onto quartz supports at the node points of bending vibrations [4]. The facilities for fixing the samples equipped with electrodes for electrostatic excitation and detection were installed in a vacuum chamber,

1063-7826/02/3602-0130$22.00 © 2002 MAIK "Nauka/Interperiodica"

which was made of stainless steel and incorporated a vessel for filling with liquid nitrogen and a furnace for heating the samples.

The samples were cut from single-crystal wafers of semi-insulating GaAs, GaP, and InP semiconductors, doped with transition-metal impurities from the melt, and grown by the Czochralski method. The samples were 20×6.0 mm^2 in area and 0.4 mm in thickness and had an orientation parallel to the (100) plane, with the long axis oriented along the piezoactive ⟨110⟩ direction. For such a crystallographic orientation of the sample, the piezoelectric field induced by flexural deformation propagates through the largest sample volume and gives rise to the highest intensity of the charge relaxation and, correspondingly, to the highest peaks in the internal friction.

Illumination of the sample was accomplished through a quartz-glass window in the vacuum-chamber body. The source of optical radiation was an IKS-21 spectrometer, the light from the exit slit of which was first passed through a focusing lens and was then directed to the sample in the vacuum chamber. The combination of the internal-friction measurement facilities with spectroscopic systems made it possible to measure the spectral dependences of relative variations in internal friction under sample exposure to optical radiation at fixed temperatures and also to measure the kinetics of the internal-friction recovery after the pulsed optical irradiation.

In addition to the above-described experiments, we used the same samples in comparative measurements of spectral curves and kinetics of dc photoconductivity using an SDL-2 spectral–computing system.

3. RESULTS

3.1. Temperature Dependence of Internal Friction in the Course of Optical Irradiation

In Fig. 1, curve *1* represents the temperature dependence of internal friction $Q^{-1} = f(T)$ for Cr-doped GaAs with a resistivity of $\rho = 6 \times 10^5$ Ω m for the flexural-vibration frequency of 8.2 kHz. In this curve, measured without illumination, the initial Debye peak of internal friction can be distinguished at the temperature T = +70°C, which is caused by electronic–mechanical relaxation due to deep levels [1] and features the relaxation-process activation energy of (0.76 ± 0.02) eV and the frequency factor of 1.6×10^{14} s^{-1}.

If the sample is exposed to the fundamental-absorption radiation with medium intensity $E = 0.3E_{max}$ (E_{max} is the highest intensity used) and with the photon energy of $h\nu = 1.4$ eV, the initially symmetric internal-friction peak broadens appreciably on the side of low temperatures (curve *2*). An increase in the radiation intensity to $E = 0.5E_{max}$ leads to a decrease in the peak height (curve *3*); for $E = E_{max}$ (~100 W/m^2), complete suppression of the initial peak to the internal-friction background occurs (curve *4*). Similar behavior of the internal-friction peak was observed under exposure of the sample to the extrinsic-absorption radiation with the photon energies in the range of 0.7–1.3 eV. Broadening of the internal-friction peak related to the deep-level electronic–mechanical relaxation to the side of negative temperatures and its suppression with a further increase in the intensity of illumination inducing the internal photoeffect occurs in all the studied samples of semi-insulating GaAs, GaP, and InP semiconductors doped with Fe, Cr, Co, Cu, Mn, and Ni transition-metal impurities.

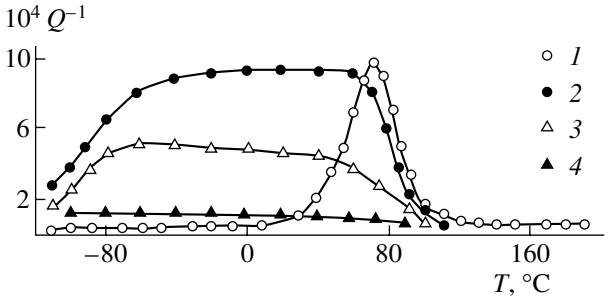

Fig. 1. Temperature dependence of internal friction in GaAs:Cr (*1*) without irradiation and (*2–4*) under optical irradiation ($h\nu$ = 1.4 eV) with intensities equal to (*2*) $0.3E_{max}$, (*3*) $0.5E_{max}$x, and (*4*) E_{max}.

Measurements of the internal-friction dependence on the intensity of radiation belonging to the intrinsic-absorption region for GaAs:Cr at room temperature showed (Fig. 2, curve *2*) that an increase in the internal friction is at first observed as a result of the peak broadening, and then a decrease in this peak sets in, which is related to optical suppression of the broadened peak. Such behavior of internal friction takes place at all temperatures below those corresponding to the peak, i.e., in the entire range of the peak broadening (Fig. 1). At the same time, when internal friction is suppressed at the temperature corresponding to its peak (+70°C), the maximum in the intensity dependence is not observed

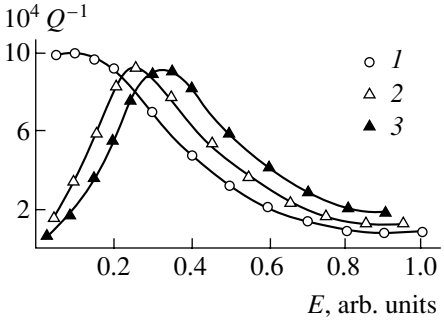

Fig. 2. Dependence of internal friction in GaAs:Cr on the irradiation intensity E at temperatures of (*1*) +70, (*2*) +20, and (*3*) –50°C.

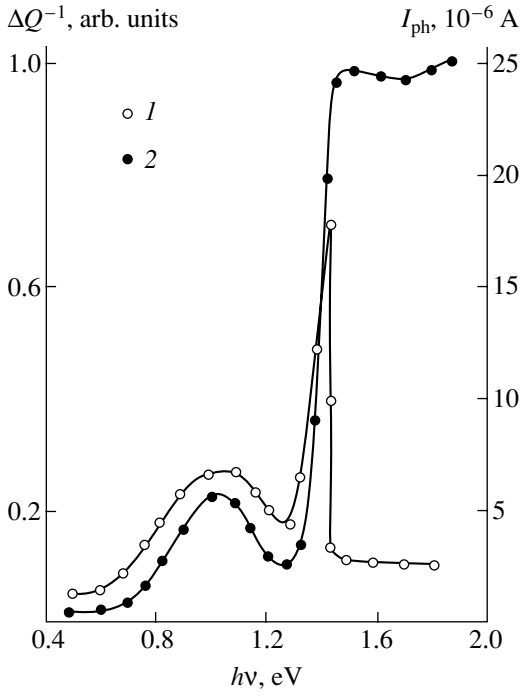

Fig. 3. (*1*) Spectral dependence of a relative decrease in internal friction $\Delta Q^{-1} = (1 - Q^{-1}/Q^{-1}_{max})$ and (*2*) spectral dependence of photocurrent I_{ph} in GaAs:Cr.

(Fig. 2, curve *1*). A decrease in the radiation intensity results in the reverse run of the curves shown in Fig. 2.

Thus, illumination of the samples leads not only to suppression of the initial internal-fiction peak but also to changes in its parameters, such as the width and the temperature position. At the same time, a decrease in the peak height, when the resistivity ρ of the sample is decreased [1, 2], occurs without variations in the peak temperature position and without changes in the main parameters of the peak. We believe that the distinction is related to differences in screening the piezoelectric field in the sample bulk; this screening can be caused either by the equilibrium concentration of free charge carriers distributed uniformly over the bulk (as in the case of variation in ρ) or by the nonequilibrium charge carriers that have a gradient over the sample depth (as in the case of illumination). Such an interpretation is generally consistent with special features of our experimental results, which are described below.

3.2. Spectral Dependence of the Internal-Friction Suppression

As was mentioned above, the degree of suppression of the internal-friction peak as a result of illumination depends on the wavelength of optical radiation. In this context, we studied the spectral characteristic of the relative decrease in the internal-friction peak $\Delta Q^{-1} = (1 - Q^{-1}/Q^{-1}_{max})$ for Cr-doped GaAs. The results are shown in Fig. 3 (curve *1*); it can be seen that an appreciable suppression of internal friction sets in with the energy of quanta close to the ionization energy of the corresponding deep-level center (0.76 eV). In the photon-energy range of $h\nu = 0.9$–1.0 eV, the curve features a resonance-type peak; in the vicinity of the photon energy of 1.4 eV corresponding to the GaAs band gap, a narrow peak with a half-width smaller than 0.1 eV is observed.

Since the degree of the internal-friction suppression is directly related to the concentration of nonequilibrium charge carriers generated by optical excitation, it is appropriate to compare the obtained curve with the photoconductivity spectrum of the same sample. Such measurements were performed for GaAs:Cr, and the results are shown in Fig. 3. In Fig. 3, it can be seen that there is a pronounced similarity between the spectral curves of relative decrease in the internal friction ΔQ^{-1} (curve *1*) and the photocurrent I_{ph} (curve *2*) in the extrinsic-absorption region; at the same time, there is a significant distinction between these curves in the intrinsic-absorption region, which may be interpreted in the following way.

The major contribution to photoconductivity is made by the regions of the sample with a higher concentration of nonequilibrium charge carriers. Therefore, a sharp increase in the intrinsic optical absorptivity and, as a result, a shift of the absorption region to the sample surface does not greatly affect the photocurrent. The intrinsic-absorption region in Fig. 3 (curve *2*) has the conventional form of a step with a threshold in the vicinity of $h\nu = 1.4$ eV. The presence of a narrow peak in this spectral region when the internal friction is measured (Fig. 3, curve *1*) can be explained in the following way. Internal friction is a manifestation of the inelasticity effect, and its magnitude depends on the volume fraction of the sample portion in which acoustic losses occur. An enhancement of the internal-friction suppression in the initial region of the intrinsic absorption is replaced by its rapid decrease during intense photoionization as a result of a shift of the absorption region to the irradiated sample surface (the optical intrinsic-absorption coefficient α in GaAs is equal to $\sim 10^4$ cm^{-1} [5]). These two competing processes form a narrow peak for the photon energy close to the semiconductor band gap. Apparently, the residual suppression of internal friction for $h\nu > 1.42$ eV is caused by the diffusion of free charge carriers to the sample bulk.

The coefficient of extrinsic absorption α is smaller by three orders of magnitude than that of intrinsic absorption [5]; therefore, the gradient of the nonequilibrium-carrier concentration across the sample thickness is small. As a result, the shapes of the curves in the extrinsic region for internal friction and for photoconductivity differ only slightly.

3.3. Kinetics of Internal Friction in the Sample Exposed to Optical Radiation

The use of the square-wave modulation of the light intensity made it possible to study the kinetics of growth and decay of the internal friction and to gain insight into the dynamics of recovery of the balance between the electronic–mechanical relaxation processes related to deep levels. In Fig. 4, we show the dependence of internal friction at the peak (+70°C) on time t for GaAs:Cr in the case of the abrupt switching on and off of the intrinsic-absorption radiation. An optical pulse resulted in a sharp suppression of internal friction. The decay and recovery of internal friction occurred in a time of ~0.2 s, which is close to the time of mechanical relaxation of flexural vibrations in the sample or to the damping time of free oscillations. This time may be considered as the lower limit of the response time for the method used. Similar dynamics of internal friction was observed at the high-temperature portion of the peak.

A radically different internal-friction kinetics was observed at temperatures lower than that of the peak. If we subject the sample to the intrinsic-absorption radiation with moderate intensity ($0.3E_{max}$), which results in a rise of the low-temperature portion of the internal friction peak, (Fig. 1, curve *2*) and then switch off the radiation, the internal friction recovers to the initial value in a time of ~1 min. The internal-friction relaxation curve corresponding to this situation is shown in Fig. 5. This curve includes two portions: portion *a* of fast relaxation and portion *b* of slow relaxation. Representation of this dependence on the semilog scale made it possible to use the slope of rectilinear segments to determine the relaxation times for both portions: $\tau_1 = (1.3 \pm 0.3)$ s (the fast-relaxation time) and $\tau_2 = (18 \pm 2)$ s (the slow-relaxation time).

When the GaAs:Cr sample was exposed to high-intensity radiation ($E = E_{max}$), which resulted in a complete suppression of internal friction (Fig. 1, curve *4*), the internal-friction kinetics was found to be more intricate, which is illustrated in Fig. 6. The presence of a spike in portion *a* (curve *1*) after the illumination was switched off can be explained by the fact that the internal friction passes through a maximum (the reverse run of curve *2* in Fig. 2) as the concentration of the photoexcited charge carriers is lowered. This spike in internal friction falls in the time range of the fast relaxation τ_1 (Fig. 6, portion *a*); after that, a slow relaxation with a characteristic time of $\tau_2 = (18 \pm 2)$ s is observed (Fig. 6, portion *b*).

Measurements of the intrinsic-photoconductivity kinetics in the same GaAs:Cr samples in which the internal-friction kinetics was measured under optical irradiation showed that there is an appreciable difference between the photoconductivity-relaxation time [(0.74 ± 0.10) ms] and the internal-friction relaxation time (18 s). This difference amounts to about four orders of magnitude.

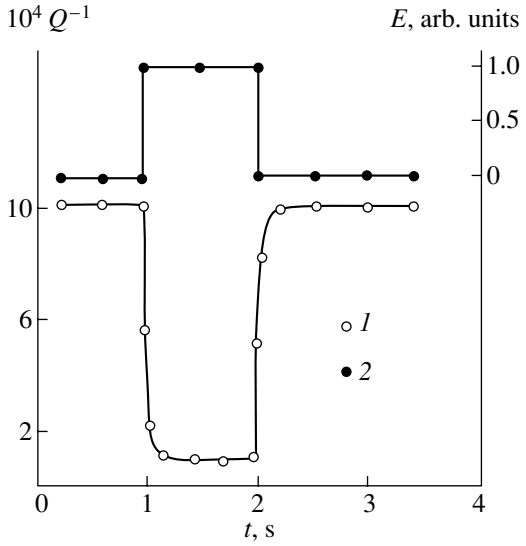

Fig. 4. (*1*) The time dependence of internal friction in GaAs:Cr at the sample temperature of +70°C under the pulsed irradiation ($h\nu$ = 1.4 eV). (*2*) The radiation-pulse shape $E(t)$.

Studying the effect of various factors on the slow-relaxation time showed that τ_2 decreases steadily as the resistivity is lowered (by ~5 s when ρ is changed by an order of magnitude). The presence of continuous intrinsic-absorption illumination reduced τ_2 by several times. On the other hand, the value of τ_2 increased from 8 to 18 s as the temperature increased from –80 to +20°C. The use of this temperature dependence, represented as $\log\tau_2 = f(1000/T)$, made it possible to determine the activation energy for the level related to the slow-relaxation process; this energy was found to be equal to (0.045 ± 0.005) eV.

4. DISCUSSION

In the absence of both optical irradiation and the accompanying generation of nonequilibrium charge carriers, the controlling stage of electronic–mechanical relaxation involving the deep-level centers in the high-resistivity semiconductors according to the model suggested in [1, 2] is the thermal emission of charge carriers from the deep-level centers. The initial curve representing the internal-friction temperature dependence of the unilluminated sample corresponds to these conditions (Fig. 1, curve *1*). An increase in the equilibrium concentration of charge carriers in the sample bulk causes the peak height of the internal friction to decrease without any changes in its shape and without a significant shift in its temperature position [1, 2]. The results obtained in this study indicate that, under exposure of the sample to optical radiation, the presence of nonequilibrium electrical conductivity results in an appreciable broadening of the internal-friction peak to lower temperatures (Fig. 1, curves *2*, *3*) and in the

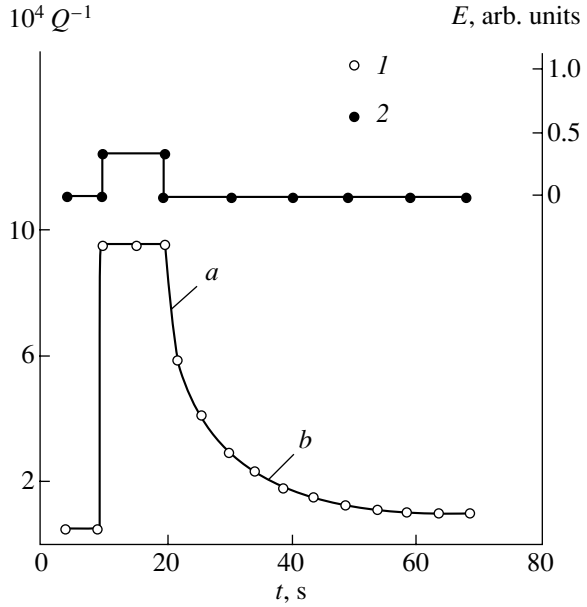

Fig. 5. (*1*) The time dependence of internal friction in GaAs:Cr at the sample temperature of +20°C and under pulsed irradiation of medium intensity ($h\nu$ = 1.4 eV). (*2*) The shape of the irradiation pulse $E(t)$.

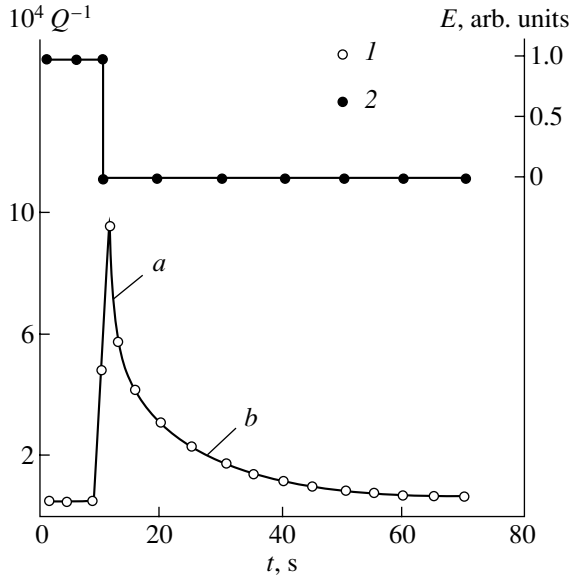

Fig. 6. (*1*) The time dependence of internal friction in GaAs:Cr at the sample temperature of +20°C and under pulsed irradiation ($h\nu$ = 1.4 eV) of high intensity. (*2*) The radiation-pulse shape $E(t)$.

emergence of slow relaxation (after the optical irradiation was switched off) of the internal friction with time constants on the order of tens of seconds. This effect is not observed at the temperature corresponding to the internal-friction peak and at higher temperatures.

At temperatures below that corresponding to the internal-friction peak, in which case the concentration of the charge carriers activated thermally from the deep-level centers is comparatively low, optical generation is found to be the major source of the free charge carriers. The flow of relaxation currents of nonequilibrium charge carriers in a sign-variable piezoelectric field induced by the sample deformation causes the internal friction to increase for certain values of electrical conductivity σ, which are governed by the condition for a maximum of the Maxwell relaxation in an ensemble of free charge carriers; i.e.,

$$\omega\tau_M = 1, \qquad (1)$$

where $\tau_M = \varepsilon\varepsilon_0/\sigma$ is the Maxwell relaxation time for electrical conductivity ($\varepsilon\varepsilon_0$ is the dielectric constant of the material). Since the thermally activated component in the quantity σ is not large in this situation, the internal friction does not feature a pronounced peak in the temperature range under consideration—in contrast to the unilluminated sample, in which case the value of σ is primarily controlled by the factor $\exp(E_F/T)$, where E_F is the Fermi energy. As a result, the temperature dependence of internal friction exhibits a certain "plateau," within which the relaxation losses are largely controlled by the radiation intensity, provided condition (1) is satisfied.

At the same time, for a medium level of illumination, thermal emission from the deep-level centers makes an appreciable contribution to the electronic–mechanical relaxation related to the deep-level centers both in the region of the internal-friction peak at T = +70°C and at higher temperatures; as a result, the shape of the peak in the region remains almost unchanged. Under the conditions of high-intensity illumination, the concentration of nonequilibrium charge carriers increases to such an extent that the suppression of internal friction occurs (Fig. 1, curve *4*); this suppression is caused by the predominance of the Maxwell relaxation.

In our opinion, the effect of slow relaxation of internal friction after the illumination was switched off is of particular interest (Figs. 5, 6); this effect is observed simultaneously with the broadening of the internal-friction peak on the low-temperature side and with the presence of a comparatively high concentration of optically excited free charge carriers. Some of the experimental data mentioned above indicate that binding of nonequilibrium charge carriers plays an important role in this relaxation. In compensated semiconductors, the shallow impurity levels are mainly unoccupied, as a result of the electron capture by deep-level traps. The fundamental-absorption irradiation results in the filling of shallow levels with electrons from the conduction band. In the temperature range under consideration, the probability of reverse thermal excitation of charge carriers from these levels to the conduction band is fairly high. Under these conditions, the shallow impurity levels act as attachment centers that are in a state of thermodynamic exchange with charge carriers from the

conduction band [6]. Termination of optical excitation gives rise to violation of the equilibrium in this exchange. The attachment levels begin to become gradually unoccupied via interaction with the conduction band; these levels can produce a decaying (with a characteristic time of $\sim\tau_2$) free-carrier concentration in the conduction band on termination of illumination and give rise to slow relaxation of internal friction (Figs. 5, 6). In its essence, this process can be compared to the effect of thermally stimulated electrical conductivity, in which case initiation of a decaying thermally stimulated current occurs after the fundamental-absorption irradiation of a high-resistivity semiconductor [6].

The involvement of the attachment centers in the internal-friction relaxation can be verified by the shape of the relaxation curve (Fig. 5), which includes an initial portion *a* of fast relaxation and a portion *b* of slow relaxation, and also by the value of the attachment-level activation energy (0.045 eV) and by an increase in τ_2 with temperature. In addition, a decrease in the slow-relaxation time τ_2 observed in our experiments under continuous illumination intensity is characteristic of the photoconductivity relaxation if the attachment centers are present [6]. In this case, the portion of slow relaxation approaches in its slope the initial portion of the fast relaxation. This effect is caused by a decrease in the role of attachment when the equilibrium charge-carrier concentration n_0 increases. The same cause can explain a decrease in the value of τ_2 as the resistivity ρ of the sample decreases, which leads to an increase in n_0 observed in our experiments.

Study of intrisic-photoconductivity kinetics in the GaAs:Cr samples showed that any significant slow relaxation was absent; the relaxation time determined from these measurements was found to be four orders of magnitude shorter than τ_2. This may serve as evidence to the effect that the relaxation parameters of nonequilibrium electrical conductivity in the sample bulk (as in the case of internal friction), or preferably at the surface (as in the case of photoconductivity), are radically different. This may be caused by the existence of a large number of recombination centers at the semiconductor surface, the presence of which suppresses the origination of the attachment effect and, consequently, decreases the relaxation time of nonequilibrium conductivity in the surface region of the semiconductor compared to the bulk relaxation time.

5. CONCLUSION

Thus, optical irradiation of single-crystal piezoelectric semiconductors containing deep-level impurity centers leads to an appreciable variation in the parameters of the sound absorption, which is related to the electronic–mechanical relaxation of deep levels. The original Debye peak of internal friction broadens by several tens of degrees centigrade to lower temperatures. In addition, a complicated dependence of internal friction on the radiation intensity is observed; this dependence is related to specific features of relaxation of nonequilibrium charge carriers generated by irradiation in a sign-variable piezoelectric field.

We discovered an unusual type of internal-friction spectral dependence. The latter features a sharp peak in the fundamental-absorption range; we explain the emergence of this peak by a shift of the optical-absorption region to the semiconductor surface layer.

The study of the internal-friction kinetics under optical irradiation made it possible to reveal the effect of the slow internal-friction relaxation after optical irradiation was terminated. We relate this effect to the Maxwell relaxation of nonequilibrium electrical conductivity under the conditions of establishing thermodynamic equilibrium between the conduction band and the attachment level.

The results we obtained may posses a certain practical importance. In particular, one can use a contactless acoustic method to rapidly determine many electrical parameters of piezoelectric semiconductors. Thus, for example, one can use the spectral dependence of the internal-friction suppression to determine the spectrum of energy levels in the band gap; also, the temperature dependence of the band gap can be studied with a high accuracy on the basis of the sharp peak in the intrinsic absorption. By studying the internal-friction relaxation kinetics under optical irradiation, one can (by analogy with the induced extrinsic photoconductivity) determine impurity-center parameters, such as the capture cross section and concentration of the centers, their occupancy after preliminary intrinsic-absorption illumination, and so on [6].

REFERENCES

1. V. I. Mitrokhin, S. I. Rembeza, V. V. Sviridov, and N. P. Yaroslavtsev, Fiz. Tverd. Tela (Leningrad) **27**, 2081 (1985) [Sov. Phys. Solid State **27**, 1247 (1985)].
2. V. I. Mitrokhin, S. I. Rembeza, V. V. Sviridov, and N. P. Yaroslavtsev, Phys. Status Solidi A **119**, 535 (1990).
3. A. N. Aleksandrov and M. I. Zotov, *Internal Friction and Defects in Semiconductors* (Nauka, Moscow, 1979).
4. V. I. Mitrokhin, N. P. Yaroslavtsev, S. I. Rembeza, *et al.*, USSR Inventor's Certificate No. 1054742, G01N 11/16 (1983).
5. É. M. Omel'yanovskiĭ and V. I. Fistul', *Transition Metal Impurities in Semiconductors* (Metallurgiya, Moscow, 1983).
6. S. M. Ryvkin, *Photoelectric Effects in Semiconductors* (Fizmatgiz, Moscow, 1963; Consultants Bureau, New York, 1964).

Translated by A. Spitsyn

Semiconductors, Vol. 36, No. 2, 2002, pp. 136–140. Translated from Fizika i Tekhnika Poluprovodnikov, Vol. 36, No. 2, 2002, pp. 144–148.
Original Russian Text Copyright © 2002 by Ageeva, Bronevoĭ, Krivonosov, Kumekov, Stegantsov.

ELECTRONIC AND OPTICAL PROPERTIES OF SEMICONDUCTORS

"LO-Phonon" Correlation between Picosecond Superluminescence Spectrum and Special Features of Absorption Spectrum in GaAs for Non-Fermi Distribution of Carriers Induced by Picosecond Light Pulse

N. N. Ageeva*, I. L. Bronevoĭ*, A. N. Krivonosov*, S. E. Kumekov, and S. V. Stegantsov***

** Institute of Radio Engineering and Electronics, Russian Academy of Sciences, Moscow, 101999 Russia*

e-mail: bil@mail.cplire.ru

*** Almaty Technological University, Almaty, 480012 Kazakhstan*

Received May 8, 2001; accepted for publication May 8, 2001

Abstract—Dense electron–hole plasma (EHP) was generated in a GaAs layer by a picosecond light pulse. Superluminescence phenomenon and local deviations of the light-absorption spectrum from that calculated for the Fermi distribution of EHP were observed. Deviations in the enhancement region, where the measured gain is less than the calculated one, and in the absorption region, where the opposite relation takes place, were named the "hole" and the "protrusion", respectively. The shape of the hole was similar to the shape of the superluminescence spectrum in the spectral region of the hole, as well as to the shape of the protrusion in the absorption spectrum. Both the spectral width of the spike, which was roughly equal to that of the hole, and its spectral position with respect to the superluminescence spectrum were governed by the energy of the longitudinal optical phonon. These correlations were attributed to superluminescence-induced depletion of levels at the conduction-band bottom and their filling with electrons due to the emission of longitudinal optical phonons. © *2002 MAIK "Nauka/Interperiodica".*

INTRODUCTION

A physical mechanism behind the local electron depletion of the levels in the conduction band was proposed in [1]. According to this mechanism, the depletion develops during picosecond superluminescence and involves intraband electron transitions via the emission of the longitudinal optical (LO) phonons. Let us consider how it works in the following situation. At room temperature, an interband absorption of an intense light pulse of 10-ps duration in a thin (~1 μm) GaAs layer resulted in generation of dense ($n = p > 10^{18}$ cm^{-3}) electron–hole plasma (EHP). EHP generation in GaAs was accompanied by superluminescence [2–5], which is the stimulated recombination radiation in an active medium without a resonator. Superluminescence intensity was estimated at >10^8 W/cm^2. Superluminescence relaxed with a characteristic time of about 10 ps and correlated with the relaxation of the concentration and the temperature of EHP [6, 7]. Presumably, the recombination superluminescence caused the depletion of inverse populations at the energy levels because of the stimulated recombination of electrons. This depletion led to a violation of the principle of the detailed balancing and to attenuation of screening [8] of the electron–LO-phonon interaction. As a result, highly intense transitions of electrons to the levels with depleted inverse populations occurred via the emission of LO phonons. The transitions accompanied by emission of LO phonons turned out to be sufficiently intense to cause the second depletion of the population in the conduction band. The second depletion region was located above the first one by the energy of an LO phonon $\hbar\omega_{LO}$ and induced a local increase in the absorption coefficient, hereafter referred to as the "spike" in the absorption spectrum.

Note that the depletion mechanism described above was used as a basis for interpreting the [1] modulation of the spectrum of transparency enhancement in a GaAs layer by "phonon" oscillations with a period

$$\Delta = \hbar\omega_{LO}(1 + m_e/m_h), \quad (1)$$

where m_e and m_h are the masses of an electron and a heavy hole, respectively. This mechanism was also used to explain the energy transport of electrons, which, according to our previous study [9], occurred via the emission of LO phonons during picosecond superluminescence.

Although this fact was not stated in [1] in an explicit form, depletion of populations discovered there due to electron transitions with the emission of LO phonons evidently implied the following approximate equality: $\tau_{e-LO} \approx \tau_{c-c}$, where τ_{e-LO} is the time of electron relaxation to the conduction band bottom with emission of one LO phonon, and τ_{c-c} is the time of the intraband

relaxation of electron energies to the Fermi distribution due to inelastic collisions between charge carriers.

In this study, correlation between the superluminescence spectrum and the local deviations of the light-absorption spectrum from that calculated for the Fermi distribution of EHP was discovered. The discrepancies between the calculated and the experimental spectra were observed in the region of light amplification (the experimental gain exceeded that calculated) and in the adjacent region of absorption (the experimental absorptivity was larger than that calculated). In what follows, the former deviation will be denoted as the hole in the enhancement region, and the latter one, as the protrusion in the absorption spectrum. The correlation was found between the shape and spectral position of the superluminescence spectrum, the hole in the amplification region, and the protrusion in the absorption spectrum. It is suggested that this correlation follows from the depletion mechanism described above [1].

EXPERIMENTAL

All the experiments were carried out at room temperature. As the experimental samples, we used $Al_{0.22}Ga_{0.78}As$–GaAs–$Al_{0.4}Ga_{0.6}As$ heterostructures grown by molecular-beam epitaxy on (100) GaAs substrate. Each epilayer was about 1 μm thick. The concentration of background impurities in the heterostructures did not exceed 10^{15} cm^{-3}. The substrate was etched over an area of 4×4 mm^2. $Al_xGa_{1-x}As$ layers, intended for stabilizing the surface recombination and mechanical rigidity, did not absorb the light with $\hbar\omega < 1.7$ eV used in the experiments. The samples were coated with SiO_2 and Si_3N_4 antireflection layers, which ensured the reflection of the normally incident light to be no more than 2% in the actual conditions of experiment. The interband absorption of a high-power 14-ps excitation pulse incident at an angle of 10° with the normal to the surface produced EHP in the GaAs layer. The excitation beam was focused to a diameter $D \approx 0.5$ mm in experiments with samples 1, 3 and to diameter $D \approx 0.25$ mm with sample 2.

The spectra of radiation from the GaAs layer and absorption in the GaAs layer were obtained. The time-integrated energy spectra of radiation $W_s(\hbar\omega)$ were measured within the space angle of 4° by the method described in [1]. To determine the absorption spectra, we measured the dependence $A = \log[T^0(\hbar\omega_p^1)/T^0(\hbar\omega_p)]$, which characterizes the spectrum of optical density A_0 of the unexcited sample ($A_0 \approx A\ln 10$, where T^0 is the transparency of the unexcited sample, $\hbar\omega_p$ is the photon energy of the probe pulse, and $\hbar\omega_p^1$ is the photon energy that is still insufficient for the interband absorption to begin. A probe pulse with a duration of 14 ps and a diameter $D_p = 0.3$ mm was used. The "pump-probe" scheme was employed to measure the spectral dependence $\log(T^1/T^0) = f(\hbar\omega_p)$, which represents the decrease in the optical density of GaAs due to EHP generation [4]; here, T^1 is the transparency of photoexcited GaAs. The probe beam was incident on the GaAs layer along the normal to the surface and propagated through the center part of the photoexcited region. The absorption coefficient in the photoexcited GaAs layer was determined from the expression $\alpha = [A - \log(T^1/T^0)]\ln 10 d^{-1}$, where d is the GaAs layer thickness.

Note that distribution of the intensity of light across the excitation beam (as well as the probe one) was approximately Gaussian. Therefore, the concentration and temperature of EHP, as well as the superluminescence radiation, may be nonuniformly distributed in space [10, 11].

The above-outlined physical mechanism for the depletion of levels in the conduction band was formulated and experimentally confirmed in [1]. More recently, under the same experimental conditions and using a sample similar to sample 1, an amplification spectral band was observed in the excited region of the GaAs layer [12]. However, the attempt to directly observe picosecond superluminescence failed in both studies for the following reason. Superluminescence radiation propagated in the radial direction, i. e., chiefly along the waveguiding GaAs heterostructure. The intensity of radially propagating superluminescence radiation considerably decreased (i) with distance from the active region and (ii) due to absorption of various nature, in particular, via the absorption by the band tails in the passive region of the GaAs layer. Because of this, the first stage of the experiments was intended to verify the radial propagation of superluminescence along the heterostructure photoexcited by a picosecond light pulse.

To do this, we used sample 2, which presented the same structure as sample 1 but was completely separated from the substrate. This heterostructure was pumped with a light beam 0.25 mm in diameter adjacent to the heterostructure end in order to minimize the absorption of the stimulated recombination radiation in the passive region of the GaAs layer. An intense directional radiation coming out of the end of the heterostructure was detected, thus confirming the longitudinal propagation of superluminescence parallel to the structure plane. The spectrum of radiation was significantly narrower than that of spontaneous luminescence at room temperature. The spectrum and the direction pattern of radiation with photon energy $\hbar\omega_s = 1.379$ eV are presented in Fig. 1. It can be seen that the maximum of radiation does not correspond to the direction parallel to the heterostructure layers. The point is that the amplification of light in an active medium is greater for the radiation that has experienced multiple total internal reflection from the GaAs/$Al_xGa_{1-x}As$ interfaces than for the radiation that has been propagating parallel to them. The radiation coming out of the heterostructure normally to the surface (corresponding angle in the

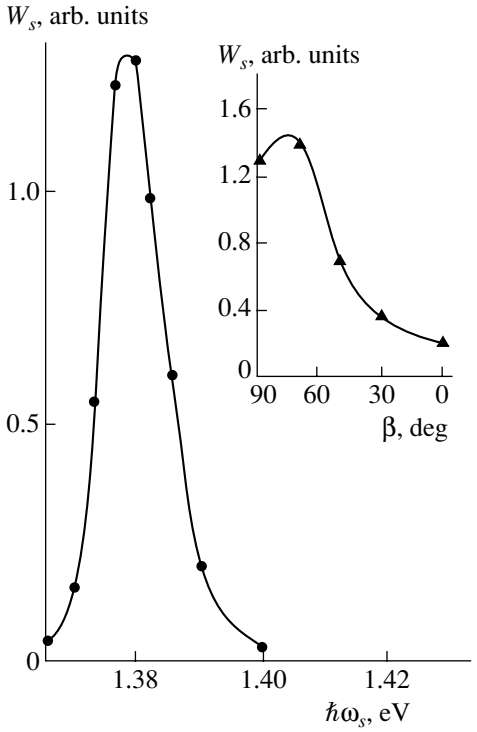

Fig. 1. Spectrum of the stimulated recombination radiation from the end of GaAs layer under excitation with photon energy $\hbar\omega_{ex}$ = 1.513 eV, sample 2. Inset shows the diagram of stimulated radiation with the photon energy $\hbar\omega_s$ = 1.379 eV. β is the angle measured from the normal to the epilayer surface.

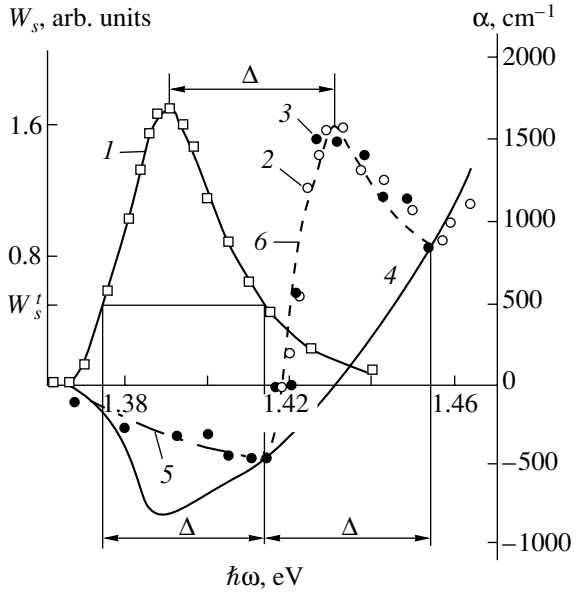

Fig. 2. (*1*) Superluminescence spectrum of GaAs, sample 3. Spectra of absorption in GaAs at τ_d = –3 ps for (*2*) sample 3 and (*3*) sample 1. (*4*) Absorption spectrum with the Fermi distribution of EHP $\alpha_{FD}(\hbar\omega)$. Curves (*5*), (*6*) are expounded in the text, $\hbar\omega_{ex}$ = 1.558 eV.

directivity pattern is β = 0) contained two comparable contributions: the spontaneous radiation and a small fraction of superluminescence that escaped from the heterostructure because of a certain imperfection in its waveguiding properties.

Note that the spectrum and other characteristics of the stimulated recombination radiation coming out of the end of the heterostructure (Fig. 1) should differ from those of superluminescence. Hence, it follows that this radiation is unsuitable for investigating the effects produced by superluminescence. The difference in characteristics stems, firstly, from the reflection of radiation from the end of the structure, which gives rise to the optical feedback affecting the characteristics of radiation. Secondly, the absorption in the passive region of the GaAs layer results in a heavy dependence of the spectrum of radiation on the distance between the active region and the end of the heterostructure, on the diameter of the pump beam, and so on.

In further experiments, we used sample 3. This heterostructure differed from sample 1, used in [1, 12], only in its reduced capacity for waveguiding. This led to the partial escape of superluminescence radiation from the heterostructure through the surface. The experiments performed in [5] with sample 3 proved that important features of superluminescence radiation are inherent in the radiation portion coming out of the heterostructure normal to the surface. Pumping sample 3 in the same manner as was done with sample 1 in [1, 12], we determined the superluminescence spectrum by measuring the radiation coming out of the structure normally to the surface (Fig. 2). Under the same pump conditions with sample 3, a protrusion in the absorption spectrum was measured for the pump–probe delay τ_d = –3 ps, i.e., near the peak of the pump pulse.

Figure 2 also shows the amplification of light and the protrusion in the absorption spectrum obtained for sample 1 even in more detail than in [12]. The protrusion in the absorption spectra looked similar for samples 1 and 3. Thus, the superluminescence spectrum, the light-amplification region, and the protrusion in the absorption spectrum shown together in Fig. 2 were obtained under the same picosecond photoexcitation of GaAs samples and may be considered simultaneously.

DISCUSSION

The interpretation of the experimental results obtained was complicated by the lack of a theoretical basis for both the kinetics of non-Fermi EHP and the picosecond superluminescence in the active region of the GaAs layer.

At highly intense superluminescence, certain inversion energy levels become less populated than those for the Fermi distribution of carriers. In other words, “hole burning” occurs in the amplification region of the

absorption spectrum. The "hole" spectrum in the amplification region is defined by the expression

$$\alpha_H(\hbar\omega) = \alpha_{FD}(\hbar\omega) - \alpha(\hbar\omega), \quad (2)$$

where $\alpha_{FD}(\hbar\omega)$ is the absorption spectrum for the Fermi distribution of EHP and $\alpha(\hbar\omega)$ is the absorption spectrum obtained experimentally.

The spectrum $\alpha_{FD}(\hbar\omega)$, shown in Fig. 2, was calculated in two stages. At the first stage, we assumed that all the holes were heavy and the electrons were located in the Γ_6 valley. Energy dependences of singe-particle states ρ_i were taken in the form $\rho_i \propto E_i^{1/2}$. For quasi-Fermi levels of electrons μ_e and holes μ_h, the following obvious relationship was valid:

$$n(T_c, \mu_e) = p(T_c, \mu_h), \quad (3)$$

where n and p are the concentrations of electrons and holes, respectively, and T_c is the temperature of the carriers. The electron concentration in the conduction band was defined as

$$n = N_c F_{1/2}(\zeta_e). \quad (4)$$

Here, N_c is the effective density of states in the conduction band

$$N_c = 2[2\pi m_e kT_c/(2\pi\hbar)^2]^{3/2}, \quad (5)$$

and $F_{1/2}(\zeta_e)$ is the Fermi-Dirac integral with the subscript 1/2 and $\zeta_e = \mu_e/(kT_c)$. The hole concentration in the valence band is defined by

$$p = N_v F_{1/2}(\zeta_h). \quad (6)$$

Here, the effective density of states in the heavy hole band N_v can be determined from an expression similar to (5) with substitution of m_e by m_{hh} $\zeta_h = (E_v - \mu_h)/(kT_c)$, where E_v is the energy of the valence-band top measured, as well as μ_e and μ_h, from the conduction band bottom.

Using the expressions presented above and taking into account the neutrality condition (3), we obtain

$$F_{1/2}(\zeta_e)/F_{1/2}(\zeta_h) = m_{hh}^{3/2}/m_e^{3/2} = 22, \quad (7)$$

where $m_e = 0.063m_0$ and $m_{hh} = 0.5\,m_0$ are the respective effective masses of the electrons and the heavy holes.

The first spectrum was calculated by fitting. Two criteria were used for the fitting. The spectrum calculated should, firstly, pass through the experimental points near the short- and the long-wavelength wings of the protrusion in the absorption spectrum and, secondly, satisfy the relationship (7). Moreover, it was required that the long-wavelength wing of the spectrum coincide with the band gap $E_g = 1.37$ eV. The latter was determined as the photon energy at which the long-wavelength slope of the superluminescence spectrum intersects the radiation energy level, which is slightly above zero, $W_s = 0.12$ arb. units [13–15]. This procedure eliminated the influence of the internal strain and impurities otherwise leading to the "smearing" of the spectrum edge. The values $T_c = 52$ meV, $\mu_e = 0.145$ eV, $\mu_h = -E_g + 0.083$ eV, and $n = p = 4.7 \times 10^{18}$ cm^{-3} were determined from the absorption spectrum calculated by fitting. A small error is introduced into the values of the parameters specified above due to the fact that, in the vicinity of the band gap edges, the $\rho_i(E_i)$ function has the shape of an abrupt step, which is slightly different from the shape assumed for the calculation, $\rho_i \propto E_i^{1/2}$ [16].

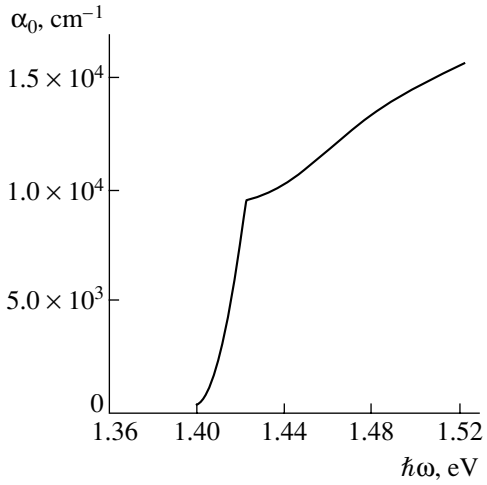

Fig. 3. Absorption spectrum of unexcited GaAs for samples 1 and 3.

The experimental spectrum of absorption $\alpha_0(\hbar\omega)$ for an unexcited sample is shown in Fig. 3. To account for the decrease in the band gap due to the Coulomb interaction, this spectrum was shifted towards the longer wavelengths to the energy $E_g = 1.37$ eV mentioned above. Using the shifted spectrum and the values of T_c, μ_e, and μ_h indicated above, we calculated the more realistic second spectrum by the following formula:

$$\alpha_{FD}(\hbar\omega) = \alpha_0(\hbar\omega - (E_{g0} - E_g)) \times \{1 - f_e(\varepsilon_e) - f_{hh}(\varepsilon_h)\}. \quad (8)$$

Here, $E_{g0} = 1.403$ eV is the band gap of the unexcited sample; ε_e and ε_h are the respective energies of the electrons and heavy holes related by a direct optical transition; and f_e and f_{hh} are the Fermi–Dirac distributions of the electrons and heavy holes, respectively.

Let us consider simultaneously the superluminescence spectrum, the hole in the amplification region, and the protrusion in the absorption spectrum (Fig. 2). The combined study enables one to reveal a number of features which may follow from the depletion of populations [1] arising during picosecond superluminescence and involving the intraband electron transitions via the emission of LO phonons.

(i) The spectral position of the minimum of the hole coincides with the peak on the superluminescence spectrum. The peak of the protrusion in the absorption spectrum is shifted by Δ with respect to the peak on the superluminescence spectrum.

(ii) The spectral width of the protrusion on the absorption spectrum, as well as the spectral width of the hole in the amplification region, turned out to be equal to Δ. The short-wavelength edge of the hole coincides with the long-wavelength edge of the projection. Apparently, the emission of LO phonons, stimulated by a violation of the principle of the detailed balancing, limits the spectral width of both the hole and the protrusion.

(iii) Let W_s^t designate the energy of superluminescence at the two values of $\hbar\omega$ corresponding to the edges of the hole. Then, we separate the portion of the superluminescence spectrum above the W_s^t level, normalize it to the fitted constant coefficient b, and add the result to the calculated spectrum $\alpha_{FD}(\hbar\omega)$. The final result,

$$\alpha_{FD}(\hbar\omega) + \{bW_s(\hbar\omega) - W_s^t\},$$

is presented in Fig. 2 by curve *5*, which is in good agreement with the experimental values in the amplification region. This fact indicates that the shape of the superluminescence spectrum above the W_s^t level is similar to the shape of the hole in the amplification region:

$$W_s(\hbar\omega) - W_s^t \approx -\alpha_H(\hbar\omega). \quad (9)$$

(iv) The superluminescence spectrum portion lying above the W_s^t level was normalized to the fitted constant coefficient b_1, shifted by Δ to the short-wavelength region, and added to the spectrum $\alpha_{FD}(\hbar\omega)$. The result is shown in Fig. 2 by curve *6*, which correlates well with the protrusion in the absorption spectrum. The protrusion is given by $\alpha_{FD}(\hbar\omega) + b_1\{W_s(\hbar\omega - \Delta) - W_s^t\}$. The protrusion was defined by the expressions

$$\alpha_p(\hbar\omega) = \alpha(\hbar\omega) - \alpha_{FD}(\hbar\omega).$$

Thus, the shape of the superluminescence spectrum above the W_s^t level is similar to the shape of the protrusion in the absorption spectrum:

$$\alpha_P(\hbar\omega) \propto W_s(\hbar\omega - \Delta) - W_s^t. \quad (10)$$

(v) As evident from items (iii) and (iv), the hole in the amplification region and the protrusion in the absorption spectrum are similar in shape: $\alpha_P(\hbar\omega - \Delta) \propto -\alpha_H(\hbar\omega)$.

ACKNOWLEDGMENTS

This study was supported by the Russian Foundation for Basic Research (project no. 01-02-16694) and the Ministry of Industry and Science of the Russian Federation.

We are indebted to V. I. Perel, Yu. D. Kalafati, and G. N. Shkerdin for their helpful participation in discussions of the results and helpful comments.

REFERENCES

1. I. L. Bronevoi, A. N. Krivonosov, and V. I. Perel, Solid State Commun. **94**, 805 (1995).
2. D. Hulin, M. Joffre, A. Migus, *et al.*, J. Phys. (Paris) **48**, 267 (1987).
3. N. N. Ageeva, I. L. Bronevoĭ, E. G. Dyadyushkin, and B. S. Yavich, Pis'ma Zh. Éksp. Teor. Fiz. **48**, 252 (1988) [JETP Lett. **48**, 276 (1988)].
4. N. N. Ageeva, I. L. Bronevoi, E. G. Dyadyushkin, *et al.*, Solid State Commun. **72**, 625 (1989).
5. I. L. Bronevoĭ and A. N. Krivonosov, Fiz. Tekh. Poluprovodn. (St. Petersburg) **32**, 537 (1998) [Semiconductors **32**, 479 (1998)].
6. Yu. D. Kalafati and V. A. Kokin, Zh. Éksp. Teor. Fiz. **99**, 1793 (1991) [Sov. Phys. JETP **72**, 1003 (1991)].
7. I. L. Bronevoĭ and A. N. Krivonosov, Fiz. Tekh. Poluprovodn. (St. Petersburg) **32**, 542 (1998) [Semiconductors **32**, 484 (1998)].
8. N. N. Ageeva, I. L. Bronevoi, and A. N. Krivonosov, in *Abstracts of the 25th International Conference on Physics of Semiconductors, ICPS-25, Osaka, Japan, 2000*, Part I, D025, p. 49.
9. I. L. Bronevoĭ and A. N. Krivonosov, Fiz. Tekh. Poluprovodn. (St. Petersburg) **33**, 13 (1999) [Semiconductors **33**, 10 (1999)].
10. Yu. D. Kalafati, V. A. Kokin, H. M. Van Driel, and G. R. Allan, in *Hot Carriers in Semiconductors*, Ed. by K. Hess *et al.* (Plenum, New York, 1996), p. 587; Yu. D. Kalafati and V. A. Kokin, in *Abstracts of the 25th International Conference on Physics of Semiconductors, ICPS-25, Osaka, Japan, 2000*, Part I, p. 53.
11. E. O. Goebel, O. Hildebrand, and K. Lohnert, IEEE J. Quantum Electron. **QE-13**, 848 (1977).
12. I. L. Bronevoi, A. N. Krivonosov, and T. A. Nalet, Solid State Commun. **98**, 903 (1996).
13. N. N. Ageeva, I. L. Bronevoĭ, and A. N. Krivonosov, Fiz. Tekh. Poluprovodn. (St. Petersburg) **35**, 65 (2001) [Semiconductors **35**, 67 (2001)].
14. D. Olego and M. Cardona, Phys. Rev. B **22**, 886 (1980).
15. S. Tarucha, H. Kobayashi, Y. Horikoshi, and H. Okamoto, Jpn. J. Appl. Phys. **23**, 874 (1984).
16. J. S. Blakemore, J. Appl. Phys. **53**, R123 (1982).

Translated by A. Sidorova-Biryukova

Semiconductors, Vol. 36, No. 2, 2002, pp. 141–147. Translated from Fizika i Tekhnika Poluprovodnikov, Vol. 36, No. 2, 2002, pp. 149–154.
Original Russian Text Copyright © 2002 by Rasulov, Salenko, Kambarov.

ELECTRONIC AND OPTICAL PROPERTIES OF SEMICONDUCTORS

Linear Photovoltaic Effect in Gyrotropic Crystals

R. Ya. Rasulov, Yu. E. Salenko, and D. Kambarov

Fergana State University, Fergana 71200, Uzbekistan

Submitted April 9, 2001; accepted for publication May 16, 2001

Abstract—The ballistic and shift linear photovoltaic effects caused by asymmetry of the probability of optical transitions between subbands M_1' and M_2' in tellurium (involving long-wave optical phonons) and by carrier shift in real space at quantum transitions, respectively, are considered. The temperature and frequency dependences of the current of both ballistic and shift linear photovoltaic effects for the photon and phonon mechanisms are analyzed. © *2002 MAIK "Nauka/Interperiodica".*

INTRODUCTION

Steady current initiation in homogeneous piezoelectrics exposed to linearly (or circularly) polarized light is referred to as the linear photovoltaic effect (LPVE) (see [1, 2]).

This effect is described by the tensor of the third rank $\chi_{\alpha\beta\gamma}$; i.e.,

$$j_\alpha = I\chi_{\alpha\beta\gamma}(e_\alpha e_\gamma^* + e_\gamma e_\beta^*)/2, \qquad (1)$$

where I is the intensity, **e** is the polarization vector of exciting light, and **j** is the LPVE current density. The tensor $\chi_{\alpha\beta\gamma}$ is symmetric with respect to the last two subscripts and similar in symmetry properties to the piezoelectric tensor; hence, the LPVE can arise in piezoelectric crystals.

The LPVE in semiconductors (Te, *n*-GaP, and *p*-GaAs, see, for example, [1, 2]) was studied at frequencies lower than the fundamental absorption edge. Under these conditions, the LPVE is obviously caused by either impurity photoionization or light absorption at free carriers. The one-phonon LPVE mechanism in semiconductors was suggested in [3, 4]. This mechanism is related to transitions between subbands of degenerate bands or between adjacent bands of the same type (*n* or *p*) and was later referred to as the ballistic LPVE (BLPVE). This effect is caused by terms of different parity in the wave vector **k** in the electron–phonon (phonon mechanism) or electron–photon (photon mechanism) interaction Hamiltonian. This mechanism was also assumed in [3] to be responsible for the LPVE observed in tellurium.

There exists one more contribution to the LPVE, i.e., the displacement LPVE (DLPVE) caused by a carrier shift to a finite distance in real space at quantum transitions. The consistent kinetic theory of the DLPVE was developed in [5] taking into account scattering and recombination. The problem of the quantitative theory of photon and phonon mechanisms of both BLPVE and DLPVE in gyrotropic crystals remains to be solved. This study is aimed at solving this problem using the example of tellurium.

We note that the question as to what mechanisms are responsible for the LPVE in specific crystals under certain experimental conditions can be solved only by the quantitative comparison of theoretical and experimental data. Before proceeding to the concrete LPVE mechanisms, we dwell briefly on the tellurium band structure. As is known, the Te conduction- and valence-band extrema are located at points *M* and *P* of the Brillouin zone, transiting from one into the other by the time reversal (see, for example, [6]). In the bases M_1 and M_2, the basis functions are $(Y_{3/2} + Y_{-3/2})/2^{1/2}$ and $(Y_{3/2} - Y_{-3/2})/2^{1/2}$, respectively. On the other hand, $\hat{I}$, σ_z and σ_x, σ_y are transformed by the representations $\Gamma_2 = M_1 \times M_1^* = M_2 \times M_2^*$ and $\Gamma_2 = M_1 \times M_2^*$, respectively, where $\hat{I}$ is a 2×2 unit matrix and σ_α ($\alpha = x, y, z$) are the Pauli matrices. If we pass to the basis $Y_{3/2}$ and $Y_{-3/2}$ using the unitary transformation

$$\hat{S} = \frac{1}{\sqrt{2}}\begin{pmatrix} 1 & 1 \\ 1 & -1 \end{pmatrix},$$

σ_z, σ_y, and σ_y are transformed into σ_x, σ_z, and $-\sigma_y$, respectively. The old and new basis notations are $\bar{\sigma}_z$, $\bar{\sigma}_x$, $\bar{\sigma}_y$ and σ_z, σ_x, σ_y, respectively.

The time reversal operator

$$\hat{K} = \begin{pmatrix} 0 & -1 \\ 1 & 0 \end{pmatrix}$$

transforms the bases M_1 and M_2 into M_2 and $(-M_1)$, respectively. The unitary transformation $\hat{K}$ changes the $\bar{\sigma}_z$ and $\bar{\sigma}_x$ signs, while the $\bar{\sigma}_y$ sign remains unchanged, since the former matrices are odd with respect to the

time reversal and σ_y is even. Then the effective Hamiltonian of charge carriers is written as

$$\hat{H} = \hat{H}_0 + \sum_{\alpha} A_\alpha \sigma_a, \tag{2}$$

where

$$\hat{H}_0 = Ak_\perp^2 + Bk_z^2 + \bar{C}(k_+^3 + k_-^3) + i\bar{\gamma}k_z(k_+^3 + k_-^3), \quad (\Gamma_1);$$

$$A_x = \Delta + C'(k_+^3 + k_-^3) - \eta_\perp k_\perp^2 - \eta_\parallel k_z^2 + i\gamma' k_z(k_+^3 - k_-^3), \quad (\Gamma_1); \tag{3}$$

$$A_y = \delta''(k_+^3 - k_-^3) + \delta'''(k_+^3 + k_-^3), \quad (\Gamma_2);$$

$$A_z = \beta k_z + i\delta'(k_+^3 - k_-^3) + \delta_0 k_z(k_+^3 + k_-^3). \quad (\Gamma_2).$$

Here, the terms $\hat{H}_0$ in parentheses are the representations according to which $\hat{H}_0$ and A_α are transformed. The $M_{1,2}'$ function phases are chosen so that the factor at k_z is real; i.e., there is no term proportional to k_z in A_y. This procedure can always be employed. Taking into account that $\hat{K}k_\alpha = -k_\alpha$, we can readily show that the constants β, δ', C', A, B, $\bar{\gamma}$, and δ''' do not reverse sign when passing from M to P, while δ_0, $\eta_\perp$, $\eta_\parallel$, γ', $\bar{C}$, and δ'' do ($k_\pm = k_x \pm ik_y$, $k_\perp^2 = |k_\pm|^2$, and 2Δ is the spin–orbit splitting of the valence band at the point $M(P)$ of the Brillouin zone). Therefore, the terms including a product of even or odd band constants are hereafter retained (when calculating the LPVE current).

The wave functions M_1' and M_2' in the upper valence bands represent the superpositions of states with the angular momentum z-component $m_z = \pm 3/2$,

$$\Psi_{M_1'} = \sum_{m_z = \pm 3/2} C_{m_z}^{(l)} |m_z\rangle, \tag{4}$$

where $C_{3/2}^{(1)} = C_{-3/2}^{(2)} = C_1 = \sqrt{(1+\eta)/2}$, $C_{-3/2}^{(1)} = -C_{3/2}^{(2)} = C_2 = \sqrt{(1-\eta)/2}$, and $\eta = \beta k_z(\Delta^2 + \beta^2 k_z^2)^{-1/2}$. Here, one should bear in mind that the choice of coefficients C_l ($l = 1, 2$) corresponds to $\Delta > 0$, i.e., $C_1 \times C_2 = 2^{-1} \times \Delta(\Delta^2 + \beta^2 k_z^2)^{-1/2}$ and contains Δ, rather than $|\Delta|$ (the subscripts "2" and "1" are related to the lower and upper hole bands, respectively). In order to readily pass from M to P, we introduce the parameter $r = -\Delta/|\Delta|$ in C_2; i.e., $C_2 = r\sqrt{(1-\eta)/2}$. Since the spectrum $E_1 \propto -\sqrt{\Delta^2 + \beta^2 k_z^2}$ in the lower valence band, the signs of C_1 and C_2 should be different and vice versa for electrons of the valence band. Then, the hole spectrum in the valence band is given by

$$E_{M_{1,2}'} = \lambda_v \pm (\Delta^2 + \beta^2 k_z^2)^{1/2}, \tag{5}$$

where $\lambda_v = Ak_\perp^2 + Bk_z^2$, $A = \hbar^2/2m_\perp$, $B = \hbar^2/2m_\parallel$, and $m_\perp$ and $m_\parallel$ are the transverse and longitudinal effective masses of holes in the subbands M_1' and M_2' and are equal to the opposite-sign effective masses of electrons.

BALLISTIC AND DISPLACEMENT LINEAR PHOTOVOLTAIC EFFECTS

Now, we successively consider the (phonon and photon) BLPVE and DLPVE mechanisms [7, 8]. First, we group the optical processes into (i) intraband and (ii) interband ones (see Figs. 1a–1d in [4]). To simplify the problem, we set 2Δ, $\hbar\omega \gg \hbar\Omega_{1,2}$, k_BT ($\hbar\omega$ is the photon energy, $\hbar\Omega_{1,2}$ is the LO phonon energy, T is the temperature, and k_B is the Boltzmann constant). Then, we regard the upper valence band M_2' as empty, and we take into account the nonparabolicity of the lower band. In general, we should take into account the processes related to the stimulated emission of a photon, assuming that it is initially emitted and then absorbed (see Fig.1e in [4]). We note that the contribution of the intraband optical transition of holes to the BLPVE differs from that discussed in [9, 10] by the following. We take into account the intraband optical transitions involving virtual states in other bands, while the virtual state in [9, 10] is in the same band during intraband light absorption (involving two phonons or double scattering at impurity atoms). In the former case, one-phonon processes or single scattering at impurity atoms can cause the LPVE (see, for example, [10]). In the latter actual case, when the operator of interaction between electrons and phonons or impurity atoms depends only on the momentum transferred to a carrier, one should consider anharmonic processes [9].

According to [4], the BLPVE current in the approximation of the momentum relaxation time is written as

$$\mathbf{j} = e\sum_{n\mathbf{k};\, n'\mathbf{k}'} (\mathbf{v}_{n'\mathbf{k}'}\tau_{n'\mathbf{k}'} - \mathbf{v}_{n\mathbf{k}}\tau_{n\mathbf{k}}) W_{n'\mathbf{k}',\, n\mathbf{k}}, \tag{6}$$

where $\mathbf{e}$ is the elementary charge and $\mathbf{v} = \hbar^{-1}\nabla_{\mathbf{k}}\hat{H}(\mathbf{k}')$ is the velocity operator. Subscripts n and n' for holes in the subbands M_1' and M_2' numerate subbands of the valence band: $n(n') = 1$ and 2 for M_1 and M_2. The effective relaxation time τ in (6) accounts for the fact that the hole momentum direction is lost during two or three sequential collisions with phonons or impurity atoms, rather than due to a single collision. The asymmetric component of the probability of a hole transition from the state (n, $\mathbf{k}$) to the final state (n', $\mathbf{k}'$) is defined by the conventional formula of quantum mechanics,

$$W_{n'\mathbf{k}',\, n\mathbf{k}}^{(\mathrm{as})} = \frac{2\pi}{\hbar}\left|M_{n'\mathbf{k}',\, n\mathbf{k}}^{(\mathrm{as})}\right|\delta(E_{n'\mathbf{k}'} - E_{n\mathbf{k}}). \tag{7}$$

To determine the photocurrent, we should calculate the transition matrix element $M_{n'\mathbf{k}',\, n\mathbf{k}}$ in the second

order of the perturbation theory using the following operators of the electron–phonon and electron–photon interactions.

(i) The interaction between electrons and polar optical phonons,

$$D_{\mathbf{q}} = iC\mathbf{u}_{\mathbf{q}}\mathbf{q}q^{-2} + d_0 u_z q_z, \tag{8}$$

where C and d_0 are the long- and short-range interaction constants, $\mathbf{u}_{\mathbf{q}}$ is the displacement operator, and $\mathbf{q} = \mathbf{k}' - \mathbf{k}$ is the phonon wavevector.[1]

(ii) The electron–photon interaction,

$$\hat{H}_{\text{el-phot}} = i\frac{e}{\omega}\mathbf{A}_0 \cdot \mathbf{v}, \tag{9}$$

where $\mathbf{A}_0$ is the electromagnetic wave vector–potential.

Then we proceed similarly to [8]. The temperature and frequency dependences of the BLPVE current are determined by formulas (4a)–(4c) of [8], delta functions fix all the wave vectors of final hole states ($\mathbf{k}'$) for each optical transition type. The values ($\mathbf{k}'$) are determined from the conditions of equal energies of the final and one of the intermediate states.

As is known, $2\Delta > \hbar\Omega$ (for tellurium, $2\Delta = 126$ meV, the LO phonons energies are $\hbar\Omega_1 = 11$ meV and $\hbar\Omega_2 = 7.7$ meV [6]). Therefore, real photonless transitions of thermalized holes from the subband M_1' to M_2' (and back) are absent.

It is noteworthy that the asymmetric distribution of carriers over momentum in the LPVE photon mechanism in semiconductors with a complex band arises due to the different (in wave vector) parity of the terms in the interband matrix element of the momentum operator. From the symmetry considerations, the latter for tellurium can be written as

$$\mathbf{e}\mathbf{p}_{21} = \langle M_2|\mathbf{e}\mathbf{p}|M_1\rangle = \frac{m_0}{\hbar}\left\langle 2\mathbf{k}\left|\mathbf{e}\frac{\partial\hat{H}}{\partial\mathbf{k}}\right|1\mathbf{k}\right\rangle$$
$$= Q(e_+k_- + e_-k_+) + D(e_+k_+^2 + e_-k_-^2),$$
$$e_\pm = (e_x \pm ie_y)/\sqrt{2}, \quad k_\pm = k_x + ik_y,$$

where Q and D are the parameters including the band constants; their dependence on k_z and ω can be determined by substituting (2) in view of (3) into the latter expression and from the energy conservation law for the considered optical transition. Then, the current of the DLPVE photon mechanism is readily found as

$$j_\alpha = 32\frac{I}{\hbar\omega}K\,\mathrm{Im}\left[\frac{D(k_z = k_{z0})}{Q(k_z = k_{z0})}\right]\chi_{\alpha xy}, \tag{10}$$
$$k_{z0} = \beta_\nu^{-1}[(\hbar\omega/2) - \Delta_2^2]^{1/2},$$
$$\chi_{\alpha xy} = (e_x^2 - e_y^2)\delta_{\alpha x} - 2e_xe_y\delta_{\alpha y},$$
$$K(\omega, T) = \frac{e^2|Q|^2(2m_\perp k_BT)^2 e^{\mu/k_BT}}{32\pi m_0^2 c n_\omega \hbar^3 \beta_\nu \sqrt{(\hbar\omega/2)^2 - \Delta^2}} \tag{11}$$
$$\times \exp\left[\frac{\hbar\omega(\hbar^2 k_{z0}^2/m_\parallel)}{2k_BT}\right],$$

where the latter is the interband absorptivity of light with polarization $\mathbf{e} \perp \mathbf{C}_3$, $\mathbf{C}_3$ is the principal crystallographic axis, and μ is the chemical potential of holes. Thus, the temperature dependence of the current of the DLFVE photon mechanism in tellurium is completely defined by the temperature dynamics of the light absorptivity $K(\omega, T)$.

It was shown in [11] that the DLPVE phonon mechanism should arise due to anisotropy in the distribution function of photoexcited holes with their asymmetric scattering by phonons (or impurity atoms). This anisotropy is proportional to $e_xe_yk_xk_y(k_x^2 - k_y^2)$ and arises at $\mathbf{e} \perp \mathbf{C}_3$ in tellurium due to the term $(1/2)\delta_0\sigma_zk_z(k_+^3 + k_-^3)$ in $\hat{H}(\mathbf{k})$. Then, the corresponding average displacement $\Delta R \approx k_z^2k_x^2k_y^2(k_x^2 - k_y^2)$ and, when averaged over the solid angle, $\mathbf{k}$ vanishes.

The contributions to the BLPVE current, produced by the processes A, B, and C were derived in [8] (see formulas (4a)–(4c) therein), where it is taken into account that this contribution arises only in the kinetic-equation term describing the arrival of carriers in the case of Boltzmann statistics (this is not always the case, for example, when taking into account the "hump" of the subbands M_1' or X_1 in tellurium or n-GaP, respectively).

For convenience in further analysis, we write the functions $\Phi_i(\mathbf{k}, \mathbf{k}')$ defined by the matrix elements of the transitions involving a photon and a phonon,

$$\Phi_1 = \mathrm{Im}(d_{22'}^{(\mu)}\mathbf{e}\mathbf{p}_{2'1'}^{(\pm)}d_{1'1}^{(\pm)}\mathbf{e}^*\mathbf{p}_{12}^{(\mu)}),$$
$$\Phi_2 = \mathrm{Im}(d_{21'}^{(\mu)}\mathbf{e}\mathbf{p}_{1'2'}^{(\pm)}d_{2'1}^{(\pm)}\mathbf{e}^*\mathbf{p}_{12}^{(\mu)}),$$
$$\Phi_3 = \mathrm{Im}(d_{22'}^{(\mu)}\mathbf{e}\mathbf{p}_{2'2'}^{(\pm)}d_{2'1}^{(\pm)}\mathbf{e}^*\mathbf{p}_{12}^{(\mu)}),$$
$$\Phi_4 = \mathrm{Im}(d_{21'}^{(\mu)}\mathbf{e}\mathbf{p}_{1'1'}^{(\pm)}d_{1'1}^{(\pm)}\mathbf{e}^*\mathbf{p}_{12}^{(\mu)}),$$
$$\Phi_5 = \mathrm{Im}(d_{21'}^{(\mu)}\mathbf{e}\mathbf{p}_{1'1'}^{(\pm)}d_{11}^{(\pm)}\mathbf{e}^*\mathbf{p}_{12}^{(\mu)}), \tag{12}$$
$$\Phi_6 = \mathrm{Im}(d_{22'}^{(\mu)}\mathbf{e}\mathbf{p}_{2'1}^{(\pm)}d_{11}^{(\pm)}\mathbf{e}^*\mathbf{p}_{12}^{(\mu)}),$$
$$\Phi_7 = \mathrm{Im}(\mathbf{e}\mathbf{p}_{22}^{(\pm)}d_{21'}^{(\mu)}d_{1'1}^{(\pm)}\mathbf{e}^*\mathbf{p}_{12}^{(\mu)}),$$
$$\Phi_8 = \mathrm{Im}(\mathbf{e}\mathbf{p}_{22}^{(\pm)}d_{22'}^{(\mu)}d_{2'1}^{(\pm)}\mathbf{e}^*\mathbf{p}_{12}^{(\mu)}),$$

[1] We note that the distribution function asymmetry can arise if one takes into account (along with (8)) the invariants $d_1(u_+q_+^2 + u_-q_-^2)$ and $d_2(u_+q_-^2 + u_-q_+^2)$ in the electron–phonon interaction operator. However, the phonon mechanism current (of both the ballistic and shift LPVE types) is proportional to $\mathbf{u}_x^2 - \mathbf{u}_y^2$ in this case, and the effect does not arise at $\mathbf{u}_x^2 = \mathbf{u}_y^2$.

where $d^{(i)}_{n'm} = d_{n\mathbf{k}', m\mathbf{k}}(\mathbf{ep}^{(+)}_{nm})$ is the matrix element of the transition with phonon (photon) absorption, and $p_{nm} = p_{n\mathbf{k}, m\mathbf{k}}(p_{n'm'} = p_{n\mathbf{k}', m\mathbf{k}'})$ is the matrix element of the momentum operator.

To make further considerations simpler, we write the asymmetric components of the squared absolute values of the matrix elements, used to determine the LPVE current for the direct interband optical transition involving a photon,

$$\mathrm{As}|M_{2\mathbf{k},1\mathbf{k}}|^2 = -\frac{2\pi}{\hbar\omega}\Bigg\{\frac{1}{\varepsilon^{(21)}}[\Phi_1[\delta(E_{1'1}) + \delta(E_{2'1} - \hbar\omega)] + \Phi_2[\delta(E_{2'1}) + \delta(E_{1'1} - \hbar\omega)]] + (\Phi_5 - \Phi_4)\delta(E_{1'1}) + (\Phi_4 - \Phi_3)\delta(E_{1'1} - \hbar\omega) + (\Phi_8 - \Phi_7)\delta(E_{2'1}) + (\Phi_7 - \Phi_6)\delta(E_{2'1} - \hbar\omega)\}\delta(E^{\omega}_{21}),$$

for the intraband indirect optical nonradiative transition, and

$$\mathrm{As}|M_{1'1}|^2 = -\frac{2\pi}{\hbar\omega}\Bigg\{(\tilde{\Phi}_5 - \tilde{\Phi}_4)\delta(E^{\omega}_{2'1'}) + (\Phi_4 - \Phi_5)\delta(E^{\omega}_{21}) - \Phi_1\left[\frac{\hbar\tilde{\omega}\delta(E^{\omega}_{21})}{E^{(21)} \pm \hbar\omega_L} + \frac{\hbar\tilde{\omega}\delta(E^{\omega}_{2'1'})}{E^{(2'1')} \pm \hbar\omega_L}\right]\Bigg\}\delta(E_{1'1}),$$

for the indirect optical transition involving a photon and a phonon,

$$\mathrm{As}|M_{1'1}|^2 = -\frac{2\pi}{\hbar\omega}\delta(E^{\omega}_{1'1})\delta(E^{\omega}_{21})\left[\Phi_3 - \Phi_4 - \frac{\hbar\omega\Phi_2}{E^{(21)}}\right],$$

where

$$E^{\omega}_{nm} = E_{n\mathbf{k}} - E_{m\mathbf{k}} - \hbar\omega, \quad E_{n'm} = E_{n\mathbf{k}'} - E_{m\mathbf{k}} \pm \hbar\omega_L,$$

$$E^{(21)} = \frac{\hbar^2}{2m_\perp}(k'^2_\perp - k^2_\perp) + \frac{\hbar^2}{2m_\parallel}(k'^2_z - k^2_{z0}),$$

$$E^{\omega}_{n'm} = E_{n'm} - \hbar\omega,$$

$$k_{z0} = \beta_v^{-1}\sqrt{(\hbar\tilde{\omega})^2 - \Delta^2}, \quad \hbar\tilde{\omega} = \hbar\omega/2;$$

$$E^{(2'1')} = E^{(21)}(k_\perp \longrightarrow k'_\perp,\ k'_z \longrightarrow k'_{z0};\ k_{z0} \longrightarrow k''_z),$$

$$\tilde{\Phi}_n = \Phi_n(\mathbf{k}_2 \longleftrightarrow \mathbf{k}'_2).$$

Phonon Mechanism of the BLPVE

In the case of the BLPVE phonon mechanism in tellurium, the functions Φ_i are given by

$$\begin{aligned}
\Phi_1 &= -A_z(\eta + \eta')p[2'1', 12],\\
\Phi_2 &= A_z(\eta - \eta')p[1'2', 12],\\
\Phi_3 &= rA_z\sqrt{1-\eta'^2}p[11, 12],\\
\Phi_4 &= rA_z\sqrt{1-\eta'^2}p[1'1', 12],\\
\Phi_5 &= rA_z\sqrt{1-\eta'^2}p[22, 12],\\
\Phi_6 &= \Phi_5, \quad \Phi_7 = -\Phi_8 = \Phi_3,
\end{aligned} \tag{13}$$

where

$$p(l\dot{l}, m\bar{m}) = \mathbf{ep}_{l\dot{l}}\mathbf{e}^*\mathbf{p}_{m\bar{m}}, \quad A_z = Cd_0u_z^2q_z^0q^{-2},$$

$$r = -\Delta/|\Delta|, \quad \eta = \beta_v k_z/\sqrt{\Delta^2 + \beta_v^2 k_z^2},$$
$$\eta' = \eta(k_z \longrightarrow k'_z),$$

$$\begin{aligned}
\mathbf{ep}_{l'k,lk} &= \frac{m_0}{\hbar}\{2\cdot\hat{I}^{(l'l)}(A_\perp\mathbf{e}_\perp\mathbf{k}_\perp + e_zk_z\beta_z)\\
&+ \beta_v\sigma_z^{(l'l)}e_z + \delta_0\sigma_z^{(l'l)}[e_z(k_x^3 - 3k_xk_y^2)\\
&- 6e_xk_xk_yk_z + 3e_xk_z(k_x^2 - k_y^2)]\},\\
\mathbf{e}_\perp\mathbf{k}_\perp &= e_xk_x + e_yk_y.
\end{aligned} \tag{14}$$

In (14), relativistically small terms are neglected. To make things simpler, we consider an experimental configuration with $e_z = 0$ (i.e., $\mathbf{e} \perp \mathbf{C}_3$ and $\mathbf{C}_3 \parallel Oz$) and take into account that

$$\begin{aligned}
\mathbf{ep}^{(ll)} &= \frac{2m_0}{\hbar}\{A_\perp\mathbf{e}_\perp\mathbf{k}_\perp\\
&+ (-1)^{l-1}3\delta_0[e_x(k_x^2 - k_y^2) - 2e_yk_xk_y]k_z\eta\},\\
\mathbf{ep}^{(\dot{l}\bar{l})} &= 3r\delta_0\frac{m_0}{\hbar}\sqrt{1-\eta^2}[e_xk_z(k_x^2 - k_y^2) - 2e_yk_xk_y].
\end{aligned} \tag{15}$$

We note that the contributions to the current of the BLPVE phonon mechanism, proportional to the functions Φ_1 and Φ'_2, are small in the parameter δ_0k_{z0}/A and are henceforth neglected. We introduce the following notation:

$$\begin{aligned}
Q^{(1)}_\alpha &= q_zk_z\{\delta_{\alpha x}[e_x^2k_xk'_x(k_x^2 - k_y^2) - 2e_y^2k_yk'_yk_x^2]\\
&+ \delta_{\alpha y}[k_yk'_y(k_x^2 - k_y^2) - 2k_xk_y^2k'_x]e_xe_y\},\\
Q^{(2)}_\alpha &= q_zk_z\{\delta_{\alpha x}[e_x^2k'_x(k_x^2 - k_y^2) - 2e_y^2k_xk'_xk_y^2]\\
&+ \delta_{\alpha y}[k'_y(k_x^2 - k_y^2) - 2k_xk'_xk_y]e_xe_y\},\\
Q^{(3)}_\alpha &= q_zk_z\{\delta_{\alpha x}[e_x^2k_xk'_x(k_x^2 - k_y^2) - 2e_y^2k_x^2k_y^2]\\
&+ \delta_{\alpha y}[k_y^2(k_x^2 - k_y^2) - 2k_x^2k_y^2]e_xe_y\},\\
Q^{(4)}_\alpha &= q_zk_z\{\delta_{\alpha x}[e_x^2k_xk'_x(k_x^2 - k_y^2) - 2e_y^2k_xk'_xk_y^2]\\
&+ \delta_{\alpha y}[k_yk'_y(k_x^2 - k_y^2) - 2k_x^2k_yk'_y]e_xe_y\}.
\end{aligned} \tag{16}$$

We have the following expedient relations:

$$\begin{aligned}\bar{\Phi}_3 &= \bar{\Phi}_5 = -\bar{\Phi}_6 = -\bar{\Phi}_8 = B_z k_\perp^4,\\ \bar{\Phi}_4 = \bar{\Phi}'_3 = -\bar{\Phi}_7 = \bar{\Phi}'_5 = -\bar{\Phi}'_6 = -\bar{\Phi}'_8 &= B_z \tilde{\mu} k'_\perp k_\perp^3,\\ \bar{\Phi}'_4 = -\bar{\Phi}'_7 &= B_z(2\tilde{\mu}^2 - 1)(k_\perp k'_\perp)^2,\end{aligned} \quad (17)$$

where

$$B_z = \frac{m_0^2}{\hbar^2}\frac{3}{4m_\perp}\delta_0 C d_0 u_z^2 \frac{q_z k_z}{q^2}\chi_{\alpha xx} r\sqrt{1-\eta'^2}, \quad (18)$$

$$\begin{aligned}\chi_{\alpha xx} &= \delta_{\alpha x}(e_x^2 - e_y^2) - 2e_x e_y \delta_{\alpha y},\\ \bar{\Phi}_n &= \langle k_\alpha \Phi_n\rangle, \quad \bar{\Phi}'_n = \langle k'_\alpha \Phi_n\rangle,\end{aligned} \quad (19)$$

the broken brackets signify averaging over solid angles $\mathbf{k}$ and $\mathbf{k}'$, $\tilde{\mu} = \cos\varphi$, and φ is the angle made by the vectors $\mathbf{k}_\perp = \{k_x, k_y, 0\}$ and $\mathbf{k}'_\perp = \{k'_x, k'_y, 0\}$. The angular averaging is given in the Appendix. Angular integration over φ yields

$$\begin{aligned}\bar{\bar{\Phi}}_3 = \bar{\bar{\Phi}}_5 = -\bar{\bar{\Phi}}_6 = -\bar{\bar{\Phi}}_8 &= B_z\sigma_1,\\ \bar{\bar{\Phi}}_4 = -\bar{\bar{\Phi}}_7 = \bar{\bar{\Phi}}'_3 = \bar{\bar{\Phi}}'_5 = -\bar{\bar{\Phi}}'_6 = \bar{\bar{\Phi}}_8 &= B_z\sigma_2,\\ \bar{\bar{\Phi}}'_4 = -\bar{\bar{\Phi}}'_7 &= B_z\sigma_3,\end{aligned} \quad (20)$$

where

$$\begin{aligned}\sigma_1 &= k_\perp^4(a^2 - b^2)^{-1/2},\\ \sigma_2 &= \frac{k'_\perp}{k_\perp b}(a\sigma_1 - 1), \quad \delta_3 = \frac{k'_\perp}{k_\perp}\frac{a}{b}\sigma_2,\\ a &= (k'_z - k_z)^2 + k'^2_\perp + k^2_\perp, \quad b = -2k_\perp k'_\perp,\end{aligned} \quad (21)$$

which, in the case $\hbar\omega \gg k_B T$, i.e., for $k' \gg k$, are written as

$$\sigma_1 = k_z k'_z k'^4_\perp / l'^2, \quad \sigma_{2,3} = 0. \quad (22)$$

Photon Mechanism of the BLPVE

General formulas (6) are used to calculate the photon contribution to the BLPVE current. In this case, only the first term is retained in (2). When calculating a matrix element of the momentum operator, all the terms in (6) are taken into account. Then, the functions $\bar{\Phi}_n$ and $\bar{\Phi}'_n$ are written as

$$\begin{aligned}\bar{\Phi}_3 = \bar{\Phi}_5 = -\bar{\Phi}_6 = -\bar{\Phi}_8 &= C_\alpha k_\perp^4 q^{-2},\\ \bar{\Phi}'_3 = \bar{\Phi}'_5 = -\bar{\Phi}'_6 = -\bar{\Phi}'_8 = \bar{\Phi}_4 = -\bar{\Phi}_7 &= C_\alpha \tilde{\mu} k_\perp^3 k'_\perp,\\ \bar{\Phi}'_4 = -\bar{\Phi}'_7 &= C_\alpha k_\perp^2 k'^2_\perp (2\tilde{\mu}^2 - 1),\end{aligned} \quad (23)$$

where

$$C_\alpha = \chi_{\alpha xx} 3C^2 u^2 A_\perp \delta''\left(\frac{eA_0}{c\hbar}\right)^2 q^{-2}.$$

Then

$$\begin{aligned}\bar{\bar{\Phi}}_3 = \bar{\bar{\Phi}}_5 = -\bar{\bar{\Phi}}_6 = -\bar{\bar{\Phi}}_8 = \bar{\bar{\Phi}}'_3\\ = \bar{\bar{\Phi}}'_5 = \bar{\bar{\Phi}}_4 = -\bar{\bar{\Phi}}_7 = \bar{\bar{\Phi}}'_4 = -\bar{\bar{\Phi}}'_7\end{aligned} \quad (24)$$

are defined as

$$\begin{aligned}S_1 &= \mathrm{ReSp}\left[\sigma_z\left(\frac{\partial \hat{t}_{l'}}{\partial k_\alpha}\hat{t}_l + \hat{t}_{l'}\frac{\partial t_l}{\partial k_\alpha}\right) - (lk_\alpha \longleftrightarrow l'k'_\alpha)\right],\\ S_2 &= \mathrm{ReSp}[\sigma_z(\hat{Q}_l^{(\alpha)}\hat{t}_l + \hat{t}_l\hat{Q}_{l'}^{(\alpha)}) - (lk_\alpha \longleftrightarrow l'k'_\alpha)],\end{aligned} \quad (25)$$

where

$$\begin{aligned}\hat{Q}_l^{(\alpha)} &= \frac{\partial \hat{C}_l(\mathbf{k})}{\partial k_\alpha}\hat{C}_l^+(\mathbf{k}) - \hat{C}_l(\mathbf{k})\frac{\partial \hat{C}^{(+)}_{l(\mathbf{k})}}{\partial k_\alpha},\\ \hat{t}_l &= \hat{C}_l\hat{C}_l^+, \quad \hat{C}_l = \begin{pmatrix} C^{(l)}_{+3/2}\\ C^{(l)}_{-3/2}\end{pmatrix},\\ \hat{t}_1 &= (\hat{1} + \eta\sigma_z + \sigma_x\sqrt{1-\eta^2})/2, \quad \hat{t}_2 + \hat{t}_1 = \hat{1},\\ Q_1^{(\alpha)} &= -Q_2^{(\alpha)} = \frac{\sigma_+ - \sigma_-}{2\times 2\sqrt{1-\eta^2}}\frac{\partial\eta}{\partial k_\alpha},\\ \sigma_\pm &= \sigma_x \pm i\sigma_y, \quad (l = 1, 2).\end{aligned} \quad (26)$$

In (25), $l = 1$ and $l' = 2$. Here we neglect the processes caused by spontaneous hole transitions from M'_2 to M'_1. It can be readily shown (after calculation of the trace in (25)) that the DLPVE phonon mechanism in tellurium does not contribute to the LPVE in the situation under consideration.

DISCUSSION

From (13), one can readily verify that the processes caused by photon emission are suppressed when photons with the energy $\hbar\omega - 2\Delta_2 \le \hbar\Omega$ are used for excitation. In this case, the temperature run of the current of both the phonon and photon mechanisms of the BLPVE is defined by (13) and (14) with $a^l_{ij} = b^l_{ij}$, i.e., by the temperature dependence of the light absorptivity in the case of the direct optical transition of holes between the subbands M'_2 and M'_1,

$$\begin{aligned}K(\omega, T) &= K_\parallel(\omega, T) + 2K_\perp(\omega, T),\\ K_\parallel(\omega, T) &= \frac{e^2 m_\perp \beta_v}{c n_\parallel \hbar^3} e^{\mu/k_B T}\frac{y}{x^2\sqrt{x^2-1}} e^{\frac{x-(x^2-1)\alpha}{y}},\\ y &= k_B T/\Delta_2,\end{aligned}$$

$$K_\perp(\omega, T) = \frac{36\beta_\nu^{-4}\delta_0^2 y^2 n_\parallel K_\parallel(\omega, T)\Delta_2^4 m_\perp^4}{n_\perp \hbar^4 x^4},$$

$$\alpha = \frac{\hbar^2\Delta_2}{2m_\parallel\beta_\nu}, \quad x = \hbar\omega/2\Delta_2.$$

The chemical potential of holes is given by

$$e^{\mu\beta} = S\frac{2\pi^2\beta\hbar^2 p}{3m_\perp},$$

$$S = \int_{-\infty}^{+\infty} dk_z \left\{ \exp\left[\beta(\Delta_2^2 + \beta_\nu^2 k_z^2)^{1/2} + \frac{\hbar^2 k_z^2}{2m_X}\right] + \exp\left[-\beta(\Delta_2^2 + \beta_\nu^2 k_z^2)^{1/2} + \frac{\hbar^2 k_z^2}{2m_X}\right]\right\}.$$

In the numerical calculations, we used the following tellurium parameters: $\hbar^2/2m_X = 0.363 \times 10^{14}$ eV cm^2, $\hbar^2/2m_\perp = 0.326\times10^{14}$ eV cm^2, $\beta_\nu^2 = 0.60\times10^{-14}$ eV cm^2, $\Delta_2 = 63.15$ meV, and $n_\perp = n_\parallel = \sqrt{\varepsilon_0} = \sqrt{2.3}$.

One can see from the last relations that the temperature and spectral dependences of the interband light absorptivity in tellurium are controlled by the parameter $K_\parallel$ at $\delta_0 \ll \beta\nu k_T^{-3}$ and $k_T^2 = k_B T/(A_2 - A_1)$. We note that in the spherical approximation (taken into account only in the delta function arguments) in the energy spectrum,

(i) the functions defined by the last two relations of (19) have the form

$$\bar{\Phi}_1 = 2C_z\beta_\nu q^{-2}\left\{[(S_3 - S_1)/\varepsilon] + \left[\frac{S_3 - S_3'}{\varepsilon'}\right]\right\},$$

$$\bar{\Phi}_1 = 2C_z\beta_\nu q^{-2}\left\{[(\tilde{S}_3 - \tilde{S}_1)/\varepsilon] + \left[\frac{\tilde{S}_3 - \tilde{S}_3'}{\varepsilon'}\right]\right\},$$

$$\tilde{S}_3 = S_3(k_z' \longrightarrow k_z),$$

$$S_1 = \bar{C}\frac{k^3 k'^3}{105}\left(P_2 + \frac{k}{k'}P_1\right);$$

$$S_2 = \bar{C}\frac{k^4 k'^2}{5\times105}\left(7P_1 - 2P_3 + 5\frac{k'}{k}P_2\right);$$

$$S_3 = \bar{C}\frac{k^4 k'^2}{105}\left(P_2 + \frac{k}{k'}P_3\right); \quad S_m = S_\nu(k \longrightarrow k'),$$

$$\bar{C} = -\frac{24m_0^2}{\hbar^2}C\bar{\eta}\sigma'\sigma,$$

$$C_z = Cd_0u_z^2, \quad \sigma = \sigma' = -\beta_\nu k_\omega.$$

These functions are used to determine the coefficients a_{phon} and b_{phon} of the ballistic LPVE, where k_ω is determined from the conservation law for the energy of the direct interband optical transition. This contribution has a smallness (relative to the contribution of the photon mechanism of the displacement LPVE) on the order of $(1 - \hbar\omega/2\Delta_2)$.

(ii) The contribution of the phonon mechanism of the ballistic LPVE has a smallness on the order $\delta_0 k_\omega/\beta_\nu$, relative to the contribution of the photon mechanism of the displacement LPVE.

(iii) The contribution of the phonon mechanism of the displacement LPVE to the effect vanishes if the anisotropy of the distribution function of photoexcited electrons is disregarded.

Finally, we note that the photocurrent is proportional to the imaginary part of the product Q^*D. Therefore, the carrier flux directions at the points M and P coincide if we bear in mind that the matrix elements of the momentum operator near these points of the Brillouin zone are related as $(\mathbf{e}\cdot\mathbf{p}_P(\mathbf{k}))_{21} = (\mathbf{e}\cdot\mathbf{p}_M(-\mathbf{k}))_{\bar{2}\bar{1}}$; the states with subscripts $\bar{m}$ and m arise from one another under the action of the time-reversal operator.

APPENDIX

To determine the photocurrent in gyrotropic crystals, one should calculate the integrals

$$\frac{1}{2\pi}\frac{1}{2\pi}\int\int d\Omega d\Omega' |\mathbf{k} - \mathbf{k}'|^{-2} o_x^a o_y^b o_x'^n o_y'^m, \qquad (A.1)$$

where Ω and Ω' are the solid angles of the vectors $\mathbf{o} = \mathbf{k}/|\mathbf{k}|$ and $\mathbf{o}' = \mathbf{k}'/|\mathbf{k}'|$. It is convenient to reduce (A.1) to the form

$$\int d\tilde{\mu}(g - \tilde{\mu})^{-2} G\langle a, b|n, m\rangle, \qquad (A.2)$$

where g is a certain quantity independent of angles and

$$G\langle a, b|n, m\rangle = \frac{1}{2\pi}\int d\varphi(\cos^2\varphi - \sin^2\varphi) o_x^a o_y^b o_x'^n o_y'^m$$

which defines the photocurrent. We introduce a frame of reference linked to the vector $\mathbf{o}$. Then, the unit vectors of the new frame are described as $e_x = (\cos\varphi, \sin\varphi)$ and $e_y = (-\sin\varphi, \cos\varphi)$, while the unit vectors directed along $\mathbf{k}'$ are defined as $O_x' = \cos(\varphi + \phi)$ and $O_y' = \sin(\varphi + \phi)$, where ϕ is the angle between the vectors $\mathbf{k}'$ and $\mathbf{k}$. Then, we analyze the G-function properties;

1) $G(a, b|n, m) = G(n, m|a, b)$;

2) $G(a, b|m, n) = G(a, b|n, m)$;

3) $G(a \pm 2, b|n, m) + G(a, b|n\pm, m) = \pm G(a, b|n, m)$;

4) $G(a + 1, b|n + 1, m) + G(a, b + 1|n, m + 1) = \tilde{\mu}\, G(a, b|n, m)$;

5) $G(a, b|n \pm 2, m) + G(a, b|n, m\pm) = \pm G(a, b|n, m)$;

6) $G(a, b|n, m) = 0$, if $a + b + n + m$ is an odd number.

For completeness, we present the explicit form of the G-functions in the case $a + b + n + m \le 8$. For $G(a, b|0, 0,) = G(a, b)$, we have

1) $G(2a, 0) = (2a - 1)!!/(2^{a+1} \cdot a!)$;
2) $G(2, 0) = 1/4$;
3) $G(4, 0) = 3/8$;
4) $G(6, 0) = 5/16$;
5) $G(8, 0) = 35/128$;
6) $G(2, 2) = 1/8$;
7) $G(4, 2) = 1/16$;
8) $G(6, 2) = 5/128$.

For the functions $G(a, b|n, m)$, we have

1) $G(1, 0|1, 0) = -G(0, 1|0, 1) = P_1(\cos\phi)/2$;
2) $G(3, 0|1, 0) = -G(0, 3|0, 1) = 3P_1(\cos\phi)/8$;
3) $G(5, 0|1, 0) = 5P_1(\cos\phi)/16$;
4) $G(7, 0|1, 0) = 35P_1(\cos\phi)/128$;
5) $G(2, 0|2, 0) = \tilde{\mu}^2/4$;
6) $G(2, 0|0, 2) = (1 - \tilde{\mu}^2)/4$;
7) $G(3, 0|0, 1) = (1 - \tilde{\mu}^2)^{1/2}/4$;
8) $G(3, 0|1, 0) = -G(0, 1|1, 0) = \tilde{\mu}/4$.

REFERENCES

1. B. I. Sturman and V. M. Fridkin, *Photovoltaic Effect in Media without a Center of Symmetry and Related Phenomena* (Nauka, Moscow, 1992).
2. R. Ya. Rasulov, Author's Abstract of Doctoral Dissertation (St. Petersburg, 1993).
3. E. L. Ivchenko and G. E. Pikus, Fiz. Tekh. Poluprovodn. (Leningrad) **13**, 992 (1979) [Sov. Phys. Semicond. **13**, 579 (1979)].
4. A. V. Andrianov, E. L. Ivchenko, G. E. Pikus, *et al.*, Zh. Éksp. Teor. Fiz. **81** (6), 2080 (1981) [Sov. Phys. JETP **54**, 1105 (1981)].
5. V. I. Belinicher, E. L. Ivchenko, and B. I. Sturman, Zh. Éksp. Teor. Fiz. **83** (2), 649 (1982) [Sov. Phys. JETP **56**, 359 (1982)].
6. P. N. Gorleĭ, V. S. Radchenko, and V. A. Shenderovskiĭ, *Transport Processes in Tellurium* (Naukova Dumka, Kiev, 1987).
7. E. L. Ivchenko, Yu. B. Lyanda-Geller, G. E. Pikus, and R. Ya. Rasulov, Fiz. Tekh. Poluprovodn. (Leningrad) **18** (1), 93 (1984) [Sov. Phys. Semicond. **18**, 55 (1984)].
8. Yu. B. Lyanda-Geller and R. Ya. Rasulov, Fiz. Tverd. Tela (Leningrad) **27** (4), 945 (1985) [Sov. Phys. Solid State **27**, 577 (1985)].
9. F. Henneberger, N. S. Averkiev, and R. Ya. Rasulov, Phys. Status Solidi B **109** (1), 343 (1982).
10. R. Ya. Rasulov, Fiz. Tekh. Poluprovodn. (Leningrad) **23** (4), 698 (1989) [Sov. Phys. Semicond. **23**, 437 (1989)].
11. M. S. Bresler and G. E. Pikus, Fiz. Tverd. Tela (Leningrad) **13** (6), 1734 (1971) [Sov. Phys. Solid State **13**, 1449 (1971)].

Translated by A. Kazantsev

Semiconductors, Vol. 36, No. 2, 2002, pp. 148–152. Translated from Fizika i Tekhnika Poluprovodnikov, Vol. 36, No. 2, 2002, pp. 155–159.
Original Russian Text Copyright © 2002 by Sobolev, Kalugin.

ELECTRONIC AND OPTICAL PROPERTIES OF SEMICONDUCTORS

Optical Properties of Fluorite in a Wide Energy Range

V. V. Sobolev and A. I. Kalugin

Udmurt State University, Izhevsk, 426034 Russia

e-mail: sobolev@uni.udm.ru

Submitted October 30, 2000; accepted for publication May 22, 2001

Abstract—The experimental, experimental–calculated, and theoretical spectra of reflectance *R*, extinction coefficient *k*, and refractive index *n* for fluorite crystal are compared in the energy range from 6 to 35 eV. Their important properties and general features are determined. Serious discrepancies between the experimental and experimental-calculated data of *R*, *k*, *n*, as well as between the results of calculations based on five theoretical models, are revealed. The most reliable *R* spectrum is ascertained. A satisfactory agreement between the experimental-calculated *k* spectra and the theoretical data for two models is found. © *2002 MAIK "Nauka/Interperiodica".*

INTRODUCTION

Ionic crystals with fluorite structure are acknowledged as promising optical materials for applications in the range of vacuum ultraviolet radiation, as matrices for impurities (particularly for rare-earth impurities), and as solid electrolytes. Therefore, the study of their electronic structure in a wide energy range is of prime importance. However, the experimental optical spectra and theoretical calculations of their energy bands are quite contradictory and incomplete [1–11]: the experimental spectra greatly differ in the numbers of peaks and intensities; and the theoretical results disagree in the magnitude of the direct band gap E_{gd}, the width of the upper valence band, and in the dispersion and structure of the conduction bands. Recent theoretical calculations of spectra for the imaginary part of dielectric constant $\varepsilon_2(E)$ of CaF_2 in the range of 10–27 eV [10] and 8–20 eV [11] do not correlate with each other, but do allow for a more complete and detailed analysis of experimental data on the electronic structure of this crystal.

Several experimental spectra are available for CaF_2, among them are the reflectance spectra $R(E)$ in the energy range E = 6–36 eV at the temperatures T = 90 and 300 K [2], E = 5–21 eV at T = 4.2 and 300 K [3], and the spectra of the real and imaginary parts of the dielectric constants $\varepsilon_1(E)$ and $\varepsilon_2(E)$ in the range E = 10–35 eV at T = 300 K obtained by ellipsometry [4] and calculated from the spectra of characteristic losses of electrons [5]. The results of these studies were not compared despite large discrepancies between them.

METHOD FOR CALCULATIONS

The most comprehensive information about the electron structure in a wide energy range of intrinsic absorption can be obtained from a large variety of fundamental functions [12]: the reflectance $R(E)$ and absorption factor $\mu(E)$, refractive index $n(E)$ and extinction coefficient $k(E)$, real $\varepsilon_1(E)$ and imaginary $\varepsilon_2(E)$ parts of the dielectric constant, the function of characteristic bulk losses of electrons $\mathrm{Im}\varepsilon^{-1}$, and so on. We calculated this set of functions on the basis of one of two (R, ε_2), or two (ε_1, ε_2) functions from [2–5, 10, 11]. In this paper, we consider the results for R, n, and k spectra. Our aim is to obtain $k(E)$, $n(E)$, and $R(E)$ spectra using available experimental data for $R(E)$, $\varepsilon_2(E)$, $\varepsilon_1(E)$ and theoretical data for $\varepsilon_2(E)$, and to compare and analyze all the experimental and calculated k(E), $n(E)$, and $R(E)$ spectra. The necessity of studying these three optical functions stems from the fact that in the most commonly used cases of normal incidence of light, R, ε_2, and ε_1 spectra are directly related to k and n by the following simple formulas: $R = [(n-1)^2 + k^2][(n+1)^2 + k^2]^{-1}$, $\varepsilon_2 = 2nk$, $\varepsilon_1 = n^2 - k^2$. The calculations of $R(E)$, $n(E)$, and $k(E)$ spectra are performed using the widely used Kramers–Kronig relations [12, 13].

RESULTS AND DISCUSSION

We calculated $R(E)$ spectra on the basis of experimental-calculated spectra $\varepsilon_2(E)$ and $\varepsilon_1(E)$, obtained from ellipsometry [4] and characteristic losses of electrons [5], and also from the theoretical $\varepsilon_2(E)$ spectra [10, 11]. They are represented in Fig. 1 by curves *3* [4] and *4* [5], and by curves *5* [10] and *6* [11]. The experimental $R(E)$ spectra [2, 3] are shown by curves *1* and *2*.

In addition, we calculated $k(E)$ and $n(E)$ spectra (Fig. 2) using experimental $R(E)$ spectra (curve *1*) [2], (curve *2*) [3], experimental-calculated $\varepsilon_2(E)$ (curve *3*) [4] and $\varepsilon_1(E)$ (curve *4*) [5] spectra, and theoretical $\varepsilon_2(E)$ spectra (curve *5*) [10] and (curve *6*) [11].

Before analyzing reflectance spectra, it is necessary to note the main features of the experimental methods used in [2–5]. The CaF samples were cleaved single crystals [2–4] and thin polycrystalline films [5]. Syn-

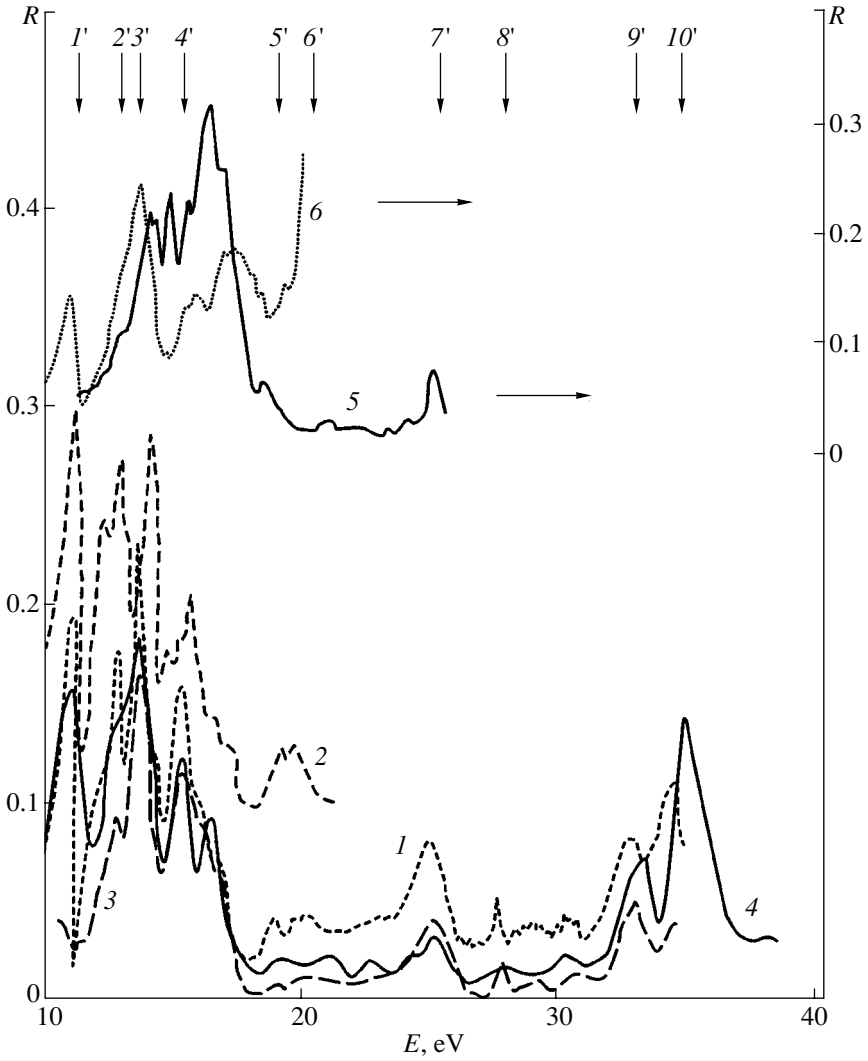

Fig. 1. Reflectance spectra of fluorite measured using (*1*) synchrotron radiation in the range of 6–36 eV at 90 K [2] and (*2*) conventional light source in the range 5–21 eV at 4.2 K [3]; and (*3*) calculated on the basis of experimental ε_2 spectra in the range of 10–35 eV at 300 K [4]; (*4*) spectrum of characteristic electron losses $-\mathrm{Im}\varepsilon^{-1}$ in the range of 10–40 eV at 300 K [5]; (*5*) and (*6*) are theoretical spectra of ε_2 from [10] and [11], respectively. The ten most intense *R* peaks [2] are numbered and indicated by arrows.

chrotron radiation [2, 4] or gaseous discharge in a capillary [3] were used as light sources. The method of determining the $-\mathrm{Im}\varepsilon^{-1}$ function from the measured parameters of electron losses usually does not ensure the sufficient accuracy of the loss function itself and, consequently, of the calculated $\varepsilon_2(E)$ and $\varepsilon_1(E)$ spectra. It was emphasized in [4] that the experimental data in the energy range $E < 11$ eV were incorrect because of the imperfections in the system of light monochromatization. This did not allow the authors of [4] to detect the long-wavelength absorption band of the free exciton in the energy region $E < 12$ eV.

As follows from the analysis of four reflectance spectra (Fig. 1, curves *1–4*), curve *2* runs too high, and curve *3* runs too low with respect to curve *1*. Curve *4* is in reasonable agreement with curve *1* in the energy region $E < 18$ eV but runs too low in the range $E > 18$ eV. From all spectra, one can single out the 10 most intense bands, which are indicated by arrows and numbered. The intensity of the *2*' band found in [4] is too low. The additional direct measurements of the reflectance spectrum in the region $E \lesssim 11$ eV showed that $R = 0.12$ at the peak of the *1*' band, which is almost two times lower than in curve 1. This clearly indicates that the reflectance $R(E)$ obtained in [4] in the range of the first two bands *1*' and *2*' is too low and incorrect. This error is so large that it casts suspicion on the magnitude of *R* in the entire energy range up to 35 eV. The occurrence of a very sharp peak and dip ($R \approx 0.02$!) in curve *1* and an appreciably larger reflection in curve *2*, with respect to the values *1* and *4* in the range $E < 10.8$ eV, counts in favor of the higher reliability of curve *1* from [2] and of the large overestimation of $R(\mathrm{E})$ in curve *2* from [3]. The position of many peaks in four $R(E)$ curves differs

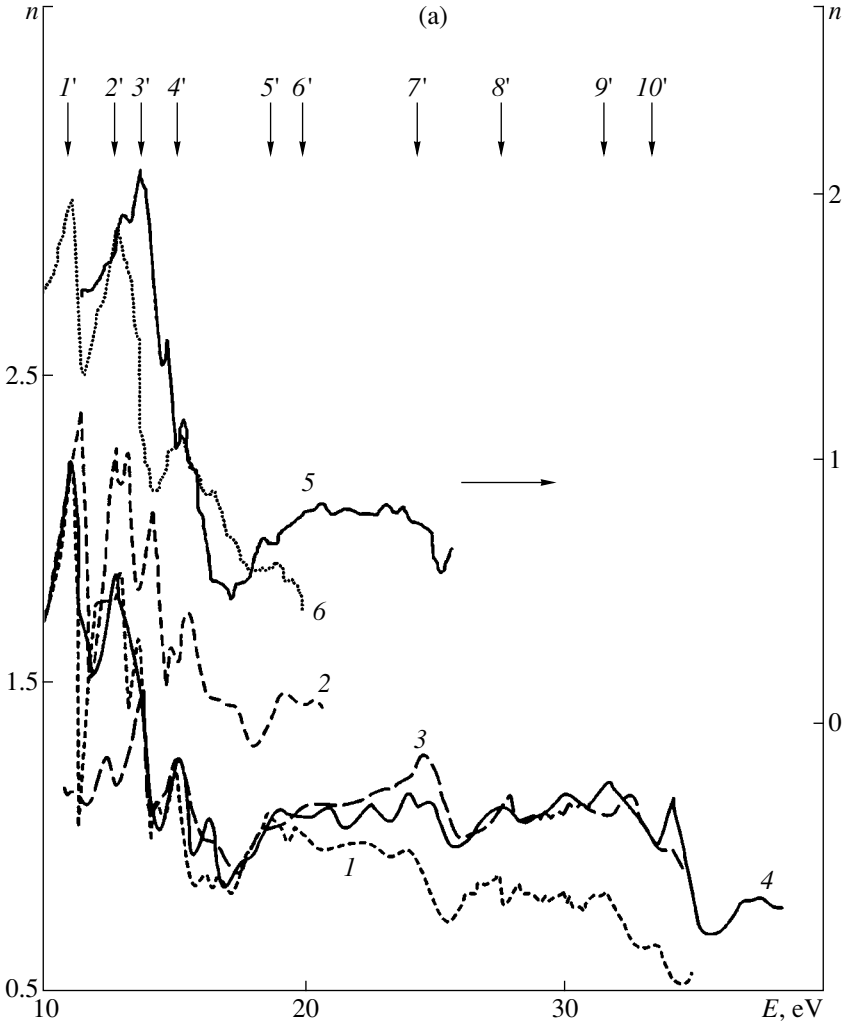

Fig. 2. (a) Spectra of refractive index n and (b) extinction coefficient k of fluorite calculated on the basis of the experimental reflectance spectra (*1*) [2], (*2*) [3], (*3*) ε_2 [4], (*4*) $-\mathrm{Im}\varepsilon^{-1}$ [5]; and theoretical spectra (*5*) ε_2 [10], (*6*) [11]. Ten most intense R peaks [2] are numbered and indicated by arrows at the top.

by 0.1—0.3 eV. This can probably be explained by the differences in calibration of the energy scale of the spectrometers used in [2–5]. Thus, the most reliable reflectance spectrum for CaF_2 is apparently obtained in [2].

The large overestimation of experimental data obtained in [3] is most clearly seen from the calculated spectra for the extinction coefficient $k(E)$ (Fig. 2a): the magnitudes of k (curve *2*) are 3–4 times larger than those for the other three curves (*1*, *3*, *4*). The data of curves *1*, *3*, and *4* are in good agreement within the energy range E = 10–18 and 25–32 eV. In the range E = 18–25 eV, the magnitudes of k in curve *1* are larger than in the other two curves by factors of ~1.4 (curve *4*) and 2 (curve *3*). This is caused by the corresponding underestimation of reflectance measured in [4, 5] in comparison with the data obtained in [2]. The largest magnitudes of k according to curve *1* are the following: 1.04 (*1*', E =11.20 eV), 1.02 (*2*', E = 13.10 eV), 1.23 (*3*', E = 13.80 eV), 0.88 (*4*', E = 15.30 eV), 0.44 (*5*', E = 19.10 eV; *6*', E = 20.20 eV), 0.51 (*7*', E = 24.75 eV), 0.38 (*8*', E = 27.60 eV; *9*', E = 32.20 eV), 0.89 (*10*', E = 34.20 eV).

In contrast to the $R(E)$ and $k(E)$ spectra, the data of the three curves (*1*, *2*, *4*) for $n(E)$ for band *1*' located at the largest wavelength are in good correlation with each other. The discrepancy between them in the range of the next two bands (*2*', *3*') is not too large. In the high-energy range, the data of curve *2* are obviously overestimated, as well as the magnitudes of $n(E)$ for curves *3* and *4* in the region $E > 20$ eV.

Analysis of the experimental and experimental-calculated $k(E)$ spectra shows that the most correct experimental spectrum $R(E)$ in the range E = 10–35 eV is obtained in [2]; the data in the range E = 20–35 eV require additional refinement by the averaging of the three spectra (curves *1*, *3*, *4*).

The theoretical spectra $\varepsilon_2(E)$ of fluorite have been calculated in the range E = 10–27 eV by three methods [10]: by the self-consistent *ab initio* OLCAO method in

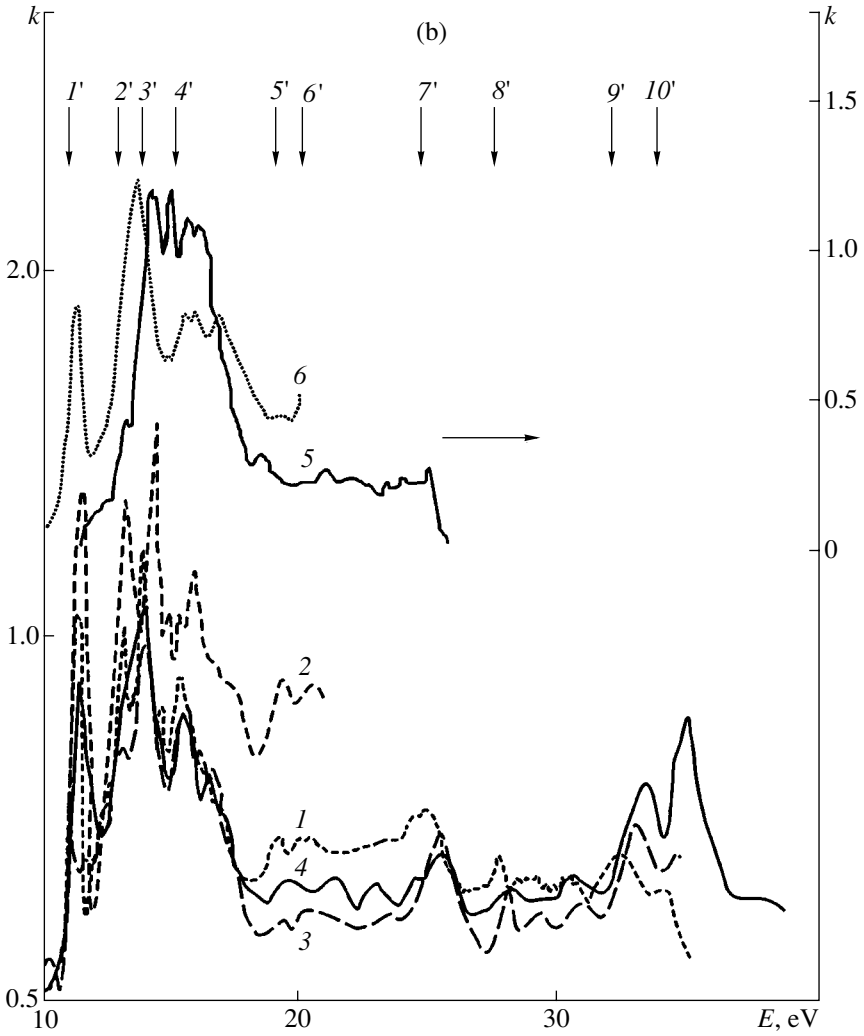

Fig. 2. (Contd.)

LDA approximation without (*G*1), or with (*G*2) self-effect correction, as well as by an additional simple shift of conduction bands upwards by ~ 5.1 eV for matching the theoretical band gap E_g with the experimental one (*G*3). The $\varepsilon_2(E)$ spectra obtained in [11] are calculated *ab initio* in the range E = 8–20 eV in the LDA and quasi-particle approximations without (*B*2) and with (*B*1) regard to the interaction of electron–hole pairs. On the basis of these five $\varepsilon_2(E)$ models [10, 11], we calculated $R(E)$, $k(E)$, and $n(E)$ spectra. Two (*B*1, *G*2) of the five calculated spectra more closely match the experimental data for $R(E)$ and experimental-calculated data for $k(E)$ and $n(E)$. Therefore, for brevity, hereafter we shall consider our theoretically calculated spectra of two models (*B*1, *G*2). The purely exciton peak *1*' located at the longest wavelength in the $k(E)$ spectrum calculated by the *B*1 model coincides with the experimentally calculated value with accuracy up to 0.05 eV (Fig. 2b, curves *1*, *6*). Next, in curve *6* the most intense peak *3*' is observed at 13.6 eV and is shifted to lower energies only by 0.2 eV relative to the experimentally calculated spectrum, and, then, a weakly pronounced step appears in place of the intense peak in curve *1*.

Peaks *3*'–*6*' in curve *6* are shifted to lower energies by 0.2 (*3*'), and 0.7–1 eV (*5*', *6*') relative to the peaks in curve *1*, and to higher energies by 0.2 eV (*4*', *7*'); a step appears in the theoretically calculated spectrum instead of the peak *1*'. The peaks in $k(E)$, calculated according to the second theoretical-calculated model (*G*2), are shifted to higher energies by ~ 0.2–0.5 eV; the exciton peak *1*', as might be expected, is absent. This points to the fact that the structure and intensity of three experimentally calculated and two theoretically calculated $k(E)$ spectra of fluorite in the range E = 9–26 eV are in very good agreement.

The same detailed similarity is found between the $n(E)$ spectra (Fig. 2a).

Theoretical $\varepsilon_2(E)$ spectra obtained in [10, 11] are compared to obviously inadequate experimental data [4] without discussion of the nature of the peaks. Three

models of bands ($G1$, $G2$, $G3$) along the ΓL, ΓX, and ΓK directions are suggested in [10]. The most correct model $G2$ yields the value of E_g which is lower by $\Delta E \approx$ 3.4 eV. Taking into account this correction, we estimated the energies of the most intense interband transitions at $E \approx 12.9$ eV for $\Gamma(V_1–C_2)$ and 13.0 eV for ΓX ($V_1–C_1$) (*2*'); 13.5 eV for $\Gamma(V_2–C_1)$; 13.4 eV for ΓX ($V_1–C_2$) and 14.4 eV ΓL ($V_1–C_1$) (*3*'); 15.4 eV for $\Gamma(V_1–C_3)$, ΓX ($V_1–C_3$, C_4), and ΓL ($V_2–C_2$) (*4*'); 17.5 eV for ΓL ($V_2–C_3$) (*5*'), 19.5 eV for $\Gamma(V_2–C_3)$ and ΓL ($V_2–C_4$) (*6*'); and 25.4 eV for ΓL ($V_2–C_4$) (*7*'). Many $k(E)$ and $R(E)$ peaks can be caused by metastable excitons. In this case, they are shifted relative to the energy of interband transitions to lower energies approximately by the binding energy.

Thus, the most correct reflectance spectrum is obtained in [2]. In the energy range of 18–35 eV, the results obtained in [2, 4] are also reliable. The results obtained for $R(E)$ spectrum in [3] are highly overestimated in the region $E < 13$ eV and $E > 17$ eV, whereas the reflectance spectrum in [4] is strongly distorted in intensities in the range $E < 13$ eV. The most pronounced overestimation of $R(E)$ [3] can be seen by comparing four $k(E)$ spectra. The theoretically calculated $k(E)$, $n(E)$, and $R(E)$ spectra that we obtained by using two models of $\varepsilon_2(E)$ proposed in [10, 11] are in good agreement with the experimental $R(E)$ spectra [2], as well as with the experimentally calculated $k(E)$ and $n(E)$ spectra derived from the experimentally calculated $\varepsilon_2(E)$ and $\varepsilon_1(E)$ spectra [4, 5].

The much more precise $R(E)$, $k(E)$, and $n(E)$ spectra obtained for fluorite in this study in a wide energy range of fundamental absorption provide the possibility for deeper insight into the optical properties of this crystal and for more substantiated and sophisticated development of the theory of the structure of fluorite-group crystals, taking excitons into account and ensuring a detailed description of peaks in $k(E)$ and $R(E)$ spectra.

ACKNOWLEDGMENTS

We are grateful to V.P. Zhukov, V.M. Zaĭnullina, N.V. Starostina, R.A. Evarestova, W.Y. Ching, G.W. Rubloff, and J. Frandon for sending us the reprints of their publications.

REFERENCES

1. V. V. Sobolev, *Bands and Excitons in Halogenides of Metals* (Shtiintsa, Kishinev, 1987).
2. G. W. Rubloff, Phys. Rev. B **5**, 662 (1972).
3. V. A. Ganin, M. G. Karin, V. K. Sidorin, *et al.*, Fiz. Tverd. Tela (Leningrad) **16**, 3545 (1974) [Sov. Phys. Solid State **16**, 2307 (1974)].
4. J. Barth, R. L. Johnson, M. Cardona, *et al.*, Phys. Rev. B **41**, 3291 (1990).
5. F. Frandon, B. Lahaye, and F. Pradal, Phys. Status Solidi B **53**, 565 (1972).
6. L. K. Ermakov, P. A. Rodnyĭ, and N. V. Starostin, Fiz. Tverd. Tela (Leningrad) **33**, 2542 (1991) [Sov. Phys. Solid State **33**, 1435 (1991)].
7. J. P. Albert, C. Jouanin, and C. Gout, Phys. Rev. B **16**, 925 (1977).
8. R. A. Evarestov, J. V. Murin, and A. V. Petrov, J. Phys.: Condens. Matter **1**, 6603 (1989).
9. V. M. Zainullina, V. P. Zhukov, and V. M. Zhukovsky, Phys. Status Solidi B **210**, 145 (1998).
10. F. Gan, Y.-N. Xu, M.-Z. Huang, and W. Y. Ching, Phys. Rev. B **45**, 8248 (1992).
11. L. X. Benedict and E. L. Shirley, Phys. Rev. B **59**, 5441 (1999).
12. V. V. Sobolev and V. V. Nemoshkalenko, *The Methods of Computational Physics in the Theory of Solid State. Electronic Structure of Semiconductors* (Naukova Dumka, Kiev, 1988).
13. V. V. Sobolev and E. L. Busygina, Fiz. Tekh. Poluprovodn. (St. Petersburg) **33**, 31 (1999) [Semiconductors **33**, 26 (1999)].

Translated by A. Zalesskiĭ

Semiconductors, Vol. 36, No. 2, 2002, pp. 153–156. Translated from Fizika i Tekhnika Poluprovodnikov, Vol. 36, No. 2, 2002, pp. 160–163.
Original Russian Text Copyright © 2002 by Kuz'menko, Ganzha, Domashevskaya, Hildenbrandt, Schreiber.

ELECTRONIC AND OPTICAL PROPERTIES OF SEMICONDUCTORS

Influence of Laser Pump Density on the Characteristic Time Constant and the Intermediate-Field Electromodulation E_0 Component of the Photoreflectance Signal

R. V. Kuz'menko*, A. V. Ganzha*, É. P. Domashevskaya*, S. Hildenbrandt, and J. Schreiber****

** Voronezh State University, Universitetskaya pl. 1, Voronezh, 394893 Russia*
e-mail: roman@ftt.vsu.ru
*** Fachbereich Physik der Martin-Luther Universität Halle-Wittenberg, 06108 Halle/Saale, Germany*
Received March 12, 2001; accepted for publication May 25, 2001

Abstract—The influence of the laser pump density L on the intensity and the characteristic time constant of the intermediate-field electromodulation E_0 component of photoreflectance spectra in a direct-gap semiconductor was studied. The experiments were carried out using GaAs samples with carrier concentration $n \approx 10^{16}$ cm^{-3} and laser pump densities in the range $L = 100$ μW/cm^2 – 1 W/cm^2. For all of the samples under study, the logarithmic dependence of the intensity of the electromodulation signal on the laser radiation density was ascertained. No effect of the attendant variations of the characteristic time constant on the measured signal was observed. © *2002 MAIK "Nauka/Interperiodica".*

INTRODUCTION

Photoreflectance (PR) spectroscopy is widely used for studying electronic, optical, and structural properties of semiconductors because of the comparatively simple experimental implementation of the method combined with the great variety of data contained in the spectra. The main body of information can be extracted by intermediate- or low-field measurements of the electromodulation component arising in the region of a direct-gap (valence band)–(conduction band) transition [1]. This component stems from the periodic modulation of the surface electric field under laser irradiation with a photon energy greater than the semiconductor band gap. According to [2–4], the main parameter that defines the spectral line shape and the intensity of the electromodulation signal is the modulation depth of the surface electric field. Thus, laser pump density (LPD) turns out to be one of the most important parameters that affects measurements of the spectra. However, only the low-field components have been considered in the studies on LPD influence reported so far [5–7]. There is little or no information available about the LPD effect on the characteristic time constant of the τ component, which is a first approximation of the delay time between the modulated reflectance signal and the pump [8, 9].

The aim of this study was to gain insight into the LPD influence on the intensity and characteristic time constant of the intermediate-field electromodulation E_0 component. The measurements were conducted at room temperature with the use of the setup described in [10]. Phase analysis (PA) of spectra [9] from GaAs samples ($E_0 = 1.424$ eV [4]) with the carrier concentration $n \approx 10^{16}$ cm^{-3} was carried out with an SR850 two-channel phase-sensitive amplifier (PSA). LPD values (a red He–Ne laser) ranged from 100 μW/cm^2 to 1 W/cm^2. Lower LPD resulted in such a weak signal that it could not be measured without switching the PSA amplification range. In contrast, for LPD exceeding 10 W/cm^2, saturation of the PR signal intensity and phase angle was observed for some of the samples. The modulation frequency was in the range $f = 50 – 500$ Hz, which excluded its influence on the modulation signal being measured.

The line shape of the PR intermediate-field E_0 spectra obtained in experiments agrees qualitatively with that recently published [4]. The one-component character of the spectra was proved by simulations in terms of a generalized multilayer model [4], as well as by plotting the phase diagrams [9].

CHARACTERISTIC TIME CONSTANT

The PR signal measured with a two-channel PSA can be represented as the square root of the sum of the squared components, one of which is in phase with the reference signal and the other is shifted with respect to the reference signal by 90° [9]. However, the intensity of the PR signal may differ from the true value $\Delta R/R(E)$ defined by the parameters of modulation. As was shown in [10], a complex PR signal depends on the cyclic fre-

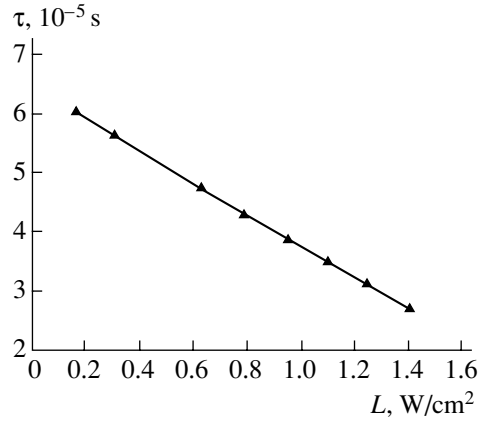

Fig. 1. Characteristic time constant of the electromodulation E_0 component τ vs. laser pump density L. The linear dependence is observed down to $L \lesssim 100$ μW/cm^2 (not shown).

quency $\omega = 2\pi f$, where f is the frequency of modulation, and on the characteristic time constant τ of the component:

$$\frac{\overline{\Delta \mathbf{R}}}{\mathbf{R}}(E, \omega, \tau) = \frac{\Delta R}{R}(E)\frac{1 + e^{-i\pi/\omega\tau}}{1 + \omega^2\tau^2}(1 + i\omega\tau). \quad (1)$$

Thus, a necessary condition for the intensity of the modulation signal obtained in experiment to coincide with its true value is $\omega\tau \ll 1$.

In the context of PA, estimating τ from the phase of delay φ implies a strictly specified time shape of the signal $\Delta R(t)$ during the laser irradiation and after the pump is turned off. One of the most frequently cited models for $\Delta R(t)$ was proposed by Seebauer [8]. According to this model, an increase in the electric field strength under the laser irradiation is due to the drift and recombination of the minority carriers with the majority carriers captured by the surface states of the traps. Since both the recombination and drift of the minority carriers occur within a nanosecond time scale, they cannot ensure a noticeable delay when the density of nonequilibrium carriers is sufficiently high. In contrast, the restoration of the surface charge after the laser pump is turned off implies the capture of the majority carriers and, thus, is characterized by the time constants from the μs–ms interval [11, 12]. Hence, it follows that the time constant of the PR signal after switching the pump off is independent of LPD. According to the model, for $1/\omega\tau \longrightarrow \infty$, we should expect $\varphi \longrightarrow 0$; in the other limiting case of $1/\omega\tau \longrightarrow 0$, $\varphi \longrightarrow 32.48°$ is expected.

Shen *et al.* [13] attribute modulation of the electric field to the interaction of the surface states with the charge carriers of both signs. Recombination with the photogenerated minority carriers reduces the amount of charge at the surface states; concurrently with this, capture of the majority carriers (the so called "restoration" current) occurs. The time required for these two processes to come to equilibrium is the same one that defines τ. This time is governed by the capacitance-related effects in the space charge region (SCR), and for low and intermediate depths of modulation it is expressed as

$$\tau = RC = \frac{dJ_{res}}{dV_s}C = \frac{\varepsilon\varepsilon_0}{d}\frac{kT}{q}\frac{1}{AT^2}\exp\left(\frac{qV_s}{kT}\right). \quad (2)$$

Here, C and R are the capacitance and resistance of the surface–SCR system, respectively; J_{res} is the density of the restoration current; ε is the permittivity; q is the elementary charge; d is the thickness of the space charge layer; k is the Boltzmann constant; T is the temperature; A is the Richardson constant; $V_s = V_{s,0} - V_p$, with $V_{s,0}$ being the surface potential in the absence of irradiation; and V_p is the photovoltage. Since V_s depends on LPD (in terms of V_p), Eq. (2) predicts a decrease in τ with LPD. On the assumption that the time constants for the growth and decay are identical, we derived τ in the following form (see [9, 10]):

$$\tan\varphi = \omega\tau. \quad (3)$$

For the spectra being studied, a decrease in LPD resulted in a reduction in the signal intensity and clockwise rotation of the phase diagram. Rotation of the phase line indicates that the phase angle increases. Since the measurements were carried out without a preset of the PSA phase, the phase angle φ might be determined as the angle between the phase line and the X axis [9]. A certain spread in the phase angle was observed, but it was no greater than a few percent. Although the values of φ obtained in the experiment were within those predicted by the Seebauer model ($\varphi = 5°$–$10°$), the variations observed are sufficient to indicate the failure of this model in the case under study.

In order to check the above-mentioned assumption of equality between the growth and the decay time constants, the dependence $\Delta R(t)$ at a fixed photon energy was read from an oscilloscope for one of the samples. Although the signal shape was only slightly different from a rectangular one, the growth and decay regions displayed a noticeable delay with respect to the pump signal. Visually, the growth and decay of $\Delta R(t)$ were judged to be exponential with approximately equal time constants. This fact allows us to calculate τ from (3). Figure 1 shows the $\tau(L)$ function recalculated for a typical dependence $\varphi(L)$. As is evident from Fig. 1, the thus obtained $\tau(L)$ can be closely approximated by a straight line. In view of the logarithmic dependence of photovoltage on LPD [5, 6], a linear $\tau(L)$ dependence is predicted by (2). This result presents another argument in favor of the Shen model.

The τ values obtained are within the range of $(3–6) \times 10^{-5}$ s. According to formula (1), this means that, for the considered LPD values, the nonzero characteristic time constant does not noticeably affect the measured signal. Therefore, the electromodulation signal intensity obtained in the experiment may be interpreted as a true

value, which is conditioned only by the parameters of the modulation process.

In order to exclude the influence of the laser wavelength, we performed a series of experiments with a blue He–Cd laser (λ = 441.6 nm). No qualitative disagreement with previously obtained results was observed. With the blue-light irradiation, however, the values of τ were smaller, which can easily be explained by shifting the region of nonequilibrium-carrier generation towards the sample surface.

THE $A(L)$ DEPENDENCE

The concept of an amplitude factor A has, thus far, only been introduced for a low-field case, when the spectral line shape depends neither on the electric field strength nor on its modulation depth. As has been shown previously [5–7], this case corresponds to a linear dependence of the electromodulation signal on photovoltage or on a variation in the surface potential ΔV_s. From the logarithmic dependence of ΔV_s on both the current of the photoinduced minority carriers towards the surface J_{pc} and the "restoration" current J_{res}, and from the linear dependence of J_{pc} on L, the logarithmic character of $A(L)$ immediately follows.

For an intermediate-field component, the concept of amplitude factor may be introduced analytically only under the conditions of (i) uniformity of the electric field over the region of PR generation and (ii) complete suppression of this field by the irradiation [14, 15]. In this case, the amplitude factor might be defined as a coefficient of proportionality between the broadened electrooptical G function [15] and the spectral line under investigation. As was previously demonstrated [3, 4], these conditions are actually not satisfiable and the spectral component shape cannot be described by a single analytical expression. Nevertheless, the calculations performed within the generalized multilayer model [4] suggest that, within the interval of the electric field modulation depth $\xi > 0.05$, the line shape, period, and energy position of Franz–Keldysh oscillations remain nearly constant and are defined merely by the electric field in the absence of irradiation and the energy of the electron–optical transition. In contrast, within the interval specified above, the signal intensity only depends on the depth of modulation of the surface electric field. The above considerations justify using the magnitude of Franz–Keldysh oscillations as an amplitude factor for an intermediate-field electromodulation signal.

The dependences $A(L)$ thus determined for several samples are plotted in Fig. 2. As an amplitude factor, the magnitude of the second positive Franz–Keldysh oscillation was used. For a fixed LPD, a considerable sample-to-sample spread of the amplitude factor was observed. Because of this, the results were normalized before being compared. Quantitative analysis indicates that all of the dependences $A(L)$ found in experiments

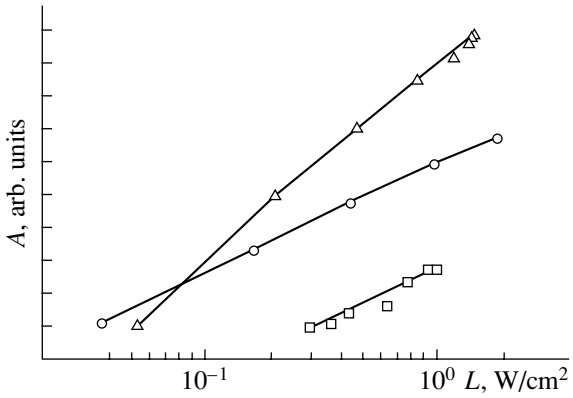

Fig. 2. Typical dependences of the photoreflectance signal on laser pump density $A(L)$ for the three samples studied.

can be well approximated by a logarithmic function. This circumstance led us to the conclusion about a linear relationship between the amplitude factor of the intermediate-field electromodulation signal and the photovoltage or variation in the surface potential ΔV_s within the LPD range considered.

CONCLUSION

To summarize, we would like to remind the reader that this study was aimed at gaining insight into the LPD influence on the characteristic time constant τ and the intensity of the intermediate-field electromodulation component. Varying LPD within the range L = 100 μW/cm^2 – 1 W/cm^2 results in a change in τ. This change, however, has practically no effect on the measured signal. Using experimental data and the results of calculations based on the generalized multilayer model, we introduced a concept of the amplitude factor for the intermediate-field component and proposed a method for determining it. For the samples under investigation, the logarithmic dependence $A(L)$ was established. By comparing the results obtained with those published elsewhere, the amplitude factor of the intermediate-field electromodulation signal was found to be a linear function of photovoltage. We may conclude that the typical response of the intermediate-field component to a change in LPD over a wide range of L values was obtained.

REFERENCES

1. D. E. Aspnes, Surf. Sci. **37**, 418 (1973).
2. H. Shen and M. Dutta, J. Appl. Phys. **78**, 2151 (1995).
3. J. P. Estrera, W. M. Duncan, and R. Glosser, Phys. Rev. B **49**, 7281 (1994).
4. R. Kuz'menko, A. Ganzha, É. P. Domashevskaya, *et al.*, Fiz. Tekh. Poluprovodn. (St. Petersburg) **34**, 1086 (2000) [Semiconductors **34**, 1045 (2000)].
5. R. Ditchfield, D. Llera-Rodríguez, and E. G. Seebauer, Phys. Rev. B **61**, 13710 (2000).

6. E. R. Wagner and A. Manselis, Phys. Rev. B **50**, 14228 (1994).
7. H. Shen, S. H. Pan, Z. Hang, *et al.*, Appl. Phys. Lett. **53**, 1080 (1988).
8. E. G. Seebauer, J. Appl. Phys. **66**, 4963 (1989).
9. A. V. Ganzha, W. Kircher, R. V. Kuz'menko, *et al.*, Fiz. Tekh. Poluprovodn. (St. Petersburg) **32**, 272 (1998) [Semiconductors **32**, 245 (1998)].
10. S. Hildebrandt, M. Murtagh, R. Kusmenko, *et al.*, Phys. Status Solidi A **152**, 147 (1995).
11. P. M. Pires, P. L. Souza, and J. P. von der Weid, Appl. Phys. Lett. **65**, 88 (1994).
12. T. Kanata, M. Matsugana, T. Takakura, and Y. Hamakawa, J. Appl. Phys. **69**, 3691 (1991).
13. H. Shen, M. Dutta, R. Lux, *et al.*, Appl. Phys. Lett. **59**, 321 (1991).
14. D. E. Aspnes, Phys. Rev. **147**, 554 (1966).
15. D. E. Aspnes, Phys. Rev. **153**, 972 (1967).

Translated by A. Sidorova-Biryukova

Semiconductors, Vol. 36, No. 2, 2002, pp. 157–159. Translated from Fizika i Tekhnika Poluprovodnikov, Vol. 36, No. 2, 2002, pp. 164–166.
Original Russian Text Copyright © 2002 by M. Ardyshev, V. Ardyshev.

ELECTRONIC AND OPTICAL PROPERTIES OF SEMICONDUCTORS

Effect of Ionization on the Behavior of Silicon in Gallium Arsenide Subjected to Electron-Beam Annealing

M. V. Ardyshev* and V. M. Ardyshev

Kuznetsov Physicotechnical Institute at Tomsk State University, pl. Revolyutsii 1, Tomsk, 634050 Russia

**e-mail: ard.rff@elefot.tsu.ru*

Submitted February 13, 2001; accepted for publication May 25, 2001

Abstract—The method of capacitance–voltage characteristics was used to study the behavior of Si implanted into GaAs after a postimplantation electron-beam annealing for 10 s under a beam-power density of 7.6 W cm^{-2}. The electron beam was incident on both the implanted and rear surfaces of the wafers. The reference samples were annealed thermally in a furnace for 30 min at 800°C. It is shown that the diffusion coefficient D is more than three orders of magnitude larger in the case of electron-beam annealing of the implanted surface than in the case of thermal annealing and by almost two orders of magnitude larger than in the case of electron-beam annealing of the rear surface. It is assumed that these distinctions are caused by a long existence time of the high steady-state concentration of nonequilibrium electrons and holes due to their spatial separation. © *2002 MAIK "Nauka/Interperiodica".*

It has been found [1, 2] that electron-beam annealing of GaAs makes it possible to attain much larger values of the diffusion coefficient and the electrical activation of implanted ^{28}Si compared to those obtained by thermal annealing at the same temperatures. It is assumed that this distinction is caused by the effect of "electronic excitations" (nonequilibrium charge carriers, the Auger processes, and plasmons) generated during the electron-beam annealing on the impurity redistribution. However, this assumption cannot be considered as unambiguous. First, in this case, a long existence time of the high concentration of nonequilibrium charge carriers (higher than 10^{19} cm^{-3}) should be assumed, which is doubted by many researchers [3]. Second, the observed effects can be caused by radiation-enhanced diffusion, which possibly proceeds during the electron-beam annealing differently from that during thermal annealing owing to a considerable difference in the heating rates of the material.

In this context, the objective of this study was to clarify the role of ionization-related and thermal effects in the diffusion-related redistribution and electrical activation of silicon implanted into gallium arsenide.

In the experiments, we used wafers of semi-insulating undoped GaAs with a resistivity higher than 10^7 Ω cm. The ^{28}Si ions were implanted at room temperature, first with an energy of 50 keV and a dose of 6.25×10^{12} cm^{-2} and then with an energy of 75 keV and a dose of 1.88×10^{12} cm^{-2}. In order to eliminate ion channeling, we used the method described elsewhere [1]. Prior to annealing, a SiO_2 film 0.1–0.3 μm thick was deposited onto both surfaces of the wafer using the plasma-chemical method. Electron-beam annealing was carried out for 10 s at a power density of 7.6 W cm^{-2}; a Modul' system was used. The electron beam was incident on both the implanted and rear surfaces of the wafers. The control thermal annealing was performed in a resistance furnace for 30 min at a temperature of 800°C in hydrogen flow. After the SiO_2 film was removed, we determined the electron-concentration profiles by measuring the capacitanance–voltage characteristics using the Schottky barriers with ohmic contacts.

In the figure, we show the electron-concentration profiles in the ion-implanted GaAs:Si layers after electron-beam annealing with the electron beam incident on the implanted surface (curve *1*) and on the rear surface (curve *2*), and also after thermal annealing (curve *3*); curve *4* represents the implanted silicon profile calculated using the ion-range parameters R_p and ΔR_p determined from secondary-ion mass spectrometry. Experimental doping profiles were processed using the Boltzmann–Motano method [1, 4].

In Table 1, we list the parameters of experimental electron-concentration profiles.

It folows from the figure and Table 1 that, after the electron-beam annealing of the ion-implanted surface, the values of the diffusion coefficient D and the degree of electrical activation η of the Si impurity are larger than those after annealing of the rear surface, which are, in turn, larger than those obtained as a result of thermal annealing. It is noteworthy that, for electron-beam annealing, the thermal field propagates to the entire thickness of the wafer in a characteristic time $\tau_c \geq 10^{-3}$ s ($\tau_c = d^2/\theta$, where d is the wafer thickness and θ is the

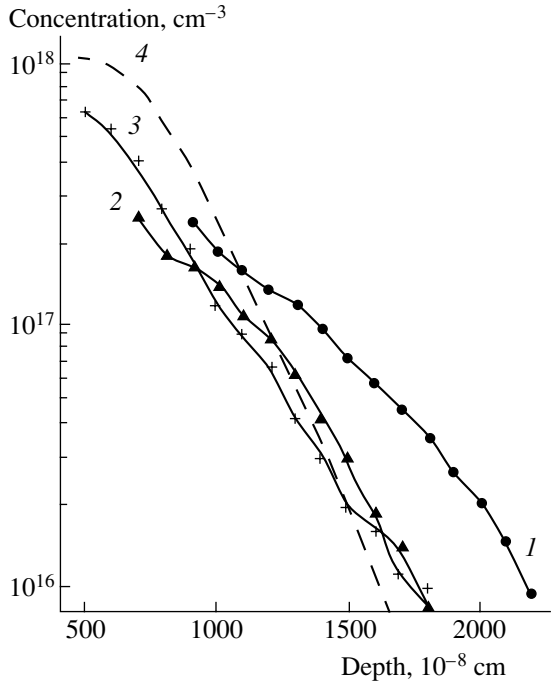

Electron-concentration profiles in GaAs:Si (*1*, *2*) after electron-beam annealing for 10 s with a power density of 7.6 W cm^{-2} when the beam was incident on the (*1*) implanted and (*2*) rear surfaces of wafers, and (*3*) after thermal annealing for 30 min at 800°C. Curve *4* represents the calculated concentration profile of silicon implanted first with an ion energy of 50 keV and dose of 6.25×10^{12} cm^{-2} and then with an energy of 75 keV and a dose of 1.88×10^{12} cm^{-2}.

thermal diffusivity) so that the temperatures at both surfaces are almost identical.

By solving the thermal-balance equation, we find that the saturation temperature T_s, the time for attaining the saturation t_s, and the heating rate of the wafers are 803°C, 294 s, and 741 K s^{-1}, respectively. Since $t_s \gg \tau_c$, the heating rate of both surfaces is almost the same. It should be noted that, in the case of thermal annealing, the value of dT/dt was equal to ~2.8 K s^{-1}. If we assume that, in the course of electron-beam annealing of the rear surface, migration of defects into the GaAs bulk occurs, the difference between the diffusion coefficients during the electron-beam and thermal annealings is caused by the impurity diffusion stimulated by defects. There are grounds to believe that this process is a consequence of the high heating rate of the sample during electron-beam treatment, owing to which the annealing of implantation-induced defects and the activation of impurities occur simultaneously [5]. However, the radiation-enhanced diffusion results in an insignificant increase in D (by a factor of 4, see Table 1). Taking into account that, in the case of electron-beam annealing of the ion-implanted surface, an increase in D amounts to several orders of magnitude and the nonequilibrium charge carriers are generated within the layer of the ion-implanted impurity, the most probable cause of the observed large values of D and η are the ionization effects.

Table 1. Parameters of electron-concentration profiles in GaAs:Si after annealings of various types

Type and conditions of annealing	Diffusion coefficient of Si D, cm^2 s^{-1}	The degree of Si activation η, %
Thermal annealing for 30 min at 800°C	2.0×10^{-15}	34.3
Electron-beam annealing for 10 s at a power density of 7.6 W cm^{-2}		
At the implanted surface	1.6×10^{-12}	40.1
At the rear surface	5.9×10^{-14}	52.6

Previously, the following mechanisms for enhancing the diffusion by the excitation of an electronic subsystem were suggested: the recombination θ-burst mechanism suggested by Lenchenko [6], the mechanism of inverse potentials suggested by Oksengendler [7], the Corbett–Bourgoin mechanism [8], and other mechanisms [9]. However, each of the above mechanisms has one or another drawback.

We represent the accumulation kinetics for nonequilibrium charge-carrier concentration as

$$\frac{\partial \Delta n}{\partial t} = G - \frac{\Delta n}{\tau} - \gamma(\Delta n)^3 + D_{n,p}\frac{\partial^2 \Delta n}{\partial x^2}, \qquad (1)$$

where G is the generation rate; τ is the lifetime of nonequilibrium charge carriers, which is controlled by their recombination; γ is the coefficient of the Auger recombination; and $D_{n,p}$ is the coefficient of ambipolar diffusion of nonequilibrium charge carriers.

A steady-state concentration of nonequilibrium charge carriers is attained during the electron-beam annealing; i.e., $\partial \Delta n/\partial t = 0$. For low generation rates, a decrease in the concentration of nonequilibrium charge carriers is governed by the second term on the right-hand side of Eq. (1); for higher generation rates, it is governed by the third term. The Auger recombination is dominant if $\gamma(\Delta n)^3 > \Delta n/\tau$. Assuming that $\tau = 10^{-8}$ s and $\gamma = 3 \times 10^{-31}$ cm^6 s^{-1} [10], we find that $\Delta n > 2 \times 10^{19}$ cm^{-3}. In order to attain such a concentration of nonequilibrium charge carriers, we have to ensure that $G \gtrsim \gamma(\Delta n)^3 = 2.4 \times 10^{27}$ cm^{-3} s^{-1}. We used the data reported in [11] to obtain the estimate of $G = \sigma_i N_0 j/e$, where σ_i is the ionization cross section, $N_0 = 4.45 \times 10^{22}$ cm^{-3} is the concentration of the semiconductor atoms, j is the electron current density ($j = 7.6 \times 10^{-4}$ A/cm^2), and e is the elementary charge. The value of σ_i was determined from the expression

$$\sigma_i = (\langle I \rangle N_0)^{-1} dE/dx, \qquad (2)$$

where $\langle I \rangle$ is the mean ionization potential for GaAs atoms, and dE/dx are the specific energy losses of electrons taking into account the backscattered particles.

In Table 2, we list the results of calculations. It can be seen that, for the electron-beam annealing used, the generation rate is much lower than the value at which the Auger recombination becomes dominant. Therefore, the steady-state concentration of nonequilibrium charge carriers Δn_{st} is controlled by the first, second, and fourth terms on the right-hand side of Eq. (1). We then take into account that the electron mobility μ_n in GaAs is much higher than the hole mobility μ_p; as a result, separation of charge carriers occurs. Assuming that the surface recombination is insignificant and that, at an annealing temperature T_{ann}, the concentration of thermally generated charge carriers $n_0(T_{ann})$ is equal to Δn_{st} at a depth of $x = 3L$ (L is the charge-carrier diffusion length), we obtain the following expression for the steady-state concentration of nonequilibrium charge carriers:

$$\Delta n_{st} = n_0(T_{ann})\left[\exp\left(\frac{eU_D}{kT_{ann}}\frac{\mu_n + \mu_p}{\mu_n - \mu_p}\right) - 1\right]. \qquad (3)$$

Here, $n_0(T_{ann}) = [N_c(T_{ann})N_v(T_{ann})]^{1/2}\exp[-\Delta E(T_{ann})/2kT_{ann}]$, where $N_c(T_{ann})$ and $N_v(T_{ann})$ are the densities of states (at the annealing temperature T_{ann}) in the conduction and valence bands, respectively; $\Delta E(T_{ann})$ is the band gap of GaAs at T_{ann}; and U_D is the potential barrier.

The values of mobilities μ_n and μ_p at $T_{ann} \approx 800$°C are mainly governed by scattering at optical phonons. Estimations show that, in this case, $\mu_n/\mu_p \approx 5$. At the same time, we have $n_0(800°C) \approx 10^{17}$ cm^{-3}. In order to satisfy the condition $\Delta n_{st} \gtrsim 10n_0(T_{ann})$, we have to assume that $U_D \approx 2(kT_{ann}/e)$; i.e., we have $U_D \approx 0.2$ V at $T_{ann} \approx 800$°C. This value of U_D appears realistic.

Thus, we substantiated experimentally the determining role of ionization-related and thermal processes in the enhancement of diffusion and the increase in the degree of electrical activation of ^{28}Si in the ion-implanted GaAs layers as a result of electron-beam annealing. We also showed that the most probable cause of the long-term existence of the high concentration of nonequilibrium charge carriers is their spatial separation.

Table 2. The results of calculating the interaction of electrons with GaAs

Electron energy E, keV	Ionization cross section σ_i, 10^{-17} cm^2	Generation rate G, 10^{20} cm^{-3} s^{-1}
5	8.5	12
10*	5.4	7.5
15	4.2	5.8

* In this study, we employed the electron-beam annealing with electron energy of 10 keV.

REFERENCES

1. M. V. Ardyshev and V. M. Ardyshev, Izv. Vyssh. Uchebn. Zaved., Fiz. **41**, 89 (1998).
2. M. V. Ardyshev and V. M. Ardyshev, Fiz. Tekh. Poluprovodn. (St. Petersburg) **32**, 1153 (1998) [Semiconductors **32**, 1029 (1998)].
3. A. V. Dvurechenskiĭ, G. A. Kachurin, E. V. Nidaev, and L. S. Smirnov, *Pulsed Annealing of Semiconducting Materials* (Nauka, Moscow, 1982).
4. A. Bakowski, J. Electrochem. Soc. **127**, 1644 (1980).
5. A. V. Chernyaev, *Ion Implantation Method in Technology of Devices and Integrated Circuits Based on GaAs* (Radio i Svyaz', Moscow, 1990).
6. V. M. Lenchenko, Fiz. Tverd. Tela (Leningrad) **11**, 799 (1969) [Sov. Phys. Solid State **11**, 649 (1969)].
7. B. L. Oksengendler, Pis'ma Zh. Éksp. Teor. Fiz. **24**, 12 (1976) [JETP Lett. **24**, 9 (1976)].
8. J. Bourgoin and J. Corbett, Phys. Lett. A **38**, 135 (1972).
9. B. Askarov, A. Sh. Makhmudov, B. L. Oksengendler, and M. S. Yunusov, *Radioactivated Processes in Silicon* (Fan, Tashkent, 1977).
10. J. Smith, Phys. Rev. B **3**, 4330 (1971).
11. I. A. Abroyan, A. N. Andronov, and A. I. Titov, *Physical Principles of Electronic and Ionic Technology* (Vysshaya Shkola, Moscow, 1984).

Translated by A. Spitsyn

Semiconductors, Vol. 36, No. 2, 2002, pp. 160–166. Translated from Fizika i Tekhnika Poluprovodnikov, Vol. 36, No. 2, 2002, pp. 167–173.
Original Russian Text Copyright © 2002 by Ballandovich, Mokhov.

ELECTRONIC AND OPTICAL PROPERTIES OF SEMICONDUCTORS

Annealing of Deep Boron Centers in Silicon Carbide

V. S. Ballandovich and E. N. Mokhov^

Ioffe Physicotechnical Institute, Russian Academy of Sciences, St. Petersburg, 194021 Russia

^e-mail: mokhov@pop.ioffe.rssi.ru;

mokhov@rednet.ru

Submitted April 25, 2001; accepted for publication May 25 2001

Abstract—The effect of annealing on the efficiency of high-temperature luminescence of 6*H*-SiC samples grown under varied conditions and doped with boron was studied. A part of the samples was subjected to neutron or fast-electron irradiation. It is shown that the efficiency of high-temperature luminescence is determined by the concentration of deep boron-related centers, revealed by capacitance spectroscopy as *D* centers. High-temperature treatment leads to dissociation of the *D* centers, which are B_{Si}–V_C complexes, with part of the boron atoms becoming electrically inactive. It is established that deep boron centers are thermally stable up to ≈1500°C. The preservation of these centers at higher temperatures (up to 2600°C) is due to the presence in SiC crystals of clusters acting as sources of nonequilibrium carbon vacancies. Clusters of this kind are contained in crystals grown with an excess of silicon or irradiated with high-energy particles. This circumstance accounts for the strong dependence of both the concentration of *D* centers and the temperature of their annealing on sample preparation conditions. *© 2002 MAIK "Nauka/Interperiodica".*

INTRODUCTION

Boron, a Group III element, forms two acceptor centers in SiC [1, 2]. One of these, having an ionization energy of 0.3–0.39 eV, is commonly observed in measuring the Hall effect in a *p*-type material. The other, a deeper energy state of boron, was originally discovered in *n*-SiC samples doped with boron by the diffusion method [3]. This state activates high-temperature luminescence (HTL) with an emission peak at 2.0–2.2 eV for the 6*H*-SiC polytype. An analysis of the spectra of boron-related luminescence [4] established that the HTL is due to radiative transitions in donor–acceptor pairs and to ⟨conduction band⟩–acceptor transitions, with the ionization energy of the acceptor equal to ~0.7 eV. A deep acceptor state with ionization energy of 0.55–0.6 eV was observed in measuring the Hall effect in *p*-SiC samples diffusion-doped with boron [2, 5]. A similar boron-related deep center (*D* center) was revealed by capacitance spectroscopy in both *n*- [6, 7] and *p*-type SiC [8].

Electron spin resonance (ESR) and electron-nuclear double resonance (ENDOR) measurements in SiC:B samples enriched in ^{13}C isotope revealed the nature of the centers generated upon introduction of boron into SiC. It was found that the shallow acceptor center in SiC:B is created by a boron atom substituting silicon at a regular lattice site [9], and an impurity–defect complex, which comprises a boron atom and carbon vacancy (B_{Si}–V_C) and is oriented along the *c* axis of the crystal, is responsible for the deep center [10].

The factors affecting the formation of deep centers have been studied in sufficient detail. It has been found that the relative fraction of these centers strongly depends on crystal growth conditions and doping methods [1, 2, 11], donor impurity concentration [12], and exposure to radiation [1].

Much less is known about the thermal stability of deep boron centers. Meanwhile, the *D* centers, being impurity-defect complexes, would be expected to disintegrate upon thermal annealing. This issue is the subject of the present study. This paper reports the results obtained in studying the efficiency of HTL and data of capacitance measurements on irradiated and unirradiated 6*H*-SiC samples of varied origin doped with boron during growth or by the diffusion method. It is demonstrated that the thermal stability of deep boron centers depends exceedingly strongly on the conditions of growth, doping, and irradiation. The effect of these factors is accounted for by the nature of the influence they exert on the structure of point defects in the SiC samples under study.

EXPERIMENTAL PROCEDURE

The *n*-type SiC samples of the 6*H* polytype, grown by sublimation and doped with nitrogen and boron, served as objects of study. Depending on the preparation conditions, they belonged to one of the following three groups:

(1) crystals grown by the Lely method at a temperature $T_g \approx 2550$–2600°C under nearly stoichiometric conditions and doped with boron in growth or by means of diffusion (*L* samples);

(2) SiC crystals or epitaxial layers grown by the sublimation sandwich method (SSM) [13] in the tempera-

ture range $T_g \approx 1800$–2050°C, with strong excess of silicon vapor (*S* samples);

(3) SiC crystals of the first and second groups irradiated with reactor neutrons or high-energy electrons (*I* samples). The irradiation dose Φ_n was in the range 10^{17}–10^{21} cm^{-2}.

The concentration of uncompensated donors (N_d–N_a) in the samples, found from *C*–*V* data or determined using the local breakdown method [14], varied between 2×10^{16} and 5×10^{18} cm^{-3}. The concentration of boron was determined, with the use of neutron activation analysis by the method of track autoradiography [2], to be within 2×10^{16}–3×10^{18} cm^{-3}.

In studying the thermal stability of *D* centers, samples were cut into several parts, which were then subjected to 10-min isochronal annealing in Ar atmosphere in the temperature range 1200–2500°C.

The effect of thermal treatment on the concentration of *D* centers was monitored by changes in the efficiency of high-temperature boron-related luminescence. The luminescence was excited by the UV light of a high-pressure mercury lamp ($\lambda = 365$ nm) with intensity $J = 10^{16}$ cm^{-2}. The illumination was performed from the carbon face side. Luminescent emission was extracted from the opposite face of the crystal, for which purpose the sample was mounted in a holder with a through aperture 1 mm in diameter and placed before the monochromator slit. The HTL intensity was evaluated by measuring the signal at the emission band peak ($\lambda = 580$ nm) at room temperature.

Deep level transient spectroscopy (DLTS) was used to study acceptor centers in *n*-SiC layers compensated with boron. Measurements were done on Schottky barriers formed by depositing semitransparent Cr films onto the $(000\bar{1})$ C faces. The *p*-type layer formed on the sample surface as a result of diffusion was preliminarily removed by short-time etching in molten alkali. The time and temperature of etching were chosen in such a way that the stripped surface was as close as possible to the interface of the diffused *p*–*n* junction. Technology of this kind was already used in our previous study concerned with boron-related acceptor centers in SiC [12]. In this study, DLTS spectra were measured on the same sample both before and after high-temperature treatment; i.e., the *p*–*n* junction stripping was done before annealing. Such a solution guaranteed that the compared results refer to one and the same spatial region of a sample. However, the sample surface itself was subject to erosion in the course of annealing. In addition, at annealing temperatures of 2000–2500°C, back diffusion of boron is possible from a surface layer whose thickness is comparable with that of the space charge region in the Schottky diode. To eliminate both these factors, the *p*-layer was removed in the present study after high-temperature treatment of the samples, and all measurements were done on different parts of one and the same crystal.

In addition to Schottky barriers, the boron-related acceptor centers were studied on epitaxial p^+–*n* structures with the base compensated with boron introduced by diffusion.

DLTS spectra of the samples under study were recorded in the temperature range 80–350°C. Deep acceptor centers were filled with holes by irradiating the Schottky barriers with the pulsed light of a UV laser. In the case of p^+–*n* structures, forward bias pulses of 1 ms duration were used for this purpose.

EXPERIMENTAL RESULTS

As shown by measurements, the efficiency of HTL from the samples under study strongly depends on their preparation method.

L samples doped with boron during growth show virtually no HTL, even though they contain boron in the amount of $(3–5) \times 10^{17}$ cm^{-3}. In samples of this kind, the HTL appears either upon repeated doping with boron or after irradiation with high-energy particles and subsequent annealing. The boron diffusion gives rise to high-efficiency HTL only in samples with nitrogen concentration $N_d > 1 \times 10^{18}$ cm^{-3}. Samples with a lower content of nitrogen show no luminescence at room temperature. In the case of exposure to radiation, the dependence of the luminescence intensity on the concentration of donors is not so pronounced. A rather strong luminescence is observed in samples with $(N_d–N_a) < 1 \times 10^{18}$ cm^{-3}, which show no HTL upon diffusion doping.

In contrast to Lely crystals, *S* samples exhibit characteristic boron HTL, whose intensity increases upon diffusion doping with boron from the very beginning. Luminescence comparable in efficiency with that in Lely single crystals is observed in *S* samples at a rather low concentration of donors, below 10^{17} cm^{-3}. It should also be noted that, at equal boron impurity concentrations, the efficiency of luminescence in *S* samples exceeds that in *L* crystals.

The efficiency of HTL in boron-doped SiC samples changes dramatically during their subsequent thermal treatment. Curves *1* and *2* in Fig. 1 represent the dependences of the HTL intensity on annealing temperature for, respectively, the Lely sample, diffusion-doped with boron, and the *S* sample, compensated with boron during growth. Curve *3* in Fig. 1 was measured on the same *S* sample after its repeated diffusion-doping with boron.

In all cases, high-temperature annealing makes the HTL efficiency lower; however, the temperature dependences of the HTL are markedly different for samples of different types. For *L* samples, the HTL intensity decreases abruptly in the temperature range 2300–2400°C. In *S* samples, the HTL efficiency decreases more gradually, with the result that these samples retain luminescence properties at higher annealing temperatures. Such an essentially weaker dependence of the luminescence intensity on the annealing temperature is characteristic of all the *S* samples studied, despite the

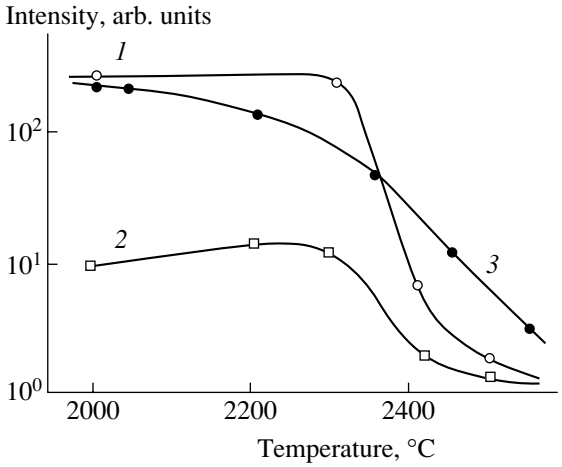

Fig. 1. Intensity of boron-related HTL vs. annealing temperature for (*1*) *L* and (*2*, *3*) *S* samples of 6*H*-SiC with various concentrations of donors, N_d, and acceptors, N_a. (*1*) $N_d = 3 \times 10^{18}$, $N_a = 2.5 \times 10^{18}$; (*2*) $N_d = 5 \times 10^{17}$, $N_a = 1 \times 10^{17}$; and (*3*) $N_d = 5 \times 10^{17}$, $N_a = 2.5 \times 10^{17}$ cm^{-3}.

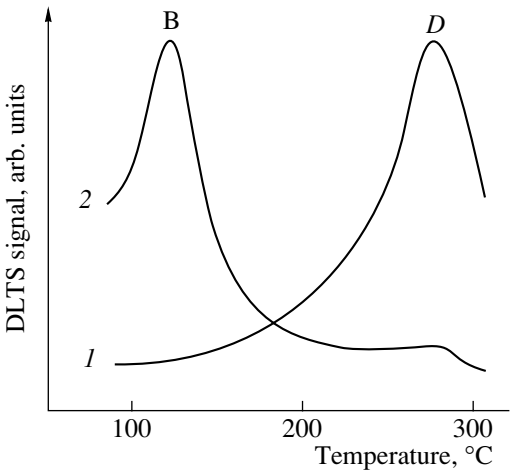

Fig. 2. DLTS spectra of *S* sample of *n*-SiC (6*H*) (*1*) before and (*2*) after annealing at $T = 2350$°C. The inverse-rate window $\tau_m = 21.7$ ms.

different concentrations of boron and nitrogen impurities in these samples.

The luminescence properties of annealed samples can be restored by repeated diffusion of boron (Fig. 1, curve *3*), with annealing leaving unchanged, at least at temperatures of up to 2300°C, all differences between *L* and *S* samples. Only annealing at $T \approx 2600$°C leads to an irreversible change in the luminescence properties of *L* samples, making them similar to Lely crystals [11]. This means that repeated diffusion of boron into samples with $N_d < 10^{18}$ cm^{-3} does not give rise to HTL. It should be emphasized that the temperature at which the luminescence properties of *L* samples are changed irreversibly is close to the temperature at which SiC crystals are grown by the Lely method.

DLTS shows that the decrease in the HTL efficiency under high-temperature annealing is due to dissociation of *D* centers. Curves *1* and *2* in Fig. 2 represent, respectively, DLTS spectra of an *S* sample diffusion-doped with boron, which were measured before and after annealing at 2350°C. Each spectrum is normalized to the highest peak intensity. The concentrations of deep and shallow boron-related acceptor centers in this sample, calculated on the basis of capacitance measurements, are presented in the table. As seen from Fig. 2, *D* centers, to which the peak at 280 K in DLTS spectra corresponds (curve *1*), dominate in the sample before the high-temperature treatment. Such a situation is characteristic of all boron-doped *L* and *S* samples exhibiting high-efficiency HTL [12]. High-temperature treatment of both *L* and *S* samples makes the HTL efficiency lower and, simultaneously, leads to a dramatic decrease in the number of *D* centers (curve *2*), so that their concentration upon annealing becomes lower than the concentration of shallow boron-related (B) centers. The peak at 130 K in DLTS spectra corresponds to these. The strict relationship between the HTL efficiency and the concentration of *D* centers indicates that it is these centers that activate the high-temperature boron-related luminescence in SiC.

Concentrations of uncompensated donors $N_d - N_a$ and boron-related acceptor centers B and *D* in a diffusion-doped *S* sample before and after high-temperature annealing ($T = 2350$°C)

Parameter	After diffusion	After annealing
$N_d - N_a$ (300 K)*, cm^{-3}	6.0×10^{16}	4.2×10^{17}
B centers, cm^{-3}	1.0×10^{17}	$(1.0–1.2) \times 10^{17}$
D centers, cm^{-3}	3.5×10^{17}	$(0.2–0.3) \times 10^{17}$

* In the starting sample $N_d - N_a = 5.1 \times 10^{17}$ cm^{-3}.

A decrease in HTL intensity under the action of high-temperature treatment is also observed in SiC samples irradiated with high-energy particles. For this group of samples, the irradiation dose is one of the main factors defining the onset of HTL annealing out. Figure 3 illustrates the effect of annealing on the HTL intensity for *L* samples of 6*H*-SiC, which were irradiated with high-energy electrons or reactor neutrons. The presented dependences have a shape characteristic of curves with a peak. The increase in the HTL intensity in irradiated crystals with increasing annealing temperature is apparently due to annealing out of nonradiative recombination centers, whereas its subsequent drop is associated with dissociation of the luminescence-active centers themselves.

At neutron irradiation doses of 10^{17}–10^{18} cm^{-2}, the HTL intensity in *L* samples already starts to decrease at temperatures $T_a \approx 1500$–1600°C (Fig. 3, curve *2*). At approximately the same temperatures, HTL is quenched in SiC crystals irradiated with high-energy electrons

(Fig. 3, curve *1*). With increasing the irradiation dose, the HTL quenching temperature increases steeply. At the neutron irradiation dose $\Phi_n \approx 10^{19}$ cm^{-2}, the HTL centers are stable up to 1800°C, whereas at $\Phi_n \approx 10^{20}$cm^{-2} HTL quenching begins only at ≈2100°C. At doses on the order of 10^{21} cm^{-2}, HTL is still preserved in samples annealed at the highest temperature possible for solid SiC, i.e., $T \approx 2600$°C. It can be seen from Fig. 3 that, with increasing irradiation dose, an increase in HTL intensity is observed simultaneously with the rise in the onset temperature of HTL annealing out.

Figure 4 shows the onset temperature of HTL annealing out versus the dose of irradiation with reactor neutrons for *S* and *L* samples (curves *1* and *2*, respectively) having approximately the same concentrations of both donor and acceptor impurities. Both the samples were doped with boron during growth. In accordance with the aforesaid, the HTL was entirely absent in the *L* sample, whereas the *S* sample exhibited rather high-intensity luminescence. After irradiation and subsequent annealing, HTL was observed in both samples. Measurements demonstrated that at irradiation dose $\Phi_n = 10^{17}$ cm^{-2} the efficiency of HTL in the *S* sample is much higher, and the onset temperature of its annealing out exceeds that for the *L* sample by 250–300°C. The revealed differences are characteristic of all *L* and *S* samples at small irradiation doses. With increasing irradiation dose, these differences between *L* and *S* samples tend to be eliminated, and at doses $\Phi_n > 10^{19}$ cm^{-2} both the intensity of HTL and the temperature of its annealing out are close in samples of different types.

The results obtained in studying the annealing of HTL in irradiated samples demonstrate that the transformation of *D* centers begins already at $T \approx 1500$°C in the absence of factors hindering this process. The binding energy of the complex, evaluated on the basis of luminescence studies, is 2.5 eV. It was natural to expect that the dissociation of a deep boron-related acceptor state would give rise to additional B centers. However, according to the results of capacitance measurements obtained previously [12] and in the present study, the annealing out of *D* centers is accompanied by a decrease in the total concentration of acceptors in a sample, and, even if the concentration of B centers increases, it does so to a very slight extent. This suggests that, in the course of annealing, part of the boron atoms pass into an electrically inactive state. Presumably, this is due to the formation of more complex structural groups incorporating boron atoms.

The possibility that part of the boron atoms are in an electrically inactive state is also indicated by the results obtained in studying SiC diffusion-doped with the ^{10}B boron isotope. Figure 5 presents diffusion distributions of the ^{10}B boron isotope in *S* and *L* samples with a comparatively low concentration of nitrogen ($N_d < 1 \times 10^{18}$ cm^{-3}), obtained by means of track autoradiography [2, 11]. This technique, relying upon the nuclear reaction $^{10}B(n, \alpha)^7Li$, determines the total concentration of

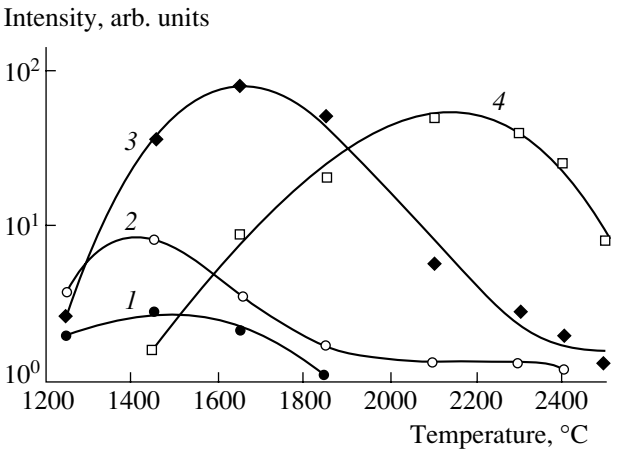

Fig. 3. Intensity of boron-related HTL vs. annealing temperature for *L* samples of 6*H*-SiC irradiated with (*1*) high-energy electrons and (*2*, *3*, *4*) reactor neutrons. Irradiation dose Φ: (*1*) 1×10^{18}, (*2*) 2×10^{17}, (*3*) 1×10^{19}, and (*4*) 1×10^{20} cm^{-2}.

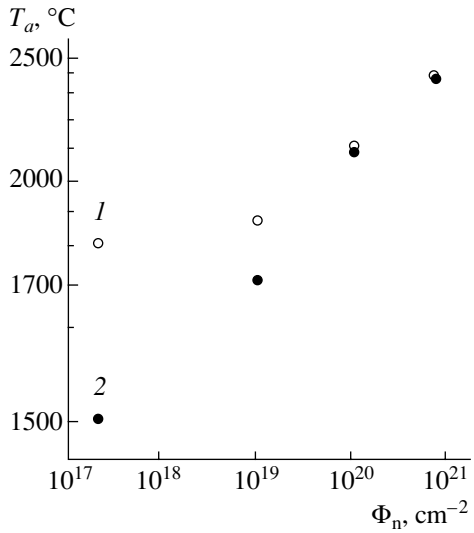

Fig. 4. Onset temperature of HTL center annealing out vs. dose Φ_n of irradiation with reactor neutrons for (*1*) *S* and (*2*) *L* samples of 6*H*-SiC with various concentrations of donors, N_d, and acceptors, N_a. (*1*) $N_d = 5.4 \times 10^{17}$, $N_a = 1 \times 10^{17}$; (2) $N_d = 5.8 \times 10^{17}$, $N_a = 1.2 \times 10^{17}$ cm^{-3}.

^{10}B isotope atoms introduced into the crystal in the course of diffusion. These dependences were compared with the acceptor distributions in the same samples, measured using the local breakdown method [14] with layer-by-layer etching-off of the diffusion layer. The comparison demonstrated that the distribution of acceptors in *S* crystals corresponds to the distribution of boron atoms, whereas in *L* samples the acceptor concentration profile is much steeper. Hence, it follows that in *L* samples with $N_d < 10^{18}$ cm^{-3} part of the introduced boron atoms do not act as acceptor impurities. It is noteworthy that the difference between the acceptor con-

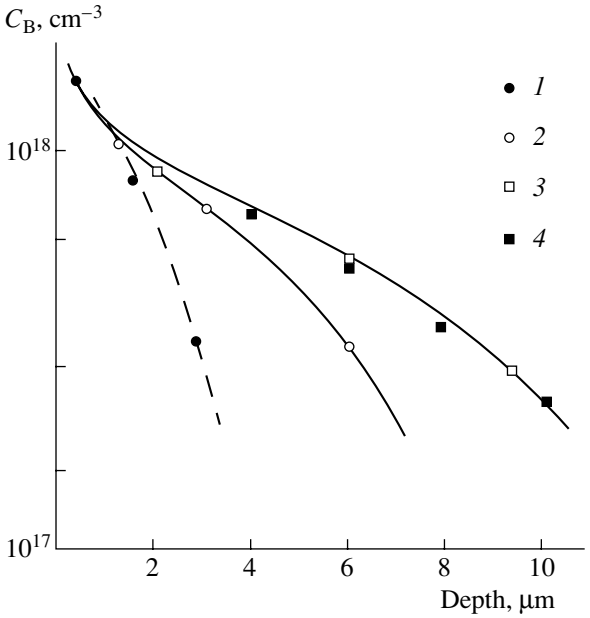

Fig. 5. Diffusion distributions of (*2*, *3*) ^{10}B boron isotope and (*1*, *4*) boron acceptors in (*1*, *2*) *L* and (*3*, *4*) *S* samples of *n*-SiC (6*H*) doped with nitrogen to donor concentrations N_d: (*1*, *2*) 5.0×10^{17} and (*3*, *4*) 5.5×10^{17} cm^{-3}. Diffusion temperature 1850°C, time of diffusion 2 h.

centration and the total concentration of boron atoms is the greatest in that part of the crystal in which the concentration of introduced boron atoms is lower than the concentration of donors ($C_B < N_d$). Possibly, it is this factor that is the reason for the absence of HTL in weakly nitrogen-doped Lely samples subjected to diffusion of boron.

Thermal treatment of boron-doped samples affects not only their photoluminescent properties. High-temperature annealing of a diode structure with a boron-compensated base can change the concentration profile of the acceptor impurity near the *p*–*n* junction. For example, Fig. 6 shows capacitance–voltage (*C*–*V*) characteristics of three *p*–*n* structures fabricated from a single sample—an aluminum-doped p^+ epitaxial layer grown on a Lely substrate with donor concentration $N_d = 1.8 \times 10^{18}$ cm^{-3}. The sample was cut into three parts, one of which served as a control, and the remaining two were boron-doped. In turn, one of the boron-doped parts was subjected to a 5-min annealing at 2350°C. Then mesa structures were formed on the basis of all the three parts, with the Al contact 300 μm in diameter to the p^+ layer and the large-area Ni contact to the *n*-substrate. The *C*–*V* characteristics of structures subjected to boron diffusion and diffusion-annealing are represented in Fig. 6b by, respectively, curves *1* and *2*. For comparison, Fig. 6a shows a *C*–*V* characteristic of the control structure.

As seen, when plotted in the $1/C^2 - V$ coordinates, the *C*–*V* characteristic of the control structure is linear, which is typical of p^+–*n* junctions with a uniformly

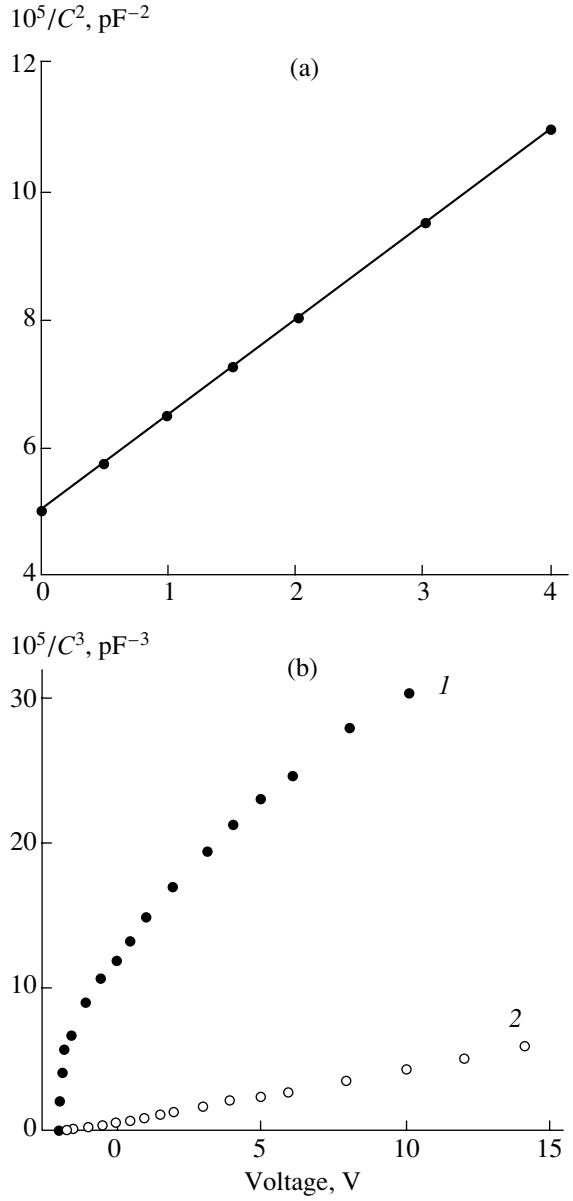

Fig. 6. *C*–*V* characteristics of p^+–*n*-SiC diode structures: (a) control structure and (b) structure with boron-compensated base (*1*) before and (*2*) after annealing at 2350°C (*t* = 5 min).

doped base. The slope of this characteristic is determined by the concentration of donors in the *n*-substrate, $N_d = 1.8 \times 10^{18}$ cm^{-3}. Diffusion of boron into the starting sample leads to a manyfold decrease in the capacitance of the p^+–*n* structure, with the capacitance depending only slightly on the reverse bias applied to the sample (Fig. 6b, curve *1*).

It is known from the general theory that, in the case of a measuring bridge with parallel equivalent circuit, a decrease in the equivalent capacitance of a sample may be due to an increase in the series resistance in the measuring circuit. However, we observed no frequency dis-

persion of capacitance, inherent in a diode with a high-resistivity base.

The above specific features are characteristic of the behavior of a *p–i–n* structure, which in turn points to the presence in the vicinity of the p^+–*n* junction of an extended, strongly compensated region. DLTS measurements show that the appearance of this region is due to introduction of *D* centers by diffusion into the *n* substrate of the starting sample. Subsequent high-temperature annealing of the sample leads to dissociation of the *D* centers, with the capacitance of the structure again increasing (Fig. 6b, curve *2*). This means that the annealing out of *D* centers causes an increase in the concentration of uncompensated donors in the diode base. This result is in agreement with the conclusion that part of the boron-related acceptor centers passes into an electrically inactive state in the course of annealing. The *C–V* characteristic of an annealed sample corresponds to the *C–V* characteristic of a *p–n* junction with linear distribution of the impurity in the base, which is typical of diffusion structures.

DISCUSSION

The obtained results indicate that the *D* centers, or boron–vacancy complexes B_{Si}–V_C, are thermally unstable at temperatures higher than 1500°C. This fact accounts for the strong dependence of the properties of boron-doped SiC samples on their growth conditions. With the structure of the *D* centers taken into account, it may be stated that the probability of their formation and preservation will largely depend on the number and type of intrinsic defects in any particular sample. Indeed, at the high temperature of SiC crystal growth by the Lely method (≈2600°C), equalization of the partial pressures of silicon and carbon in the vapor phase occurs, which leads to a decrease in the content of carbon vacancies associated with deviations from the stoichiometry [15, 16]. At the same time, this temperature markedly exceeds the dissociation temperature of associates and clusters incorporating both intrinsic defects and impurity atoms [15]. As a result of both of these factors, only B centers (isolated boron atoms in the silicon sublattice) are formed in Lely crystals doped with boron during growth.

Irradiation of Lely single crystals with high-energy particles leads to generation of intrinsic defects of the vacancy type. The interaction of these defects with boron atoms results in the formation in the samples of *D* centers, which is indicated by the appearance of HTL. With increasing irradiation dose, the number of radiation defects must grow. This must, in turn, lead to the formation of a greater number of *D* centers and an increase in the HTL efficiency, which is the case in the experiment (Fig. 3).

In the diffusion doping of SiC with boron, carbon vacancies generated at the surface are injected inside the crystal together with boron atoms [15]. Therefore, the probability of *D* center formation in the diffusion zone is also high.

SiC crystals and epitaxial layers grown by SSM at temperatures by 500–800°C lower than those in the Lely process, under the conditions of strong enrichment of the vapor phase in silicon, are characterized by an increased content of carbon vacancies from the very beginning [16]. This fact, combined with the lower growth temperature, increases the probability of *D* center formation in SiC synthesis by SSM. It is not surprising that both B and *D* centers are observed in *S* samples doped with boron during growth. The concentration of carbon vacancies is particularly high in *S* samples grown with additional introduction of Si vapor into the growth zone. At equal concentrations of boron atoms, samples of this kind show the highest efficiency HTL [11], which indicates that they contain an increased number of *D* centers. A similar effect of the Si/C ratio on the concentration of deep and shallow boron-related acceptor centers was observed in the CVD growth of epitaxial 4*H*-SiC layers [17]. As shown in [17], the concentration of shallow boron-related acceptor centers in layers grown at a small Si/C ratio was two orders of magnitude higher than the concentration of *D* centers. Only shallow boron-related low-temperature luminescence was observed in these layers. At the same time, layers grown at a large Si/C ratio exhibited characteristic high-temperature boron-related luminescence.

The number and structure of intrinsic defects affect not only the formation of *D* centers in SiC doping with boron; the same factors determine the thermal stability of *D* centers in annealing. This is most clearly manifested in studying the luminescence properties of crystals exposed to radiation. At small irradiation doses, the HTL intensity already starts to decrease in such samples at a temperature of ≈1500°C. Presumably, this is the lowest temperature at which the transformation of *D* centers occurs. With increasing irradiation dose, the onset temperature of HTL annealing-out becomes higher. To explain this effect, account should be taken of the fact that the increasing irradiation dose raises the concentration of vacancy defects in a sample, and a substantial part of these defects will be present in the form of clusters. The existence of such clusters in irradiated SiC crystals is confirmed by studies of these crystals by means of positron diagnostics [18]. In our opinion, it is the formation of vacancy clusters that increases the thermal stability of *D* centers. In the course of annealing, the clusters partly dissociate and may serve as a source of isolated vacancies [15], whose increased concentration will hinder the dissociation of *D* centers. This effect is well known as Ostwald ripening and is widely described in the literature. Maintaining the existence of boron–vacancy complexes at high temperatures, the clusters also lead to a decrease in the apparent activation energy of annealing (Fig. 4).

Similar processes occur in the annealing of unirradiated *S* samples grown at moderate temperatures in an

excess of Si. The only difference is in the cluster formation mechanism. In contrast to the case of classical semiconducting materials, clusters in SiC retain their activity, i.e., the ability to grow or dissociate up to high temperatures at which crystal growth or doping takes place. [15]. Therefore, it seems quite possible that clusters can be introduced into a crystal not only during its irradiation with high-energy particles, but also during its growth. As mentioned above, the very conditions of SiC growth in an excess of silicon lead to a higher concentration of stoichiometric defects and carbon vacancies in particular. In the grown crystals, these vacancies can only exist as secondary defects or more complex structural groups, since single vacancies of carbon in silicon carbide are already annealed out at ≈150°C [19]. The presence of vacancy clusters in *S* samples increases the probability of *D* center formation upon additional introduction of boron (e.g., by diffusion). Therefore, at equal boron concentrations, such samples show higher HTL efficiency, compared with Lely crystals. The same factor is responsible for the enhanced thermal stability of *D* centers in *S* samples during their annealing (Fig. 1). It is noteworthy that enhanced stability is also characteristic of another defect complex in *S* samples which incorporates a carbon vacancy, namely, the D_1 center [20]. Only prolonged annealing of *S* samples at $T \approx$ 2600°C leads to the irreversible transformation of stoichiometric intrinsic defects, e.g., via their migration to drains or because of the increasing cluster size (to the point of microvoid formation), thereby making their properties closer to those of Lely crystals.

The increased concentration of vacancy defects in *S* samples is revealed in comparing the luminescence properties of *L* and *S* samples irradiated with small doses. As already noted, at an irradiation dose $\Phi_n = 10^{17}$ cm^{-2}, the efficiency of HTL in *S* samples is much higher and the temperature of its annealing-out exceeds that for *L* samples by 250–300°C (Fig. 4). At high irradiation doses, the concentration of radiation defects exceeds manyfold that of stoichiometric defects both in *L* and in *S* samples, and, therefore, the sample prehistory has no effect on the HTL efficiency and the temperature of *D* center annealing out.

Thus, the whole set of the obtained data is explained as follows: deep boron-related centers are metastable at temperatures higher than 1500°C, and their preservation in this temperature range is due to the presence of clusters of intrinsic defects introduced into SiC crystals during growth, boron diffusion, or irradiation of the samples with high-energy particles.

ACKNOWLEDGMENTS

We thank Yu.A. Vodakov for his helpful participation in discussions of the results and E.E. Goncharova for measuring the boron concentration in the samples.

REFERENCES

1. S. H. Hagen and A. W. C. Kemenade, Phys. Status Solidi A **33**, 97 (1976).
2. Yu. A. Vodakov, N. Zhumaev, B. P. Zverev, *et al.*, Fiz. Tekh. Poluprovodn. (Leningrad) **11**, 373 (1977) [Sov. Phys. Semicond. **11**, 214 (1977)].
3. É. E. Violin and G. F. Kholuyanov, Fiz. Tverd. Tela (Leningrad) **6**, 1696 (1964) [Sov. Phys. Solid State **6**, 1331 (1964)].
4. H. Kuwabara and S. Yamada, Phys. Status Solidi A **30**, 739 (1975).
5. A. I. Veĭnger, Yu. A. Vodakov, Yu. I. Kozlov, *et al.*, Pis'ma Zh. Tekh. Fiz. **6**, 1319 (1980) [Sov. Tech. Phys. Lett. **6**, 566 (1980)].
6. V. S. Ballandowich, Yu. N. Tairov, and G. N. Violina, Phys. Status Solidi A **65**, 109 (1981).
7. M. M. Anikin, A. A. Lebedev, A. L. Syrkin, and A. V. Suvorov, Fiz. Tekh. Poluprovodn. (Leningrad) **19**, 114 (1985) [Sov. Phys. Semicond. **19**, 69 (1985)].
8. W. Suttrop, G. Pensl, and P. Lanig, Appl. Phys. A: Solids Surf. **A51**, 231 (1990).
9. A. G. Zubatov, I. M. Zaritskiĭ, S. N. Lukin, *et al.*, Fiz. Tverd. Tela (Leningrad) **27**, 322 (1985) [Sov. Phys. Solid State **27**, 197 (1985)].
10. A. Van Duijn-Arnold, T. Ikoma, O. G. Poluektov, *et al.*, Phys. Rev. B **57**, 1607 (1998).
11. Yu. A. Vodakov, G. G. Goncharov, G. A. Lomakina, *et al.*, Fiz. Tekh. Poluprovodn. (Leningrad) **21**, 207 (1987) [Sov. Phys. Semicond. **21**, 126 (1987)].
12. V. S. Ballandovich and E. N. Mokhov, Fiz. Tekh. Poluprovodn. (St. Petersburg) **29**, 370 (1995) [Semiconductors **29**, 187 (1995)].
13. Yu. A. Vodakov, E. N. Mokhov, G. Ramm, and A. D. Roenkov, Krist. Tech. **14**, 729 (1979).
14. E. I. Radovanova, R. G. Verenchikova, and Yu. A. Vodakov, Fiz. Tekh. Poluprovodn. (St. Petersburg) **17**, 1115 (1983) [Sov. Phys. Semicond. **17**, 701 (1983)].
15. Yu. A. Vodakov and E. N. Mokhov, Inst. Phys. Conf. Ser. **137**, 197 (1994).
16. A. I. Girka and E. N. Mokhov, Fiz. Tverd. Tela (St. Petersburg) **37**, 3374 (1995) [Phys. Solid State **37**, 1855 (1995)].
17. S. G. Sridhara, L. L. Clemen, R. P. Devaty, *et al.*, J. Appl. Phys. **83**, 7909 (1998).
18. A. I. Girka, A. D. Mokrushin, E. N. Mokhov, *et al.*, Zh. Éksp. Teor. Fiz. **97**, 578 (1990) [Sov. Phys. JETP **70**, 322 (1990)].
19. M. Itoh, Phys. Status Solidi B **202**, 173 (1997).
20. Yu. A. Vodakov, G. A. Lomakina, E. N. Mokhov, *et al.*, Fiz. Tekh. Poluprovodn. (Leningrad) **20**, 2153 (1986) [Sov. Phys. Semicond. **20**, 1347 (1986)].

Translated by M. Tagirdzhanov

Semiconductors, Vol. 36, No. 2, 2002, pp. 167–170. Translated from Fizika i Tekhnika Poluprovodnikov, Vol. 36, No. 2, 2002, pp. 174–177.
Original Russian Text Copyright © 2002 by Kovalenko, Litvinova, Shutov.

ELECTRONIC AND OPTICAL PROPERTIES OF SEMICONDUCTORS

Edge-Photoluminescence Concentration Dependence in Semi-Insulating Undoped GaAs

V. F. Kovalenko, M. B. Litvinova, and S. V. Shutov

Institute of Semiconductor Physics, National Academy of Sciences of Ukraine, Kherson, 73008 Ukraine

Submitted October 2, 2000; accepted for publication June 4, 2001

Abstract—Dependences of the spectral peak position of edge photoluminescence, its half-width, resistivity, charge carrier mobility in crystals of semi-insulating undoped GaAs on the carbon concentration N_C at 77 K (3.0×10^{15} cm^{-3} ≤ N_C ≤ 4.3×10^{16} cm^{-3}) were studied. The dependences observed are explained by the interaction of charge carriers with ionized impurity atoms and with structural defects. © *2002 MAIK "Nauka/Interperiodica".*

INTRODUCTION

Interest in semi-insulating undoped (SIU) GaAs is the result of its use in the fabrication of integrated circuits and microwave devices. The SIU GaAs crystals contain carbon atoms in the range of $\approx 2 \times 10^{14}$–3×10^{16} cm^{-3} [1–3]. Carbon is the main background impurity, and it plays an important and diverse role in the formation of the electrical properties of crystals. On the one hand, reducing its concentration (N_C) results in the enhancement of the electron mobility [3]. On the other hand, carbon atoms, occupying the arsenic sites and being shallow acceptors, control the semi-insulating properties of the material and provide the electrical compensation of shallow (Si, S) [4] and deep (*EL*2) [1, 2] donors. This makes it necessary to maintain the carbon concentration at the level which corresponds to the level of contamination of material with donor impurities and defects.

The previous study of the edge photoluminescence (PL) of SIU GaAs crystals, which is related to the annihilation of excitons and the direct recombination of free electrons and holes [5, 6], was restricted to the study of crystals with various specific values of N_C [1]. Along with this, the appearance and enhancement of the interimpurity interaction and an increase in the role of scattering with an increase in carbon concentration in the aforementioned range can affect the PL characteristics. Therefore, it is of interest to examine the edge PL in relation to the electrical properties in the wide range of variations in the carbon concentration.

In this paper, we report the results of such studies.

EXPERIMENTAL

Studies of emission-peak energy $h\nu_m$ and half-width W of the edge PL band in relation to carbon content were carried out using Czochralski-grown, nominally undoped GaAs crystals. The carbon concentration varied in the range of 3×10^{15} cm^{-3} ≤ N_C ≤ 4.3×10^{16} cm^{-3}. The value of N_C was estimated using the calibration dependence $I_{1.49}/I_{1.51} = f(N_C)$ [7], where $I_{1.49}$ is the intensity of the "carbon" PL with $h\nu_m \lesssim 1.495$, and $I_{1.51}$ is the intensity of the edge emission band under study with $h\nu_m \lesssim 1.510$ eV.

The resistivity ρ of crystals at 300 K was measured by the two-probe method, and the mobility of the majority charge carriers μ was determined from Hall coefficient measurements at 300 K. The type of conduction was determined by the thermoelectric-power sign.

The PL spectra of samples at 77 K were measured using an SDL-1 setup in the wavelength range of 0.8–1.2 μm. The argon laser (λ = 0.488–0.514 μm) with radiation intensity $I_0 = 3 \times 10^{21}$ cm^{-2} s^{-1} served as the PL excitation source. An FEU-62 photomultiplier was used as the photodetector.

The concentration of the *EL*2 deep-level donor centers in the GaAs crystals was determined by measuring the optical absorption in the range of 1.0–1.2 μm at 300 K; an SF-6 spectrophotometer was used. The concentration of these centers was independent of N_C and amounted to $N_{EL2} = (1 - 2.5) \times 10^{16}$ cm^{-3}.

RESULTS

The PL spectrum of the crystals studied contained a band of edge emission and a band at a longer wavelength; the latter band has a lower intensity, is separated from the edge band by 15–17 meV, and is associated with the participation of C_{As}-centers in the radiative transitions [1]. The shape of the emission spectrum for crystals with various carbon concentrations is shown in Fig. 1. The dependence of the PL peak energy $h\nu_m$ and of the edge band half-width W on N_C is presented in Fig. 2.

1063-7826/02/3602-0167$22.00 © 2002 MAIK "Nauka/Interperiodica"

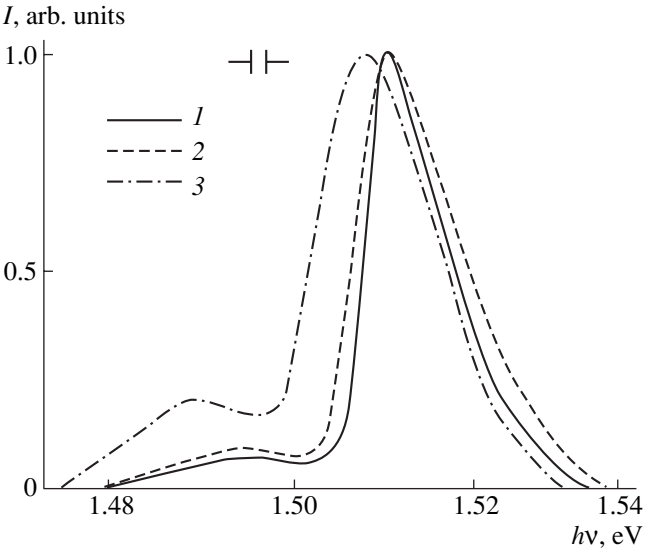

Fig. 1. PL spectra of crystals with various concentrations of carbon N_C. T = 77 K, N_C = (*1*) 4×10^{15}, (*2*) 1.4×10^{16}; and (*3*) 3×10^{16} cm^{-3}.

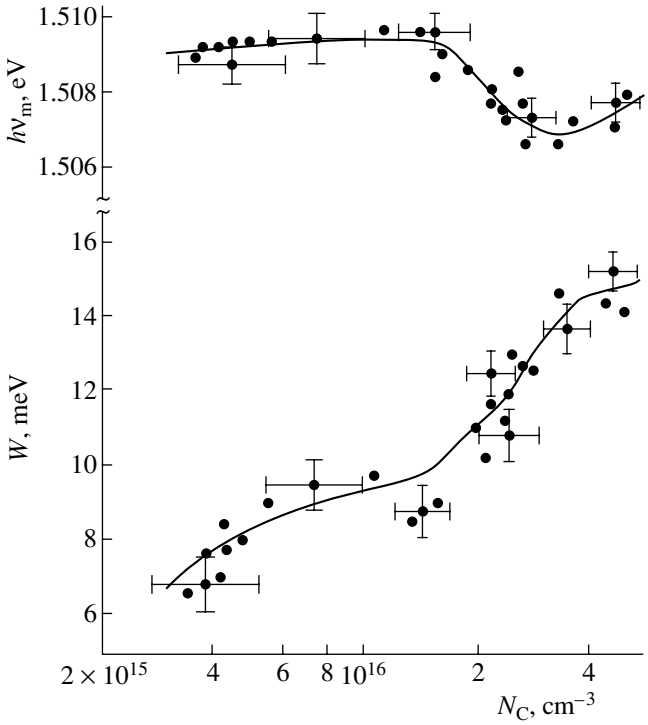

Fig. 2. Dependence of the peak energy $h\nu_m$ and half-width W of the edge PL band on the carbon concentration. T = 77 K.

A slight increase of $h\nu_m$ in the range 1.509–1.510 eV was observed with the carbon concentration increase in crystals with $N_C \lesssim 1.4 \times 10^{16}$ cm^{-3}; for $N_C > 1.4 \times 10^{16}$ cm^{-3}, a significant decrease in the PL peak energy to values of $h\nu_m \cong 1.507$ eV for $N_C \cong 3 \times 10^{16}$ cm^{-3} occurred; in the range 3×10^{16} cm$^{-3} < N_C \leq 4.3 \times 10^{16}$ cm^{-3}, a slight increase in $h\nu_m$ was observed. With the increase in the carbon concentration, the band half-width continuously increased from $W \cong 6.5$ meV in the purest crystals to $W \cong 15$ meV in the crystals with the highest carbon content owing to broadening predominantly in the low-energy region, and to a lesser extent, in the high-energy region. As can be seen from Fig. 2, the shift of $h\nu_m$ to the low-energy region is accompanied by a substantial increase in W with increasing N_C.

The electrical properties of the crystals studied also depended on the carbon content. The crystals with $N_C \lesssim 3 \times 10^{16}$ cm^{-3} were of the *n*-type, and those with $N_C > 3 \times 10^{16}$ cm^{-3} were of the *p*-type. Resistivity ρ and mobility μ dependences on the carbon content are presented in Fig. 3. In the crystals with $N_C \lesssim 2 \times 10^{16}$ cm^{-3}, resistivity was independent of N_C and $\rho \cong 5 \times 10^7$–5×10^8 Ω cm. With the carbon concentration increase in the region $N_C > 2 \times 10^{16}$ cm^{-3}, the ρ decreased to $\approx 10^2$ Ω cm. The electron mobility μ decreased from 6500 cm^2 V^{-1} s^{-1} in the purest crystals to $\mu \cong 0$ for $N_C \cong (2.5–3) \times 10^{16}$ cm^{-3}; in this case, the most significant decrease in mobility occurred in the range 1.3×10^{16} cm^{-3} < $N_C \lesssim 2.5 \times 10^{16}$ cm^{-3}, in which $h\nu_m$ decreased. In crystals with $N_C > 3 \times 10^{16}$ cm^{-3}, some increase in the hole mobility was observed with an increase in N_C ($\mu \cong 500$ cm^2 V^{-1} s^{-1} for $N_C \cong 4.3 \times 10^{16}$ cm^{-3}).

DISCUSSION

The peak position $h\nu_m \cong 1.509$ eV in the purest crystals indicates that the emission band observed is not associated with exciton annihilation, since the difference E_g–$h\nu_m$ is less than the exciton binding energy [8]. On the other hand, the band width in these crystals is characteristic of excitonic radiative recombination. These features of the edge PL can be explained as follows. According to [9], the theoretical emission band width should be equal to 1.8 kT and the PL peak energy should be close to E_g in direct-gap semiconductors for interband radiative transitions of nondegenerate electrons and holes with their interaction and scattering disregarded. In the presence of Coulomb interaction, the interband luminescence should be considered a result of the annihilation of excitons, with the latter being in the continuous spectrum states. In this case, the interaction of recombining charge carriers results in the reduction of the band width to 0.7 kT and in a shift of the band peak to longer wavelengths by a value smaller than the binding energy of a free exciton. In the presence of Coulomb interaction, the scattering of recombining electrons and holes yields values of W that are intermediate between the values given above.

The fact that the values of W observed in the purest crystals are close to the theoretical value of the half-

width $W \cong 0.7kT$ allows us to assume the predominant contribution of interacting charge carrier transitions in the states of the allowed spectrum to the formation of the edge emission band. The encrease in both $h\nu_m$ and W with increasing carbon concentration in the region $N_C \lesssim 1.4 \times 10^{16}$ cm^{-3} is associated, in our opinion, first, with the screening of the electron–hole interaction by impurity atoms and with an increase in the fraction of interband transitions of noninteracting carriers and, second, with the enhancement of the indirect radiative transitions caused by scattering at the ionized impurity atoms. The latter fact is confirmed by the broadening of the band towards the short-wavelength region within the indicated range of N_C increase.

The most probable cause of the change in $h\nu_m$ and W with the carbon concentration increase in the region $N_C > 1.4 \times 10^{16}$ cm^{-3} is the participation of the tail states in the radiative transitions; these states are formed near the edges of allowed bands and are caused by fluctuations of the total concentration N_Σ of electrically active impurities and defects (C_{As}, Si_{Ga}, $EL2$, etc). It is known [10] that, in lightly doped semiconductors under conditions of pronounced compensation, nonuniform distribution of impurities in the bulk induces large-scale fluctuations of the impurity potential due to weak screening of this potential by the free charge carriers owing to their low concentration.

We believe that, in the high-resistivity crystals studied, the parameters of tails in the density of states (the depth γ of potential wells and their size r) are governed by screening by impurities and defects characterized by a correlated distribution rather than by free electrons, the concentration of which is lower than N_Σ by several orders of magnitude.

Estimations of parameters r and γ taking into account the impurity screening carried out for $N_C = 3 \times 10^{16}$ cm^{-3} and $N_{EL2} = 2 \times 10^{16}$ cm^{-3} (which corresponds to a minimum value of $h\nu_m$) according to formulas from [10]

$$r_i = \sqrt{\frac{\varepsilon kT}{4\pi N_\Sigma e^2}},$$

$$\gamma = \frac{e^2}{\varepsilon}\sqrt{N_\Sigma r},$$

yield the values of $r_i \cong 4 \times 10^{-6}$ cm and $\gamma \cong 5.3$ meV.

For such parameters of potential wells, the localization condition $\hbar^2/m^*r^2 \ll \gamma$ is well satisfied for holes and poorly satisfied for electrons; it follows that, in the region $N_C > 1.4 \times 10^{16}$ cm^{-3}, the edge band is associated mainly with the recombination of nonlocalized electrons, with holes localized in the valence band tails. The difference between the width of the GaAs band gap at 77 K ($E_g = 1.5115$ eV [11]) and the measured value of $h\nu_m$ for $N_C \cong 3 \times 10^{16}$ cm^{-3} ($h\nu_m = 1.5067 \pm 0.0005$ eV) is equal to 4.8 ± 0.5 meV and is in satisfactory agreement with the calculated magnitude of γ, which confirms the validity of the conclusion about the mechanism of radiative transitions.[1] The tendency towards an increase in the PL peak energy $h\nu_m$ and the stabilization of the edge emission band width W with the increase in the carbon concentration in the region $N_C > 3 \times 10^{16}$ cm^{-3}, in which the crystals acquire the p-type conduction and low resistivity, are presumably caused by the increase in the screening of the impurity potential by free holes with concentration p_0 and in the change of the potential-well parameters as a result of screening. The estimate of the screening radius r_0 by holes carried out for $N_C = 4 \times 10^{16}$ cm^{-3}, $N_{EL2} = 2 \times 10^{16}$ cm^{-3}, and $p_0 = 2 \times 10^{16}$ cm^{-3} using the formula [10]

$$r_0 = \frac{N_\Sigma^{1/3}}{p_0^{2/3}},$$

yields $r_0 \cong 5 \times 10^{-6}$ cm, practically coinciding with the radius of impurity screening r_i for $N_C = 3 \times 10^{16}$ cm^{-3}. This fact confirms the assumption of the change in the screening character in this region of carbon concentration. In this context, the character of dependence $h\nu_m(N_C)$ with increasing carbon concentration for $N_C > 4.3 \times 10^{16}$ cm^{-3} can be easily foreseen. An increase in the free-hole concentration p_0 causes the complete screening of the impurity potential fluctuations ($r_0 \longrightarrow 0$), which results in an increase in the spectrum-peak energy up to $h\nu_m \cong 1.510$ eV and to the absence of its dependence on the carbon concentration with a further increase of the latter; this is characteristic of low and intermediate doping levels [9].

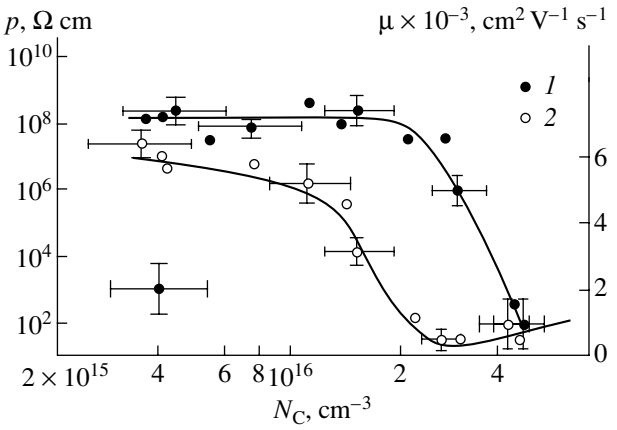

Fig. 3. Dependence of (*1*) the resistivity and (*2*) mobility of charge carriers on the carbon concentration. $T = 300$ K.

[1] There is an ambiguity caused by the difference of numerical coefficients in the formula for γ presented in various references. Thus, the estimate of γ according to [9], $\gamma = \sqrt{\pi}\frac{e^2}{\varepsilon}\sqrt{Nr}$, yields $\gamma \cong 9$ meV, which somewhat worsens the correlation between the calculated and measured values of γ but does not eliminate it.

In conclusion, we note that the presence of fluctuations of the impurity potential in the SIU GaAs crystals under study allows us also to associate the sharp lowering of the electron mobility in the region $N_C \gtrsim 1.4 \times 10^{16}$ cm^{-3} with the increase in the scattering efficiency by the atomic clusters, in contrast to scattering by the individual ionized impurity atoms.

REFERENCES

1. K. D. Glinchuk, V. I. Guroshev, and A. V. Prokhorovich, Optoélektron. Poluprovodn. Tekh. **24**, 66 (1992).
2. M. Suemitsu, M. Nishijima, and N. Miyamoto, J. Appl. Phys. **69**, 7240 (1991).
3. M. W. Duncan, G. H. Westphal, and A. J. Purdes, J. Appl. Phys. **66**, 2430 (1989).
4. Yu. N. Bol'sheva, M. A. Il'in, and A. V. Markov, Vysokochist. Veshchestva, No. 4, 210 (1989).
5. M. I. Kalinin, M. T. Lisitsa, and F. V. Motsnyĭ, Ukr. Fiz. Zh. **37** (3), 330 (1992).
6. M. I. Kalinin, M. T. Lisitsa, and F. V. Motsnyĭ, Ukr. Fiz. Zh. **37** (4), 528 (1992).
7. K. D. Glinchuk, N. M. Litovchenko, A. V. Prokhorovich, and O. N. Strel'chuk, Optoélektron. Poluprovodn. Tekh. **32**, 61 (1997).
8. V. S. Bagaev, L. I. Paduchikh, and T. S. Sakhonenko, *Excitons in Semiconductors* (Nauka, Moscow, 1971), p. 54.
9. A. P. Levanyuk and V. V. Osipov, Usp. Fiz. Nauk **133** (3), 427 (1981) [Sov. Phys. Usp. **24**, 187 (1981)].
10. B. I. Shklovskiĭ and A. L. Efros, *Electronic Properties of Doped Semiconductors* (Nauka, Moscow, 1979; Springer-Verlag, New York, 1984).
11. E. Grilli, M. Guzzi, R. Zamboni, and L. Pavesi, Phys. Rev. B **45**, 1638 (1992).

Translated by T. Galkina

Semiconductors, Vol. 36, No. 2, 2002, pp. 171–175. Translated from Fizika i Tekhnika Poluprovodnikov, Vol. 36, No. 2, 2002, pp. 178–182.
Original Russian Text Copyright © 2002 by Shmagin, Andreev, Antonov, Krasil'nik, V. Kuznetsov, O. Kuznetsov, Uskova, Ammerlaan, Pensl.

ELECTRONIC AND OPTICAL PROPERTIES OF SEMICONDUCTORS

Electrically Active Centers in Si:Er Light-Emitting Layers Grown by Sublimation Molecular-Beam Epitaxy

V. B. Shmagin*^, B. A. Andreev*, A. V. Antonov*, Z. F. Krasil'nik*, V. P. Kuznetsov, O. A. Kuznetsov**, E. A. Uskova**, C. A. J. Ammerlaan***, and G. Pensl******

**Institute for Physics of Microstructures, Russian Academy of Sciences, Nizhniĭ Novgorod, 603950 Russia*
^e-mail: shm@ipm.sci-nnov.ru
***Physicotechnical Institute, Nizhniĭ Novgorod State University, Nizhniĭ Novgorod, 603600 Russia*
****Van der Waals-Zeeman Institute, University of Amsterdam, 1018 XE Amsterdam, The Netherlands*
*****Institute of Applied Physics, University of Erlangen-Nurnberg, Gebaude A3, D-91058, Erlangen, Germany*
Submitted May 29, 2001; accepted for publication June 5, 2001

Abstract—Electrically active centers in light-emitting Si:Er layers grown by sublimation molecular-beam epitaxy (SMBE) on single-crystal Si substrates have been investigated by admittance spectroscopy with temperature scanning and by DLTS. The total density of electrically active centers is defined by shallow donor centers with ionization energies of 0.016–0.045 eV. The effect of growth conditions and post-growth annealing on the composition and density of electrically active centers has been studied. Significant differences in composition of the electrically active centers with deep levels and in channels of energy transfer from the electron subsystem of a crystal to Er^{3+} ions between Si:Er layers grown by SMBE and ion implantation have been revealed. © *2002 MAIK "Nauka/Interperiodica".*

1. INTRODUCTION

Erbium-doped silicon is attracting much attention as a material for the fabrication of efficient light emitters operating at the wavelength of 1.54 μm, which lies in the maximum transparence window of quartz optical communication fibers. Promising methods for creating effectively emitting Si:Er/Si structures are molecular-beam epitaxy (MBE) [1, 2] and its variation, sublimation molecular-beam epitaxy (SMBE), in which the Si and Er molecular beams are produced by sublimation of a Si crystal initially doped with Er and other necessary impurities [3]. SMBE has been used to fabricate structures with uniformly doped light-emitting Si:Er layers [4–8], as well as periodic multilayer structures with alternating pure silicon and Si:Er layers, which demonstrate record-breaking photoluminescence (PL) intensity per unit thickness of light-emitting layer [7, 8].

Optical properties of SMBE structures, including the classification of optically active centers and their transformation under post-growth annealing, have been studied in sufficient detail [4–8]. The electrically active centers and their role in the excitation and de-excitation of optically active Er^{3+} ions have been studied to a lesser extent [5, 9]. The goal of this study was to investigate, by means of capacitance spectroscopy, the electrically active centers in light-emitting SMBE Si:Er layers, their transformation under post-growth thermal treatment, and their effect on the optical properties of the layers.

2. EXPERIMENTAL

Uniformly doped Si:Er layers were grown on *p*- and *n*-type (100) Si substrates with 20, 10 and 0.008 Ω cm resistivity in a vacuum chamber with a residual pressure of 2×10^{-7} mbar. Wafers cut from Si:Er ingots with an Er and O content of up to 5×10^{20} and 1×10^{19} cm^{-3}, respectively, were used as sublimating sources. The growth temperature T_g was varied from 400 to 600°C, and the layer thickness, from 0.2 to 3 μm. Several structures were additionally annealed in hydrogen at T_{ann} = 900°C for 30 min.

The electrically active centers in the Si:Er layers were studied by admittance spectroscopy with temperature scanning and by deep level transient spectroscopy (DLTS) in the temperature range T = 10–350 K. The admittance was measured in the frequency range f = 0.1–1000 kHz. The active (G) and capacitive (C) components of the current flowing through the structure were selected using the lock-in technique. DLTS measurements were done at 400 kHz using a dual-gated signal averager (double boxcar) [10]. It is necessary to note that the combination of DLTS with admittance spectroscopy allowed us to identify both shallow and deep levels in a single experiment, thus enhancing the bulk and the reliability of the obtained data.

The Schottky contacts for capacitance measurements were fabricated by thermal evaporation of Pd onto the preliminarily treated surface of a sample at a residual pressure of $\sim 6 \times 10^{-6}$ mbar. The ohmic contact

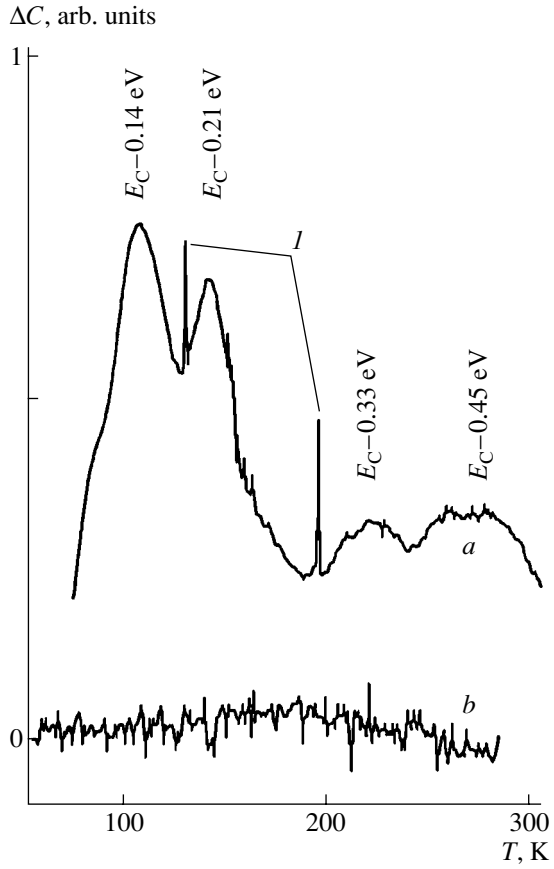

Fig. 1. DLTS spectra of a Si:Er/Si structure: (*a*) before and (*b*) after annealing. Substrate KÉF-0.008, growth temperature T_g = 430°C; annealing conditions: 900°C/30 min/H_2. Spectrum recording conditions: τ_{window} = 0.6 ms, voltage U = –2 V. (*1*) calibration pulse amplitude $\Delta C = 10^{-3}C$, where C is the structure capacitance at the calibration temperature.

was formed by rubbing In–Ga alloy in the back surface of a sample or by sputtering a large-area Schottky contact near the measuring contact (for structures on high-resistivity *p*-type substrates).

3. RESULTS AND DISCUSSION

All the epitaxial layers studied had *n*-type conduction, irrespective of the growth temperature. The type of conduction did not change upon subsequent thermal treatment of the structures. The free carrier density determined from capacitance–voltage and the Hall effect measurements was 10^{16}–10^{18} cm^{-3} at T = 300 K.

3.1. Unannealed Layers

Electrically active centers with deep levels with ionization energies in the 0.15–0.45 eV range were observed in unannealed Si:Er layers (Fig. 1). Their density was $N_T \lesssim 2 \times 10^{15}$ cm^{-3}, with relative density $N_T/(N_D - N_A) \lesssim 0.03$. Earlier studies [3, 11] have shown that the background level of contaminants introduced by the equipment in the process of SMBE growth is on the order of $\sim 2 \times 10^{13}$ cm^{-3} [3, 11]. Therefore, the origin of the observed electrically active centers is related to the process of Er introduction. The N_T value is defined by the conditions of fabricating the Si:Er layers, being the largest in layers grown at a lower temperature ($T_g \lesssim$ 500°C) and decreasing as the growth temperature is raised. Presumably, N_T is independent of the type of substrate: deep level densities were nearly the same in Si:Er layers grown on low-resistivity (KÉF-0.008) and relatively high-resistivity (KDB-10, KDB-20) substrates. KÉF-0.008 stands for *n*-Si:P with ρ = 0.008 Ω cm; and KDB-10 and KDB-20 stand for *p*-Si:B ρ = 10 and 20 Ω cm, respectively.

A specific feature of this group of electrically active centers is that they are completely annealed out upon additional post-growth annealing (900°C, 30 min, H_2). Earlier studies of isochronous (30 min) annealing of uniformly doped SMBE-structures have shown that the type of emitting center is modified by annealing. The intensity of PL related to Er^{3+} ions is the lowest at annealing temperature T_{ann} = 750°C and increases upon annealing of Si:Er/Si structures at T_{ann} = 800–900°C [6, 7]. This suggests that the electrically active centers revealed in unannealed Si:Er layers are not involved in the transfer of excitation from the electron subsystem of the Si crystal to Er^{3+} ions. In all probability, they should be classified as growth defects.

Another specific feature of unannealed layers is the strong temperature dependence of the measured barrier capacitance (Fig. 2a). The observed $C(T)$ dependence cannot be accounted for by the effect of deep levels localized in the space charge region (SCR), because the relative density of deep levels in this structure is too low: $N_T/(N_D - N_A) \lesssim 0.03$. The effect of thermally stimulated capacitance [12], which might be evidence in favor of the hypothesis relating the observed variation of the barrier capacitance to recharging of deep levels in the SCR, is observed neither in this nor in similar structures. It is possible that the observed $C(T)$ dependence is defined by the fluctuations of the band potential in the SCR. It is known that these fluctuations, which arise, e.g., in the case of a nonuniform distribution of impurities, yield an anomalous temperature dependence of the barrier capacitance, similar to that presented in Fig. 2a, with the magnitude of the derivative $|dC/dT|$ proportional to the dispersion which characterizes the fluctuations of the band potential [13]. A nonuniform distribution of impurities may arise from the fact that the Er density in the Si:Er layer is several orders of magnitude higher than the equilibrium solubility of Er in Si, which is equal to $\sim 10^{16}$ cm^{-3} at 1300°C [14]. High-temperature annealing in hydrogen (Fig. 2b) eliminates this anomaly of the $C(T)$ dependence. It is noteworthy that, in this case, we are dealing with equilibrium changes in barrier capacitance, which are not related to nonequilibrium thermally stimulated processes.

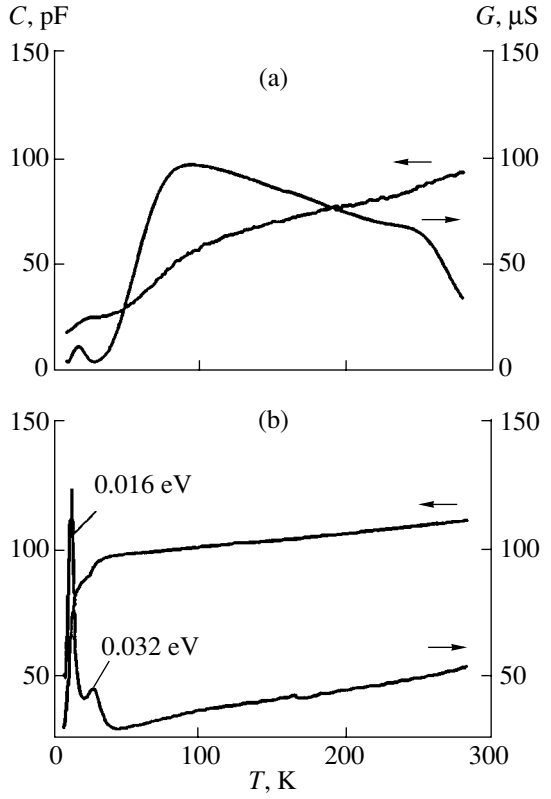

Fig. 2. Admittance spectra of a Si:Er/Si structure: (a) before and (b) after annealing. The structure and the annealing conditions are the same as in Fig. 1. Spectra recorded at frequency $f = 1$ MHz, voltage $U = 0$.

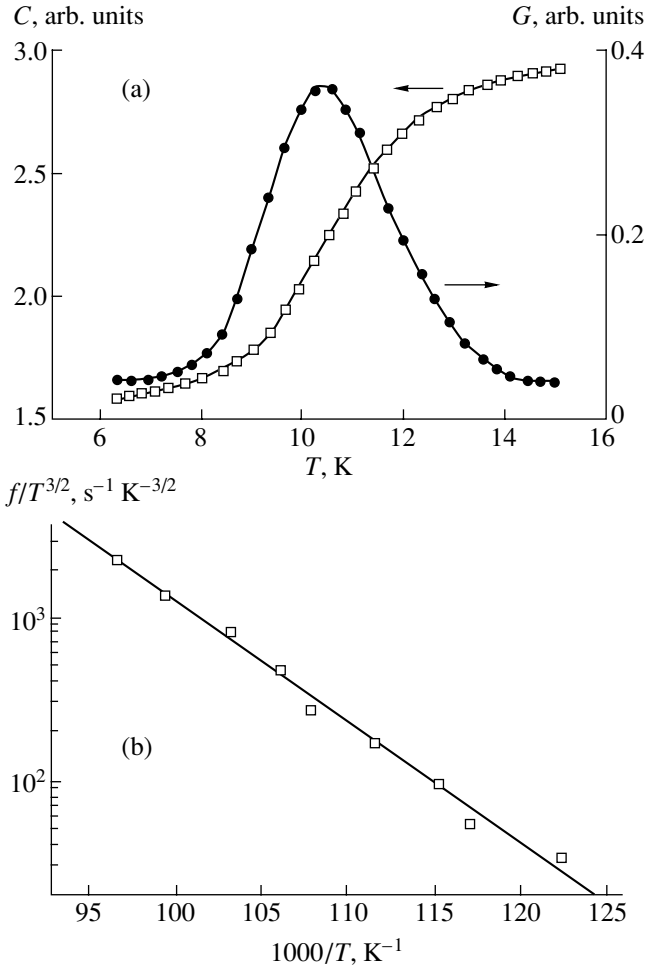

Fig. 3. Determining the ionization energy of shallow donors from the admittance-spectroscopy data: (a) admittance spectra, (b) Arrhenius plot. Spectra recorded at frequency $f = 8 \times 10^2$–8×10^4 Hz, voltage $U = 0$.

3.2. Annealed Layers

The only type of electrically active centers observed in annealed Si:Er layers are shallow donor centers with ionization energies of 0.016–0.045 eV. Figure 3a shows the admittance spectra $C(T)$ and $G(T)$ of a Si:Er/Si structure, recorded at zero bias with the probing signal frequency $f = 80.6$ kHz. It is worth noting that, for this case, the peak in the $G(T)$ and the step in $C(T)$ curves are due to carrier freeze-out to the main (shallow) impurity in the neutral region of the diode [12]. If the probing frequency is varied, the observed dependences shift along the temperature axis. Figure 3b presents the temperature at which $G(T)$ has a maximum as a function of the probing-signal frequency in the Arrhenius coordinates. The ionization energy of the level, which defines the slope of the Arrhenius dependence, is 0.016 eV. In determining the ionization energy, account was taken of the temperature dependence of the effective density of states in the conduction band, $N_C(T) \propto T^{3/2}$, and the temperature dependence of the carrier mobility was disregarded.

The type of conduction defined by these impurity centers and the behavior under post-growth annealing suggest that the observed shallow centers can be classified as quenched-in donors, i.e., impurity-defect complexes arising in oxygen-enriched silicon crystals under thermal treatment. The role of Er in their formation is not quite clear. Probably, Er atoms, which are larger than Si atoms, introduce significant distortions into the silicon crystal lattice, thus accelerating the generation of thermodonors [15]. Noteworthy is the difference between the compositions of shallow, electrically active centers in SMBE layers grown from different Si:Er sources. In our opinion, the most probable reason is the effect of residual impurities, especially, O, C, and N, (and, possibly, other light element impurities), which can be incorporated into the observed shallow centers.

Figure 4 presents the admittance spectra $C(T)$ of an SMBE Si:Er/Si structure grown on a high-resistivity KDB-20 substrate (see the inset). An interesting feature of these spectra is that, depending on the measuring circuit, they allow for the observation of carrier freeze-out to electrically active centers localized either in the substrate or in the Si:Er layer. If an In–Ga contact is used as the ohmic contact (Fig. 4, curve *1*), the neutral region of the diode includes the in-series connected substrate

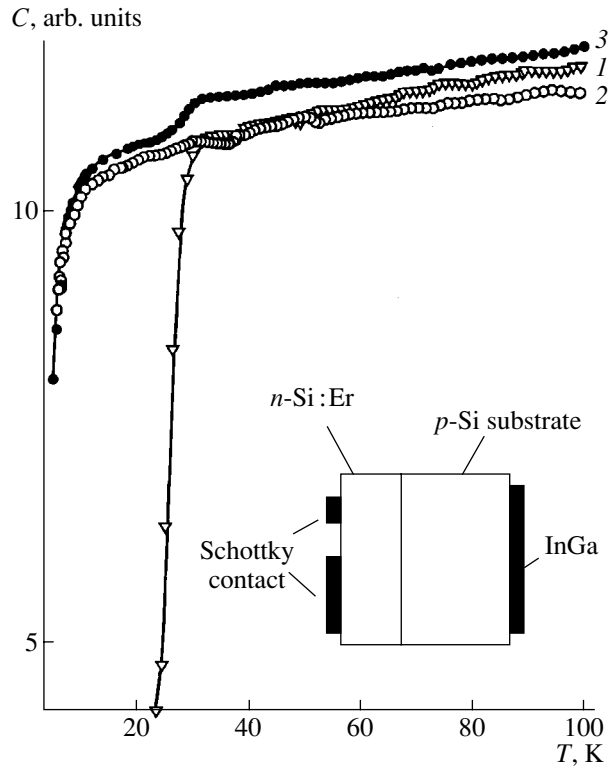

Fig. 4. Admittance spectra of a Si:Er/Si structure for different circuit connections. For explanation, see text.

and part of the epitaxial Si:Er layer. In this situation, with temperature lowered, we observe carrier freeze-out to the impurity with a higher ionization energy (boron in the substrate). If the large-area Schottky contact (planar configuration of contacts) is used as the ohmic contact, the neutral region of the diode includes only some part of the epitaxial layer and not the substrate, and, therefore, the freeze-out in the substrate does not affect the measured barrier capacitance (Fig. 4, curve *2*). In this case, we observe carrier freeze-out to shallow centers localized in the epitaxial Si:Er layer at a lower temperature, which indicates the lower ionization energies of the electrically active centers as compared with boron. When the substrate and the epitaxial layer in the neutral region of the diode are connected in parallel (Fig.4, curve *3*), we observe carrier freeze-out to the impurities localized both in the substrate and in the Si:Er layer. The freeze-out in the substrate is less pronounced, because the epitaxial layer is a well-conducting parallel (shunting) channel at this temperature.

4. CONCLUSION

The most pronounced difference between the structures grown by SMBE and by ion implantation is as follows. In the implanted structures, deep levels are reliably observed at ionization energies of 0.1–0.2 eV, including the level $E_C - 0.15$ eV, which, according to current concepts, is responsible for the transfer of excitation to Er^{3+} ions in the implanted layers [16]. In the SMBE layers, all attempts to observe deep levels in this range of ionization energies failed despite the intensive PL related to optically active Er^{3+} ions. For example, in a Si:Er/Si structure exhibiting intensive Er PL, the density of Er-related optically active centers at liquid helium temperature was $N_{Er}^{opt} = 2 \times 10^{16}$ cm^{-3} [17] at a total Er density of $N_{Er}^{tot} = 1 \times 10^{18}$ cm^{-3}. According to DLTS data, the density of deep levels with ionization energy in the range 0.1–0.3 eV, which could be involved in the transfer of energy to Er^{3+} ions (via the mechanism of exciton capture by deep levels, described in [16, 18]), was $N_{Er}^{el} < 1 \times 10^{13}$ cm^{-3}. We believe that such a large difference between N_{Er}^{opt} and N_{Er}^{el} densities indicates that additional (compared with implanted layers) channels of excitation transfer from the electron subsystem of a Si crystal to Er^{3+} ions, unrelated to the $E_C - 0.15$ eV level, exist in SMBE layers.

ACKNOWLEDGMENTS

The authors express their gratitude to Yu. A. Karpov (Institute for Chemical Problems of Microelectronics, Moscow) who placed at our disposal the sources for the SMBE process.

This study was supported by the Russian Foundation for Basic Research (project nos. 99-02-17750, 99-03-32757, 01-02-16439), INTAS (grant no. 99-01872), and MWO (project no. 047.009.013).

REFERENCES

1. J. Stimmer, A. Reittinger, J. F. Nutzel, *et al.*, Appl. Phys. Lett. **68**, 3290 (1996).
2. R. Serna, J. H. Shin, M. Lohngmeier, *et al.*, J. Appl. Phys. **79**, 2658 (1996).
3. V. P. Kuznetsov and R. A. Rubtsova, Fiz. Tekh. Poluprovodn. (St. Petersburg) **34**, 519 (2000) [Semiconductors **34**, 502 (2000)].
4. M. Stepikhova, A. Andreev, B. Andreev, *et al.*, Acta Phys. Pol. A **94**, 549 (1998).
5. A. Yu. Andreev, B. A. Andreev, M. N. Drozdov, *et al.*, Fiz. Tekh. Poluprovodn. (St. Petersburg) **33**, 156 (1999) [Semiconductors **33**, 131 (1999)].
6. B. A. Andreev, A. Yu. Andreev, H. Ellmer, *et al.*, J. Cryst. Growth **201/202**, 534 (1999).
7. M. V. Stepikhova, B. A. Andreev, V. B. Shmagin, *et al.*, Thin Solid Films **381**, 164 (2001).
8. M. Stepikhova, B. Andreev, Z. Krasil'nik, *et al.*, Mater. Sci. Eng. B **81** (1–3), 67 (2001).
9. V. B. Shmagin, B. A. Andreev, A. V. Antonov, *et al.*, Izv. Akad. Nauk, Ser. Fiz. **65**, 276 (2001).
10. D. V. Lang, J. Appl. Phys. **45**, 3023 (1974).

11. V. P. Kuznetsov, A. Yu. Andreev, O. A. Kuznetsov, *et al.*, Phys. Status Solidi A **127**, 371 (1991).

12. L. S. Berman and A. A. Lebedev, *Capacitance Spectroscopy of Deep Centers in Semiconductors* (Nauka, Leningrad, 1981).

13. S. V. Bulyarskiĭ and N. S. Grushko, *Generation-Recombination Processes in Active Elements* (Mosk. Gos. Univ., Moscow, 1995), Chap. 1, p. 23.

14. F. Y. G. Ren, J. Michel, Q. Sun-Paduano, *et al.*, in *Rare Earth Doped Semiconductors*, Ed. by G. S. Pomrenke, P. B. Klein, and D. W. Langer; Mater. Res. Soc. Symp. Proc. **422**, 87 (1996).

15. V. V. Emtsev, V. V. Emtsev, Jr., D. S. Poloskin, *et al.*, Fiz. Tekh. Poluprovodn. (St. Petersburg) **33**, 1192 (1999) [Semiconductors **33**, 1084 (1999)].

16. S. Libertino, S. Coffa, G. Franzo, and F. Priolo, J. Appl. Phys. **78**, 3867 (1995).

17. B. A. Andreev, M. S. Bresler, O. B. Gusev, *et al.*, Izv. Akad. Nauk, Ser. Fiz. **65**, 271 (2001).

18. M. S. Bresler, O. B. Gusev, B. P. Zakharchenya, and I. N. Yassievich, Fiz. Tverd. Tela (St. Petersburg) **38**, 1474 (1996) [Phys. Solid State **38**, 813 (1996)].

Translated by D. Mashovets

Semiconductors, Vol. 36, No. 2, 2002, pp. 176–179. Translated from Fizika i Tekhnika Poluprovodnikov, Vol. 36, No. 2, 2002, pp. 183–186.
Original Russian Text Copyright © 2002 by Veĭs.

ELECTRONIC AND OPTICAL PROPERTIES OF SEMICONDUCTORS

Optical Absorption in $(Pb_{0.78}Sn_{0.22})_{1-X}In_XTe$ (X = 0.001 – 0.005)

A. N. Veĭs

St. Petersburg State Technical University, St. Petersburg, 195251 Russia

Submitted June 18, 2001; accepted for publication June 20, 2001

Abstract—Optical absorption spectra of $(Pb_{0.78}Sn_{0.22})_{1-X}In_XTe$ (X = 0.001 – 0.005) have been studied at T = 300 K. Asymmetric bands of additional absorption α_0 and α_1, characterized by steep long-wavelength edges, were revealed. The optical energy and the half-width of localized levels are determined, and assumptions concerning their nature are made. © *2002 MAIK "Nauka/Interperiodica".*

Specific features of the energy spectrum of indium-doped $Pb_{0.78}Sn_{0.22}Te$ have lately attracted markedly increasing interest [1–8]. These studies have revealed new effects, which were explained in terms of hopping conduction via indium impurity states and self-compensation of the donor effect of impurity. These effects must be accompanied by considerable modifications of the $(Pb_{0.78}Sn_{0.22})_{1-X}In_XTe$ energy spectrum. Such variations could have been observed in studying the $(Pb_{0.78}Sn_{0.22})_{1-X}In_XTe$ optical absorption spectra. However, the data presented in [1–8] were mostly obtained by electrical investigation techniques, whereas the optical methods were not applied in full measure. The character of possible modifications of the $(Pb_{0.78}Sn_{0.22})_{1-X}In_XTe$ energy spectrum, appearing under the conditions of hopping conduction, or resulting from the self-compensation of the donor impurity, cannot be judged from the available published data on the optical properties of $Pb_{1-Y}Sn_YTe$:In [9, 10]. These data are not complete, and their interpretation is ambiguous.

In the present study, spectral dependences of the absorption coefficient α in $(Pb_{0.78}Sn_{0.22})_{1-X}In_XTe$ with a low density of free electrons were investigated with the goal of revealing specific features of the energy spectrum.

The samples used for this study were fabricated by a hot pressing technique; the details of preparation and annealing were described elsewhere [2]. The In content in the charge, X, was not higher than 0.005. Based on [11], we believe that this level of indium doping does not noticeably affect the parameters of the $Pb_{0.78}Sn_{0.22}Te$ energy spectrum, such as the energy gap E_g and the free carrier effective masses. The electron density determined from the Hall effect, n_H, did not exceed 3.6×10^{17} cm^{-3}. All the experiments were performed at T = 300 K.

Figure 1 shows some of the obtained results. The $\alpha(\hbar\omega)$ spectra of the investigated solid solutions exhibit two additional absorption bands, α_0 and α_1, with steep long-wavelength edges at photon energies $\hbar\omega \approx 0.09$ and ≈0.05 eV. The asymmetric shape of the $\alpha_0(\hbar\omega)$ and $\alpha_1(\hbar\omega)$ dependences, along with the existence of long-wavelength edges for both the components of the additional absorption, suggest that these bands are related to optical transitions of electrons from localized states E_0 and E_1 in the band gap to allowed states in the conduction band (see the energy diagram in Fig. 1).

The energy positions of the levels responsible for the α_0 and α_1 features in the $\alpha(\hbar\omega)$ spectra were found by calculating the coefficient of additional absorption. For this purpose, the spectral dependences $\alpha_0 + \alpha_1$ were isolated from the experimental curves by subtracting the free carrier absorption extrapolated to the short-wavelength range. Figure 1 shows, as an example, the thus obtained results for a sample with X = 0.005.

Spectral dependences $\alpha_0 + \alpha_1$ were calculated using relation (2) from [12], which allows one to determine the energy position of localized centers and evaluate the half-width of impurity bands Γ. The Fermi energies E_F, which are necessary for these calculations, were determined in terms of Kane's model of nonparabolicity, using relation (6.27) from [13] and parameters of the $Pb_{0.78}Sn_{0.22}Te$ energy spectrum taken from [7]. The applicability of these parameters was verified by analyzing the $\alpha(\hbar\omega)$ dependences at the fundamental absorption edge. It was found that, for the samples studied, the obtained absorption coefficients at the fundamental absorption edge are in agreement with the available experimental data for "pure" indium-free $Pb_{0.8}Sn_{0.2}Te$ [14], and the band gap in these samples is 0.20 ± 0.01 eV.

Curves *6–8* in Fig. 1 represent the calculated $\alpha_0(\hbar\omega)$ and $\alpha_1(\hbar\omega)$. Good agreement between the calculated and the experimental data allowed us to determine the energies E_0^{opt} and E_1^{opt} and to evaluate the half-widths Γ_0 and Γ_1 of these bands. In the samples under study, E_0^{opt} and E_1^{opt} are $-(0.09 \pm 0.01)$ and $-(0.050 \pm 0.005)$ eV, respectively, and the half-width of the localized bands Γ_0 and Γ_1 does not exceed 8 meV. It is noteworthy that the broadening of the impurity bands in solid solutions, compared with their width in binary lead chalcogenides,

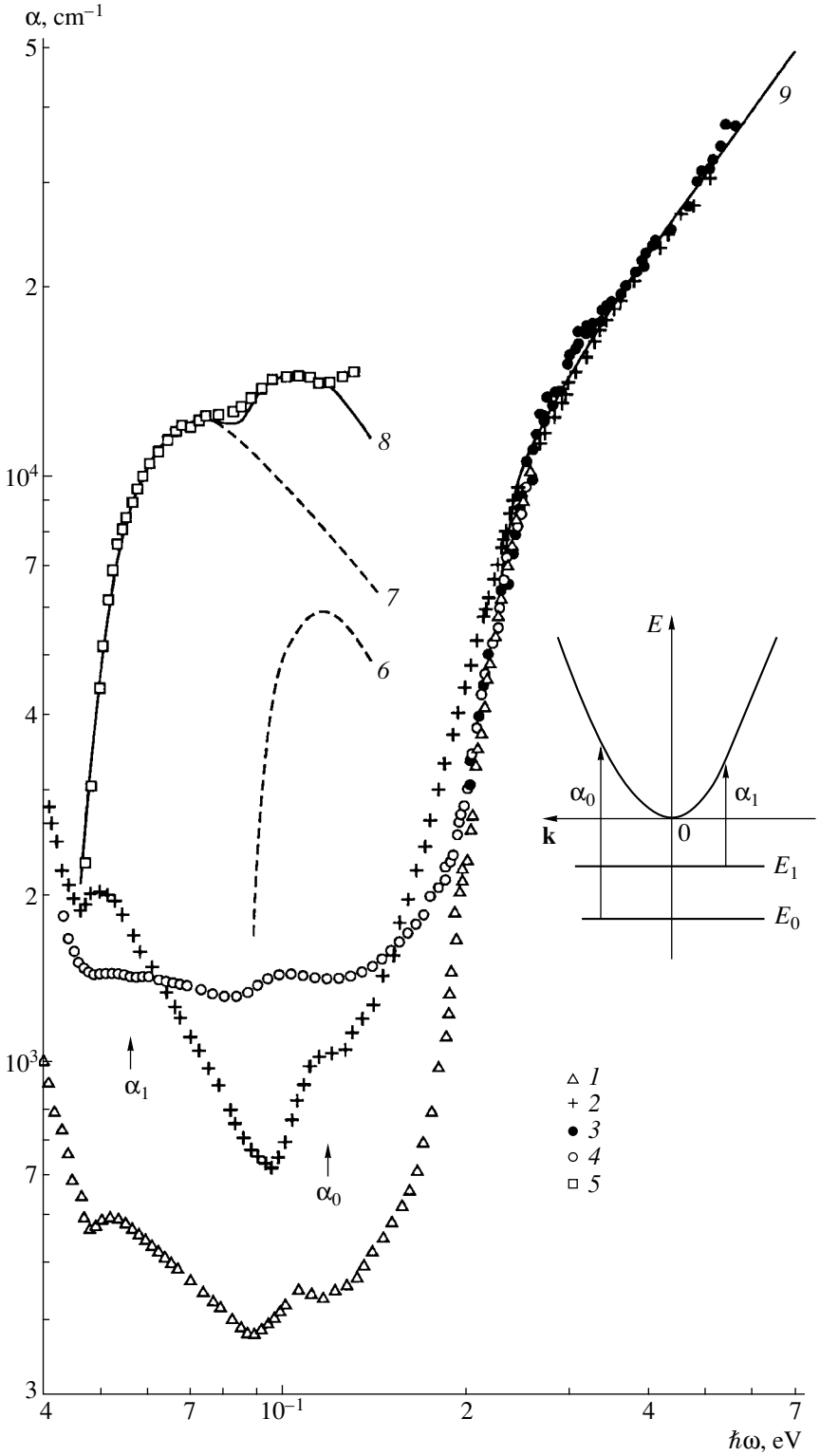

Fig. 1. Spectral dependences of the absorption coefficient α for $(Pb_{0.78}Sn_{0.22})_{1-X}In_XTe$ at T = 300 K. X ($n_H^* \times 10^{-17}$): (*1*) 0.001 (2.1), (*2*) 0.003 (3.6), and (*3*, *4*) 0.005 (1.7 cm^{-3}); sample thickness d: (*1*) 8.9, (*2*) 3.4, (*3*) 2.6, and (*4*) 5.7 μm. The spectrum of additional absorption in $(Pb_{0.78}Sn_{0.22})_{0.0995}In_{0.005}Te$. Points: (*5*) experiment, lines: calculation by relation (2) from [12] for E_0^{opt} = 0.09 eV, E_1^{opt} = 0.05 eV, $\Gamma_0 = \Gamma_1$ = 8 meV: (*6*) $\alpha_0(\hbar\omega)$, (*7*) $\alpha_1(\hbar\omega)$, and (*8*) $\alpha_0 + \alpha_1$. For curves (*5*)–(*8*), the α values are multiplied by 10. (*9*) Experimental data for "pure" indium-free $(Pb_{0.8}Sn_{0.2})Te$. Inset: energy diagram of $(Pb_{0.78}Sn_{0.22})_{1-X}In_XTe$. Arrows indicate the observed optical transitions related to recharging of E_0 and E_1 localized states.

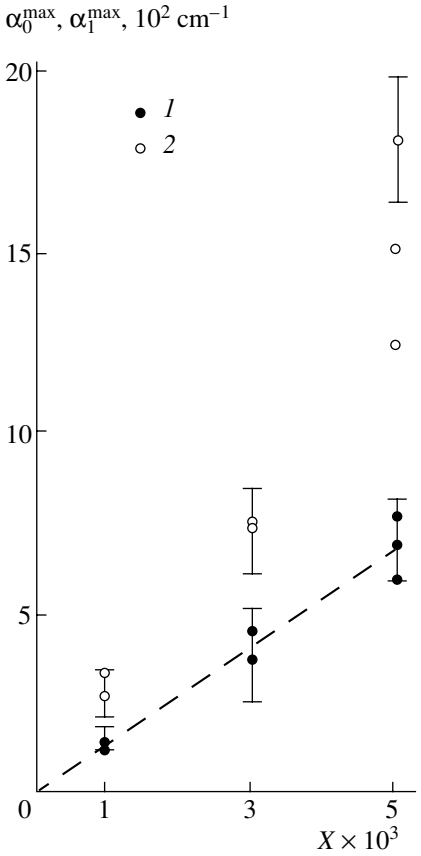

Fig. 2. Intensity of the additional absorption bands (*1*) α_0^{max} and (*2*) α_1^{max} vs. In content X in $(Pb_{0.78}Sn_{0.22})_{1-X}In_XTe$ at $T = 300$ K.

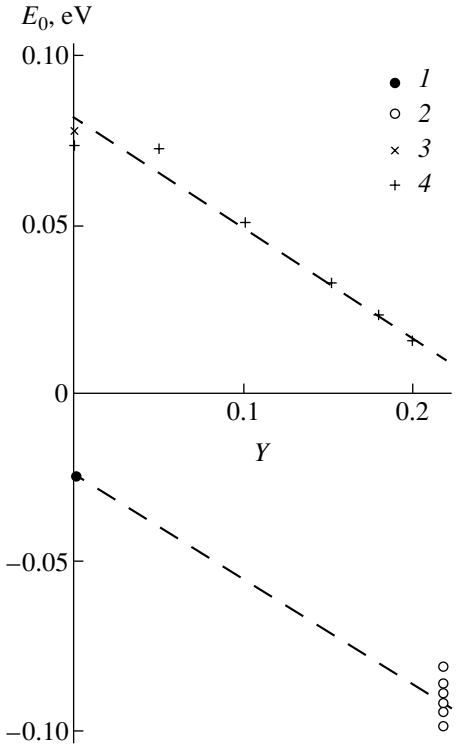

Fig. 3. Energy position E_0 of the In-related impurity level in $Pb_{1-Y}Sn_YTe$:In vs. Sn content in the stock, Y, obtained by analyzing the results of investigations of (*1*, *2*) optical absorption and (*3*, *4*) transport phenomena. (*1*) Present study, (*2*) [16], (*3*) [17], and (*4*) [11]. T: (*1*, *2*) 300, (*3*) 4.2, and (*4*) 0 K.

has been observed previously in $Pb_{1-X}Ge_XTe$:In [12] and $PbSe_{1-X}S_XTe$:Tl [15] and was related to the influence of nonequivalence of the crystalline environment of defects. The intensities of the α_0 and α_1 bands were also calculated, and the relevant data are presented in Fig. 2.

Passing to a discussion of the possible nature of the features in the $\alpha(\hbar\omega)$ spectra of the solid solutions under study, we note, first of all, that the α_0 bands have not been observed previously in $Pb_{1-Y}Sn_YTe$. As follows from Fig. 2, their intensity grows in proportion to the indium content in the charge, X. Therefore, it seems natural to relate these bands to optical recharging of In. This assumption is supported by the results presented in Fig. 3, which shows the energy E_0 of the indium impurity level in $Pb_{1-Y}Sn_YTe$:In in relation to the tin content Y in the charge, obtained by studying the optical absorption (E_0^{opt}) and transport phenomena (E_0^{therm}). The E_0^{opt} value for PbTe, presented in the same figure, was obtained from experimental data for samples with *n*-type conduction [16] by linear extrapolation from the high-temperature range to $T = 300$ K. The correctness of this extrapolation was verified in [16]. The E_0^{therm} values in Fig. 3, taken from [11, 17], refer to 0 K. As seen from Fig. 3, the rates of E_0^{opt} and E_0^{therm} variation with composition in $Pb_{1-Y}Sn_YTe$:In are close: $dE_0/dY \approx 0.3$.

Unlike E_0, the E_1 level in $Pb_{1-Y}Sn_YTe$ has not been observed earlier in studies of optical or transport phenomena. Therefore, the assumptions concerning the possible origin of α_1 bands revealed in $(Pb_{0.78}Sn_{0.22})_{1-X}In_XTe$ must be based, in the first place, on specific properties of the material under study. In this connection, it should be noted that analysis of the Hall electron densities n_H shows that indium centers are not necessarily the only donors in the samples studied.

Indeed, according to [18], the indium-related impurity band contains two states per impurity atom. Therefore, E_F cannot be higher than E_0^{therm} in the absence of additional donors or acceptors, irrespective of the value of the electronic correlation energy U at the indium impurity center at $U \le 0$ [18]. The E_0^{therm} in $(Pb_{0.78}Sn_{0.22})_{1-X}In_XTe$ can be evaluated on the assumption that the difference $|E_0^{opt} - E_0^{therm}|$ in $Pb_{1-Y}Sn_YTe$:In is independent of y and equal to 0.045 eV, as in PbTe:In

[16]. In this case, E_0^{therm} in $(Pb_{0.78}Sn_{0.22})_{1-X}In_XTe$ must be –0.045 eV, and the Hall densities of electrons must not exceed $n_H^* = 2.4 \times 10^{17}$ cm^{-3}. It is noteworthy that the presented estimation for E_0^{therm} in $(Pb_{0.78}Sn_{0.22})_{1-X}In_XTe$ is in agreement with [1], where $E_0^{\text{therm}} = -0.05$ eV was obtained for the solid solutions under study at $T = 300$ K.

If we now consider the n_H^* values in the samples studied, it can be seen that $n_H = 3.6 \times 10^{17}$ cm^{-3} in $(Pb_{0.78}Sn_{0.22})_{0.997}In_{0.003}Te$ is much higher than n_H^*. This discrepancy between n_H and n_H^* may occur for the following two reasons. First, it may be assumed that the indium impurity in $(Pb_{0.78}Sn_{0.22})_{1-X}In_XTe$ can have two charge states: In^- and In^0 (in designations of [18]). In terms of this interpretation of the experimental data and in accordance with the data of [19], the α_0 band must be related to the optical recharging of indium, $In^- \longrightarrow In^0$, and α_1, to $In^0 \longrightarrow In^+$. Second, all the samples studied may be self-compensated. According to [1], the indium donor effect is compensated by vacancies V_m formed in the metal sublattice. Here, account should be taken of the fact that indium was introduced as a substitutional impurity in these samples. Therefore, we may assume that vacancies in the metal sublattice may appear not only as Schottky defects, but as Frenkel defects as well. In this situation, a noticeable amount of interstitial metal, which is known to be a single-charged donor [20], may appear in the samples. Then, the α_1 band can be related either to an interstitial metal or to complexes including an interstitial metal.

The data obtained thus far give no way of deciding between the above assumptions. The first of these is supported by the rise in the intensity of the α_1 bands with increasing x, and the second, by the absence of correlation between the intensity of the α_1 bands and the E_F values.

ACKNOWLEDGMENTS

I am grateful to S.A. Nemov for the samples provided for study.

REFERENCES

1. S. A. Nemov, Yu. I. Ravich, M. K. Zhitinskaya, and V. I. Proshin, Fiz. Tekh. Poluprovodn. (St. Petersburg) **26**, 1493 (1992) [Sov. Phys. Semicond. **26**, 839 (1992)].
2. S. A. Nemov, Yu. I. Ravich, A. V. Berezin, *et al.*, Fiz. Tekh. Poluprovodn. (St. Petersburg) **27**, 299 (1993) [Semiconductors **27**, 165 (1993)].
3. Yu. I. Ravich, S. A. Nemov, and V. I. Proshin, Fiz. Tekh. Poluprovodn. (St. Petersburg) **29**, 1448 (1995) [Semiconductors **29**, 754 (1995)].
4. T. G. Abaĭdulina, S. A. Nemov, V. I. Proshin, and Yu. I. Ravich, Fiz. Tekh. Poluprovodn. (St. Petersburg) **30**, 2173 (1996) [Semiconductors **30**, 1133 (1996)].
5. S. A. Nemov, V. I. Proshin, and T. G. Abaĭdulina, Fiz. Tekh. Poluprovodn. (St. Petersburg) **30**, 1285 (1996) [Semiconductors **30**, 676 (1996)].
6. S. A. Nemov, V. I. Prishvin, and Yu. I. Ravich, Fiz. Tekh. Poluprovodn. (St. Petersburg) **30**, 2173 (1996) [Semiconductors **30**, 1133 (1996)].
7. A. N. Veĭs and S. A. Nemov, Fiz. Tekh. Poluprovodn. (St. Petersburg) **32**, 1047 (1998) [Semiconductors **32**, 937 (1998)].
8. S. A. Nemov, V. É. Gasumyants, V. I. Proshin, and Yu. I. Ravich, Fiz. Tekh. Poluprovodn. (St. Petersburg) **34**, 926 (2000) [Semiconductors **34**, 889 (2000)].
9. I. A. Drabkin, Yu. Ya. Eliseeva, G. F. Zakharyugina, *et al.*, Fiz. Tekh. Poluprovodn. (Leningrad) **8**, 1947 (1974) [Sov. Phys. Semicond. **8**, 1261 (1974)].
10. A. N. Veĭs, V. I. Kaĭdanov, Yu. I. Ravich, *et al.*, Fiz. Tekh. Poluprovodn. (Leningrad) **10**, 104 (1976) [Sov. Phys. Semicond. **10**, 62 (1976)].
11. N. A. Erasova, B. A. Efimova, G. F. Zakharyugina, and V. I. Kaĭdanov, Izv. Akad. Nauk SSSR, Neorg. Mater. **14**, 870 (1978).
12. T. V. Bocharova, A. N. Veĭs, N. A. Erasova, and V. I. Kaĭdanov, Fiz. Tekh. Poluprovodn. (Leningrad) **16**, 1462 (1982) [Sov. Phys. Semicond. **16**, 933 (1982)].
13. Yu. I. Ravich, B. A. Efimova, and I. A. Smirnov, *Semiconducting Lead Chalcogenides* (Plenum, New York, 1970); Yu. I. Ravich, B. A. Efimova, and I. A. Smirnov, *Methods for Researching Semiconductors as Applied to Lead Chalcogenides: PbTe, PbSe, PbS* (Nauka, Moscow, 1968).
14. I. A. Drabkin, L. Ya. Morgovskiĭ, I. V. Nel'son, and Yu. I. Ravich, Fiz. Tekh. Poluprovodn. (Leningrad) **6**, 1323 (1972) [Sov. Phys. Semicond. **6**, 1156 (1972)].
15. A. N. Veĭs, V. I. Kaĭdanov, and S. A. Nemov, Fiz. Tekh. Poluprovodn. (Leningrad) **14**, 1054 (1980) [Sov. Phys. Semicond. **14**, 628 (1980)].
16. A. N. Veĭs and S. A. Nemov, Fiz. Tekh. Poluprovodn. (Leningrad) **16**, 1130 (1982) [Sov. Phys. Semicond. **16**, 725 (1982)].
17. V. G. Golubev, N. I. Grechko, S. N. Lykov, and I. A. Chernik, Fiz. Tekh. Poluprovodn. (Leningrad) **11**, 1704 (1977) [Sov. Phys. Semicond. **11**, 1001 (1977)].
18. V. I. Kaĭdanov and Yu. I. Ravich, Usp. Fiz. Nauk **145**, 51 (1985) [Sov. Phys. Usp. **28**, 31 (1985)].
19. S. A. Rykov, Author's Abstract of Doctoral Dissertation (S-Peterb. Gos. Tech. Univ., St. Petersburg, 1999).
20. H. Heinrich, in *Proceedings of the International Summer School on Narrow-Cap Semiconductors: Physics and Applications, Nimes, France, 1979*, p. 407.

Translated by D. Mashovets

Semiconductors, Vol. 36, No. 2, 2002, pp. 180–184. Translated from Fizika i Tekhnika Poluprovodnikov, Vol. 36, No. 2, 2002, pp. 187–191.
Original Russian Text Copyright © 2002 by Kamilov, Stepurenko, Kovalev.

ELECTRONIC AND OPTICAL PROPERTIES OF SEMICONDUCTORS

Distribution of Charge Carriers in Dissipative Semiconductor Structures

I. K. Kamilov, A. A. Stepurenko^, and A. S. Kovalev

Institute of Physics of the Dagestan Scientific Center, Russian Academy of Sciences, Makhachkala, 367003 Russia

^e-mail: kamilov@datacom.ru

Submitted May 8, 2001; accepted for publication July 12, 2001

Abstract—It was experimentally shown that redistribution of the charge-carrier concentration occurred in nonequilibrium electron–hole plasma during formation and excitation of the dissipative structure by a strong electric field in the bulk of Te and InSb single crystals. In this case, if there are only longitudinal autosolitons in the dissipative structure, the carrier concentration decreases outside the autosolitons. The charge-carrier concentration increases outside autosolitons if the transverse autosolitons are present. It is suggested that the longitudinal autosolitons formed in the nonequilibrium electron–hole plasma developed by the Joule heating are "cold" and the transverse autosolitons are "hot". © *2002 MAIK "Nauka/Interperiodica".*

It has been shown in theoretical [1–7] and experimental studies that the localized regions of the extreme carrier concentration and temperature, i. e., autosolitons (ASs), occur in nonequilibrium excited electron–hole plasma (EHP) both in the form of current strata and moving layers characterized by a strong electric field. This plasma is induced by the impact ionization or injection in *n*-GaAs [8, 9], by photogeneration in *n*-Ge [10], and by the Joule heating in InSb [11, 12].

Localized regions of high temperature and low carrier concentration (hot ASs) and localized regions of low temperature and high carrier concentration (cold ASs) have been considered and described [13]. These ASs occupy an insignificant localized fraction of the sample volume, on the order of $[(Ll)^{1/2}/2]^3$, where L is the bipolar diffusion length and l is the cooling length of hot electrons. Concentration and temperature of the localized regions, as well as their topology, were adequately described in [1–7, 13]. The processes occurring in the remainder of the sample volume, which interact with AS, have been inadequately studied theoretically and experimentally.

The aim of this study was to gain insight into the influence of the formation and evolution of the localized EHP (autosolitons) on the concentration and mobility distribution in the sample bulk. We also intended to study the longitudinal AS formed in EHP by the Joule heating. InSb samples of various sizes with the carrier concentration $p = (2–4) \times 10^{12}$ cm^{-3} and the mobility $\mu \approx 4000$ cm^2/(V s) at $T = 77$ K and Te samples with the carrier concentration $p = 1.45 \times 10^{14}$ cm^{-3} and the mobility $\mu \approx 2400$ cm^2/(V s) at $T = 77$ K were studied. Copper wires, soldered using indium or welded, were used as current leads. The InSb sample was divided into two regions (Fig. 1a): activator (A) and detector (D). ASs were excited in the activator in the same way as in [11, 12]; a voltage sufficient for the detection of the conductivity variation was applied to the detector. Any variations of the carrier concentration in the activator affected the detector conductivity.

Acoustic probing is another method for studying the dissipative structure. It is well known [14–19] that a pronounced acoustoelectric effect is observed in Te. In a high electric field when the carrier drift velocity v_d becomes higher than the phase velocity of sound v_s, phonons are generated and interact with the charge carriers in the crystal. It is experimentally shown [16] that acoustoelectronic interaction in tellurium depends linearly on the charge-carrier concentration n

$$\gamma = Cn, \tag{1}$$

where

$$C = \frac{K^2 e^3 v_s^4 \beta}{2\varepsilon k^2 T^2 \omega^2 \mu};$$

K is the electromechanical coupling coefficient, $\beta = 1 - v_d/v_s$ is the drift parameter, ε is the dielectric constant, ω is the angular frequency of the generated sonic waves, and μ is the charge-carrier mobility.

Experimental results for the InSb samples are shown in Figs. 1 and 2. The activator current–voltage (*I–V*) characteristic in the field of sawtooth voltage before AS formation and excitation is displayed in Fig. 1b. All portions of the *I–V* characteristic, except for those which are marked by the arrows, are reproducible and stable. Oscillograms of the time dependence of the activator current I_A, corresponding to this *I–V* characteristic, and variation of the detector conductivity $\sigma_D \propto I_D$ are shown in Figs. 2a and 2b, respectively. An increase in the detector conductivity in the AB section (Fig. 2b) is the result of an increase in the carrier concentration

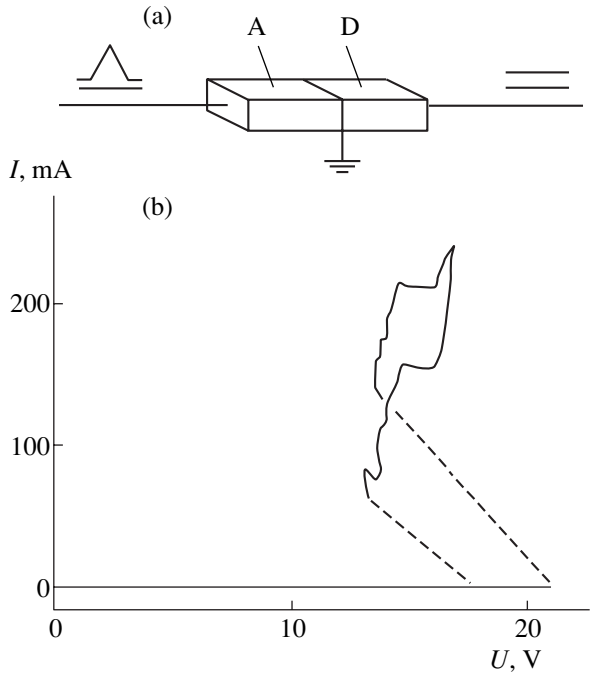

Fig. 1. (a) Scheme of the InSb sample: activator (A) and detector (D), and scheme of the sample connection in a circuit. (b) The current–voltage characteristic of the activator.

in the activator due to the Joule heating. The further increase of heating gives rise to intrinsic conductivity in the activator, and, due to this fact, an abrupt increase of the nonequilibrium carrier concentration occurs (Fig. 2a, section BC). Due to the diffusion of the nonequilibrium carriers, the detector conductivity also abruptly increases (Fig. 2b, section BC).

The BC portion indicates that the EHP is formed in the activator and is transformed into a dissipative structure (DS) as voltage increases; i. e., EHP is segregated into the localized regions with extreme temperatures. The carrier concentration is presented in these regions in the form of current pinches and electric field strata [1–7]. It can be seen in Fig. 2a (section CD) that the electric current pinch is formed (longitudinal AS). The magnitude of the current is determined by the applied voltage. If there are localized regions of reduced or increased carrier concentration in the sample bulk, then the carrier concentration should increase or decrease, respectively, in the remaining part of the sample volume, resulting in the increase or decrease of the detector conductivity. In this case, the experiment shows that the detector conductivity drops in a steplike manner (Fig. 2b, portion CD). At the same time, the activator current increases (Fig. 2a, portion CD). This means that the carrier concentration in the activator bulk decreases as DS is formed and excited. This fact is indicative of an increase in the charge-carrier concentration in the localized regions, the temperature of which decreases reference to the remaining part of the sample volume [13]. The steplike drop of the detector conductivity

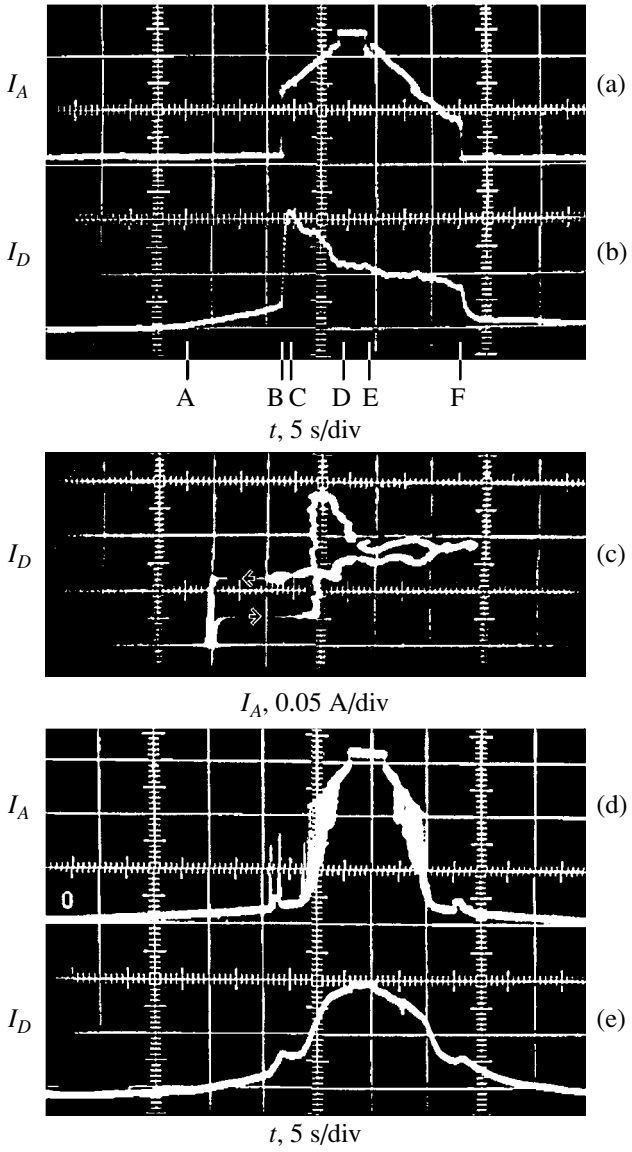

Fig. 2. Oscillograms: the time dependences (a) of the activator current and (b) the detector conductivity under excitation of the longitudinal autosolitons in the activator. Units: $I_A = 0.1$ A/div., $I_D = 2 \times 10^{-4}$ A/div. (c) The dependence of the detector conductivity on the activator current. Units: $I_D = 1.5 \times 10^{-4}$ A/div. Oscillograms: the time dependences (d) of the activator current and (e) the detector conductivity under the excitation of the transverse autosolitons in the activator. Units of the I_A and I_D current measurements are the same as in the (a) and (b) oscillograms.

indicates that additional longitudinal ASs are formed as the applied voltage increases, i. e., as the DS excitation level increases. In this case, an abrupt decrease of the carrier concentration in the activator bulk is observed.

The dependence of the detector conductivity $\sigma_D \propto I_D$ on the activator current I_A is shown in Fig. 2c. One can see that, as the activator current increases, the detector conductivity and, therefore, carrier concentration in the activator significantly decrease. The detector conduc-

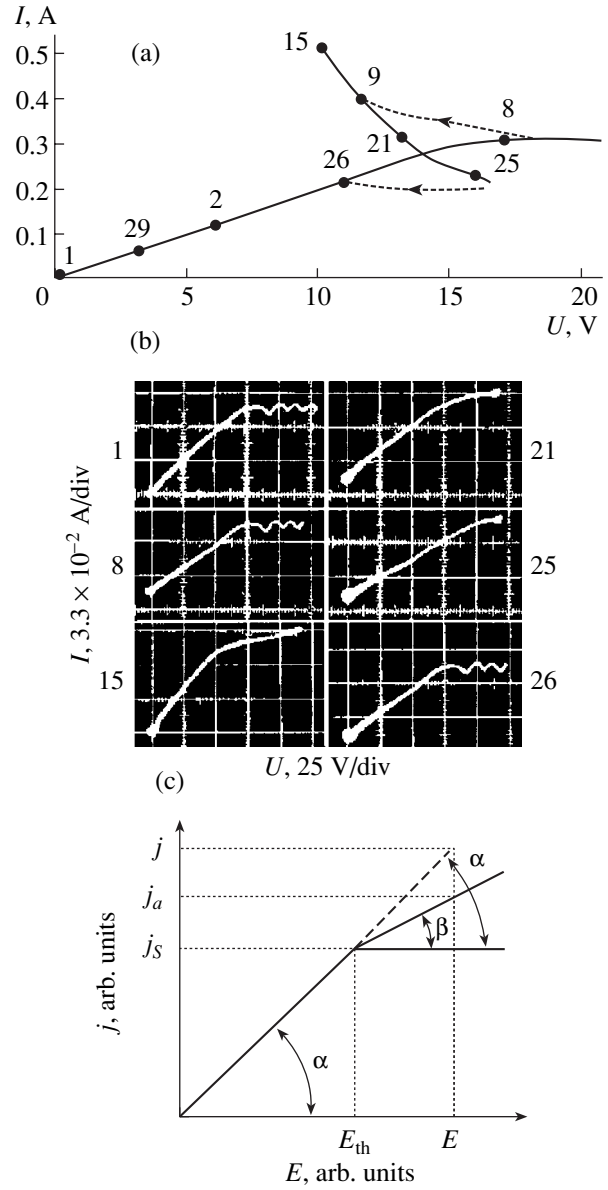

Fig. 3. (a) Quasi-steady current–voltage characteristic of the Te sample. (b) Oscillograms of the dynamic current–voltage characteristics of the Te sample. (c) Typical current–voltage characteristic of Te under conditions of acoustoelectronic interaction. Numbers at the oscillograms (Fig. 3b) correspond to those in Fig. 3a.

tivity drop does not coincide with the onset of the current drop in the activator due to the delay of variation in the detector conductivity in relation to EHP generation in the activator. Therefore, as the pinch current in the activator increases, the carrier concentration decreases in the remaining part of the activator.

Oscillograms of the time dependences of the current in the activator and the detector conductivity for the applied voltages that excite electric field strata, which move along the sample (AS) in the activator, and the current oscillations in the external circuit are displayed in Figs. 2d and 2e. It can be seen that the detector conductivity does not decrease if there are moving ASs in the activator. In addition, the detector conductivity increases, which indicates that the carrier concentration increases in the activator. Since the detector conductivity does not oscillate when the current in the external circuit of the activator oscillates, we may state that the current oscillations in the external circuit of the activator are controlled by the electric-field strata moving outside the current pinch rather than by the conductivity variation in this pinch.

Results of the investigations of the Te samples are shown in Figs. 3 and 4.

The scheme of the electric measurements of the Te samples was described in [20]. Longitudinal ASs were excited and sustained by the applied quasi-constant voltage. A well-reproducible quasi-steady *I–V* characteristic measured for the forward and reverse voltages is shown in Fig. 3a. Unstable portions of the curve are plotted by the dashed lines. The dynamic *I–V* characteristics, whose nonlinear portion is caused by the acoustoelectrical effect, were measured in a strong triangular-pulse electric field. The dynamic *I–V* characteristics were measured at a fixed direct current (dc) through the sample, which corresponded to different portions of the quasi-steady *I–V* characteristic (Fig. 3a, points 1–29).

Points 1–8 and 26–29 lie along the section of the quasi-steady *I–V* characteristic, which obeys the Ohm law (Fig. 3a); points 9–25 lie along the section determined by the voltages at which the longitudinal AS is formed (AS-sample). In Fig. 3b, we show the dynamic *I–V* characteristics measured at a current corresponding to points 1, 8, 15, 25, and 26 in the quasi-steady *I–V* characteristic (Fig. 3a). One can see in Fig. 3b (points 1 and 8) that *I–V* characteristics are identical, although they were measured at different currents of the ohmic portion of the quasi-stationary *I–V* characteristic. The dynamic *I–V* characteristics for points 15, 21, and 25 are shown in the oscillograms (Fig. 3b). In this case, there are ASs in the sample. It can be seen that acoustoelectric oscillations disappeared, and the slope of the nonlinear portion of the *I–V* characteristic increased. This fact indicates that the interaction of the charge carriers with the acoustic vibrations decreases due to a decrease in the phonon-flux density. This circumstance, in its turn, is related to a decrease in the carrier concentration in the sample volume containing AS. The carrier concentration can be determined from the experimental dynamic *I–V* characteristics. The current density at an electric field higher than the critical value $E > E_{th}$ (Fig. 3c) under the saturation conditions ($\beta = 0$) is equal to

$$j_S = en_a\mu E = en_a v_d, \quad n_a = n.$$

If $\alpha > \beta > 0$, only a fraction of the carriers n_a are involved in the acoustoelectronic interaction; the other fraction n_0 is involved in the ohmic current (α and β

angles can be obtained from Fig. 3c). As a result, we obtain

$$j = en_a\mu E + en_0\mu E = en_a v_d + en_0\mu E, \quad n = n_a + n_0. \tag{2}$$

In this case, on the one hand, we have the ratio

$$\frac{j - j_a}{j - j_S} = \frac{n_a}{n},$$

where $j = \sigma E = en\mu E$. On the other hand, we obtain, according to Fig. 3c,

$$\frac{j - j_a}{j - j_S} = \frac{\tan\alpha - \tan\beta}{\tan\alpha},$$

and, as a result,

$$\frac{n_a}{n} = \frac{\tan\alpha - \tan\beta}{\tan\alpha}.$$

In the experimental curve of the dynamic *I–V* characteristic (Fig. 3b, points 1, 8), the coefficient $\beta = 0$ so that $n_a/n = 1$. The following ratio holds for the *I–V* characteristics of the sample with AS (Fig. 3b, points 15, 21, 25):

$$\frac{n_{a\mathrm{AS}}}{n} = \frac{\tan a_{\mathrm{AS}} - \tan\beta_{\mathrm{AS}}}{\tan\alpha_{\mathrm{AS}}}, \tag{3}$$

where α_{AS} and β_{AS} are the slope angles of the linear and nonlinear portions of the dynamic *I–V* characteristic of the sample with AS. The α_{AS} and β_{AS} angles depend on the AS excitation level, i. e., on the current I_A. The dependence of the concentration ratio n_a/n for the carriers involved in the acoustoelectric interaction on the AS current is shown in Fig. 4. A steady decrease in the ratio n_a/n is observed as the AS current increases.

Thus, it is experimentally shown that, in the bulk of the InSb and Te single crystals, the carrier concentration varies during formation and excitation, by strong electric field, of the dissipative structure (DS) in the nonequilibrium electron–hole plasma (EHP) formed by the Joule heating. In the case when there are only longitudinal autosolitons (ASs) in DS, the carrier concentration in the sample volume decreases with increasing excitation level of these ASs. This is caused, first of all, by the increase in the carrier concentration in the localized regions and by a decrease in their temperature (cold ASs) [13]. The current of these ASs is independent of the carrier concentration, because EHP is dense, but it depends on temperature: $j = e\mu nE \propto T^{3/2}E$ ($\mu = e\tau/m^* \propto T^{3/2}/n$). According to this expression, the current in the presence of cold ASs can attain, at the same electric field, significantly lower values than those following from Ohm's law ($j = e\mu nE$). By the example of the Te samples, it was shown that AS was not destroyed even when the difference between the ohmic current and the AS current $\Delta j = j_0 - j_{\mathrm{AS}}$ attained the value of $\Delta j/j_0 = 50\%$ relative to the ohmic current.

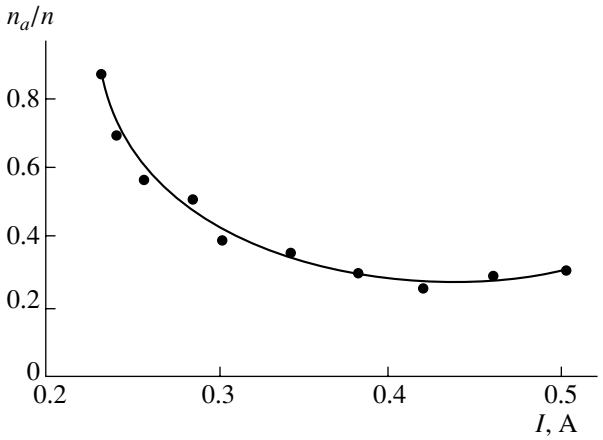

Fig. 4. The dependence of carrier-concentration ratio n_a/n (carriers are involved in the acoustoelectronic interaction) on the autosoliton current in the Te samples.

When there are transverse ASs in DS (in the InSb samples), the volume carrier concentration becomes higher, and it increases with the increasing excitation level of these ASs. Because the transverse ASs correspond to the localized regions with reduced carrier concentration and raised temperature (hot ASs), the remaining part of the sample volume is, naturally, more enriched with the charge carriers. Obviously, we may conclude that the longitudinal ASs, being formed in the nonequilibrium EHP induced by the Joule heating, are cold.

ACKNOWLEDGMENTS

This study was supported by the Russian Foundation for Basic Research, project nos. 00-02-17329 and 01-02-16195.

REFERENCES

1. B. S. Kerner and V. V. Osipov, Zh. Éksp. Teor. Fiz. **71**, 1542 (1976) [Sov. Phys. JETP **44**, 807 (1976)].
2. B. S. Kerner and V. V. Osipov, Pis'ma Zh. Éksp. Teor. Fiz. **41**, 386 (1985) [JETP Lett. **41**, 473 (1985)].
3. B. S. Kerner and V. V. Osipov, Pis'ma Zh. Éksp. Teor. Fiz. **18**, 122 (1973) [JETP Lett. **18**, 70 (1973)].
4. B. S. Kerner and V. V. Osipov, Fiz. Tekh. Poluprovodn. (Leningrad) **13**, 891 (1979) [Sov. Phys. Semicond. **13**, 523 (1979)].
5. B. S. Kerner and V. V. Osipov, Fiz. Tverd. Tela (Leningrad) **21**, 2342 (1979) [Sov. Phys. Solid State **21**, 1348 (1979)].
6. B. S. Kerner and V. V. Osipov, Fiz. Tekh. Poluprovodn. (Leningrad) **13**, 721 (1979) [Sov. Phys. Semicond. **13**, 424 (1979)].
7. A. L. Dubitskiĭ, B. S. Kerner, and V. V. Osipov, Fiz. Tverd. Tela (Leningrad) **28**, 1290 (1986) [Sov. Phys. Solid State **28**, 725 (1986)].
8. B. S. Kerner and V. F. Sinkevich, Pis'ma Zh. Éksp. Teor. Fiz. **36**, 359 (1982) [JETP Lett. **36**, 436 (1982)].

9. B. S. Kerner, V. V. Osipov, M. T. Romanenko, and V. F. Sinkevich, Pis'ma Zh. Éksp. Teor. Fiz. **44**, 77 (1986) [JETP Lett. **44**, 97 (1986)].
10. M. N. Vinoslavskiĭ, Fiz. Tverd. Tela (Leningrad) **31** (8), 315 (1989) [Sov. Phys. Solid State **31**, 1461 (1989)].
11. A. A. Stepurenko, Fiz. Tekh. Poluprovodn. (St. Petersburg) **28**, 402 (1994) [Semiconductors **28**, 243 (1994)].
12. I. K. Kamilov and A. A. Stepurenko, Phys. Status Solidi B **194**, 643 (1996).
13. V. V. Gafiĭchuk, B. S. Kerner, V. V. Osipov, and A. G. Yuzhanin, Fiz. Tekh. Poluprovodn. (Leningrad) **22**, 2051 (1988) [Sov. Phys. Semicond. **22**, 1298 (1988)].
14. T. Ishiguro and T. Tanaka, Jpn. J. Appl. Phys. **6** (7), 864 (1967).
15. G. Quentin, *Phenomenes acoustoelectriques dans les semiconducteurs piezoelectriques—Application at tellure* (Paris, 1967).
16. T. Shiosaki, H. Matsumoto, H. Chiharo, and A. Kawabata, Jpn. J. Appl. Phys. **12** (3), 337 (1973).
17. H. Kuzmany, Phys. Status Solidi A **25** (1), 9 (1974).
18. H. Kuzmany and W. Liederer, Phys. Status Solidi A **15** (1), 121 (1973).
19. A. A. Stepurenko, Author's Abstract of Candidate's Dissertation (Makhachkala, 1982).
20. I. K. Kamilov, A. A. Stepurenko, and A. S. Kovalev, Vestn. Dagist. Nauchn. Tsentra Akad. Nauk, No. 8, 15 (2000).

Translated by I. Kucherenko

Semiconductors, Vol. 36, No. 2, 2002, pp. 185–188. Translated from Fizika i Tekhnika Poluprovodnikov, Vol. 36, No. 2, 2002, pp. 192–196.
Original Russian Text Copyright © 2002 by Kovalenko, Mironchenko, Shutov.

ELECTRONIC AND OPTICAL PROPERTIES OF SEMICONDUCTORS

The Effect of Charge-Carrier Drift in the Built-in Quasi-Electric Field on the Emission Spectrum for Graded-Gap Semiconductors

V. F. Kovalenko, A. Yu. Mironchenko, and S. V. Shutov

Institute of Semiconductor Physics, Kherson Branch, National Academy of Sciences of Ukraine, Kherson, 73008 Ukraine

Submitted January 4, 2001; accepted for publication June 20, 2001

Abstract—The effect of bulk (τ) and radiative (τ_r) charge-carrier lifetimes on the degree of spatial separation of the regions of the carriers' generation and radiative recombination in graded-gap semiconductors with the drift transport mechanism in the built-in quasi-electric field of the crystal was investigated experimentally and theoretically. It was found that the degree of spatial separation increases with increasing τ and/or τ_r. The effect of spatial separation of the regions of radiative recombination, which correspond to transport mechanisms with various τ_r, was observed. The data obtained are related to the coordinate dependence of recombination probability for graded-gap semiconductors. © *2002 MAIK "Nauka/Interperiodica".*

INTRODUCTION

The presence of the built-in quasi-electric field $E = e^{-1}\nabla E_g$ in graded-gap semiconductors, which determines the drift of nonequilibrium charge carriers, leads to variation in their major luminescent characteristics compared to conventional semiconductors. Transport of nonequilibrium carriers from the wide-gap to the narrower gap parts of the crystal during the drift time $t_{dr} < \tau_r$ (τ_r is the radiative lifetime) for semiconductors with medium and large E was investigated [1]. It was demonstrated [1] that the transport, which competes with radiative recombination, leads to the coordinate dependence of the radiative recombination probability. On excitation with highly absorbing light, this dependence leads to the spatial shift of the region of radiative recombination to the part of the crystal with a band gap narrower relative to the generation region of nonequilibrium carriers. The shift increases with increasing E. In this study, which continues the study in [1], the dependence of the degree of separation for the regions of generation and radiative recombination of nonequilibrium carriers on the bulk and radiative lifetimes is investigated.

THEORETICAL CONSIDERATION

According to [1], the shape of the emission spectrum for the semiinfinite crystal of the graded-gap semiconductor with the linear recombination and surface absorption of the excitation radiation is described by the expression

$$I(z) = \tau_r^{-1}\exp\left(-\frac{\tau_r V_{dr}}{z}\right)\left[\left(\frac{\beta J_0}{V_{dr}+S_0} + \frac{\beta J_0 \alpha\tau}{\alpha l_+ - \exp(-l_+/z)}\right)\exp\left(-\frac{z}{l_+}\exp\left(-\frac{l_+}{z}\right)\right)\right]. \quad (1)$$

Here, J_0 is the intensity of the photoexcitation, β is the quantum yield of the internal photoeffect, α is the absorption coefficient for the excitation radiation, $V_{dr} = \mu E$, μ is the mobility of nonequilibrium charge carriers, S_0 is the rate of the surface recombination on the illuminated wide-gap surface, $l_+ = V_{dr}\tau$ is the effective drift length for nonequilibrium carriers, $\tau = (\sum_i \tau_i^{-1})^{-1}$ is the bulk lifetime, and τ_i is the lifetime of nonequilibrium carriers corresponding to the ith mechanism of recombination.

The conditions of applicability of expression (1) are as follows:

(i) the variation of the band gap E_g along the coordinate z for medium and large built-in fields E is linear if the drift of nonequilibrium carriers in the field E dominates over the diffusion;

(ii) the coordinate dependence of radiative recombination probability has the form

$$W(z) = \tau_r^{-1}\exp(-\tau_r V_{dr}/z),$$

where V_{dr} is the drift velocity for nonequilibrium charge carriers in the field E.

In what follows, we will use formula (1) for the investigation of the influence of the time factor on the degree of spatial separation of the regions of generation and radiative recombination.

The calculated shapes of the emission spectrum for a graded-gap semiconductor at E = 200 V/cm for various bulk and radiative lifetimes are shown in Fig. 1. It can be seen that the shift of the band peak of the emission spectrum from the illuminated wide-gap surface to the narrow-gap part of the crystal increases with increasing the bulk and/or radiative lifetime. This means that the spatial separation of the regions of gen-

1063-7826/02/3602-0185$22.00 © 2002 MAIK "Nauka/Interperiodica"

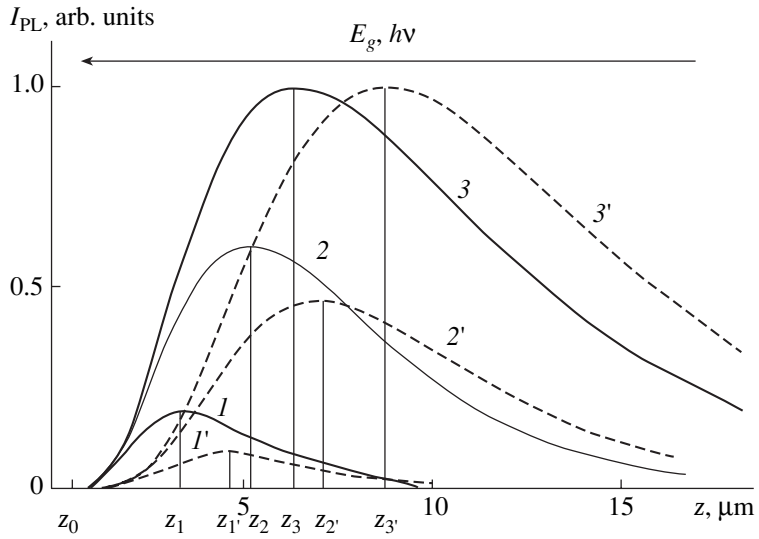

Fig. 1. Emission spectra for the graded-gap semiconductor with ∇E_g = 200 eV/cm calculated using formula (1) for T = 77 K, $\alpha = 2.72 \times 10^4$ cm^{-1}, $S_0 = 10^5$ cm/s, $\beta = 1$, and $J_0 = 10^{20}$ cm^{-2} s^{-1}. The lifetimes, τ_r = (*1*–*3*) 5×10^{-9} and (*1*'–*3*') 10^{-8} s; τ = (*1*, *1*') 10^{-9}, (*2*, *2*') 2×10^{-9}, and (*3*, *3*') 3×10^{-9} s.

eration of nonequilibrium carriers and their radiative recombination also increases. The magnitude of the spatial separation $z_n^* = z_n - z_0$. Here, z_n is the coordinate of location of the band peaks for the emission spectrum $h\nu_n^{\max}$, and n is the number of the spectrum in Fig. 1 (n = *1*, *2*, *3*, *1*', *2*', and *3*'). This result is also the evident consequence of the coordinate dependence of recombination probability. Specifically, with increasing τ and/or τ_r, nonequilibrium charge carriers move away from the illuminated surface for larger distances without nonradiative and/or radiative recombination, respectively. In Fig. 1, the coordinate $z = 0$ corresponds to the wide-gap illuminated surface; $z_0 = \alpha^{-1}$ is the extension of the region of recombination for nonequilibrium carriers; and z_1, z_2, z_3, $z_{1'}$, $z_{2'}$, and $z_{3'}$ are the coordinates of the location of band peaks for corresponding emission spectra.

Two specific features of radiative recombination spectra for graded-gap semiconductors follow from the data represented in Fig. 1.

(I) With the presence of several simultaneously effective channels of radiative recombination with various τ_r, the partial separation of radiative recombination regions occurs in the wide-gap part of the crystal. These regions correspond to different mechanisms of transitions. Specifically, for the transition with the longer radiative lifetime, the shift of the radiative recombination region to the narrow-gap part of the crystal is larger ($z_{1'} > z_1$, $z_{2'} > z_2$, and $z_{3'} > z_3$).

(II) The shift of the peak of the corresponding emission band to the narrow-gap part of the crystal with increasing bulk lifetime should be larger for the mechanism of radiative recombination with the longer τ_r compared to the mechanism with the shorter τ_r. For example, $(z_{3'} - z_{1'}) > (z_3 - z_1)$.

COMPARISON WITH THE EXPERIMENT

The excitation level dependences of the photoluminescence (PL) spectrum for epilayers of graded-gap $Al_xGa_{1-x}As$ solid solutions, both undoped ($n \lesssim 10^{16}$ cm^{-3}) and Te-doped $n \lesssim (0.5\text{–}1) \times 10^{18}$ cm^{-3} ones, were measured. The characteristics of the investigated solid solutions, as well as the procedure for measuring the PL spectra, were described previously [1]. The effective drift length for nonequilibrium carriers l_+ under the accelerating effect of the field E was determined from the slope of the low-temperature falloff of the edge emission band [2].

The PL spectra measured at 300 K, which contain only a single emission band, are shown in Fig. 2a. Figure 2b demonstrates the dependences of the spectral band peaks $h\nu^{\max}$ and effective length l_+ on the excitation level J_0 for one of the undoped epilayers with the excitation from the wide-gap side (from the $E_g^{\max}$ side). It can be seen that the short-wavelength peak $h\nu^{\max}$ shifts to lower energies with increasing J_0. Thus, the degree of separation for the regions of generation and radiative recombination of nonequilibrium carriers increases.

It is our opinion that the experimentally observed dependence $h\nu^{\max}(J_0)$ represents the dependence $h\nu^{\max}(\tau)$ (see Fig. 1). The experimental dependence can be explained by an increase in the bulk lifetime for nonequilibrium charge carriers with increasing J_0, as revealed by increasing l_+ with increasing J_0. The latter circumstance is apparently associated with the satura-

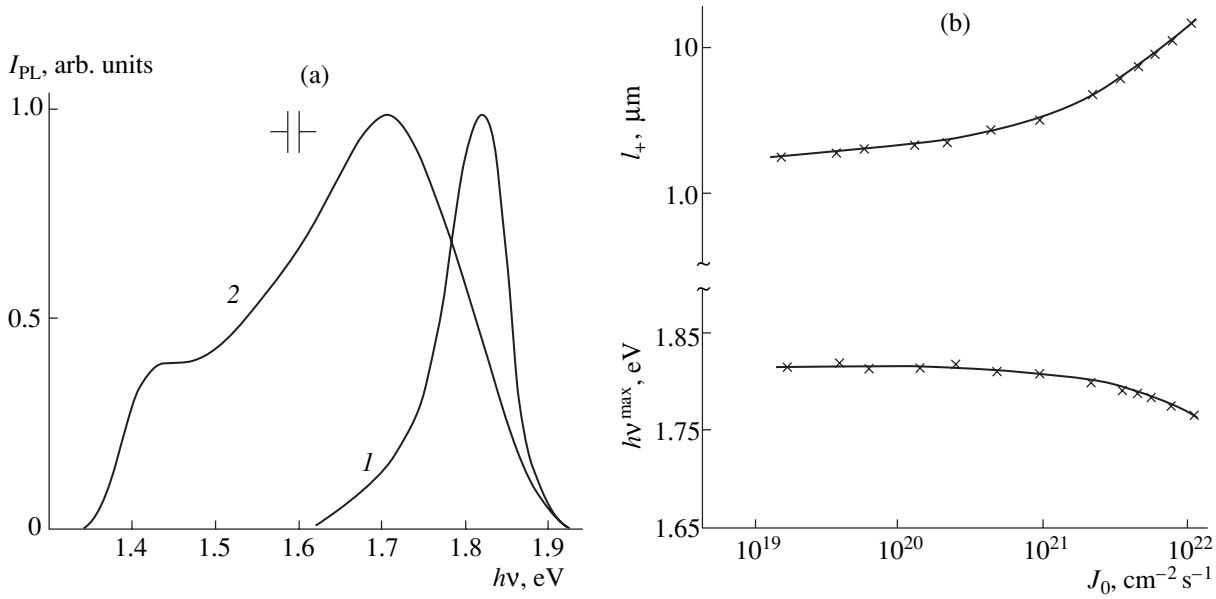

Fig. 2. (a) Emission spectra and (b) effective shift length for nonequilibrium charge carriers l_+ and peak energies of the $h\nu^{max}$ spectra for undoped epilayer of the $Al_xGa_{1-x}As$ solid solution with ∇E_g = 89 eV/cm as a function of the excitation intensity at 300 K. J_0 = (*1*) 10^{19} and (*2*) 10^{22} cm^{-2} s^{-1}.

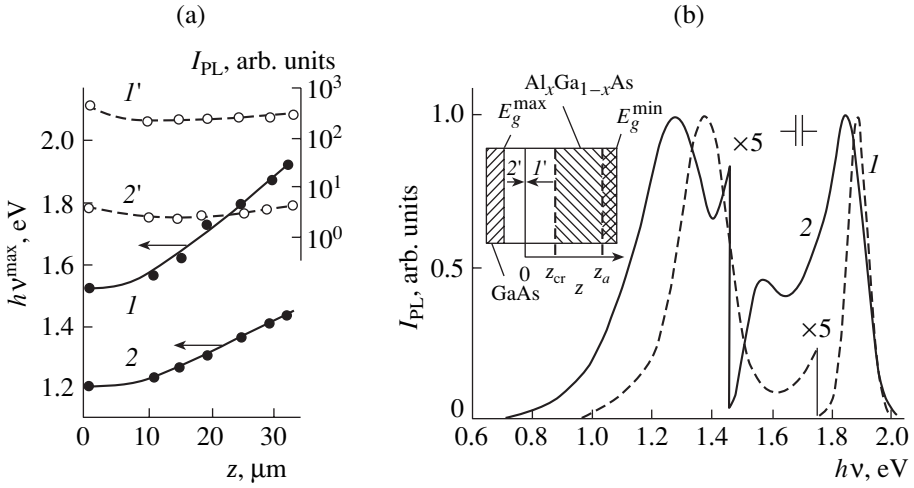

Fig. 3. (a) Distribution of peak energies for (*1*) the edge and (*2*) impurity PL bands and their intensity (*1*', *2*') over the thickness of one of the $Al_xGa_{1-x}As$: Te layers with $n \approx 7 \times 10^{17}$ cm^{-3}; excitation from the narrow-gap side, T = 77 K. (b) Emission spectra for the same epilayer on excitation from (*1*) the narrow-gap and (*2*) wide-gap sides for identical compositions of the solid solution on the surface illuminated, as shown in the inset. The spectra are normalized to unity by intensity; T = 77 K and $J_0 = 10^{20}$ cm^{-2} s^{-1}. The scheme of the experiment is shown in the inset. The arrows *1*' and *2*' point to the location of the excitation light probe for various directions of excitation. The mixed hatching denotes the part of the crystal in which the impurity PL occurs.

tion of the channels of the bulk nonradiative recombination with increasing nonequilibrium-carrier density.

The PL spectra of doped graded-gap solid solutions, which were measured at 77 K, included the edge and impurity emission bands. On excitation from the narrow-gap side (from the E_g^{min} side), the built-in field E decelerates the nonequilibrium carriers generated and keeps them close to the illuminated surface. As a result, the regions of generation and radiative recombination become coincident [1]. The dependence of the peak position for the impurity emission band $h\nu_a^{max}$ on the solid solution composition ($h\nu_a^{max} \approx 1.20$ eV for $x = 0$) is similar to that found previously [3]. The distributions of the peak energies of spectral bands and the intensities of edge and impurity emission PL bands along the thickness of one of the layers for excitation from the E_g^{max} side are shown in Fig. 3a. The nearly uniform dis-

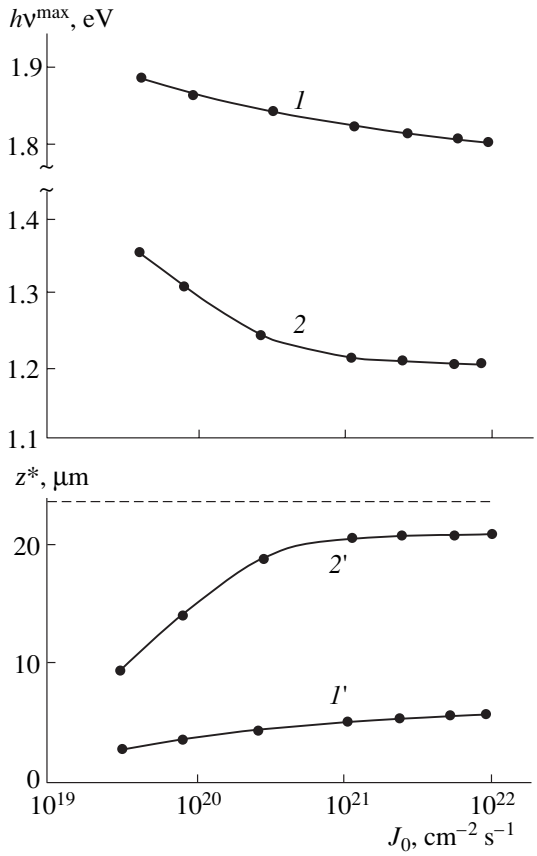

Fig. 4. Location of peaks for (*1*) the edge and (*2*) impurity emission bands as well as the spatial separation of the regions of generation of nonequilibrium charge carriers and their (*1*') edge and (*2*') impurity radiative recombination as a function of the excitation intensity for the epilayer with $\nabla E_g = 154$ eV/cm at 77 K. The dashed line denotes the location of the rear narrow-gap surface.

tribution of band intensities indicates that the distributions of the majority-carrier density and deep radiative-recombination centers along the thickness are fairly uniform. The PL spectra of the same layer measured for the identical intensity of excitation from (*1*) the narrow-gap and (*2*) wide-gap sides with the same composition of the solid solution on the illuminated side are shown in Fig. 3b. The scheme of the experiment is shown in the inset to Fig. 3b. Let us compare these spectra using curves *1* and *2* from Fig. 3a, which are obtained for excitation from the E_g^{max} side. It follows from the comparison that the peak energy $h\nu_a^{max}$ is shifted to longer wavelengths (correspondingly, to the narrow-gap part of the layer) to a greater extent than the energy $h\nu_{cr}^{max}$ (see corresponding coordinates z_a and z_{cr} in inset). Thus, the edge and impurity PL regions are partially spatially separated. This separation is caused by the fact that $\tau_{r_a} > \tau_{r_{cr}}$. In the case under consideration, $\tau_{r_a} \approx 7 \times 10^{-7}$ s [4], and $\tau_{r_{cr}} \approx 2 \times 10^{-8}$ s [5, 6]. This confirms the conclusion that the shift of the radiative recombination region to the narrow-gap part of the crystal should be larger for the recombination channel with a longer radiative lifetime compared to the channel with a shorter τ_r.

On excitation from the E_g^{max} side, the edge and impurity PL bands broadened with increasing excitation intensity, whereas their peaks were shifted to the longer wavelengths (Fig. 4). The $h\nu_a^{max}$ magnitude shifted to $h\nu_a^{max} \approx 1.20$ eV. This value is characteristic of the narrow-gap part with $x \approx 0$, as can be seen from Fig. 3a. A further increase in the excitation intensity J_0 led to the stabilization of the location of the peak value and to the narrowing of the impurity PL band. This points to the localization of the impurity PL region at the rear narrow-gap surface for high excitation intensities $J_0 > 10^{21}$ cm^{-2} s^{-1}. Figure 4 also demonstrates the dependences of spatial separation z^* for the edge and impurity PL regions on J_0 for one of the epilayers. It can be seen that, over the entire range of the excitation variation, $z_a^* > z_{cr}^*$. In addition, these data confirm the conclusion that the separation of the regions of generation and recombination for nonequilibrium charge carriers with increasing τ for the recombination channel with a longer radiative lifetime is larger compared to the channel with the shorter τ_r.

CONCLUSION

Thus, the agreement between the experimental data and the results of calculations confirms the validity of the notion of the coordinate dependence of recombination in graded-gap semiconductors with the drift transport of nonequilibrium charge carriers in the built-in electric field.

REFERENCES

1. A. I. Bazyk, V. F. Kovalenko, A. Yu. Mironchenko, and S. V. Shutov, Fiz. Tekh. Poluprovodn. (St. Petersburg) **35** (1), 53 (2001) [Semiconductors **35**, 54 (2001)].
2. V. F. Kovalenko, G. P. Peka, and L. G. Shepel', Fiz. Tekh. Poluprovodn. (Leningrad) **14** (7), 1350 (1980) [Sov. Phys. Semicond. **14**, 798 (1980)].
3. N. K. Dryapiko, V. F. Kovalenko, and G. P. Peka, Fiz. Tekh. Poluprovodn. (Leningrad) **17** (5), 863 (1983) [Sov. Phys. Semicond. **17**, 541 (1983)].
4. K. D. Glinchuk, A. V. Prokhorovich, and V. E. Rodionov, Fiz. Tekh. Poluprovodn. (Leningrad) **11** (1), 35 (1977) [Sov. Phys. Semicond. **11**, 18 (1977)].
5. D. Z. Garbuzov, V. B. Khalfin, and A. Abdullaev, in *Physics of III-V Compounds* (Leningr. Politekh. Inst., Leningrad, 1979), p. 21.
6. A. I. Bazyk, V. F. Kovalenko, G. P. Peka, and V. A. Petryakov, Fiz. Tekh. Poluprovodn. (Leningrad) **15** (7), 1363 (1981) [Sov. Phys. Semicond. **15**, 786 (1981)].

Translated by N. Korovin

Semiconductors, Vol. 36, No. 2, 2002, pp. 189–190. Translated from Fizika i Tekhnika Poluprovodnikov, Vol. 36, No. 2, 2002, pp. 197–198.
Original Russian Text Copyright © 2002 by Baimbetov, Ibraev, Zhukeshov.

SEMICONDUCTOR STRUCTURE, INTERFACES, AND SURFACES

Silicon Surface Treatment by Pulsed Nitrogen Plasma

F. B. Baimbetov, B. M. Ibraev, and A. M. Zhukeshov

Kazakh State National University, Almaty, 480012 Kazakhstan

e-mail: anuar_zhukeshov@mail.ru

Submitted March 26, 2001; accepted for publication May 11, 2001

Abstract—The structure of silicon single crystals after plasma treatment was studied by infrared spectroscopy and electron microscopy. It is shown that on irradiation by pulsed nitrogen plasma a silicon nitride is formed in the surface region. © *2002 MAIK "Nauka/Interperiodica".*

Insulating layers of silicon dioxide and nitride obtained by the conventional method of ion implantation are widely used in semiconductor device technology. The relatively novel trend of ionic synthesis is implantation using pulsed ion beams [1]. The use of such beams makes it possible to carry out implantation and annealing in a single stage.

In addition to pulsed methods, in this paper a method of silicon pulsed plasma treatment is suggested as an alternative method. The aim of this study was to assess the feasibility of pulsed plasma treatment for forming a nitride layer at the silicon surface. Treatment was carried out using a pulsed plasma accelerator (PPA) [2]. PPA forms a plasma flux with the temperature amounting to 100 eV, and pulse duration of 20 μs. The discharge current of PPA can be as high as 400 kA, with the plasma flux moving with the velocity of ~10^5 m/s.

The (100) surface of silicon single crystals KDB-10 (*p*-Si:B, ρ = 10 Ω cm) was treated with the pulsed flux of nitrogen plasma. The initial samples were placed in a vacuum chamber with a residual pressure of 10^{-3} Torr at room temperature. The measurements of incident energy density were performed by thermocouple sensors located in the immediate vicinity of the sample. Methods of infrared (IR) spectroscopy and electron microscopy were used to study the plasma-treated samples. The measurements of IR absorption spectra of the samples treated were carried out using a Nicolet-560 spectrometer. Typical resolution of the setup was 4 cm^{-1}.

The difference absorption spectra for silicon samples treated in nitrogen plasma relative to untreated samples are presented in Fig. 1. Curves *1–4* correspond to the samples treated with the energy density of 20, 30, 38, and 48 J/cm^2, respectively, relative to the untreated sample. As is known, the stretching and bending vibrations of the Si–N bond lie in the region of 800–830 and 500 cm^{-1} [3, 4]. The analysis of positions and shapes of absorption bands in Fig. 1 allows us to relate the presence of the peak at 800 cm^{-1} to silicon nitride formation. The absence of a clearly defined band at 500 cm^{-1} is caused by the water-vapor background in the range indicated. One should note that the main band intensity increases with an increase in the plasma-flux density. For a density lower than 30 J/cm^2, Si–N bond formation does not occur. After removal of the 20 μm thick surface layer, the band related to silicon nitride disappears.

To verify the assumption of the Si–N bond formation by nitrogen plasma treatment, studies of treatment with other gases were carried out. The IR spectra taken after the treatment of silicon samples by argon plasma (curve *1*) and carbon dioxide plasma (curve *2*) are shown in Fig. 2. The treatment parameters for argon and carbon dioxide are approximately the same as for nitrogen: 32 and 45 J/cm^2, respectively. It can be seen from experimental data in Fig. 2 that, in the region of 800 cm^{-1}, all features are absent and only the absorption by silicon itself is observed. The absorption bands at 1100 and 605 cm^{-1} are present for all the samples. The oxygen and carbon dioxide molecules absorbed at

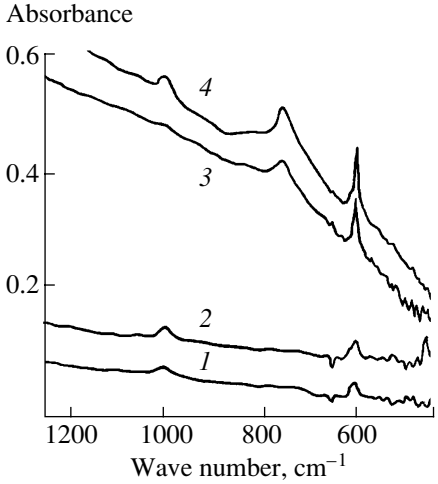

Fig. 1. Difference spectra of IR absorption for silicon samples treated with energy density of 20 (*1*), 30 (*2*), 38 (*3*), and (*4*) 48 J/cm^2 in comparison to the unprocessed sample.

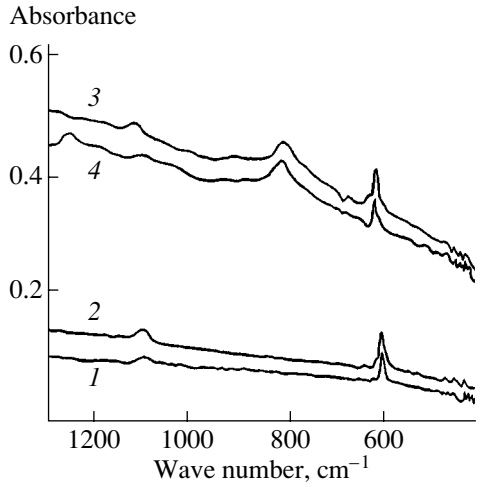

Fig. 2. Difference spectra of IR absorption for silicon samples (*1*) treated with argon (32 J/cm^2), (*2*) treated with carbon dioxide (45 J/cm^2), (*3*) treated with nitrogen without annealing, and (*4*) treated with nitrogen (48 J/cm^2) and annealed at 750°C.

the surface are likely responsible for the origin of these bands.

It is known that, as a result of amorphous silicon nitride crystallization, the main IR absorption band becomes split, which is caused by structural reconstruction and crystalline phase formation [3]. As is shown in [5], for amorphous silicon nitride layer crystallization, annealing at a temperature no lower than 600°C is necessary. The spectra of silicon samples treated in nitrogen plasma prior and after annealing (curves *3* and *4*, respectively) are shown in Fig. 2. Annealing was carried out in a vacuum chamber (residual pressure of 10^{-2} Torr) at a temperature of 750°C for 30 min. As can be seen, the annealing insignificantly affects the shape and position of the 800 cm^{-1} band which is related to silicon nitride. One should note that total absorption somewhat decreases, which is caused by the partial annealing of defects.

The studies of surface microstructure using a scanning electron microscope have shown that, under a high density of plasma flux, melting of the sample surface occurs and a peculiar relief is formed [6]. The relief formation is likely caused by nonequilibrium thermal processes, which are characteristic of pulsed treatment. The presence of large temperature and pressure gradients in the course of treatment results in the formation of defects at the surface and in the bulk of a crystal.

Thus, we may state with certain confidence that, by treatment with pulsed nitrogen plasma flux, the compound of nitrogen with silicon is produced in the surface layer. The silicon nitride is formed only for a relatively high energy density (higher than 30 J/cm^2). The dependence of silicon nitride formation on the plasma-flux density is monotone.

REFERENCES

1. F. F. Komarov, A. P. Novikov, V. S. Solov'ev, and S. Yu. Shiryaev, *Structural Defects in Ion-Implanted Silicon* (Beloruss. Gos. Univ., Minsk, 1990).
2. F. B. Baimbetov and B. M. Ibraev, in *Nuclear and Radiation Physics* (Inst. Yad. Fiz., Almaty, 1998), Vol. 2, p. 218.
3. Yu. N. Volgin and Yu. I. Ukhanov, Opt. Spektrosk. **38** (4), 727 (1975) [Opt. Spectrosc. **38**, 412 (1975)].
4. V. I. Bachurin, P. A. Lepshin, V. K. Smirnov, and A. B. Churilov, Izv. Ross. Akad. Nauk, Ser. Fiz. **62** (4), 703 (1998).
5. N. E. Lobanova, P. A. Pavlov, D. I. Tetel'baum, and L. V. Potapova, Fiz. Tekh. Poluprovodn. (Leningrad) **23** (12), 2149 (1989) [Sov. Phys. Semicond. **23**, 1330 (1989)].
6. B. M. Ibraev and A. M. Zhukeshov, in *Proceedings of the 3rd International Conference on Plasma Physics and Plasma Technology, Minsk, 2000*, Vol. 2, p. 456.

Translated by T. Galkina

Semiconductors, Vol. 36, No. 2, 2002, pp. 191–196. Translated from Fizika i Tekhnika Poluprovodnikov, Vol. 36, No. 2, 2002, pp. 199–204.
Original Russian Text Copyright © 2002 by Orlov, Ivina.

SEMICONDUCTOR STRUCTURES, INTERFACES, AND SURFACES

Role of Surface Segregation in Formation of Abrupt Interfaces in $Si/Si_{1-x}Ge_x$ Heterocompositions Grown by Molecular-Beam Epitaxy with Combined Sources

L. K. Orlov* and N. L. Ivina**

** Institute of Physics of Microstructures, Russian Academy of Sciences, Nizhniĭ Novgorod, 603600 Russia*

*** Nizhniĭ Novgorod State University, Nizhniĭ Novgorod, 603600 Russia*

Submitted May 18, 2001; accepted for publication May 25, 2001

Abstract—The coefficients of segregation of germanium atoms were measured for the $Si_{1-x}Ge_x$ system grown by molecular-beam epitaxy with combined $Si–GeH_4$ sources under the conditions of efficient filling of surface bonds by the products of the decomposition of hydrides. In their turn, these measurements made it possible to determine for the first time the ratio between the coefficients of the incorporation of Si and Ge atoms into the growing $Si_{1-x}Ge_x$ layer using the developed kinetic model of growth. For the $Si–Si_{1-x}Ge_x$ structures grown by molecular-beam epitaxy with the $Si–GeH_4$ combined sources, the role of various mechanisms (pyrolysis, segregation, etc.) in the formation of the profile of metallurgical layer interfaces was compared for a wide range of technological parameters. © *2002 MAIK "Nauka/Interperiodica".*

In the last decade, a tendency of moving away from investigating fundamental properties of heteroepitaxial structures based on silicon and germanium toward the practical use of these heterocompositions as active elements in various semiconductor devices has become evident. The production of device heterostructures necessitates the development of technological and inexpensive gas-phase methods of epitaxy for their growth using Si and Ge hydrides both at low and atmospheric pressures in the reactor [1]. The gas methods make it possible to grow highly homogeneous films on large-diameter substrates without using expensive equipment and are more efficient than traditional molecular-beam epitaxy (MBE). Furthermore, the growth of films in a rarefied hydrogen medium makes it possible to stabilize some of their properties, while a reduction in the surface-diffusion rate for Si and Ge atoms adsorbed by the substrate due to filling of the surface bonds by products of the decomposition of hydrides, in particular, by hydrogen, decreases the probability of upset of the two-dimensional growth of the epitaxial layer, thus inducing a planar character of inner interfaces in stressed heterostructures.

However, the wide application of this method of growing complicated semiconductor heterostructures is hindered by the difficulty in obtaining abrupt (within one monolayer) heteroboundaries necessary for the formation of compositions with layers of subnanometer thickness with the simultaneous preservation of acceptable growth rates using the gas-phase method. The last circumstance, and, specifically, the abruptness and high structural perfection of interfaces, is a defining factor for the stressed heterocompositions, providing the attainment of necessary characteristics of charge carriers in the layers and also ensuring the manifestation of many properties useful for practical applications.

On the one hand, the importance of the problem stimulated the application of atomic fluxes of matter in MBE devices with gas sources (GPMBE) in addition to molecular ones. The atomic fluxes can be formed on an additional heated element, e.g., a tungsten wire [2] or a sublimating silicon bar [3] arranged inside the reactor. On the other hand, an understanding of this problem assisted in the development of physical methods for the investigation of both the planar characteristics of interfaces between epitaxial layers and the character of the alloy-composition distribution in the neighborhood of interfaces of $Si(Ge)/Si_{1-x}Ge_x$ pseudomorphic heterostructures. Nowadays, transmission electron microscopy [4, 5], X-ray diffraction [6, 7], Auger and mass spectrometry, and other methods are the most widely used methods for investigating the composition profile in strained $Si_{1-x}Ge_x$ layers of nanometer thickness. All the listed methods point to the presence of asymmetric spreading of the alloy composition in the neighborhood of heteroboundaries even in the case of the structure growth by the most sophisticated methods of molecular-beam epitaxy with solid-phase sources [1–7]. However, nowadays, none of the analytical methods used can provide insight into the reasons behind the observed mixing of the alloy composition near interfaces, nor can any of them explain the different steepness of the profile of solid-solution composition in the neighborhood of various interfaces in the $Si_{1-x}Ge_x$ layer.

The purpose of this study is to determine values of the parameters which are of the most importance in technological experiments for a particular growth

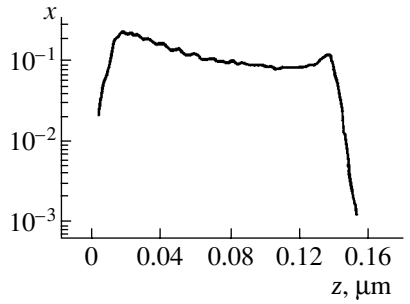

Fig. 1. SIMS distribution of germanium over a thickness z in the layer of $Si_{1-x}Ge_x$ solid solution grown by the (Si–GeH_4)-MBE.

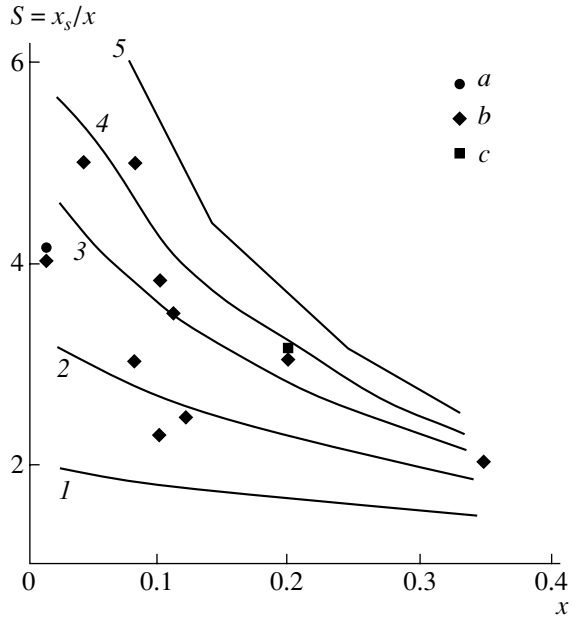

Fig. 2. Segregation coefficients S in $Si_{1-x}Ge_x$ samples. The dots are the SIMS data for the samples grown at temperatures T_{gr} = (*a*) 600, (*b*) 700, and (*c*) 800°C. The solid lines are the calculation for T_{gr} = 700°C and $k = r_{Si}/r_{Ge}$ = (*1*) 2, (*2*) 3.3, (*3*) 5, (*4*) 6.7, and (*5*) 10.

method {the combined (Si–GeH_4)-MBE, i.e., the MBE with the combined solid- and gas-phase sources [3, 8]}. These parameters are the coefficients of incorporation (crystallization) of silicon and germanium atoms adsorbed by the epitaxial surface into the growing $Si_{1-x}Ge_x$ layer. Furthermore, our aim was to use the refined values of these coefficients for the analytical estimate of the width of transition regions in the neighborhood of heteroboundaries of the structure. The results of the analysis, which was carried out with an unsteady variant of the growth model, used by us [9] for the indicated growth method, make it possible to better understand the role of the surface segregation in the formation of the alloy-composition profile at interfaces of layers.

The solution of the formulated problem is based on the numerical solving of a set of kinetic equations relating variations in concentrations (θ_i) of Ge and Si atoms and H_2, SiH_3, and GeH_3 molecules adsorbed by the growing surface to atomic and molecular fluxes of matter arriving at a substrate and to substrate temperature. Previously [9, 10], we considered the general set of equations describing how the effect of hydride-decomposition kinetics at the surface of an epitaxial film acts on the steady growth of the $Si_{1-x}Ge_x$ layer. For this reason, the form of the equations used is not discussed here. We note only that the applicability of the set of kinetic equations chosen and the scheme of the surface chemical reactions

$$GeH_4(gas) + \underline{2} \longrightarrow \underline{GeH_3} + \underline{H},$$

$$\underline{GeH_3} + \underline{3} \longrightarrow \underline{Ge} + 3\underline{H},$$

$$Ge,Si + \underline{1} \longrightarrow \underline{Ge,Si}, \quad \underline{Ge,Si} \longrightarrow Ge,Si(crystal),$$

$$\underline{Ge,Si} \longrightarrow Ge,Si(gas), \quad \underline{H} \longrightarrow H(gas)$$

(the underlining points to the atom–surface relation) were previously tested by us while analyzing steady characteristics for actual growth processes [9, 11]. From this analysis and for various conditions of technological experiment, we obtained values of the effective times of hydride-molecule decomposition required for the subsequent calculations and values of the coefficient of crystallization of silicon atoms.

The major factor responsible for the spreading of the alloy composition in $Si_{1-x}Ge_x$ layers grown by the combined (Si–GeH_4)-MBE can be, in some cases, the finite rate of hydride-pyrolysis reactions; and in other cases, this is the finite rate of the crystallization of the atoms of matter in the growing layer, as was shown in [10]. However, the calculations [10] were carried out assuming that the crystallization coefficients for Si and Ge atoms are identical; i.e., $r_{Si} = r_{Ge}$, which implies the lack of surface segregation in the system.

At the same time, the majority of films grown by (Si–GeH_4)-MBE [3, 8] have a marked gradient of composition, so that germanium accumulates at the growth surface according to the data of secondary-ion mass spectrometry (SIMS). This fact is associated with the different rate of incorporation of silicon and germanium atoms into the growing layer. One of the curves representing the gradient composition of the solid solution in the epitaxial $Si_{1-x}Ge_x$ layer is shown in Fig. 1.[1]

In Fig. 2, the corresponding values of the surface-segregation coefficients determined as the ratio

[1] The SIMS composition profile was measured at the State Research Institute for the Rare-Metal Industry (Moscow) for the series of samples grown in the mid-1990s in the Physicotechnical Research Institute, Nizhniĭ Novgorod State University, by V.A. Tolomasov and A.V. Potapov using the combined (Si–GeH_4)-MBE. We previously discussed individual characteristics of the obtained solid-solution layers in a number of papers (see, for example, [3, 8]).

between the concentration of germanium atoms on the surface and their concentration in bulk ($S = x_s/x$) are shown by dots as functions of the alloy composition in the layer. The corresponding theoretical curves obtained in terms of the kinetic model developed in [9] are also shown for several values of the parameter $k = r_{Si}/r_{Ge}$ and a growth temperature $T_{gr} = 700°C$. According to Fig. 2, the optimal value of k amounts to 5 for the given experiment within the spread in values of parameters. It is necessary to note that the crystallization coefficients themselves are generally not constant and depend on both the growth temperature and the degree of occupation of surface states by silicon and germanium atoms [11], which was accounted for in the growth model. The characteristic shape of dependences of the coefficient r_{Si} for various values of surface concentrations and growth temperatures was displayed in [11]. In this study, we obtained the dependence of the crystallization rate $r_{Si} = (F_{Si} + \nu_{Si}/n_s)V_{gr}n_0/(F_{Si} - V_{gr}n_0)n_s$ for silicon atoms both at a growth temperature T_{gr} and at a silicon-atom concentration $\theta_{Si} = (F_{Si} + V_{gr}n_0)/(F_{Si} + \nu_{Si}n_s)$ on the surface. Here, F_{Si} is the silicon-atom flux from the sublimating source, $V_{gr} = r_{Si}\theta_{Si}n_s/n_0$ is the layer-growth rate, ν_{Si} is the frequency of silicon-atom desorption from the surface, $n_0 = 5.5 \times 10^{22}$ cm^{-3} is the silicon-atom concentration in the bulk, and $n_s = 6.8 \times 10^{14}$ cm^{-2} is the adsorption-center concentration at the crystal surface.

In spite of the fact that the germanium concentration on the film surface grows with the germanium concentration in the layer [the larger the value of k, the more pronounced is this dependence (Fig. 3a)], the surface-segregation coefficient decreases with increasing x (Fig. 2). The values of growth rates V_{gr} used in this experiment are shown in Fig. 3b as functions of germane-vapor pressure P_{GeH_4} in the reactor (diamonds *1* represent experimental data, and curve *2* was calculated). A significant spread in experimental values of the growth rate is associated both with the critical behavior of values V_{gr} relative to the germane-vapor pressure in the reactor (Fig. 3b) and with the difficulty of exactly reproducing, from experiment to experiment, the temperature of the sublimating source providing the silicon-atom flux into the reactor. The atomic flux is very sensitive to the temperature of heating in the narrow range of 1250–1300°C.

Note that the values of the segregation coefficient we obtained and, correspondingly, the ratios between the coefficients of incorporation for silicon and germanium atoms into the growing layer are several times smaller than those observed by other authors in the structures grown by traditional MBE [12] at the same temperatures. The discrepancies can be easily understood if we note that, in our case, the germanium-atom concentration on the growth surface must be considerably lower than in the case of conventional MBE because of the significant filling of the growth surface

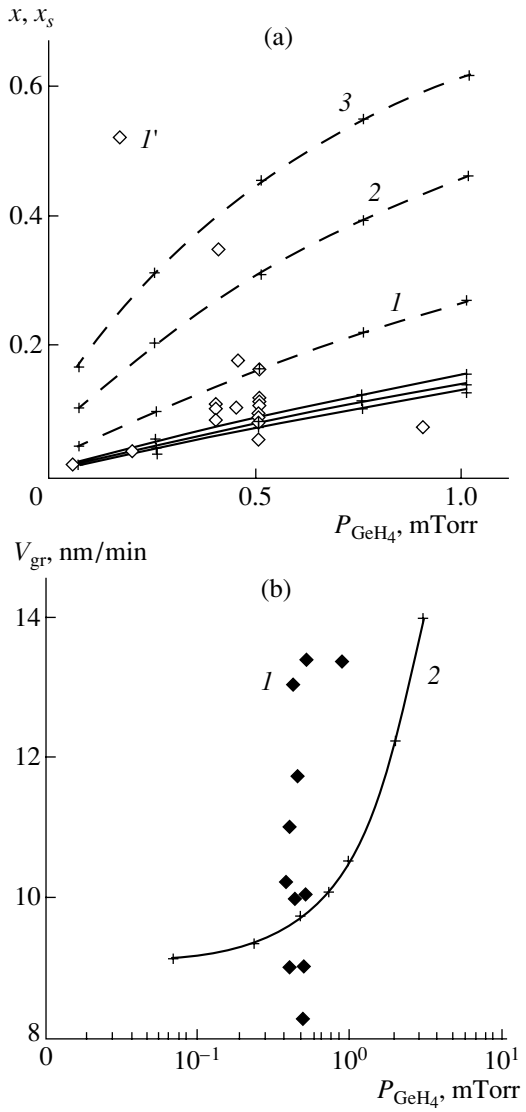

Fig. 3. (a) Theoretical dependences of germanium concentration at $T_{gr} = 700°C$ on a germane-vapor pressure in the reactor: the solid lines are the concentrations x in the bulk of the layer, and the dashed lines are the concentrations x_S at the surface for a series of samples; (b) (*1*) experimental and (*2*) calculated values of layer-growth rate.

by products of the hydride decomposition, mainly by the radicals of germanium and by hydrogen [13]. Of course, it is difficult to totally rule out the limitations in the used measurement methods, which lead to errors in measuring the germanium-atom concentrations both directly on the surface of the grown film and in its bulk.

We analyze the hydride pyrolysis and investigate features of the formation of transition regions in the neighborhood of heteroboundaries of the structure using the conventional scheme of a technological experiment. We consider the growth of the $Si_{1-x}Ge_x$ layer in the GPMBE setup under conditions when a pulsed germane molecular flux with extremely abrupt pulse edges is superimposed on a constant silicon

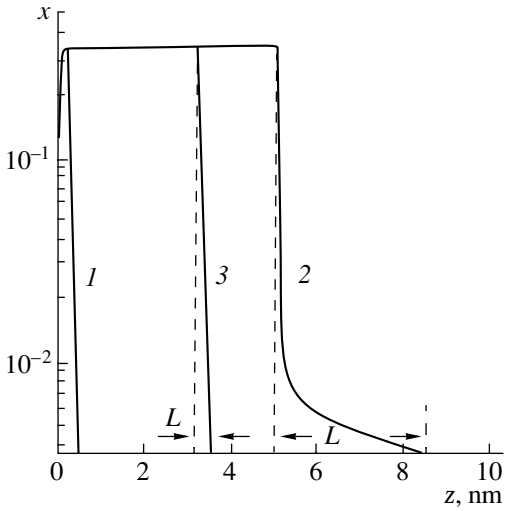

Fig. 4. Composition profiles over a thickness z calculated for the solid solution in the $Si/Si_{1-x}Ge_x/Si$ heterostructures with the highest content $x_{max} = 0.35$ in the solid-solution layer. The parameters of calculation: $T_{gr} = 500°C$, $k = 5$, P_{GeH_4} = (*1*) 0.01, (*2*) 1, (*3*) 10 mTorr.

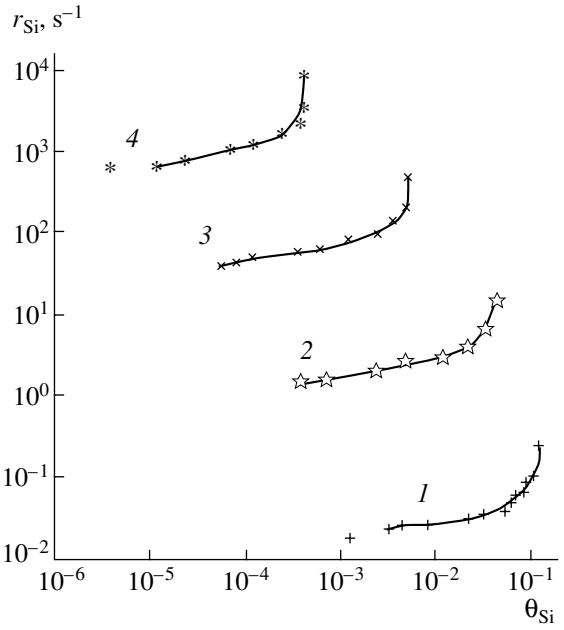

Fig. 5. Coefficients r_{Si} of incorporation of silicon atoms into the crystal as functions of a dimensionless surface concentration $\theta_{Si} = n_{Si}/n_s$ at the growth temperatures T_{gr} = (*1*) 500, (*2*) 600, (*3*) 700, and (*4*) 800°C.

atomic flux. The admissibility of such a model is based on the actual existing possibility of switching a flux virtually instantaneously in modern technological setups.

The composition profile calculated taking into account the found value of k, i.e., in the general case with allowance made for the surface segregation in the system, for the pulsed injection of the germane flux into the growth chamber is shown in Fig. 4. This profile has a pronounced asymmetry in the character of decrease in the germanium concentration in the neighborhood of the upper (right-hand) and lower (left-hand) interfaces of the layer. We calculate the composition profile here for three cases: curves *1* and *2* correspond to the situation when the atomic fluxes are unimportant; the spreading of composition on the interface is exceptionally associated with a finite time of pyrolysis of hydrides on the growth surface; and the width L of the interface depends heavily on the gas pressure in the reactor, which attains a maximum value at a pressure of ~1 mTorr (curve *2*); curve *3* is obtained when the germanium atomic fluxes from the sublimating source play a very important role. In the last case, a dominant mechanism inducing the spreading of the interface is the mechanism associated with a finite time of incorporation of germanium atoms into the crystal lattice. In this region of gas pressure, the pyrolysis of hydrides is unimportant and the segregation accumulation of germanium on the surface manifests itself in the broadening of the layer interface. Henceforth, analyzing the growth processes, we choose values of technological parameters approaching those most frequently used in experiments: the substrate temperature is $T_{gr} = 500°C$, and the partial pressure of hydrides in the setup reactor is $P_{Ge(Si)H_4} = (0.01–10) \times 10^{-3}$ Torr. The constants of the crystallization rate $r_{Ge(Si)}$ for the atoms adsorbed by the surface generally depend on the degree of filling of the surface by the products of the decomposition of hydrides, which we took into account in calculations.

The curves in Fig. 4 show a pronounced asymmetry of the composition profile in the structure. This asymmetry is associated with the different role of various mechanisms involved in the formation of transition regions in the neighborhood of heteroboundaries. The asymmetry of interfaces can be easily understood if we note that the crystallization coefficients increase abruptly as the corresponding atoms of matter are accumulated on the surface (Fig. 5). On the lower interface, the rate of accumulation of germanium atoms is determined by the rate of their arrival from the sources (virtually instantaneous), as a consequence of which the incorporation of germanium atoms into the growing layer occurs at maximum rate for the given process, thus causing an abrupt composition profile for the solid solution on the interface. When the germane molecular flux is interrupted, the concentration of germanium atoms on the surface and the corresponding rate of their crystallization decrease abruptly at the subsequent moments of time leading to extended tails in the composition distribution for a solid solution on the upper interface of the layer due to a low rate of incorporation of germanium atoms into the growing layer. This fact agrees well with the current available experimental data [4–7].

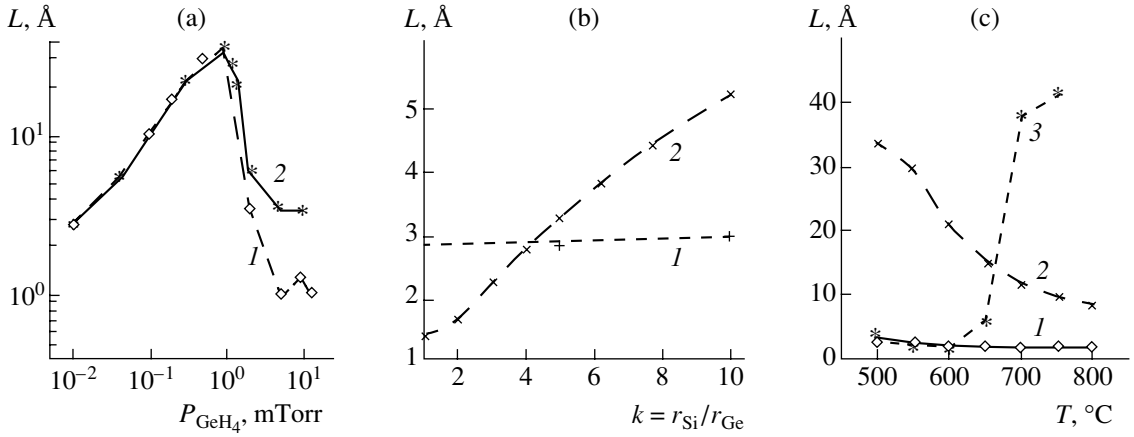

Fig. 6. The magnitude L of spreading of composition in the neighborhood of the right-hand interface of the $Si_{1-x}Ge_x$ layer as a function of (a) germane-vapor pressure in the reactor for k = (*1*) 1 and (*2*) 5, and T_{gr} = 500°C; (b) a ratio between the coefficients of incorporation of silicon and germanium atoms into the growing layer at P_{GeH_4} = (*1*) 0.01 and (*2*) 10 mTorr, and T_{gr} = 500°C; and (c) the growth temperature T_{gr} for k = 5 and P_{GeH_4} = (*1*) 0.01, (*2*) 1, (*3*) 10 mTorr.

Now, in more detail and for various values of technological parameters, we consider the effect of a difference in the coefficients of incorporation of silicon and germanium atoms into the growing layer on the magnitude of the layer-interface broadening. In other words, we discuss how strongly, as compared with other mechanisms, the surface segregation affects the broadening of heteroboundaries. As the analyzed parameter, we choose a width L of the upper interface of the $Si_{1-x}Ge_x$ layer at the level of $x = 0.01x_{max}$ (Fig. 4). The corresponding curves representing the dependences on the germane-vapor pressure in the reactor are shown in Fig. 6; these curves were calculated for the following values of parameters: $x_{max} = 0.35$, $T_{gr} = 500$°C, and $k = 1$ and 5. We can use the data in Fig. 6 not only to estimate the value of the possible broadening of the layer interface, but also to find out in which range of values of technological parameters one or another mechanism of broadening prevails. It can be seen from Fig. 6a that the value of L remains reasonably small (smaller than 10 Å) in the region of low germane-vapor pressure ($P < 10^{-4}$ Torr) due to very low growth rates for the solid-solution layer under the chosen conditions. With an increase in the germane-vapor pressure in the reactor and, correspondingly, in the growth rate of the layer, the spreading of the composition profile increases and, at $P_{GeH_4} \approx 10^{-3}$ Torr, amounts to ~30 Å. The spreading of the alloy composition in the neighborhood of heteroboundaries is caused by a long-term process of pyrolysis of germane molecules on the growth surface; thus, a difference in the coefficients of incorporation of germanium atoms into the crystal lattice (eventually, the surface-segregation effect) in the range of parameters under consideration (when the major role in the growth process is played only by molecular beams towards the surface) by no means manifests itself in the spreading of heteroboundaries of the structure.

The calculations show that the highest abruptness of the interface is attained in the region of fairly high gas pressures in the reactor (Fig. 6a). In this case, the atomic fluxes of both silicon and germanium coming from the hot sublimating source are dominant in the growth process, and the system approaches most closely the conventional MBE. Exactly in this region, the surface segregation can manifest itself most clearly, thus leading to an additional broadening in the layer interface, which can be easily seen from the comparison between curves *1* and *2* in Fig. 6a.

In Fig. 6b, we show the quantity L in relation to the coefficients of the incorporation of silicon and germanium atoms into the growing layer for two gas pressures in the reactor: a high one (curve *2*), when the atomic fluxes of germanium atoms from the sublimating source are dominant in the growth process, and a low one (curve *1*), when the molecular flux of GeH_4 is dominant and the growth of the solid-solution layer of a given composition is associated mainly with the pyrolysis of hydride molecules on the substrate. The virtually steady dependence *1* testifies to the fact that the formation of the composition profile in the region of heteroboundaries is independent of the surface segregation. The fact that curve *2* ascends with increasing coefficient k (or S) indicates that the role of segregation is dominant in the formation of the composition profile on the interface if the mechanism of growth from atomic beams prevails.

We now discuss how the pattern shown in Fig. 6a can vary with increasing temperature. In Fig. 6c, we show how the spreading L of the interface varies with increasing substrate temperature for three values of the germane-vapor pressure in the reactor. The temperature

dependence of the kinetic coefficients in the balance equations substantially affects the run of the curves. With an increase in temperature, the degree of surface coverage by the products of the decomposition of hydrides, including hydrogen, changes and, simultaneously, the crystallization coefficients increase as is shown in Fig. 5.

The indicated circumstance leads to the curves in Fig. 6a shifting entirely into the region of higher pressures, thereby causing a decrease in the spreading of interfaces in the region of low and intermediate germane-vapor pressures (curves *1* and *2* in Fig. 6c) and an abrupt increase in the value of L in the region of high pressures of gas in the reactor (curve *3* in Fig. 6c). Thus, in the region of high growth temperatures (T_{gr} > 700°C), virtually for all real germane-vapor pressures used in practice, the effect of atomic fluxes on the growth process in the combined (Si–GeH_4)-MBE is weakened considerably; this causes a high degree of spreading of the composition profile in the neighborhood of interfaces in the solid-solution layer.

In conclusion, we stress once more that there are generally several factors decisively responsible for the magnitude of spreading of the composition profile in the neighborhood of heteroboundaries in the structure of the (Si–GeH_4)-MBE, and their role changes with both growth temperature and germane-vapor pressure in the reactor. One of these factors is associated with the decrease in the lifetime of the molecules, adsorbed by the surface, when there is a rise in the substrate temperature. Another factor is the redistribution of the role of molecular and atomic fluxes in the mass transfer of matter to the growing surface. In the range of relatively high gas pressures, the second factor has a stronger effect on the width of transition regions at low temperatures, bringing about the small width of the interface. In this case, the width is related mainly with the effect of surface segregation.

ACKNOWLEDGMENTS

We thank staff members Yu.N. Drozdov, A.V. Potapov, and S.V. Ivin of the Institute of the Physics of Microstructures, RAS; professors V.A. Tolomasov and E.S. Demidov of the Physicotechnical Research Institute of NNSU; and V.I. Vdovin and P.B. Orlov of the State Research Institute for the Rare-Metal Industry, without whose help and support it would have been difficult to carry out this study.

This study was supported by the Russian Foundation for Basic Research (project no. 01-02-16778), by the Program "Universities of Russia" (grant no. 992849), and by the Research and Technological Program "Physics and Technology of Solid Nanostructures" (grant no. 7(00)-P).

REFERENCES

1. D. W. Greve, Mater. Sci. Eng. B **18**, 22 (1993).
2. J. Thiesen, E. Iwaniczko, K. M. Jones, *et al.*, Appl. Phys. Lett. **75**, 992 (1999).
3. L. K. Orlov, V. A. Tolomasov, A. V. Potapov, *et al.*, IEEE Trans. Semicond. Manuf. **SIMC-9**, 215 (1996).
4. O. P. Karpenko, S. M. Yalisove, and D. J. Eaglesham, J. Appl. Phys. **82**, 1157 (1997).
5. V. I. Vdovin, K. D. Shcherbachev, M. Mironov, *et al.*, Kristallografiya **45** (4), 722 (2000) [Crystallogr. Rep. **45**, 661 (2000)].
6. W. C. Tsai, C. Y. Chang, T. G. Jung, *et al.*, Appl. Phys. Lett. **67**, 1092 (1995).
7. J. M. Baribeau, D. J. Lockwood, and R. L. Headrick, J. Electron. Mater. **24**, 341 (1995).
8. V. A. Tolomasov, L. K. Orlov, S. P. Svetlov, *et al.*, Kristallografiya **43**, 535 (1998) [Crystallogr. Rep. **43**, 493 (1998)].
9. L. K. Orlov, A. V. Potapov, and S. V. Ivin, Zh. Tekh. Fiz. **70** (6), 102 (2000) [Tech. Phys. **45**, 770 (2000)].
10. L. K. Orlov, N. L. Ivina, and A. V. Potapov, Fiz. Tekh. Poluprovodn. (St. Petersburg) **34**, 1153 (2000) [Semiconductors **34**, 1103 (2000)].
11. A. V. Potapov, L. K. Orlov, and S. V. Ivin, Thin Solid Films **336**, 191 (1998).
12. Y. J. Zheng, A. M. Lam, and J. R. Engstrom, Appl. Phys. Lett. **75**, 817 (1999).
13. L. K. Orlov, S. V. Ivin, A. V. Potapov, and N. L. Ivina, Zh. Tekh. Fiz. **71** (4), 53 (2001) [Tech. Phys. **46**, 417 (2001)].

Translated by V. Bukhanov

Semiconductors, Vol. 36, No. 2, 2002, pp. 197–202. Translated from Fizika i Tekhnika Poluprovodnikov, Vol. 36, No. 2, 2002, pp. 205–210.
Original Russian Text Copyright © 2002 by Dmitriev, Markin.

SEMICONDUCTOR STRUCTURES, INTERFACES, AND SURFACES

Segregation of Mobile Ions on Insulator–Semiconductor Interfaces in Metal–Insulator–Semiconductor Structures

S. G. Dmitriev and Yu. V. Markin

Institute of Radio Engineering and Electronics, Russian Academy of Sciences (Fryazino Branch), pl. Vvedenskogo 1, Fryazino, Moscow oblast, 141120 Russia

Submitted December 22, 2000; accepted for publication June 22, 2001

Abstract—The equilibrium distribution of mobile ions was considered in metal–insulator–semiconductor (MIS) structures with ionic surface states at the insulator–semiconductor interface. The quasi-steady current–voltage characteristics were calculated for ion currents in MIS structures. The population of surface states by ions was described by the Gibbs distribution. © *2002 MAIK "Nauka/Interperiodica".*

1. INTRODUCTION

The high-temperature stages of technological processes in semiconductor structures are often accompanied by the diffusion of impurity atoms and ions [1–4]. Of special interest are the processes of accumulation (segregation) of defects at free surfaces and interfaces. On the other hand, the ion mobility can be used for probing an interface with the aim of investigating the nature of electron surface states, nonuniformities of the surface potential, and other issues [4–7]. In particular, the equilibrium distributions of ions in thin insulator films can be investigated using the quasi-steady (quasi-equilibrium) current–voltage (*I–V*) characteristics of ion currents [8, 9].

The equilibrium distributions in insulator and semiconductor films have been calculated using either the hydrodynamic model [10–12] or the Boltzmann ion-energy distribution in explicit form [8, 9]. A peculiar segregation of ions at the insulator–semiconductor interface owing to their attraction by charge carriers in the semiconductor was noted in [8, 9]. In experiment, the ion-delocalization thresholds manifest themselves in *I–V* characteristics as an increase in currents. In this study, we consider a more conventional segregation mechanism based on the fact that the ion bonding energy in a lattice increases on the interface (i.e., due to the presence of ion surface states). The surface-state population by ions is described by the Gibbs distribution [13].

2. THEORETICAL MODEL

In terms of a hydrodynamic model, the equilibrium ion distribution $N(z)$ in an insulator (one-dimensional configuration) is typically described on the basis of the condition of zero current density $j(z)$ of singly charged positive ions:

$$j(z) = qN(z)\mu\mathscr{E}(z) - qD\frac{dN}{dz} = 0. \quad (1)$$

This expression is written taking into account the Einstein relation $\mu = qD/kT$ between mobility μ and ion diffusivity D, where q is the elementary charge, k is the Boltzmann constant, T is the temperature, and $\mathscr{E}$ is the electric-field strength. The distribution of potential is described by the Poisson equation

$$\varepsilon_i\frac{d^2\varphi}{dz^2} = -4\pi qN(z), \quad (2)$$

where ε_i is the permittivity of the insulator. The Einstein relation follows from (1) for the Boltzmann energy distribution of charge carriers [14–16] (its analogue in the case of degenerate distribution is of more complicated form [16]). Thus, the hydrodynamic model represented by formula (1) and Eq. (2) is equivalent to the Poisson equation with the Boltzmann distribution for $N(z)$. Specific solutions are determined by the boundary conditions for the potential and the electric-field strength on the insulator–film interfaces $z = 0$ (the interface with metal) and $z = d$ (the interface with semiconductor) taking into account the constancy of the total ion number N_s in the film, which can also be taken into account in the field boundary conditions [8, 9].

As a rule, the ions are localized in the lattice, and their motion represents relatively seldom jumps to neighboring lattice sites [1–4]. This situation corresponds to a monoenergetic (narrow) ion-energy level E_i. In addition to interstitial states in the insulator bulk and at the interface, the ion states can be related also to defects. For example, sodium atoms are bonded to phosphorus and chlorine atoms in SiO_2 [4]. Of special interest are the surface states of ions, because their density N_{0s} can attain atomic values $N_{0s} \sim 10^{15}$ cm^{-2}. These

can be both intrinsic states associated with the presence of an interface and defect states arising due to a lattice mismatch. In the latter case, a fraction of defects is localized in a narrow relaxation (transition) layer ~100 Å thick near the interface, rather than at the interface itself [2, 4]. However, the presence of high-density surface states does not necessarily lead to segregation by itself if the bonding energy of ions to these states is insufficient. As the first step, we consider the model with two levels of ion states: E_i for the bulk states with a concentration (number of available lattice sites) N_0 and E_{is} for the surface states with a concentration N_{0s}.

In the general case, the population of these states is described by the Gibbs distribution [13]. For the surface states of ions, this distribution has (in terms of the model under consideration) the form (see *Appendix*)

$$f_i = \frac{1}{1 + \exp[(E_{is} + q\varphi_s - F_i)/kT]}, \quad N_{ss} = N_{0s} f_i, \quad (3)$$

where F_i is the Fermi level (chemical potential) of ions, $\varphi_s = \varphi(d)$ is the surface potential, and N_{ss} is the concentration of ions captured at the surface states. Here and henceforth, the degeneracy multiplicities of levels will be taken to equal unity, as this can be expected, for example, in the case of interstitial states.

The bulk-state concentration is usually high, i.e., on the order of an atomic one, $N_0 \sim 10^{22}$–10^{23} cm^{-3}. In this case, the degeneracy effects are negligible [8], and, for describing the bulk states, it is possible to use the Boltzmann distribution to which the Gibbs distribution is reduced in the case of low probabilities of occupation of levels:

$$f_i(z) = \exp[-u(z)]; \quad N(z) = N_0 f_i(z);$$
$$u(z) = \frac{E_i + q\varphi(z) - F_i}{kT}, \quad (4)$$

where $u(z)$ is the normalized ion energy counted from the Fermi level.

An attractive feature of the hydrodynamic model is that it involves no microparameters (ion-energy levels and concentrations of states), whereas formulas (3) and (4) require that these be taken into account in explicit form. The apparent contradiction is associated with the fact that the solution to problem (2), (4), without the surface states ($N_{0s} = 0$), is actually independent of these parameters, because variations in the bonding energy and N_0 are compensated by the variation (renormalization) of the Fermi level by virtue of the constancy condition for N_s, which can also be shown explicitly [8, 9]. However, this property, which exactly ensures the applicability of the hydrodynamic model, is affected if there are several ion states in the lattice. In this case, the redistribution of ions between the states is defined by statistical formulas and depends on microparameters. Furthermore, the population of strongly bound states (ion traps) can be appreciable. In this case, it is necessary to use the general Gibbs distribution (3).

3. METHOD OF CALCULATION

The Poisson equation with $N(z)$ in the form of (4) in terms of dimensionless energy $u(z)$ acquires the following form:

$$\frac{d^2u(z)}{dz^2} = -\frac{4\pi q^2}{\varepsilon_i kT} N_0 \exp[-u(z)]. \quad (5)$$

It has two types of solutions depending on the sign of its first integral I^* and includes either hyperbolic or trigonometric functions [8–11]. In this case,

$$I^* = \frac{q^2\mathscr{E}^2(z)}{(2kT)^2} - \frac{2\pi q^2 N(z)}{\varepsilon_i kT} = \text{const}; \quad L = |I^*|^{-1/2} \quad (6)$$

determines characteristic lengths (L) of variation in the potential in the film. The parameters of the problem are determined by the boundary conditions for the field at the film interfaces ($z = +0$, $z = d - 0$). Let $\mathscr{E}_0 = \mathscr{E}(+0)$. In this case, the field at the other side of the film is $\mathscr{E}(d - 0) = \mathscr{E}_s = \mathscr{E}_0 + \mathscr{E}_i^*$ from the Gauss theorem. Here,

$$\mathscr{E}_i^* = \frac{4\pi q}{\varepsilon_i} N_s^*,$$
$$N_s^* = N_s - N_{ss} = N_s - \frac{N_{0s}}{1 + \exp(u_s + \Delta e_i)}, \quad (7)$$

where $u_s = u(d)$, $\Delta e_i = \Delta E_i/kT$, $\Delta E_i = E_{is} - E_i$ is the change in the bonding energy of an ion at the interface, and N_s^* is the total concentration of ions in the film bulk. If there are no surface states ($N_{0s} = 0$), $(4\pi q/\varepsilon_i)N_s = \mathscr{E}_i$ is the ion field strength ($\mathscr{E}_i \approx 4.6 \times 10^5$ V/cm for $N_s = 10^{12}$ cm^{-2} and $\varepsilon_i = 3.9$). In these designations, the boundary conditions can be represented (after cumbersome calculations) in the form

$$\left(\frac{\mathscr{E}_0}{\mathscr{E}_d}\right)^2 + \frac{\mathscr{E}_0}{\mathscr{E}_d}\frac{\mathscr{E}_i^*}{\mathscr{E}_d} - \frac{\mathscr{E}_i^*}{\mathscr{E}_d} y\coth y - y^2 = 0, \quad I^* > 0, \quad (8)$$

$$\left(\frac{\mathscr{E}_0}{\mathscr{E}_d}\right)^2 + \frac{\mathscr{E}_0}{\mathscr{E}_d}\frac{\mathscr{E}_i^*}{\mathscr{E}_d} - \frac{\mathscr{E}_i^*}{\mathscr{E}_d} y\cot y + y^2 = 0, \quad I^* < 0,$$
$$\mathscr{E}_d = \frac{2kT}{qd}, \quad (9)$$

where $\mathscr{E}_d$ is the field strength characteristic of the film ($\mathscr{E}_d \approx 0.86 \times 10^4$ V/cm for $d = 1000$ Å, and $T = 500$ K), and $y = d/L$. If $N_{0s} = 0$, $\mathscr{E}_i^* = \mathscr{E}_i$, and formulas (8) and (9) determine y for the given $\mathscr{E}_0$; after this, the remaining parameters can also be found. In this case, the distribution $N(z)$ and the *I–V* characteristic for ion currents are independent of N_0 and other microparameters [8, 9].

If $N_{0s} \neq 0$, then $\mathscr{E}_i^*$ depends on u_s and the microparameters by virtue of (7), and, to solve the problem, one more equation is necessary, for example, equation (6)

for $z = d$. Equations (8), (9), and (6) make it possible to determine the dependences $u_s(\mathscr{E}_0)$ and $y(\mathscr{E}_0)$ by numerical calculation. In this case, equations (8) and (9) have four solutions (two solutions each) with various domains of definition, whose totality encompasses the entire range of variations in $\mathscr{E}_0 \in (-\infty; \infty)$ and in the voltage V_g across the structure. Here, the calculations are cumbersome, and, from now on, we present only the results of numerical calculations. Then, the remaining quantities—the voltage drop $V_i = \varphi_0 - \varphi_s$ across the film and V_g across the entire structure, the energy-band bending φ_s in the semiconductor, the ion distribution $N(z)$, and their number in the surface states—were determined similarly to [8, 9].

4. QUASI-STEADY CURRENT–VOLTAGE CHARACTERISTICS AND THE CAPTURE OF IONS BY SURFACE STATES

The current density j in the film in the case of a linear voltage sweep $dV_g/dt = \beta_V$ can be determined from the formula [8]

$$\frac{j(V_g)}{j_0} = d\frac{\partial \mathscr{E}_0(V_g)}{\partial V_g}, \quad j_0 = \beta_V C_i, \quad C_i = \frac{\varepsilon_i}{4\pi d}, \quad (10)$$

where C_i is the insulator capacitance (per unit area). In this form, the quantity $j(V_g)/j_0$ represents the quasi-steady (normalized) *I–V* characteristic of the structure. This characteristic is independent of β_V, and it is convenient for the experimental investigation of ion distributions [9]. The *I–V* characteristic of the film itself (without the semiconductor) is also useful for comparison:

$$\frac{j_i(V_i)}{j_0} = d\frac{\partial \mathscr{E}_0(V_i)}{\partial V_i}. \quad (11)$$

Conventionally, we call this the *I–V* characteristic of the metal–insulator–semiconductor (MIS) structure.

The calculation was carried out for an *n*-type semiconductor with parameters of silicon [16] (see [8]); in particular, we set the donor concentration $N_d = 10^{15}$ cm^{-2} and the ionization energy $E_d = 0.045$ eV (phosphorus) for the donor level. The insulator thickness $d = 1000$ Å, $\varepsilon_i = 3.9$, the ion-state concentration $N_0 = 3 \times 10^{22}$ cm^{-3} in the film bulk [9], the variation of ion bonding energy $\Delta E_i = -1$ eV at the interface with semiconductor, the total ion concentration $N_s = 10^{12}$ cm^{-2} in the film, and the temperature $T = 500$ K. In Figs. 1 and 2, we show the *I–V* characteristics for the cases of high ($N_{0s} \gtrsim N_s$) and low ($N_{0s} < N_s$) concentrations N_{0s} of ion surface states (traps) at the interface with the semiconductor. The shape of the *I–V* characteristics in Fig. 1 is the same as the shape of a single (broadened and shifted) peak of ion currents with a capacitance dip in it. The dip is associated with the effect of capacitance division of voltage between the insulator and semiconductor [9]. The *I–V* characteristic of the MIS structure in the inset does not feature the second ion peak. This characteristic is plotted for the same values of parameters as those for curve *3* in the main part of the figure; this *I–V* characteristic has no dip. Thus, the shape of *I–V* characteristics is associated with a certain mechanism—the ion capture by surface states ($\beta_V > 0$) or the "emission" from them ($\beta_V < 0$). Curve *3*' illustrates the effect of the concentration N_0 of states in the film bulk on the *I–V* characteristics.

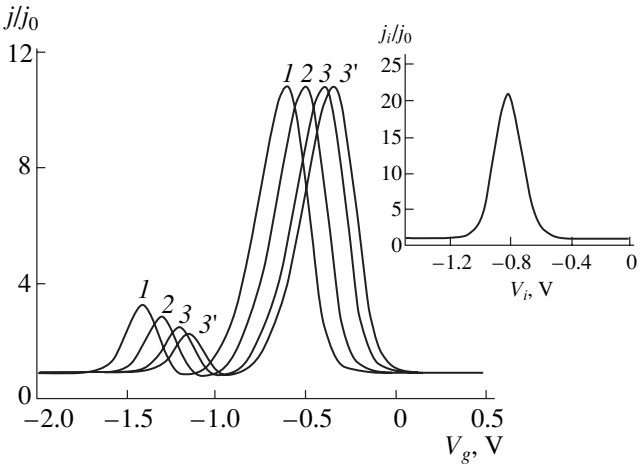

Fig. 1. Quasi-static *I–V* characteristics $j(V_g)$ for ion currents in a MIS structure with $N_0 = 3 \times 10^{22}$ cm^{-3} and high densities of ion surface states N_{0s} = (*1*) 10^{15}, (*2*) 10^{14}, and (*3*) 10^{13} cm^{-2}, and also with $N_0 = 10^{23}$ cm^{-3} and (*3*') $N_{0s} = 10^{13}$ cm^{-2}. In the inset, the *I–V* characteristic $j_i(V_i)$ of an MIS structure corresponding to the parameters (*3*) for $j(V_g)$ is shown. The remaining parameters: $N_s = 10^{12}$ cm^{-2}, $d = 1000$ Å, $\Delta E_i = -1$ eV, $T = 500$ K, and j_0 is the capacitance current in the film.

The *I–V* characteristics in Fig. 2 involve two ion peaks and a capacitance dip (see the inset); however, the presence of the dip can give the impression that the number of ion peaks is large. The dots correspond to a conventional peak without traps ($N_{0s} = 0$), which is associated with the displacement of ions from one film interface to the other [9]. With increasing trap concentration, we observe a "transfer" of ions from the conventional peak to the "trap" one, which is brought to completion for $N_{0s} \approx N_s$ (curve *1*). In Si–SiO_2 systems, we observe curves ($\beta_V < 0$) resembling the theoretical *I–V* characteristics with a low trap concentration ($N_{0s} \sim 10^{10}$–10^{11} cm^{-2} or lower); although, the trap peaks are usually nonequilibrium and their nature remains unclarified. Nevertheless, it is of interest to note that the presence of such peaks, if they are separated from the conventional peak by the capacitance dip, is considered a consequence of the neutralization of a fraction of ions by electrons at an interface (see, for example, [7]). As can be seen from Fig. 2, this fact is not always true.

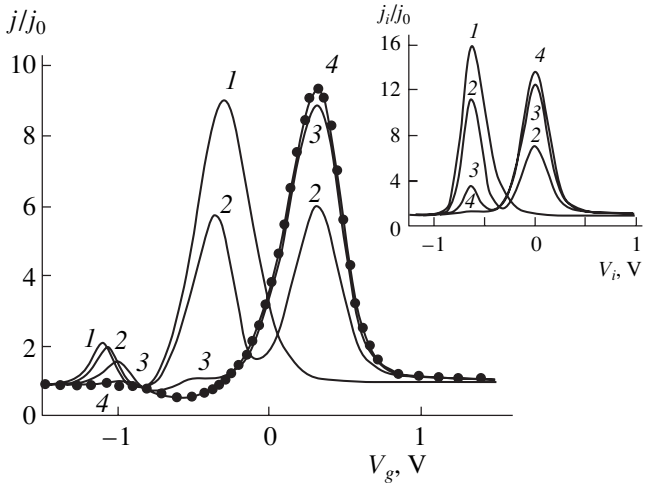

Fig. 2. Quasi-static *I–V* characteristics $j(V_g)$ of ion currents in a MIS structure with low ion-trap densities N_{0s} = (*1*) 10^{12}, (*2*) 5×10^{11}, (*3*) 10^{11}, and (*4*) 10^{10} cm^{-2}; $N_{0s} = 0$ (dots). In the inset, the *I–V* characteristics $j_i(V_i)$ of a MIS structure corresponding to the parameters (*1–4*) for $j(V_g)$ are represented. The remaining parameters: $N_0 = 3 \times 10^{22}$ cm^{-3}, $N_s = 10^{12}$ cm^{-2}, $d = 1000$ Å, $\Delta E_i = -1$ eV, $T = 500$ K, and j_0 is the capacitance current in the film.

The capture of ions by the surface states weakens (stabilizes) the dependence $\varphi_s(V_g)$ (Fig. 3) and gives rise to characteristic features in it. In this case, the population f_i of the ion surface states is not low ($f_i \approx 1$) if $N_{0s} \lesssim N_s$ (see inset in Fig. 3).

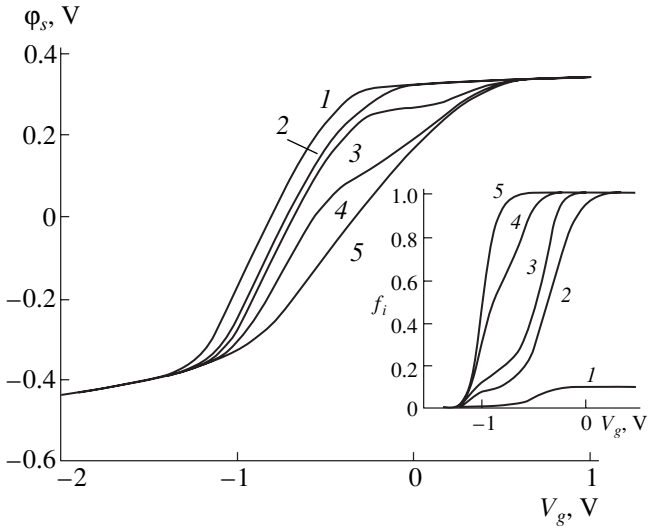

Fig. 3. Stabilization of the surface potential $\varphi_s(V_g)$ by the ion traps at the interface: N_{0s} = (*1*) 10^{13}, (*2*) 10^{12}, (*3*) 5×10^{11}, (*4*) 10^{11}, and (*5*) 10^{10} cm^{-2}. In the inset, the trap population $f_i(V_g)$ is shown for curves *1–5*. The remaining parameters: $N_0 = 3 \times 10^{22}$ cm^{-3}, $N_s = 10^{12}$ cm^{-2}, $d = 1000$ Å, $\Delta E_i = -1$ eV, and $T = 500$ K.

There are always a large number of ion intrinsic states ($N_{0s} \sim 10^{15}$ cm^{-2}) at the interface; however, the degree of their manifestation depends on the ion bonding energy at the interface (Fig. 4) and becomes negligible even for $\Delta E_i \gtrsim 0.1$ eV (curve *3*). It should be noted that, under actual conditions, an increase in concentrations is limited by the effect of stresses on the ion bonding energy. The source of stresses can be the ions themselves, a mismatch of lattices at the interface, and other factors. In particular, the attainment of high surface ion concentrations ($N_{ss} \gtrsim 10^{12}$ cm^{-2}) can be hampered.

In study [17], the authors investigated the samples in which the number of ions corresponding (as to a peak area) to the trap peak (~10^{12}–10^{13} cm^{-2}) is an order of magnitude larger than their number in the conventional peak. Such a relation corresponds to the case of a high density of states ($N_{0s} \approx N_s$). In this case, the width of the trap peak is noticeably larger than that of the conventional peak. This fact may be associated with the nonequilibrium character of the process (high β_V) and with a spread in the surface-state level energies.

The model under consideration is consistent with experimental data [9, 17]. For a more detailed comparison, it is necessary to take the charge incorporated in the insulator into account, as well as the spreading of trap levels and excited ion states, the potential of image forces; surface inhomogeneities (in particular, dipole spots [6, 18]), and other important factors. Special attention is required for the experimental analysis of the obscuring effect of the semiconductor on the *I–V* char-

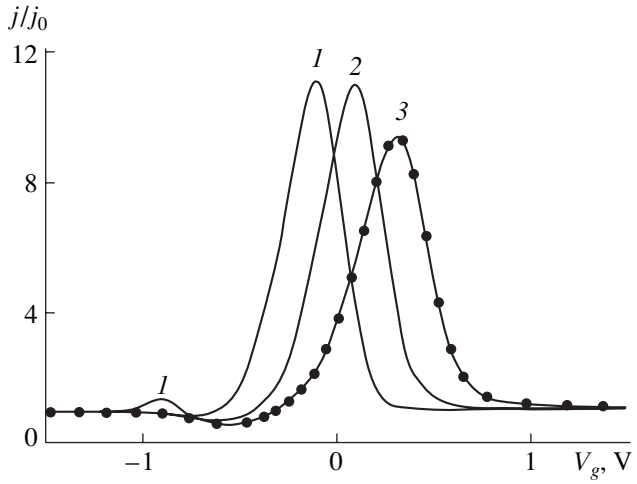

Fig. 4. Effect of the ion–interface bonding energy on the *I–V* characteristics $j(V_g)$ of ion currents. ΔE_i = (*1*) –0.5, (*2*) –0.3, (*3*) 0.1 eV; $N_{0s} = 10^{15}$ cm^{-2}, and j_0 is the capacitance current in the film. The dots correspond to $N_{0s} = 0$, $N_0 = 3 \times 10^{22}$ cm^{-3}, $N_s = 10^{12}$ cm^{-2}, $d = 1000$ Å, and $T = 500$ K.

acteristic $j(V_g)$ being measured. These data will be published in a future publication.

5. CONCLUSION

We presented the results of calculating the quasi-steady *I–V* characteristics for ion currents in MIS structures with ion surface states (traps) at the semiconductor–insulator interface (Figs. 1 and 2). The population f_i of surface traps is described by the Gibbs distribution (3) (*Appendix*), because the probability of their population can be appreciable [$f_i \approx 1$ (Fig. 3)] if the trap concentration N_{0s} is not high, i.e., $N_{0s} \lesssim N_s$. For low N_{0s}, $N_{0s} < N_s$, there are two ion peaks in the *I–V* characteristics and a capacitance dip (Fig. 2). In the case of high N_{0s}, $N_{0s} \gtrsim N_s$, there is only a single peak with a capacitance dip (Fig. 1). The "trap" peak is associated with the "emission" of ions from the traps, and the second (conventional) peak is related to the drift of ions in the film. The ion capture by the surface states leads to the emergence of characteristic features in the voltage dependence $\varphi_s(V_g)$ of the surface potential (Fig. 3). For a low ion-bonding energy at the interface ($\Delta E_i \gtrsim 0.1$ eV), the effect of surface states is minimal even for high (on the order of atomic) concentrations of ion surface states ($N_{0s} \sim 10^{15}$ cm^{-2}) (Fig. 4).

The intrinsic surface states for ions at the Si–SiO_2 interface do not manifest themselves. The large trap peaks in the experimental *I–V* characteristics [17] correspond to a high density of defect ion traps ($N_{0s} \gtrsim 10^{12}$ cm^{-2}) in a narrow region near the interface.

APPENDIX

THE GIBBS DISTRIBUTION FOR IONS

The Gibbs distribution in its most general form (for subsystems with a variable particle number N) describes the probability w_{nN} of occupation of N-particle states with an energy E_{nN} (n is the number of an energy level) in the form

$$w_{nN} = A\exp\left(\frac{\mu N - E_{nN}}{kT}\right), \qquad \text{(A.1)}$$

where $\mu = (\partial F/\partial N)_{T, V}$ is the chemical potential (F is the free energy and V is the volume), and A is the normalization factor [13, 19], which is determined from the condition that the total probability of finding a subsystem in even a single state (also including the unoccupied ones) is equal to unity: $\sum_{n, N} w_{nN} = 1$. Because each state of an ion in a lattice can be occupied by only a single ion, for a subsystem containing only the states of interest with a single energy level (bonding energy) E_i, the normalization condition leads to the following energy-distribution function:

$$f_i = \frac{g_1\exp[(F_i - E_i)/kT]}{g_0 + g_1\exp[(F_i - E_i)/kT]} = \frac{1}{1 + (g_0/g_1)\exp[(E_i - F_i)/kT]}, \qquad \text{(A.2)}$$

where g_0 and g_1 are the degeneracy multiplicities for unoccupied and occupied states, respectively; the energy E_i is counted from the energy of the unoccupied state; and F_i is the chemical potential of ions. Distribution (A.2) has the same form as the electron distribution over defect levels in a semiconductor [15, 16], i.e., the form of the Fermi distribution, and, if $g_0 = g_1 = 1$, (A.2) coincides (formally) with this distribution. Therefore, the quantity F_i is also named the Fermi level. In the case of interstitial diffusion, we may expect that $g_0 = g_1 = 1$. If the ion states are induced by defects (for example, vacancies), then these factors can also differ from unity. The probability of the occurrence of an unoccupied state is $f_0 = 1 - f_i$. If there is an electric field in the sample, the energy E_i is replaced by the total ion energy $E_i + q\varphi(z)$ in the field [see (3)], and the chemical potential (the Fermi level) is also referred to as the electrochemical potential. In this case, the Fermi level is constant over the entire system [13], so that the Fermi levels for different subsystems (for example, for ions in the insulator bulk and those at the interface) coincide.

REFERENCES

1. J. P. Stark, *Solid State Diffusion* (Wiley, New York, 1976; Énergiya, Moscow, 1980).
2. E. R. Nicollian and J. R. Brews, *MOS (Metal–Oxide–Semiconductor) Physics and Technology* (Wiley, New York, 1982).
3. T. Bechshtedt and R. Enderlein, *Semiconductor Surfaces and Interfaces. Their Atomic and Electronic Structures* (Akademie-Verlag, Berlin, 1988; Mir, Moscow, 1990).
4. *Thin Films: Interdiffusion and Reactions*, Ed. by J. M. Poate, K. Tu, and J. Meier (Wiley, New York, 1978; Mir, Moscow, 1982).
5. T. Ando, A. B. Fowler, and F. Stern, Rev. Mod. Phys. **54**, 437 (1982); T. Ando, A. B. Fowler, and F. Stern, *Electronic Properties of Two-dimensional Systems* (Mir, Moscow, 1985).
6. S. G. Dmitriev and Yu. V. Markin, Fiz. Tekh. Poluprovodn. (St. Petersburg) **30**, 1231 (1996) [Semiconductors **30**, 649 (1996)].
7. S. G. Dmitriev and Yu. V. Markin, Fiz. Tekh. Poluprovodn. (St. Petersburg) **32**, 1439 (1998) [Semiconductors **32**, 1284 (1998)].
8. S. G. Dmitriev and Yu. V. Markin, Fiz. Tekh. Poluprovodn. (St. Petersburg) **34**, 970 (2000) [Semiconductors **34**, 931 (2000)].
9. S. G. Dmitriev and Yu. V. Markin, Fiz. Tekh. Poluprovodn. (St. Petersburg) **35**, 192 (2001) [Semiconductors **35**, 185 (2001)].

10. A. G. Tangena, J. Middelhoek, and N. F. de Rooij, J. Appl. Phys. **49**, 2876 (1978).
11. V. P. Romanov and Yu. A. Chaplygin, Phys. Status Solidi A **53**, 493 (1979).
12. V. V. Gavrilovets, V. B. Bondarenko, Yu. A. Kudinov, and V. V. Korablev, Fiz. Tekh. Poluprovodn. (St. Petersburg) **34**, 455 (2000) [Semiconductors **34**, 441 (2000)].
13. L. D. Landau and E. M. Lifshitz, *Course of Theoretical Physics*, Vol. 5: *Statistical Physics* (Nauka, Moscow, 1976; Pergamon, Oxford, 1980), Part I.
14. E. M. Lifshitz and L. P. Pitaevskiĭ, *Physical Kinetics* (Nauka, Moscow, 1979; Pergamon, Oxford, 1981).
15. S. Sze, *Physics of Semiconductor Devices* (Wiley, New York, 1981; Mir, Moscow, 1984).
16. V. L. Bonch-Bruevich and S. G. Kalashnikov, *Physics of Semiconductors* (Nauka, Moscow, 1990).
17. A. G. Tangena, N. F. de Rooij, and J. Middelhoek, J. Appl. Phys. **49**, 5576 (1978).
18. S. G. Dmitriev and Yu. V. Markin, Radiotekh. Élektron. (Moscow) **45**, 220 (2000).
19. C. Kittel, *Thermal Physics* (Wiley, New York, 1973; Nauka, Moscow, 1977).

Translated by V. Bukhanov

Semiconductors, Vol. 36, No. 2, 2002, pp. 203–207. Translated from Fizika i Tekhnika Poluprovodnikov, Vol. 36, No. 2, 2002, pp. 211–215.
Original Russian Text Copyright © 2002 by Bumaĭ, Gobsch, Goldhahn, Stein, Golombek, Nakov, Cheng.

LOW-DIMENSIONAL SYSTEMS

Photoluminescence of Anti-Modulation-Doped GaAs/AlGaAs Single Quantum Well Structures Exposed to Hydrogen Plasma

Yu. A. Bumaĭ*, G. Gobsch, R. Goldhahn**, N. Stein**, A. Golombek**, V. Nakov**, and T. S. Cheng*****

** Belarussian State Polytechnical Academy, Minsk, 220027 Belarus*

*** Institut für Physik, Technische Universität Ilmenau, PSF 327, D-98684 Ilmenau, FRG*

**** School of Physics and Astronomy, University of Nottingham, Nottingham NG7 2RD, UK*

Submitted January 30, 2001; accepted for publication May 25, 2001

Abstract—Techniques of low-temperature photoluminescence (PL), photoluminescence excitation, and photoreflectance were used to study the effect of hydrogen plasma treatment at 260°C on antimodulation Si-doped GaAs/AlGaAs heterostructures with near-surface single quantum wells (QWs) grown by molecular-beam epitaxy. It was found that, in the case of excitation below the AlGaAs band gap, exciton PL from the QW is quenched due to an increase in the electric field in the structure. The reason for this is that the passivation of surface states by hydrogen results in the Fermi level depinning from the midgap of the nominally undoped *p*-type GaAs cap layer, while shallow-level impurities present in the layers of the structure are not neutralized (their complexes with hydrogen dissociate under the influence of illumination and strong electric fields). © *2002 MAIK "Nauka/Interperiodica".*

1. INTRODUCTION

Passivation of deep-level defects and shallow-level impurities by atomic hydrogen, which takes place under hydrogen plasma treatment, can be used to improve the optical properties of a wide range of semiconductor heterostructures. In particular, most of the studies indicate that exposure of GaAs/AlGaAs heterostructures with quantum wells (QWs) to hydrogen plasma leads to improved luminescence characteristics due to passivation of nonradiative recombination centers in epitaxial layers and at heterointerfaces [1]. A significant increase in luminescence intensity after plasma hydrogenation was reported, for example, for multiple-QW GaAs/AlGaAs structures [2, 3] and short-period GaAs/AlAs superlattices [4]. Luminescence enhancement due to surface-state passivation was also observed in the structures with near-surface QWs upon exposure to a low-energy hydrogen-ion beam [5].

To reduce radiation damage to the surface layers, hydrogen ions of low energy (below 100 eV) are commonly used for defect passivation in GaAs and AlGaAs [1]. Meanwhile, hydrogen's ability to passivate most of the deep-level defects in these materials [1, 6] makes it possible to use plasma treatments with ion energies exceeding the threshold energy of intrinsic-defect formation. At the same time, photoluminescence (PL) studies of epitaxial GaAs layers on semi-insulating substrates gave evidence that, even with low-energy ions, pronounced hydrogenation of the material (with H dose in excess of $\approx 10^{19}$ cm^{-2}) results in hydrogen accumulation at the interface between the substrate and the epilayer and in the appearance of strong electric fields, which quench exciton luminescence [7]. Degradation of GaAs/AlGaAs heterointerfaces due to Al/Ga intermixing upon prolonged hydrogenation was noted in [8], and deterioration of the device parameters upon structure treatment in H-containing plasma under high energy densities was observed in [9].

In this paper, we report the results of studying the influence of hydrogenation, introduced by H-plasma exposure, on the low-temperature PL of antimodulation-doped structures with near-surface single QW. It is shown that, for these structures, a positive effect associated with hydrogenation, i.e., surface state passivation, can lead to the emergence of strong built-in electric fields, which quench the radiative recombination of excitons.

2. EXPERIMENTAL

Two GaAs/AlGaAs structures (NU790 and NU 791), grown by molecular-beam epitaxy (MBE) on semi-insulating (100)-oriented GaAs substrates, were studied. They contain the following layers: a 1-μm-thick GaAs buffer, the first $Al_{0.33}Ga_{0.67}As$ barrier of thickness L_{b1} = 0.5 μm, the GaAs QW, the second $Al_{0.33}Ga_{0.67}As$ barrier of thickness L_{b2} = 15 nm, and a GaAs cap layer of thickness L_{cap} = 20 nm. The QW width L_z was 6.2 and 4.3 nm for the structures NU790 and NU791, respec-

1063-7826/02/3602-0203$22.00 © 2002 MAIK "Nauka/Interperiodica"

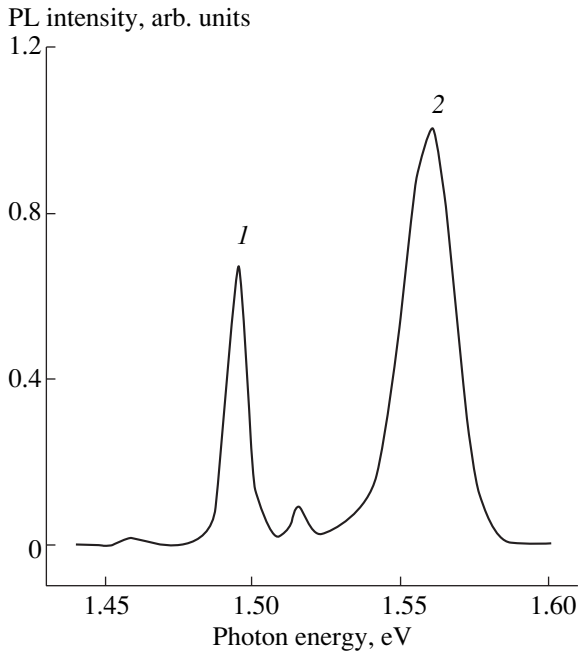

Fig. 1. Photoluminescence spectrum of as-grown structure NU790 at $T = 5$ K under 720-nm excitation: (*1*) bulk GaAs line and (*2*) QW line.

tively. The central part of the QW (one-third of its thickness) was doped with Si to a concentration of 1.0×10^{16} cm^{-3}. Other layers of the structure were nominally undoped.

Structure hydrogenation was carried out using 10-min exposure to H plasma in a dc glow discharge of low power density at a temperature of 260°C in a reactor with parallel electrodes. The voltage between the electrodes was 375 ± 25 V, and the current density was 25 μA/cm^2. The samples were mounted directly at the cathode. The corresponding H dose ($\approx 5 \times 10^{16}$ cm^{-2}) can be estimated approximately as half of the number of charge carriers passed through the electrodes.

The structures were characterized before and after plasma exposure by PL, PL excitation (PLE), and photoreflectance spectra measured at 5 K. The luminescence was excited by an Ar-ion laser (with a wavelength of 488 nm and a power of 13–200 mW) or by a Ti:Al_2O_3 laser (a wavelength of 720 nm and a power of 100–300 mW). The laser radiation was focused onto the samples in ≈0.2-mm-diameter spot. The PLE spectra were recorded using the tunable Ti:Al_2O_3 laser. In the photoreflectance studies, an Ar-laser beam was used to modulate the sample reflectance. Analysis of the PL data obtained with 488-nm (both the QWs and the barriers are excited) and with 720-nm (only the QWs are excited) lasers makes it possible to separate the effects related to the barriers and to the QWs. When the PL is excited by 488-nm radiation, nearly flat-band conditions can be attained.

3. RESULTS AND DISCUSSION

The PL spectrum of an as-grown NU790 structure under 720-nm excitation is shown in Fig. 1. Three intense lines are clearly observed. A high-intensity band at 1.495 eV corresponds to an electron transition e-A^0 from the conduction band to the carbon acceptor level C_{As} in the GaAs cap and buffer layers. The band peaked at 1.515 eV originates from unresolved free and bound exciton emission in GaAs layers. The most intense and broad band around 1.560 eV is related to the QW emission. Similar spectra were recorded for the structure NU791, the only difference being the position of the QW line (1.616 eV). It can be concluded from the spectra that, in these structures, a considerable amount of carbon (which is the typical background MBE impurity) is present in the GaAs layers. It should be noted that an intense e–C_{As} line is also observed in the PL from AlGaAs layers excited by 488-nm radiation. The presence of residual carbon results in *p*-type conductivity of nominally undoped GaAs and AlGaAs layers, while the central one-third of the QW is *n*-type doped. The broad QW luminescence band, which is dominant in the PL spectrum for $\lambda_{exc} = 720$ nm, is related to electron transitions from the first electron subband to residual C_{As} shallow acceptor levels in the QW ($1e$-A^0_{QW} band). The line width is mainly determined by the difference between the acceptor ionization energy at the center of the QW and near the heterointerface [10, 11]. The position and the width of this line depend on the excitation level. This results from variation in the overlap between the spatial distributions of the nonequilibrium charge carriers and the acceptors under the presence of nonuniform electric field. Such factors as close proximity to the surface, residual doping of the barriers, and the QW doping contribute to the field strength and spatial profile.

The QW luminescence spectra under 720-nm and 488-nm excitation and the PLE spectra of the structure NU790, recorded before and after the sample was exposed to plasma, are shown in Fig. 2. First, consider the spectra of the as-grown structure (Fig. 2a). In the PL spectrum obtained with $\lambda_{exc} = 720$ nm (curve *1*), emission originating from $1e$-A^0_{QW} transitions is dominant. Under the higher excitation level achieved in the case of $\lambda_{exc} = 488$ nm (curve *2*), another line, related to the transitions between the shallow donor level of the Si_{Ga} impurity and the first heavy-hole subband (D^0_{QW}-$1hh$ line) [12–14], is also observed. Despite the fact that the QW emission lines are broad and no evidence of exciton luminescence can be seen, the PLE spectrum (represented by curve *3*) contains two sharp peaks corresponding to the excitonic transitions between the first heavy- and light-hole and first electron QW subbands (peaks $1e$–$1hh$ and $1e$–$1lh$, respectively). Similar observations can be made about the spectra of the NU791 structure with a narrower QW (Fig. 3), only the

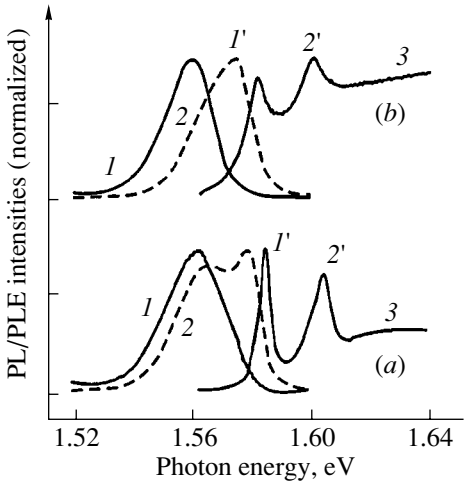

Fig. 2. (*1*, *2*) Photoluminescence and (*3*) photoluminescence excitation spectra of the QWs in (*a*) as-grown and (*b*) hydrogenated structure NU790 at 5 K; curves (*1*) and (*2*) correspond to the PL excitation at 720 and 488 nm, respectively. Peaks in the PLE spectra originate from excitonic transitions (*1*') 1*e*–1*hh* and (*2*') 1*e*–1*lh*.

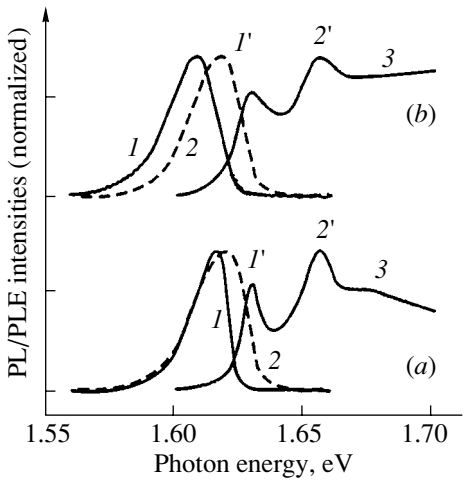

Fig. 3. (*1*, *2*) Photoluminescence and (*3*) photoluminescence excitation spectra of the QWs in (*a*) as-grown and (*b*) hydrogenated structure NU791 at 5 K; curves (*1*) and (*2*) correspond to the PL excitation at 720 and 488 nm, respectively. Peaks in the PLE spectra originate from excitonic transitions (*1*') 1*e*–1*hh* and (*2*') 1*e*–1*lh*.

ratio between the 1*e*–1*hh* and 1*e*–1*lh* peak intensities being different. Relatively low intensities of excitonic peaks in the PLE spectra (implying low oscillator strength of excitonic transitions) is evidence of a stronger electric field within the QW of the NU791 structure in comparison to NU790.

After the samples were exposed to hydrogen plasma, the peak intensity of the $1e\text{-}A^0_{QW}$ line in the PL spectra recorded at λ_{exc} = 720 nm increased somewhat (nearly by a factor of 2) for NU790 and remained virtually unchanged for NU791. At the same time, in the spectra recorded at λ_{exc} = 488 nm, the PL intensity increased significantly (about eight times) for NU790 and to a lesser extent (about two times) for NU791. Both impurity transitions are enhanced, and the D^0_{QW}-1*hh* transition becomes dominant. Additional investigation of the barrier PL under 488-nm excitation revealed a strong increase in the intensity of the dominant e–C_{As} transition in AlGaAs layers in the NU790 structure (by more than an order of magnitude) and a much slighter increase in the NU791 structure (nearly by a factor of 1.5). This means that atomic hydrogen passivates deep-level defects in the barrier layers (rather than at hetero-interfaces), which leads to an increase in the lifetime of the charge carriers in the structure. This results in an increase in the number of photoexcited carriers that reach the QW.

Hydrogenation can lead both to a decrease (in the case of sample NU790) and to an increase (in the case of sample NU791) in the width of the PL line corresponding to $1e\text{-}A^0_{QW}$ transitions (Figs. 2, 3, curves *1*). At the same time, the clear low-energy shift of the line peaks is common to the spectra of both samples. Hydrogen treatment of sample NU790 also results in a pronounced low-energy shift of the excitonic transitions in the PLE spectrum. Such a shift is typical of the Stark effect; i.e., it is related to an enhancement of the electric field in the QW. An increase in the field strength causes a large reduction in intensities of the excitonic peaks in the PLE spectra, especially, of the 1*e*–1*hh* peak. A decrease in the oscillator strength of excitonic transitions after hydrogenation can also be seen in the PLE spectra of the NU791 structure. However, no detectable energy shift is observed, most probably, because of a much lower value of the Stark shift for narrow QWs (in weak electric fields, $\Delta E \propto L_z^4$).

Photoreflection measurements also confirm that electric fields in the samples are enhanced after exposure to plasma. The PR spectrum of as-grown sample NU790, presented in Fig. 4, contains two groups of oscillations. One of them, with a dominating excitonic component, originates from the E_0 transition in bulk GaAs, and the other is due to the QW. After hydrogenation, the bulk GaAs-related PR feature is reduced in amplitude somewhat and its shape changes, which is most likely due to the appearance of strain in the buffer layer. The amplitude of the QW-related signal increases heavily, and its spectrum widens appreciably, which indicates that there is a strong electric field in the QW.

Thus, the results obtained indicate that exposure of the structures to hydrogen plasma has two main effects:

(a) the integrated PL intensity from the QWs increases significantly only when the barrier layers are photoexcited, and

(b) electric fields in the QWs are enhanced.

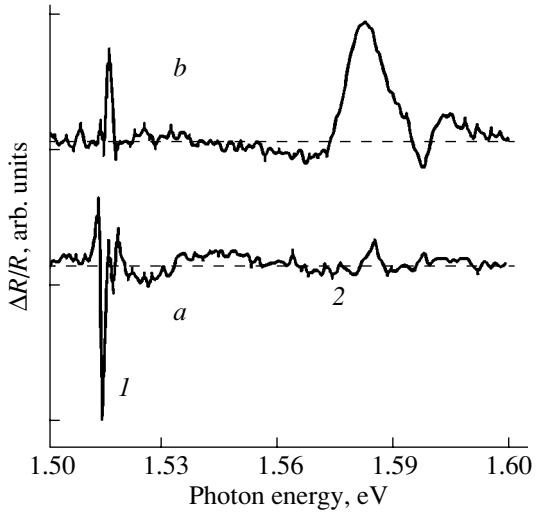

Fig. 4. Photoreflectance spectra of (*a*) as-grown and (*b*) hydrogenated structure NU790 at 5 K. Features (*1*) and (*2*) correspond to bulk GaAs and to the QW, respectively.

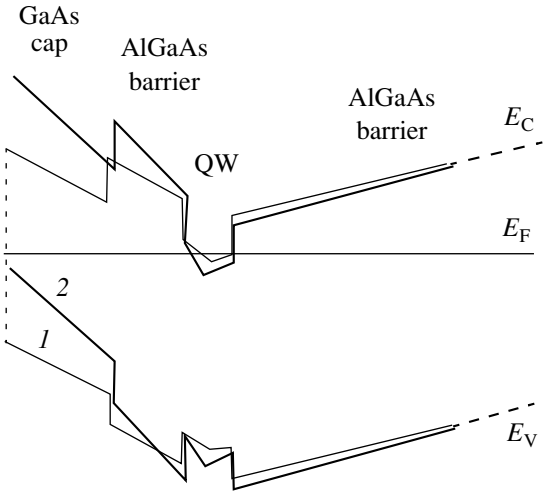

Fig. 5. Schematic energy-band diagram of anti-modulation-doped GaAs/AlGaAs structure (*1*) before and (*2*) after hydrogenation.

The first effect occurs due to the ability of atomic hydrogen to passivate deep-level defects in epilayers (in this case, in the barrier layers), which results in an enhanced recombination lifetime of the charge carriers in the structure [1]. Observation of the second effect is at variance with other results found in the literature: it is commonly reported that the intensity of luminescence from near-surface QWs increases due to a reduction in the strength of electric fields in the structure (see, e.g., [5]). It is known that the Fermi level at the surface of GaAs is pinned approximately at the midgap, which is related to the high density of surface states [15]. This results in the emergence of an electric field near the surface, which reduces the PL intensity from the QWs located in the surface-field region due to a decrease in the optical-transition oscillator strengths under the conditions of the quantum-confined Stark effect and due to exciton dissociation [16]. Nevertheless, we believe it is the surface-state passivation that causes the observed increase in surface electric field strength in antimodulation-doped structures. The reason for this effect is the fact that residual shallow-level impurities in undoped parts of the structure are not neutralized by atomic hydrogen. Unlike the more stable complexes of H atoms with deep-level impurities, complexes formed with shallow-level impurities dissociate rapidly under the influence of both strong built-in electric fields and illumination of the sample, resulting in the appearance of nonequilibrium charge carriers (in particular, under PL excitation) [1]. A decrease in the surface state density leads to depinning of the Fermi level from the midgap and its shift to the position of the acceptor level in the *p*-type CaAs cap layer. This gives rise to additional band bending and, consequently, to an enhancement of the surface electric field (see Fig. 5). Enhancement of the field by hydrogenation entails further quenching of exciton transitions, which can be seen from the PLE spectra (Figs. 2, 3, curves *3*).

It follows from the above discussion that neutralization by atomic hydrogen of residual carbon impurities present in the structure layers with no intentional doping could enhance the excitonic PL from the QWs. However, such neutralization was not observed. Assuming the diffusion coefficient of an H atom to be $D_H = 2.9 \times 10^{-10}$ cm^2 s^{-1} (the value characteristic of undoped GaAs at 260°C), we find that the diffusion length $L_H = (D_H t)^{0.5}$ for a 10-min-long plasma treatment is ≈4 μm. Thus, under the given hydrogenation conditions, hydrogen penetrates into the structure down to the substrate. Its concentration can be sufficiently high, since the dose of incorporated H atoms exceeds 10^{16} cm^{-2}. The absence of neutral C^-–H^+ and Si^+–H^- complexes is probably related to their dissociation, facilitated by the existence of strong built-in electric fields and by the sample illumination. Dissociation of neutral complexes formed by hydrogen with shallow-level impurities and drift of the H atoms from the high-field region were observed, for instance, in GaAs structures with Schottky barriers [1]. An order-of-magnitude estimation of electric-field strengths in the upper and lower barrier layers of as-grown structures, obtained by the expressions $F \approx 0.5E_g/(L_{b2} + L_{cap})$ and $F \approx E_g/L_{b1}$ (where E_g is the GaAs band gap), yields the values of ≈200 and ≈30 kV/cm, respectively. Obviously, such fields are strong enough to enhance dissociation of a complex [1].

We also studied the effect of plasma treatment under the conditions of increased H ion energies (up to 400 eV) exceeding the threshold for the formation of point defects in GaAs. TRIM calculations [17] indicate that the H ions with such energies can produce point

defects only in the cap GaAs layer of the structure. However, intrinsic defects in GaAs have high mobility even at low treatment temperatures. Typically, the QW luminescence efficiency in GaAs/AlGaAs structures can be significantly affected by point defects within a range of ≈100 nm, according to ion etching experiments [18, 19]. In the case under study, we did not observe degradation of the PL either in the barriers or in the QWs. This can probably be explained by the hydrogen passivation of most of the radiation defects induced by plasma treatment. It may be argued that slight radiation damage does takes place near the surface, as is shown by the appearance of a weak e-V_{Ga} line (≈1.48 eV) in the spectra of GaAs layers of plasma-treated structures (this line is usually observed as a result of exposure to radiation [20]).

4. CONCLUSION

Thus, we reported the results of low-temperature (T = 5 K) studies of the PL, PLE, and photoreflection spectra for MBE-grown antimodulation Si-doped GaAs/AlGaAs single QW structures exposed to hydrogen plasma.

In the PL spectra of QWs in as-grown structures under 720-nm excitation, transition from the conduction band to the carbon acceptor level ($1e$-A^0_{QW}) dominates. Under 488-nm excitation, both $1e$-A^0_{QW} and D^0_{QW}-$1hh$ transitions, related to C_{As} and Si_{Ga} impurities, were observed. Excitonic $1e$–$1hh$ and $1e$–$1lh$ transitions were present only in the PLE spectra. Exposure of the structures to hydrogen plasma resulted in a large increase in the intensities of $1e$-A^0_{QW} and D^0_{QW}-$1hh$ transitions only under the above-barrier PL excitation. The increase is due to passivation of deep-level defects in AlGaAs barrier layers by hydrogen. At the same time, the intensity of excitonic transitions was reduced. Analysis of the PLE and photoreflection spectra indicates that the electric field in the surface region of the structures was enhanced after their exposure to plasma.

An increase in the electric-field strength in antimodulation-doped QW structures after plasma treatment occurs due to the fact that the surface states are passivated by atomic hydrogen, while the shallow-level impurity states in the structure epilayers are not, which is caused by the dissociation of hydrogen–impurity complexes. This results in the depinning of the Fermi level at the surface from the middle of the band gap and its shift to the energy position of the acceptor level in the nominally undoped p-type GaAs cap layer.

REFERENCES

1. S. J. Pearton, Mater. Sci. Forum **148/149**, 393 (1994).
2. L. Pavesi, F. Martelli, D. Martin, and F. K. Reinhart, Appl. Phys. Lett. **54**, 1522 (1989).
3. J. M. Zavada, F. Voillot, N. Lauert, *et al.*, J. Appl. Phys. **73**, 8489 (1993).
4. R. Fisher, G. Peter, E. O. Göbel, *et al.*, Appl. Phys. Lett. **60**, 2788 (1992).
5. Y.-L. Chang, I.-H. Tang, Y.-H. Zhang, *et al.*, Appl. Phys. Lett. **62**, 2697 (1993).
6. J. Chevallier, B. Clerjand, and B. Pajot, in *Semiconductors and Semimetals* (Academic, San Diego, 1991), Vol. 34, p. 447.
7. F. Sarto, M. Capizzi, and A. Frova, Semicond. Sci. Technol. **8**, 1231 (1993).
8. P. O. Holz, A. C. Ferreira, Q. X. Zhao, B. Monemar, M. Sundaram, K. Campman, J. L. Merz, and A. C. Gossard, *Shallow-Level Centers in Semiconductors* (North-Holland, Amsterdam, 1996), p. 67.
9. T. Maeda, J. W. Lee, C. R. Abernathy, *et al.*, Mater. Res. Soc. Symp. Proc. **510**, 209 (1998).
10. W. T. Masselink, Yia-Chung Chang, and H. Morkoc, Phys. Rev. B **32**, 5190 (1985).
11. G. C. Rune, P. O. Holtz, M. Sundaram, *et al.*, Phys. Rev. B **44**, 4010 (1991).
12. L. E. Oliveira and G. D. Mahan, Phys. Rev. B **47**, 2406 (1993).
13. D. C. Reynolds, C. E. Leak, K. K. Bajaj, *et al.*, Phys. Rev. B **40**, 6210 (1989).
14. J. A. Brum, C. Priester, and G. Allan, Phys. Rev. B **32**, 2378 (1985).
15. M. D. Pashley, K. W. Haberern, R. M. Feenstra, and P. D. Kirchner, Phys. Rev. B **48**, 4612 (1993).
16. C. Weisbuch and B. Vinter, *Quantum Semiconductor Structures: Fundamentals and Applications* (Academic, San Diego, 1991).
17. *Handbook of Ion Implantation Technology*, Ed. by J. F. Ziegler (North-Holland, Amsterdam, 1992).
18. H. F. Wong, D. L. Green, T. Y. Liu, *et al.*, J. Vac. Sci. Technol. B **6**, 1906 (1988).
19. R. Germann, A. Forchel, M. Bresch, and H. P. Meier, J. Vac. Sci. Technol. B **7**, 1475 (1989).
20. S. M. Khanna, A. Jorio, C. Carlone, *et al.*, IEEE Trans. Nucl. Sci. **42**, 2095 (1995).

Translated by M. Skorikov

Semiconductors, Vol. 36, No. 2, 2002, pp. 208–212. Translated from Fizika i Tekhnika Poluprovodnikov, Vol. 36, No. 2, 2002, pp. 216–220.
Original Russian Text Copyright © 2002 by Krevchik, Levashov.

LOW-DIMENSIONAL SYSTEM

Energy Spectrum and Optical Properties of the Quantum Dot–Impurity Center Complex

V. D. Krevchik and A. V. Levashov

Penza State University, Penza, 440017 Russia

Submitted December 5, 2000; accepted for publication June 3, 2001

Abstract—The impurity absorption of light in the quantum dot (QD) with a spherically symmetric potential has been considered within the framework of the zero-range potential model in the effective mass approximation. The dynamics of formation of the localized D^- state as a superposition of QD states with different orbital quantum number values is demonstrated. The impurity absorption coefficient is calculated taking into account the QD size dispersion, which leads to broadening of discrete impurity absorption lines. Numeric estimates of the D^- state binding energy and the impurity absorption coefficient are presented for the heterophase QD system ⟨CdS⟩–⟨transparent silicate glass matrix⟩. The sensitivity of the impurity absorption edge to the impurity level depth and to the mean QD radius was studied. © *2002 MAIK "Nauka/Interperiodica".*

1. Optical properties of semiconductor quantum dots (QD) synthesized in a glass matrix are of interest for the development of new optoelectronic devices [1]. Currently, the most pressing problem of the optics of such structures is the reliable identification of optical transitions. Such identification was carried out using calculation of the corresponding oscillator strengths for the band-to-band light absorption by the spherically symmetric QD [2, 3]. Development of the delta-doping technique (see review in [4]) evoked significant interest in the study of impurity light absorption in structures with QDs. In this paper, we study the effect of the positional disorder due to the presence of impurity centers in QDs synthesized in a transparent dielectric matrix. The QD is described within the framework of the spherically symmetric well model ("hard-wall" model). The zero-range potential model is used for the impurity center [5–8]. The impurity absorption coefficient is calculated in the effective mass approximation with account of the QD size dispersion described by the Lifshits–Slezov formula [9].

2. Let us consider the positional disorder effect in the spherically symmetric QD. We assume that the impurity center is located in the point $\mathbf{R}_a = (x_a, y_a, z_a)$, and the energy is reckoned from the bottom of the spherically symmetric potential well. The Lippmann–Schwinger equation for the bound state reads

$$\Psi_\lambda(\mathbf{r}, \mathbf{R}_a) = \int d\mathbf{r}_1 G(\mathbf{r}, \mathbf{r}_1; E_\lambda) V_\delta(\mathbf{r}, \mathbf{R}_a) \Psi_\lambda(\mathbf{r}_1, \mathbf{R}_a), \quad (1)$$

where $\Psi_\lambda(\mathbf{r}, \mathbf{R}_a)$ is the wave function of the electron localized by the short-range potential, $E_\lambda = -\hbar^2\lambda^2/2m^*$ is the binding energy for the impurity center, m^* is the electron effective mass, $V_\delta(\mathbf{r}, \mathbf{R}_a)$ is the zero-range potential with strength $\gamma = 2\pi/\alpha$,

$$V_\delta(\mathbf{r}, \mathbf{R}_a) = \gamma\delta(\mathbf{r} - \mathbf{R}_a)[1 + (\mathbf{r} - \mathbf{R}_a)\nabla_\mathbf{r}], \quad (2)$$

the parameter α is determined by the binding energy E_i of the localized electron state for the same impurity center in a bulk semiconductor, and $G(\mathbf{r}, \mathbf{r}_1: E_\lambda)$ is the one-electron Green's function for a source in the point $\mathbf{R}_a$ and energy E_λ,

$$G(\mathbf{r}, \mathbf{r}_1; E_\lambda) = \sum_{l=0}^{\infty}\sum_{n=1}^{\infty}\sum_{m=-l}^{l} \frac{4m^*}{\hbar^2} \frac{J_{l+1/2}(X_{n,l}r/R_0)J_{l+1/2}(X_{n,l}r_1/R_0)}{J^2_{l+3/2}(X_{n,l})(rr_1)^{1/2}[(i\lambda R_0)^2 - X^2_{n,l}]} \times Y_{l,m}(\theta, \varphi)Y_{l,m}(\theta_1, \varphi_1). \quad (3)$$

Here, $J_\nu(z)$ is the half-integer-order Bessel function of the first kind; $Y_{l,m}(\theta, \varphi)$ are spherical harmonics; $X_{n,l}$ is the n-th root of the Bessel function of the order $l + 1/2$; l and m are, respectively, the orbital and magnetic quantum numbers; $E_{n,l} = \hbar^2 X^2_{n,l}/2m^*R_0^2$ is the electron energy in the spherically symmetric potential well; R_0 is the QD radius; and r, θ, and φ are spherical coordinates.

Summation in (3) over m and n can be done using known relations [10]:

$$\sum_{m=-l}^{l} Y_{l,m}(\theta_1, \varphi_1)Y^*_{l,m}(\theta_2, \varphi_2) = \frac{2l+1}{4\pi}P_l(\cos w), \quad (4)$$

$$\sum_{n=1}^{\infty}\frac{J_\nu(x, X_{n,l})J_\nu^*(X, X_{n,l})}{J_{\nu+1}^2(X_{n,l})(z^2 - X_{n,l}^2)} = \frac{\pi J_\nu(x, z)}{4J_\nu(z)}[J_\nu(z)N_\nu(X, z) - J_\nu(X, z)N_\nu(z)], \quad (5)$$

where $\cos w = \cos\theta_1\cos\theta_2 + \sin\theta_1\sin\theta_2\cos(\varphi_1 - \varphi_2)$, $0 \le x \le X$, $X \le 1$. As a result, we obtain

$$G(\mathbf{r}, \mathbf{r}_1; E_\lambda) = \frac{m^*}{2\pi\hbar^2} \times\left[-\pi\sum_{l=0}^{\infty}\frac{(-1)^l(l+1/2)P_l(\cos w)J_{l+1/2}(i\lambda r_1)J_{-l-1/2}(i\lambda r_2)}{(r_1 r_2)^{1/2}} \times\frac{N_{l+1/2}(i\lambda R_0)}{J_{l+1/2}(i\lambda R_0)}\right], \quad (6)$$

where $N_{l+1/2}(z)$ is a half-integer-order Neumann function. Then, taking into account that [10]

$$\sum_{l=0}^{\infty}(-1)^l(l+1/2)P_l(\cos w)J_{l+1/2}(z)J_{-l-1/2}(Z) = \frac{R^{-(l+1/2)}J_{-l-1/2}(R)}{\Gamma(l+1/2)2^{l+1/2}}(zZ)^{l+1/2}, \quad (7)$$

where $R = \sqrt{z^2 + Z^2 - 2zZ\cos w}$, we obtain

$$G(\mathbf{r}, \mathbf{r}_1; E_\lambda) = \frac{m^*}{2\pi\hbar^2}\left[-\frac{\cosh\lambda R}{R} - \frac{\pi}{2}\sum_{l=0}^{\infty}(2l+1) \times\frac{J_{l+1/2}(i\lambda r)J_{l+1/2}(i\lambda r_1)N_{l+1/2}(i\lambda R_0)}{J_{l+1/2}(i\lambda R_0)}\frac{P_l(\cos w)}{(rr_1)^{1/2}}\right]. \quad (8)$$

Isolating the diverging part in (8), we obtain

$$G(\mathbf{r}, \mathbf{R}_a; E_\lambda) = G_0(\mathbf{r}, \mathbf{R}_a; E_\lambda) + G_{\text{reg}}(\mathbf{r}, \mathbf{R}_a; E_\lambda), \quad (9)$$

where

$$G_0(\mathbf{r}, \mathbf{R}_a; E_\lambda) = -\frac{m^*\cosh\lambda R}{2\pi\hbar^2 R}, \quad (10)$$

$$G_{\text{reg}}(\mathbf{r}, \mathbf{R}_a; E_\lambda) = -\frac{m^*}{4\hbar^2} \times\sum_{l=0}^{\infty}\frac{(2l+1)P_l(\cos w)J_{l+1/2}(i\lambda r)J_{l+1/2}(i\lambda R_a)N_{l+1/2}(i\lambda R_0)}{(rR_a)^{1/2}J_{l+1/2}(i\lambda R_0)}, \quad (11)$$

$$R = \sqrt{r^2 + R_a^2 - 2rR_a\cos w}.$$

The wave function of an electron localized at a short-range potential coincides with the Green function up to some multiplier. Indeed, substituting (2) into (1), we obtain

$$\Psi_\lambda(\mathbf{r}, \mathbf{R}_a) = \gamma G(\mathbf{r}, \mathbf{R}_a; E_\lambda)(\hat{T}\Psi_\lambda)(\mathbf{R}_a, \mathbf{R}_a), \quad (12)$$

where

$$(\hat{T}\Psi_\lambda)(\mathbf{R}_a, \mathbf{R}_a) \equiv \lim_{\mathbf{r}\to\mathbf{R}_a}[1 + (\mathbf{r} - \mathbf{R}_a)\nabla_{\mathbf{r}}]\Psi_\lambda(\mathbf{r}, \mathbf{R}_a). \quad (13)$$

Applying the operator $\hat{T}$ to both sides of (12) and taking into account (11), we obtain the equation that defines the dependence of the binding energy E_λ of the impurity center on the QD parameters and the position of the impurity R_a:

$$\eta_i = -\frac{\pi}{4R_a^*}\sum_{l=0}^{\infty}(1+2l)J_{l+1/2}(i\eta R_a^*)J_{l+1/2}(i\eta R_a^*) \times\frac{N_{l+1/2}(i\eta R_0^*)}{J_{l+1/2}(i\eta R_0^*)}. \quad (14)$$

Here, $\eta_i = \sqrt{|E_i|/E_d}$, $\eta = \sqrt{|E_\lambda|/E_d}$, $E_d = m^*e^4/2\hbar^2\varepsilon^2$ is the effective Bohr energy for the effective mass m^* and the dielectric constant ε; $E_i = \hbar^2\alpha^2/2m^2$ is the ground state energy of the impurity center in the bulk semiconductor; $R_a^* = R_a/a_d$, where a_d is the effective Bohr radius; and $R_0^* = R_0/a_d$.

As is known [7], the zero-range potential model satisfactorily describes D^- states related to the binding of an additional electron to a shallow donor. Such states were studied in the GaAs/GaAlAs structures [11, 12]. Similar states of acceptors, the so-called A^+ centers (acceptor with an additional hole) were found in Si/GeSi/Si structures doped with boron [13]. It is noteworthy that both the D^- states and the A^+ centers can exist in bulk semiconductors only under nonequilibrium conditions [7]. For example, in the case of donors in a QD, they can exist in thermodynamic equilibrium due to the emergence of excess carriers in doping of the barrier layers with shallow impurities [7]. The zero-range potential model applies well both to local states induced by isoelectronic impurities and to states of the negative hydrogen ion [7] (the second electron in the H^-

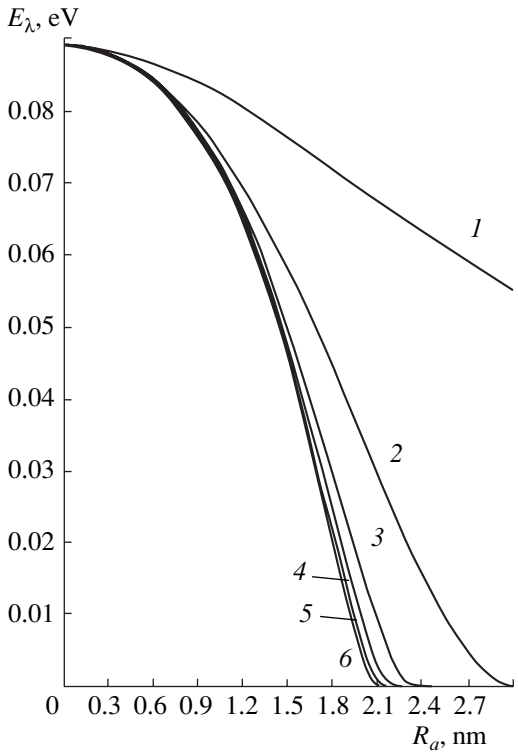

Fig. 1. Position of the localized level E_λ of the D^- state vs. the coordinate R_a of the impurity center in CdS QD at E_i = 0.14 eV, $\bar{R}$ = 3 nm and varied parameter L: (*1*) 1, (*2*) 2, (*3*) 3, (*4*) 4, (*5*) 5, and (*6*) 50.

ion is bound owing to the existence of an electron–electron correlation energy, rather than being confined by the Coulomb potential).

Results of the numeric analysis of Eq. (14) for D^- states in the CdS semiconductor microcrystals dispersed in the transparent dielectric matrix of silicate glass are presented in Fig. 1. The effective electron mass and the dielectric constant are, respectively, $m^* = 0.205m_0$ and $\varepsilon \approx 9.3$, while the effective Bohr energy equals $E_d \approx 0.035$ eV. It is seen from the figure that the positional disorder effect takes place in CdS QDs with D^- centers: $E_\lambda(R_a)$ is a decreasing function of R_a. Such behavior of $E_\lambda(R_a)$ is characteristic for films with quantum confinement [6] and quantum wells [7, 8]; this is due to a fundamental modification of the localized electron states near the structure boundaries. In plotting curves *1–6*, the series (14) is truncated in such a way that the number L of terms remaining in (14) increases with the curve number. This allows us to trace the contribution of the superposition of L QD states with different l to the formation of a localized center at the impurity center. As seen from Fig. 1, the conditions for the existence of bound states in the QDs become more stringent with increasing L (compare curves *1* and *2*, *2* and *3*). In this case, the binding energy of the D^- state in this structure may vary with the center position by nearly an order of magnitude: from 0.09 eV at the QD center to 0.01 eV at the distance of about 1.1 nm from its boundary.

3. Let us consider the impurity light absorption in a QD with a spherically symmetric potential. The wave function of an electron localized by the short-range potential at the point $\mathbf{R}_a = 0$ reads

$$\Psi_\lambda(\mathbf{r}, 0) = C\left(\frac{\cosh\lambda r}{r} + \frac{\sinh\lambda r}{r}\frac{\cosh\lambda R_0}{\sinh\lambda R_0}\right), \quad (15)$$

where $C = 2\sinh\lambda R_0\sqrt{\lambda/(\sinh 4\lambda R_0 - \sinh 2\lambda R_0 - 2\lambda R_0)}$ is a normalization factor. The wave function of the final state is taken in the form

$$\Psi_{fn,l,m}(r) = C_{n,l}\frac{J_{l+1/2}(X_{n,l}r/R_0)}{\sqrt{r}}Y_{l,m}(\theta, \varphi), \quad (16)$$

where $C_{n,l} = \sqrt{2}/R_0 J_{l+3/2}(X_{n,l})$ is a normalization factor. Such a choice of the wave function of the final state is justified if the inequality $|E_\lambda| \gg E_{1,0}$ holds. By virtue of the spherical symmetry of the problem, the conventional selection rule for optical transitions in the dipole approximation is valid: transitions from the ground S state of the impurity center to excited P states of the QD are possible. The squared module of the matrix element, which determines the oscillator strength for the dipole optical transition, has the form

$$|M_{fl}|^2 = \frac{128\hbar^2\alpha^2\lambda_0^2 I_0 a_d^2}{J_{5/2}^2(X_{n,1})} \times \frac{u^3\bar{R}^{*3}\eta E_d^2}{X_{n,1}^3[\sinh(u\bar{R}^*\eta) - \sinh(2u\bar{R}^*\eta) - 2u\bar{R}^*\eta]} \times \frac{1}{(\bar{R}^*)^4 u^4 (u^2\bar{R}^{*2}\eta^2 + X_{n,1}^2)^2} \times \{u^3\bar{R}^{*3}\eta^3\cosh(2\eta u\bar{R}^*)\sin X_{n,1} - X_{n,1}[u^3\bar{R}^{*3}\eta^3\cos X_{n,1}\cosh(2u\bar{R}^*\eta) + X_{n,1}\{u\bar{R}^*\eta\sin X_{n,1}(u\bar{R}^*\eta\sinh(2u\bar{R}^*\eta) - 3\cosh(2u\bar{R}^*\eta)) + X_{n,1}[\cos X_{n,1}(u\bar{R}^*\eta\cosh(2u\bar{R}^*\eta) + 2\sinh(2u\bar{R}^*\eta)) - 2\sinh(u\bar{R}^*\eta) + X_{n,1}\sin X_{n,1}\sinh(2u\bar{R}^*\eta)]\}]\}^2, \quad (17)$$

where $u = R_0/\bar{R}_0$; R_0 and $\bar{R}_0$ are, respectively, the QD radius and its mean value; $\bar{R}^* = \bar{R}_0/a_d$; α^* is the fine structure constant accounting for the dielectric constant; I_0 is the intensity of light; and λ_0 is the local field correction factor.

We assume that the QD size dispersion appears in the process of the phase decomposition in the supersat-

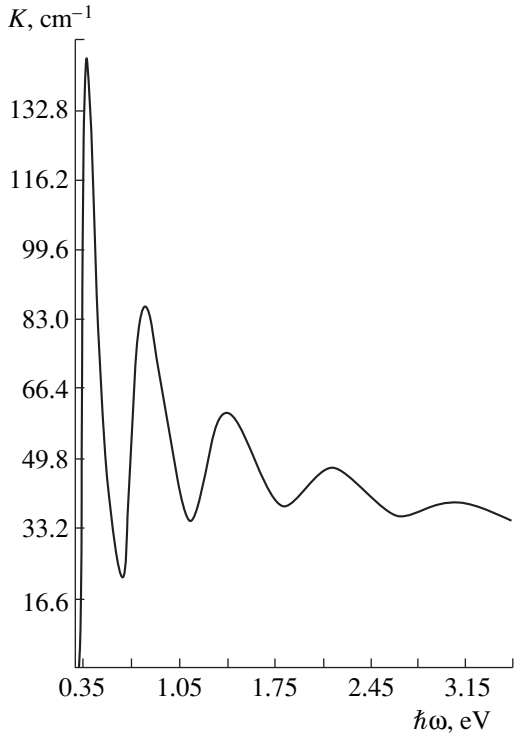

Fig. 2. Spectral dependence of the impurity absorption coefficient for CdS QDs dispersed in the transparent dielectric matrix at $E_i = 0.14$ eV and $\bar{R}_0 = 4.5$ nm.

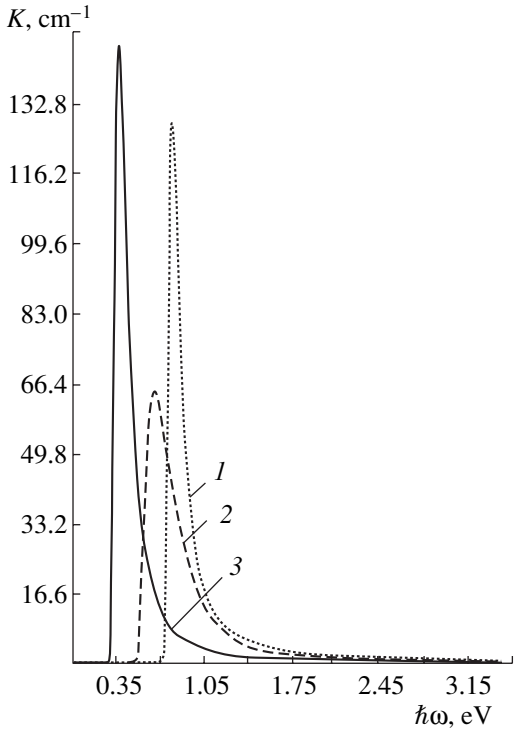

Fig. 3. Spectral dependence of the coefficient of impurity absorption in CdS QDs dispersed in the transparent matrix for the optical transition with the maximum oscillator strength ($n = 1$) at varied η_i and $\bar{R}_0$ parameters: (*1*) $\eta_i = 4$, $\bar{R}_0 = 4.5$ nm; (*2*) $\eta_i = 2$, $\bar{R}_0 = 3.0$ nm; and (*3*) $\eta_i = 2$, $\bar{R}_0 = 4.5$ nm.

urated solid solution and can be satisfactorily described by the Lifshits–Slezov formula [9]

$$P\left(u = \frac{R_0}{\bar{R}_0}\right) = \begin{cases} \dfrac{3eu^2 e^{-1/(1-2u/3)}}{2^{5/3}(3+u)^{7/3}(3/2-u)^{11/3}}, & u < 3/2, \\ 0, & u > 3/2, \end{cases} \quad (18)$$

where e is the Napierian base.

With account taken of the QD size dispersion, the expression for the impurity absorption coefficient can be represented as

$$K = K_0 \sum_{n=1}^{N} \frac{A}{B},$$

$$A = \delta_n \eta P(\delta_n) F_n(X, \eta)(X_{n,1}^2 + \delta_n^2 \bar{R}^{*2}\eta^2)^{-2}, \quad (19)$$

$$B = \sqrt{\Delta} X J_{5/2}^2(X_{n,1}) X_{n,1}^4 [\sinh(4\bar{R}^*\delta_n\eta) - \sinh(4\bar{R}^*\delta_n\eta) - 2\bar{R}^*\delta_n\eta],$$

where $X = \hbar\omega/E_d$; ω is the light wave frequency; $\Delta = X - \eta^2$, $\delta_n = X_{n,1}/(\bar{R}^*\sqrt{\Delta})$; $K_0 = (128/3)\lambda_0^2 N_0 \pi^2 \alpha^* a_d^2$; N is the root of the equation $X_N = (3\bar{R}^*/2)\sqrt{X - \eta^2/2}$ for the index; the function $P(\delta_n)$ is defined by (18); N_0 is the QD concentration in the dielectric matrix; and the function $F_n(X, \eta)$ has the following form:

$$\begin{aligned} F_n(X,\eta) &= \delta_n^3 \bar{R}^{*3}\eta^3 \cosh(2h\delta_n\bar{R}^*)\sin X_{n,1} \\ &- X_{n,1}\{\delta_n^3\bar{R}^{*3}\eta^3\cos X_{n,1}\cosh(2\delta_n\bar{R}^*\eta) \\ &+ X_{n,1}[\delta_n\bar{R}^*\eta\sin X_{n,1}(\delta_n\bar{R}^*\eta\sinh(2\delta_n\bar{R}^*\eta) \\ &- 3\cosh(2\delta_n\bar{R}^*\eta)) + X_{n,1}[(\delta_n\bar{R}^*\eta\cosh(2\delta_n\bar{R}^*\eta) \\ &+ 2\sinh(2\delta_n\bar{R}^*\eta))\cos X_{n,1} - 2\cosh(\delta_n\bar{R}^*\eta) \\ &+ X_{n,1}\sin X_{n,1}\sinh(2\delta_n\bar{R}^*\eta)]]\}. \end{aligned} \quad (20)$$

The impurity absorption spectrum of the CdS microcrystals dispersed in the transparent dielectric matrix, calculated using (19), is presented in Fig. 2. The concentration of CdS microcrystals in the glass matrix was assumed to be 10^{16} cm^{-3}, and their mean radius $\bar{R}_0 \approx 4.5$ nm [14]. The impurity absorption coefficient near the threshold is 0.14×10^3 cm^{-1} at such a QD concentration (light wavelength ~3.5 μm); i.e., it is quite measurable. The evolution of the impurity absorption

spectrum with changing CdS QD size $\bar{R}_0$ and parameter η_i for the optical transition with the maximum oscillator strength ($n = 1$) is represented by curves *1–3* in Fig. 3. It can be seen (compare curves *3* and *2*) that the impurity absorption edge shifts to shorter wavelengths with decreasing $\bar{R}_0$, which reflects a shift of the lower quantum-well level. Sensitivity of the impurity absorption edge to the parameter $\eta_i = \sqrt{|E_i|/E_d}$ is shown by curves *1* and *3*. With decreasing η_i (increasing localized state radius), the oscillator strength of the optical dipole transition grows (compare curves *1* and *3*) and the impurity absorption edge shifts to longer wavelengths.

4. Thus, states localized by the short-range potential in a QD described by the "hard-wall" model were considered. The dynamics of formation of a localized state at the impurity center by a superposition of the QD states with different l was demonstrated. Taking into account the QD size dispersion markedly changes the spectral behavior of the impurity absorption coefficient. In the case of CdS QDs ($a_d \approx 3$ nm, $E_d \approx 0.035$ eV), a change in its mean radius from 4.5 to 3 nm is followed by the impurity absorption edge shift (see Fig. 3) to shorter wavelengths by about 0.18 eV. It should be noted that the dependence of the optical transition energies on QD size furnishes an opportunity to "tune" the heterophase system under consideration to the wavelength of one or another radiation source. In this case, the wavelength of this source must fall within the transparency window of the bulk crystal. The presence of QD–⟨impurity center⟩ complexes gives one more degree of freedom for such "tuning;" that is, the impurity level position depends on the impurity center coordinates and on QD parameters.

REFERENCES

1. J. Yumoto, S. Fukushima, and K. Kubodera, Opt. Lett. **12**, 832 (1987).
2. Al. L. Éfros and A. L. Éfros, Fiz. Tekh. Poluprovodn. (Leningrad) **16**, 1209 (1982) [Sov. Phys. Semicond. **16**, 772 (1982)].
3. A. I. Ekimov and A. A. Onushchenko, Fiz. Tekh. Poluprovodn. (Leningrad) **16**, 1215 (1982) [Sov. Phys. Semicond. **16**, 775 (1982)].
4. A. Ya. Shik, Fiz. Tekh. Poluprovodn. (St. Petersburg) **26**, 1161 (1992) [Sov. Phys. Semicond. **26**, 649 (1992)].
5. E. Z. Imamov and V. D. Krevchik, Phys. Status Solidi B **114**, 201 (1982).
6. V. D. Krevchik and É. Z. Imamov, Fiz. Tekh. Poluprovodn. (Leningrad) **17**, 1235 (1983) [Sov. Phys. Semicond. **17**, 780 (1983)].
7. A. A. Pakhomov, K. V. Khalipov, and I. N. Yassievich, Fiz. Tekh. Poluprovodn. (St. Petersburg) **30**, 1387 (1996) [Semiconductors **30**, 730 (1996)].
8. V. D. Krevchik, R. V. Zaĭtsev, and V. V. Evstifeev, Fiz. Tekh. Poluprovodn. (St. Petersburg) **34**, 1244 (2000) [Semiconductors **34**, 1193 (2000)].
9. I. M. Lifshits and V. V. Slezov, Zh. Éksp. Teor. Fiz. **35** (2), 479 (1958) [Sov. Phys. JETP **8**, 331 (1959)].
10. *Heigher Transcendental Functions (Bateman Manuscript Project)*, Ed. by A. Erdelyi (McGraw-Hill, New York, 1953; Nauka, Moscow, 1974), Vol. 2.
11. T. S. Huant, S. P. Najda, and B. Etinne, Phys. Rev. Lett. **65**, 1486 (1990).
12. D. M. Larsen and S. Y. McCann, Phys. Rev. B **46**, 3966 (1992).
13. M. S. Kagan, I. V. Altukhov, K. A. Korolev, *et al.*, Izv. Akad. Nauk, Ser. Fiz. **63**, 359 (1999).
14. N. R. Kulish, V. P. Kunets, and M. P. Lisitsa, Fiz. Tverd. Tela (St. Petersburg) **39**, 1865 (1997) [Phys. Solid State **39**, 1667 (1997)].

Translated by S. Ktitorov

Semiconductors, Vol. 36, No. 2, 2002, pp. 213–218. Translated from Fizika i Tekhnika Poluprovodnikov, Vol. 36, No. 2, 2002, pp. 221–226.
Original Russian Text Copyright © 2002 by Berashevich, Kamenev, Borisenko.

LOW-DIMENSIONAL SYSTEMS

Injection Excitation of Luminescence in Multilayer *nc*-Si/Insulator Structures

Yu. A. Berashevich*, B. V. Kamenev, and V. E. Borisenko***

** Belarussian State University of Information Science and Radio Engineering, ul. Brovki 17, Minsk, 220072 Belarus*

e-mail: julia@nano.bsuir.edu.by

*** IMEL/NCSR Demokritos, Athens, 60228 Greece*

Submitted May 14, 2001; accepted for publication June 20, 2001

Abstract—A model of recombination of nonequilibrium charge carriers in multilayer structures (nanocrystalline Si–insulator) was suggested. It was found that the restriction of carrier transport through the localized states of the insulator leads to a nonlinear increase in the intensity of electroluminescence (EL) with an increase in the current flowing across the structure. The subsequent leveling off of this dependence is associated with the increasing role of Auger recombination with increasing current. A decrease in the contribution of the nonradiative Auger process can be accomplished by increasing the concentration of nanodimensional clusters in Si and the number of periods of the structure. It was demonstrated that one of the main ways to increase the EL intensity is increasing the hole density at the hole-injecting contact. © *2002 MAIK "Nauka/Interperiodica".*

INTRODUCTION

The discovery of the efficient photoluminescence (PL) of porous Si [1] stimulated intense investigations of various Si nanostructures (*nc*-Si) because of the possible development of light-emitting devices on its basis, which can be easily integrated into modern microelectronics. The structures which contain Si nanocrystallites embedded into the insulator matrix are of special interest. In this case, the insulator serves as the natural barrier for the quantum-well confinement of charge carriers excited within Si. Such structures can be obtained, for example, by chemical deposition of Si and insulator [2–4], ion implantation of Si into the insulator matrix [5], plasma breakdown of SiH_4 [6], and molecular-beam epitaxy of Si on orienting insulator layers of CaF_2 or SiO_2 with the subsequent high-temperature annealing [7–9]. To date, the optoelectronic properties of *nc*-Si/insulator structures under optical excitation have been studied intensively [3, 6–8, 10]. However, another important aspect of the problem, specifically, the injection excitation of such structures, has not been developed properly.

It is known that the PL for Si nanostructures is restricted to the recombination of a single electron–hole pair in a single nanocrystallite during radiative recombination. The reason is that the presence of more than one pair of charge carriers in a single nanocrystallite causes rapid (~1 ns) Auger recombination [11]. However, in the case of injection excitation, the electron–hole pair is formed by the sequential injection of the electron and hole into the nanocrystallite. Thus, in this case, luminescence is mainly determined by transport properties of the structure, which especially manifests itself in multilayer *nc*-Si/insulator structures.

Previously, we theoretically considered carrier transport via localized states in the band gap of the insulator for *nc*-Si/insulator multilayer structures [12]. In this study, this model was used for the analysis of mechanisms of recombination of nonequilibrium carriers in nanodimensional Si crystals.

MODEL

Let us consider the periodic nanodimensional *nc*-Si/insulator structure consisting of N Si layers separated by $N + 1$ potential barriers of insulator. We assume that this structure contains no impurities and carriers are injected from its contacts.

It should be noted that Si layers in actually obtainable *nc*-Si/insulator structures consist of crystalline nanodimensional clusters. The electron interaction between clusters can be suppressed to a large extent [10]. Thus, let us assume that each Si layer in the structure considered is formed from isolated clusters of equal size. Let us also assume that the cluster surfaces are adequately passivated. Due to this, centers of nonradiative recombination are absent in the band gap of Si. This assumption is quite justified due to the slight temperature dependence of the PL intensity for the structures mentioned in the vicinity of room temperature, which points to low efficiency of nonradiative recombination [3, 10].

Let us consider the mechanism of excitation and recombination in nanodimensional Si clusters in more detail. Although the nature of luminescence for *nc*-Si is

not quite clear, we assume that light is emitted due to electron–hole radiative recombination. The injection of a single carrier, for example an electron, into the empty nanocluster leads to a considerable increase in the electron energy due to the Coulomb interaction between the injected electron and the field induced by this electron [13, 14]. With the injection of a second electron into the cluster containing the first electron, the increase in energy can be as large as 1–2 eV, depending on the cluster size and dielectric constant. This makes the injection of the second electron extremely improbable [13]. However, hole injection into the cluster, which already contains an electron, leads to charge compensation due to the Coulomb interaction between an electron and a hole, and injection of the third carrier becomes possible. The presence of three charge carriers in the cluster leads to rapid Auger recombination, due to a high local carrier density [11]. For this reason, we can neglect the contribution of clusters which contain more than three charge carriers. We restrict our consideration to nanodimensional clusters, which contain no charge carriers, have one electron (N_0^e) or one hole (N_p^0), two charge carriers of opposite signs (N_p^e), as well as two electrons and one hole (N_p^{2e}) or two holes and one electron (N_{2p}^e).

Let us keep in mind that the rate of Auger recombination considerably exceeds the rate of radiative recombination. In this case, we can write the following set of continuity equations, which describe the process of injection and recombination in the *i*th layer of the structure considered:

$$\frac{dN_{0,i}^0}{dt} = \frac{N_{p,i}^e}{\tau_{RR}} - G_{e,i}N_{0,i}^0 - G_{p,i}N_{0,i}^0, \quad (1)$$

$$\frac{dN_{0,i}^e}{dt} = G_{e,i}N_{0,i}^0 + \frac{N_{p,i}^{2e}}{\tau_A} - G_{p,i}N_{0,i}^e, \quad (2)$$

$$\frac{dN_{p,i}^0}{dt} = G_{p,i}N_{0,i}^0 + \frac{N_{2p,i}^e}{\tau_A} - G_{e,i}N_{p,i}^0, \quad (3)$$

$$\frac{dN_{p,i}^e}{dt} = G_{e,i}(N_{p,i}^0 - N_{p,i}^e) + G_{p,i}(N_{0,i}^e - N_{p,i}^e) - \frac{N_{p,i}^e}{\tau_{RR}}, \quad (4)$$

$$\frac{dN_{p,i}^{2e}}{dt} = G_{e,i}N_{p,i}^e - \frac{N_{p,i}^{2e}}{\tau_A}, \quad (5)$$

$$\frac{dN_{2p,i}^e}{dt} = G_{p,i}N_{p,i}^e - \frac{N_{2p,i}^e}{\tau_A}, \quad (6)$$

$$N_{SUM} = N_{0,i}^0 + N_{0,i}^e + N_{p,i}^0 + N_{p,i}^e + N_{p,i}^{2e} + N_{2p,i}^e. \quad (7)$$

Here, $G_{e,i}$ and $G_{p,i}$ are the rates of injection of electrons and holes into the cluster; N_{SUM} is the total concentration of clusters in the layer, which is constant for all periods; τ_A is the time of Auger recombination; and τ_{RR} is the time of radiative recombination.

Analysis of the set of Eqs. (1)–(7) demonstrates that the luminescence intensity for the steady-state case is determined by the ratio of the rates for the electron and hole injection $G_{e,i}$ and $G_{p,i}$. Specifically, with the proviso $G_{e,i} \gg G_{p,i}$, the EL intensity for the *i*th layer is defined as

$$I_{EL}^i \equiv \frac{N_{p,i}^e \hbar\omega}{\tau_{RR}} = \frac{G_{p,i}N_{SUM}\hbar\omega}{1 + G_{e,i}\tau_{RR}}, \quad (8)$$

where $\hbar\omega$ is the energy of the photon emitted. For high injection levels, if $G_{e,i}\tau_{RR} \gg 1$, the EL intensity is proportional to the ratio of probabilities of the electron and hole injection into the cluster. However, the ratio of $G_{e,i}$ and $G_{p,i}$ quantities, which is governed by the carrier transport across the structure, differs considerably for various layers.

In order to describe the carrier transport for multilayer *nc*-Si/structures, we use the set of equations [12] which accounts for the kinetics of variation in the electron density n_i and hole density p_i in the *i*th Si layer:

$$\frac{\partial n_i}{\partial t} = \frac{n_{i-1}}{n_c}g_{n,i-1}(n_{i-1}, n_i) - \frac{n_i}{n_c}g_{n,i}(n_i, n_{i+1}) - R_i(n_i, p_i), \quad (9)$$

$$\frac{\partial p_i}{\partial t} = \frac{p_{i+1}}{p_c}g_{p,i+1}(p_{i+1}, p_i) - \frac{p_i}{p_c}g_{p,i}(p_i, p_{i-1}) - R_i(n_i, p_i). \quad (10)$$

Here, the first term on the right-hand side of the equations describes the rate of transport of electrons or holes into the *i*th well, and the second term describes the rate of escape of charge carriers from this well; n_c and p_c are the carrier densities at injecting contacts; and

$$R_i(n_i, p_i) = \frac{N_{e,i}^p}{\tau_{RR}} + \frac{N_{p,i}^{2e}}{\tau_A} + \frac{N_{2p,i}^e}{\tau_A} \quad (11)$$

is the rate of electron and hole recombination in the *i*th layer, which is determined from the set of Eqs. (1)–(7).

The experimental data [15, 16] demonstrate that the mechanism of carrier transport across the structure considered is predominantly of the activation type, which implies that the localized states in the band gap of the insulator are involved in this process. However, it should be noted that the final density of such states should lead to the leveling-off of the rate of carrier transport for large external biases. This is confirmed experimentally and was observed previously [15] in the investigation of current–voltage (*I–V*) characteristics of Si/CaF_2 periodic structures.

The rate of carrier injection into the cluster depends on the probability of carrier location in the *i*th quantum well, as well as carrier density in this well, and can be described as follows:

$$G_{e,i} = \frac{n_{i-1}g_{i-1}(n_{i-1}, n_i)}{n_c N_{\mathrm{SUM}}} - \frac{n_i g_i(n_i, n_{i+1})}{n_c N_{\mathrm{SUM}}}, \quad (12)$$

$$G_{p,i} = \frac{p_{i+1}g_{i+1}(p_{i+1}, p_i)}{p_c N_{\mathrm{SUM}}} - \frac{p_i g_i(p_i, p_{i-1})}{p_c N_{\mathrm{SUM}}}. \quad (13)$$

We used the simultaneous solution of Eqs. (1)–(6) and (9)–(13) for the steady-state case with allowance made for condition (7) for simulating the excitation and recombination for the multilayer *nc*-Si/CaF_2 structure. The times of recombination, density of nanodimensional Si clusters and traps in the insulator, the coefficient of carrier capture by the traps, and thicknesses of the insulator and semiconductor layers were accepted as identical for all periods of the structure. The numerical values of the parameters used in calculations are given in the table.

RESULTS OF SIMULATION AND DISCUSSION

The intensity of radiative recombination for Si clusters is controlled by charge carriers with a lower density or lower mobility. For this reason, we choose a constant electron density at the contact, which is close to the density of trap states for the insulator. On the other hand, the hole density at the opposite contact was varied in a wide range, which led to various values of the hole current, with the electron current remaining unchanged.

The results of calculation of the hole and electron currents as a function of the bias voltage applied to the 4-period Si/CaF_2 structure for various hole densities at the injecting contact are shown in Fig. 1. For the parameters selected, the electron component of the current rapidly saturates and actually remains constant with the bias voltage increasing above 3 V as a result of limiting the carrier transport by the finite trap density. On the other hand, the leveling off of the hole component of the current depends on the bias applied and the hole density at the contact. For this reason, the region of leveling off of the hole component shifts to higher voltages with decreasing hole density at the contact. For equal carrier densities at the injecting contact, the difference between the electron and hole currents is controlled by several factors. These are differing barrier heights for electron and holes, various injection conditions at the contacts, and the heavy dependence of the effective hole mass on the configuration of the nanodimensional structure [18].

Figure 2 demonstrates the calculated dependences of EL intensity on the current density for the same hole densities at injecting contacts as in Fig. 1. For equal

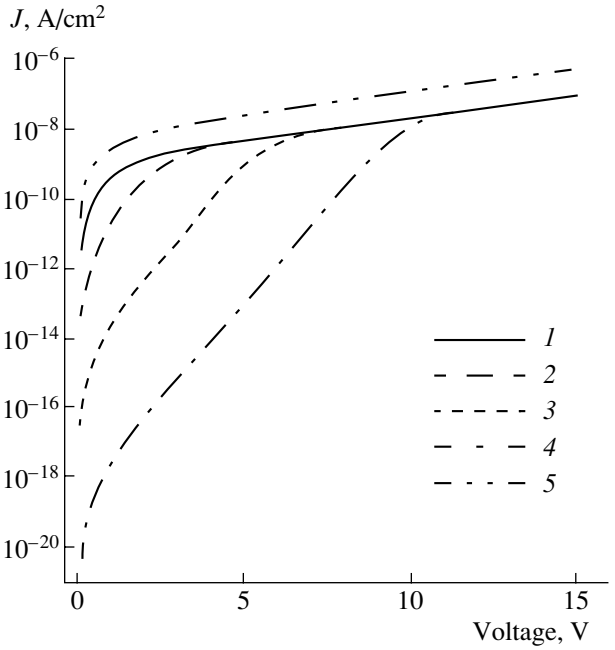

Fig. 1. Dependence of the density of (*1–4*) hole and (*5*) electron currents on the applied bias voltage for $N_{\mathrm{SUM}} = 10^{17}$ cm^{-3}. Carrier densities at injecting contacts p_c, n_c: (*1*) $p_c = 10^{18}$, (*2*) $p_c = 10^{16}$, (*3*) $p_c = 10^{13}$, (*4*) $p_c = 10^{9}$, and (*5*) $n_c = 10^{18}$ cm^{-3}.

concentrations of both types of charge carriers, the linear increase in EL intensity is observed with increasing current density. A decrease in the hole density at the injecting contact gives rise to superlinear dependence in the current density range of 3×10^{-9}–10^{-7} A/cm^2, which corresponds to the voltages of 2–7 V. In this case, the electron current is saturated, whereas the hole current is far from saturation. Under these conditions, the

Parameters used for the investigation of recombination in nanocrystalline Si in multilayered *nc*-Si/CaF_2 structures

Parameter	Value
Number of periods in the structure	4–20
Auger recombination time	10^{-9} s [11]
Radiative recombination time	10^{-4} s [16]
Energy of photon emitted	1.65 eV [3, 4, 6, 8]
Cluster density	10^{16}–10^{19} cm^{-3}
Electron density at the contact	10^{18}–10^{19} cm^{-3}
Hole density at the contact	10^{11}–5×10^{19} cm^{-3}
Voltage applied	0.1–25 V
Thickness of Si layer	1.5 nm
Thickness of CaF_2 layer	2 nm
Effective electron mass	$0.35m_0$ [17]
Effective hole mass	$0.42m_0$ [17]

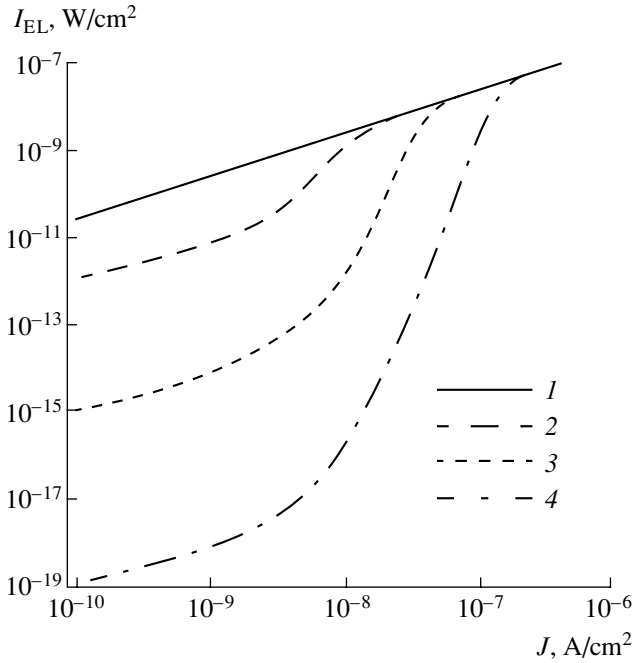

Fig. 2. Dependences of electroluminescence intensity (I_{EL}) on the current density (J) for $N_{SUM} = 10^{17}$ cm^{-3} and hole density at the injecting contact p_c = (*1*) 10^{18}, (*2*) 10^{16}, (*3*) 10^{13}, and (*4*) 10^9 cm^{-3}.

EL intensity is controlled by the hole current, whereas the total current is determined by the electron current. The linear dependence is restored with the saturation of the hole current.

With a further increase in the current, the EL intensity tends toward a constant value, since Auger recombination begins to prevail. For this reason, the efficiency of radiative recombination, which is defined as $\eta = (I_{EL}/\hbar\omega)/R(n, p)$, decreases with increasing majority-carrier current. The dependence of the EL intensity on the current density for the four-period Si/CaF_2 structure with equal electron and hole densities at contacts is shown in Fig. 3. The efficiency of radiative recombination decreases rapidly with increasing current, which leads to the limiting of the EL intensity given by

$$\frac{N_{SUM}C_p\hbar\omega}{G_e\tau_{RR}}.$$

The results of calculations are in good agreement with the data from the experimental EL investigations for Si/CaF_2 periodic structures, which demonstrated a nonlinear increase in EL intensity with increasing current [19]. With external biases, for which current saturation in the *I–V* characteristic is observed, an increase in the EL intensity with increasing current is characterized by a linear dependence. With a further increase in the external bias, the EL intensity remains constant and independent of current [19].

We also found that EL intensity depends on the density of Si clusters. The reason is that a decrease in this density leads to an increase in the probability of trapping the third carrier in the cluster and, as a consequence, to Auger recombination (Fig. 4). In this case, the efficiency of radiative recombination drops, and the

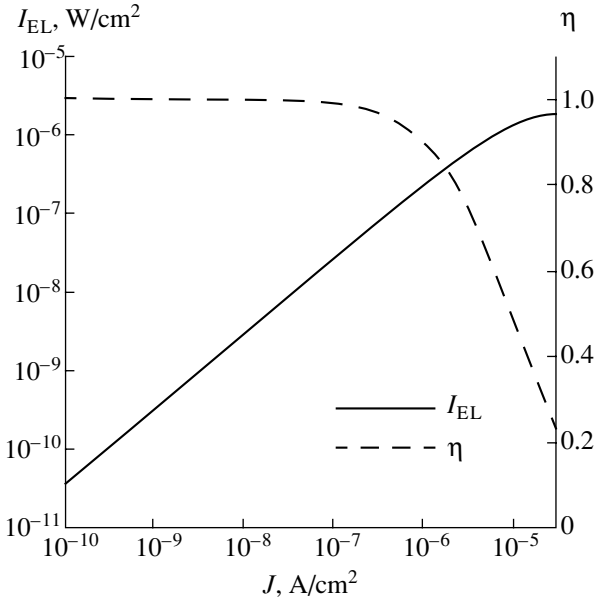

Fig. 3. Dependences of electroluminescence intensity (I_{EL}) and efficiency of radiative recombination (η) on the current density for the four-period structure Si/CaF_2 with $N_{SUM} = 10^{17}$ cm^{-3}, and $n_c = p_c = 10^{18}$ cm^{-3}.

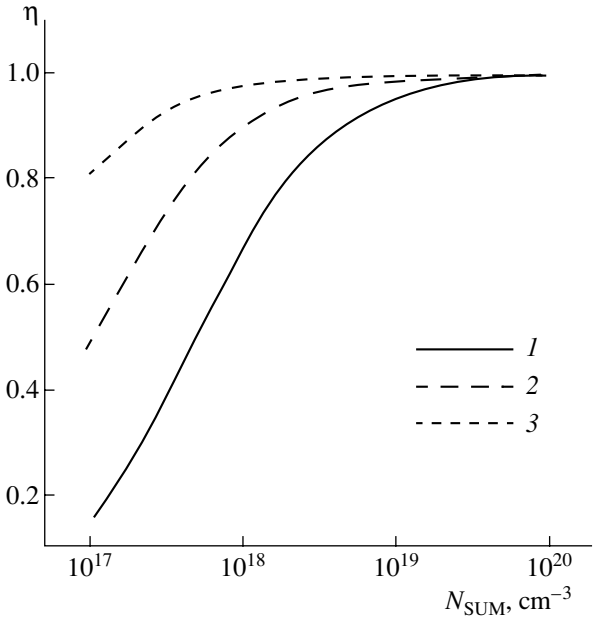

Fig. 4. Dependences of efficiency of radiative recombination on the density of Si clusters (N_{SUM}) calculated for a four-period Si/CaF_2 structure with $n_c = p_c = 10^{18}$ cm^{-3} and bias voltage V = (*1*) 15, (*2*) 10, and (*3*) 5 V.

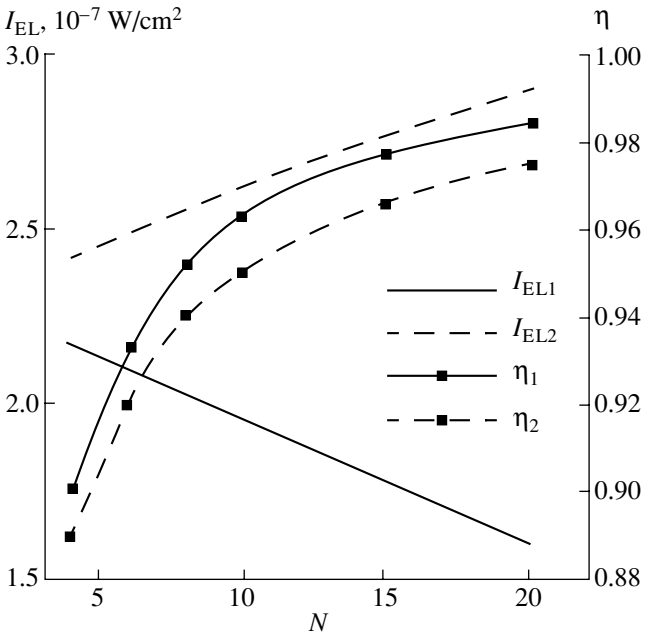

Fig. 5. Dependences of electroluminescence intensity (I_{EL}) and efficiency of radiative recombination (η) on the number of periods (N) with the current density $J = 10^{-6}$ A/cm^2 for the following carrier densities at injecting contacts: (*1*) $n_c = 10^{17}$ cm^{-3}, $p_c = 5 \times 10^{18}$ cm^{-3}; and (*2*) $n_c = 10^{18}$ cm^{-3}, $p_c = 10^{17}$ cm^{-3}.

drop steepness increases with the increasing rate of injection of the third carrier into the cluster.

It is evident that the EL intensity is highest when the rates of the electron and hole injection into the cluster are equal ($G_e = G_p$). As was already noted above, due to the significant distinction between the barrier heights for electrons and holes, as well as their effective masses, the rate of tunneling carrier transport for electrons via the traps in an insulator can considerably exceed the rate for holes even at equal densities of these carriers at the contacts (Fig. 1). For this reason, variation in the EL intensity from layer to layer is monotonic, and the intensity increases on approaching the hole-injecting contact, at which $G_p \longrightarrow G_e$. From this it follows that, in the region of the hole contact (where G_p increases and G_e decreases), the EL intensity increases with the increase in the number of periods of the structure and decreases at the electron contact. This should lead to the dependence of EL intensity on the number of periods in the structure, which was confirmed by the results of calculations shown in Fig. 5. General carrier densities at the contacts were chosen for simulation in order to consider two cases: (i) the rate of hole injection into nanoclusters is higher compared to that of electron injection and (ii) the opposite case.

In the case of excessive hole density, the EL intensity reaches the largest value at the electron contact. However, since the probability of hole transport is much lower compared to that for electron transport, an increase in the number of periods shifts this value to the edge of the electron contact and further outside this contact. As a result, the overall EL intensity for the structure decreases. Under reversed conditions, the EL peak approaches the hole contact. However, the probability of transport for electrons is already higher than that for holes, and an increase in the number of periods shifts the largest value to the middle of the structure. On the other hand, the EL efficiency increases in both cases, since the ratio of probabilities of the electron and hole injection into the cluster, which is averaged by layers, increases with an increase in the number of layers. An increase in the rate of carrier injection into the nanodimensional cluster enhances these effects.

CONCLUSION

The model suggested for carrier recombination in nanodimensional Si clusters in periodic *nc*-Si/CaF_2 structures is used for the investigation of the dependence of EL intensity on the current flowing across the structures. The distinctions in the rise of electron and hole currents with increasing external bias are found to be caused by the finite density of trap states for the insulator. These distinctions constitute the reasons for the nonlinearity of the dependence of EL intensity on the current. In addition, a decrease in the efficiency of radiative recombination due to an increase in the contribution of the Auger process for high bias voltages leads to the leveling off of EL intensity. It is found that the relative decrease in the contribution of nonradiative Auger recombination can be accomplished by increasing the density of nanodimensional clusters in Si and the number of periods of the structure. However, an increase in the number of periods of the Si/CaF_2 structure does not always lead to an increase in the EL intensity. The coefficient for hole transport across the potential barrier is always less than that for electrons. For this reason, one of the main methods for increasing the PL intensity at the metal contact consists in increasing the hole density at the hole contact: the larger the number of periods of the structure, the higher the hole density.

ACKNOWLEDGMENTS

We are grateful to A.L. Danilyuk for his helpful participation in discussions of the results and constructive comments.

This study was supported by the Belarussian Foundation for Basic Research (project no. T99-102) and the Interuniversity Program on Nanoelectronics.

REFERENCES

1. L. T. Canham, Appl. Phys. Lett. **57**, 1046 (1990).
2. L. Tsybeskov, K. D. Hirschman, S. P. Duttagupta, *et al.*, Appl. Phys. Lett. **72** (1), 43 (1998).
3. G. Pucker, P. B. Bellutti, C. Spinella, *et al.*, J. Appl. Phys. **88** (10), 6044 (2000).

4. P. Photopoulos and A. G. Nassiopoulou, Appl. Phys. Lett. **77**, 1816 (2000).
5. V. I. Klimov, Ch. J. Schwarz, D. W. McBranch, and C. W. White, Appl. Phys. Lett. **73** (18), 2603 (1998).
6. Y. Kanemitsu, T. Ogawa, K. Shiraishi, and K. Takeda, Phys. Rev. B **48**, 4883 (1993).
7. D. J. Lokwood, Z. H. Liu, and J. M. Baribeau, Phys. Rev. Lett. **76**, 539 (1996).
8. F. Bassani, L. Vervoot, I. Mihalescu, *et al.*, J. Appl. Phys. **79**, 4066 (1996).
9. M. Zacharias, L. Tsybeskov, K. D. Hirschman, *et al.*, J. Non-Cryst. Solids **227–230**, 1132 (1998).
10. V. Vinciguerra, G. Franzó, F. Priolo, *et al.*, J. Appl. Phys. **87** (11), 8165 (2000).
11. D. Kovalev, H. Hecler, G. Polisski, and F. Koch, Phys. Status Solidi B **215**, 871 (1999).
12. Yu. A. Berashevich, A. L. Danilyuk, A. N. Kholod, and V. E. Borisenko, Fiz. Tekh. Poluprovodn. (St. Petersburg) **35** (1), 110 (2001) [Semiconductors **35**, 112 (2001)].
13. M. Lannoo, C. Delerue, and G. Allan, Phys. Rev. Lett. **74** (17), 3415 (1995).
14. C. Delerue, M. Lannoo, and G. Allan, Phys. Rev. Lett. **84** (11), 2457 (2000).
15. V. Ioannou-Sougleridis, T. Ouisse, A. G. Nassiopoulou, *et al.*, J. Appl. Phys. **89** (1), 610 (2001).
16. J. M. Shannon and B. A. Morgan, J. Appl. Phys. **86** (3), 1548 (1999).
17. C. Svensson and I. Lundström, J. Appl. Phys. **44**, 4657 (1973).
18. *Spectroscopy of Isolated and Assembled Semiconductor Nanocrystals*, Ed. by L. E. Brus, Al. L. Efros, and T. Itoh, J. Lumin. **70** (1996).
19. G. Pucke, Z. Caburro, V. Mulloni, *et al.*, in *European Projects: Silicon Modules for Integrated Light Engineering, Marseille, France, 2000*, p. 133.

Translated by N. Korovin

Semiconductors, Vol. 36, No. 2, 2002, pp. 219–223. Translated from Fizika i Tekhnika Poluprovodnikov, Vol. 36, No. 2, 2002, pp. 227–231.
Original Russian Text Copyright © 2002 by V. Kunets, Kulish, Vas. Kunets, Lisitsa, Malysh.

LOW-DIMENSIONAL SYSTEMS

Temperature Dependence of the Optical Energy Gap for the CdS_xSe_{1-x} Quantum Dots

V. P. Kunets^, N. R. Kulish, Vas. P. Kunets, M. P. Lisitsa, and N. I. Malysh

Institute of Semiconductors, National Academy of Sciences of Ukraine, Kiev, 03028 Ukraine

^e-mail: kunets@qdots. semicond. kiev.ua

Submitted May 14, 2001; accepted for publication June 20, 2001

Abstract—A temperature dependence of the optical energy gap $E_g(T)$ for the CdS_xSe_{1-x} quantum dots synthesized in a borosilicate glass matrix was investigated in the range of 4.2–500 K. It was demonstrated that this dependence reproduced the dependence $E_g(T)$ for bulk crystals and is described by the Varshni formula for $\bar{r} > a_B$ over the entire temperature range. Here, $\bar{r}$ is the average dot radius, and a_B is the Bohr radius for the exciton in a bulk crystal. With the transition to quantum dots with $\bar{r} < a_B$, a decrease in the thermal coefficient of the band gap and a deviation from the Varshni dependence were observed in the temperature range of 4.2–100 K. The specific features observed are explainable by a decrease in the resulting macroscopic potential of the electron–phonon interaction and by modification of the vibration spectrum for dots as their volume decreases. © *2002 MAIK "Nauka/Interperiodica".*

The band gap (E_g) for most of the bulk semiconductors decreases with increasing temperature. This is determined by (i) mutual repulsion of levels in bands with increasing electron–phonon interaction (second order Fan's terms in the perturbation theory), (ii) thermal expansion of the lattice (vibration anharmonicity) and corresponding dependence of the energy gap on the lattice constant, (iii) smoothening of the periodic potential described by the Debye–Waller factor, and (iv) interaction of interband states (Fan's terms for the interband coupling) [1–4]. The dependence $E_g(T)$ for bulk semiconductors is investigated in detail. It was found that the first two mechanisms make the largest contribution to the E_g variation.

The data on the energy gap of semiconductor quantum dots (QDs) in the literature are scattered; as for the temperature dependence of the energy gap, these data are actually nonexistent. Thus, in order to describe the dependence $E_g(T)$ for the self-organized InAs QDs, the authors of [5] used the empiric Varshni formula [6] and a similar relation for the InAs/GaAs QDs [7]. The E_g magnitude for the CdS_xSe_{1-x} QDs, which were synthesized in a borosilicate glass matrix, was determined for several fixed temperatures only: 4.2, 77, and 300 K [8]. On the other hand, temperature-dependent measurements yield information about the electron–phonon interaction, which has its own specific features in QDs due to their small sizes (consequently, a small number of atoms and the effect of interfaces, strains, and so on.

The purpose of this study was to gain insight into specific features of the temperature dependence of the optical energy gap for the CdS_xSe_{1-x} QDs with $\bar{r} > a_B$, whose properties are close to those for a bulk crystal, and with $\bar{r} < a_B$, in which quantum-confinement effects occur. Here, $\bar{r}$ is the average dot radius, and a_B is the Bohr radius of the exciton for the bulk crystal.

The parameters of the QDs investigated and bulk crystals with the same composition are given in the table. The band gap for the QDs was determined from the absorption spectra, which were measured by the conventional method and were processed using the procedure reported elsewhere [8, 10]. The sample temperature was monitored with copper–constantan and chromel–alumel thermocouples and was kept constant with the error < 2 K during measurements. For QDs with $\bar{r} < a_B$, the energy gap between the conduction band bottom and valence band top was identified with the E_g magnitude (Fig. 1a). As for QDs with $\bar{r} < a_B$, the distance between the lowest hole and electron quantum-confinement levels E_{01}^h and E_{01}^e was identified with this gap (Fig. 1b). For the absorption-coefficient K spectra, these energy gaps correlate, in the first case, with the point where the dependence $K(\hbar\omega) \propto (\hbar\omega - E_g)^{1/2}$ intercepts the abscissa, and, in the second case, with the first quantum-confinement absorption maximum [11], if the correction for the asymmetry of the distribution of QDs by size is disregarded. The random error in determining E_g from the absorption spectra was no larger than 0.01 eV. The size variance occurs for the structures investigated. For this reason, the dependences presented in this paper correspond to medium-size QDs.

1063-7826/02/3602-0219$22.00 © 2002 MAIK "Nauka/Interperiodica"

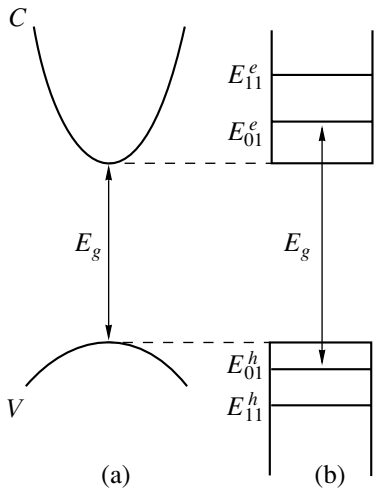

Fig. 1. (a) Band gap E_g for the bulk direct-gap semiconductor and (b) corresponding energy gap for a quantum dot with $\bar{r} < a_B$.

The experimental dependence $E_g(T)$ for a KS-19 glass with the CdS_xSe_{1-x} QDs ($\bar{r} \approx 7.63$ nm) is shown in Fig. 2a (squares). The corresponding dependence calculated for a bulk crystal is also shown in Fig. 2a by the dashed line. For the KS-19 glass with $\bar{r} > a_B$ (see table), the energy spectrum of the QDs is similar to the spectrum for bulk crystals and the dependence $E_g(T)$ is described by the Varshni formula [6]

$$E_g = E_0 - \alpha T^2 (T + \beta)^{-1} \quad (1)$$

over the entire temperature range investigated (Fig. 2). In formula (1), $E_0 = E_g$ at $T = 0$ K and α and β are constants, where α is usually identified with the temperature coefficient of the band gap $\partial E_g/\partial T$, while β is identified with the Debye temperature θ. It can be seen from formula (1) that $\Delta E_g \propto T^2$ at $T \gg \beta$ and $\Delta E_g \propto T$ at $T \gg \beta$. These specific features are clearly seen from Fig. 2a, namely, the dependence $E_g(T)$ is nonlinear at low temperatures, whereas the E_gg quantity linearly decreases with increasing T at high temperatures. The same dependence in Fig. 2b is also shown in the form $E_g = f[T^2/(T + \beta)]$, which permits the determination of the coefficients $\alpha \approx \partial E_g/\partial T$ with the relative error <6 % and <10 %, respectively. They are found to be close to corresponding values for bulk crystals of the same composition (see table and solid line in Fig. 2a).

The temperature dependences of the energy gap for glasses containing the $CdS_{0.32}Se_{0.68}$ QDs with $\bar{r} < a_B$ are shown in Fig. 3. Their energy spectrum consists of the set of discrete levels, whereas the quantum-confinement energy is ~0.25 eV [11]. In this case, the dependence $E_g(T)$ is linear over the entire temperature range and is not described by formula (1) in the range of 4.2–100 K (Fig. 3b). Furthermore, the coefficient $\lambda \approx \partial E_g/\partial T$ is much smaller than that for a bulk crystal and glass with QDs $\bar{r} > a_B$ (see table). This is also clearly seen from Fig. 3a, where the dashed line represents the corresponding dependence $E_g(T)$, which is calculated for a bulk crystal using formula (1).

For polar semiconductors CdS and CdSe, the electron–phonon interaction and distortion of the crystal lattice are considered as the main mechanisms of decreasing E_g with increasing T. On the other hand, it is known that the temperature dependence of the volume thermal expansion coefficient $\gamma(T)$ for these crystals has a clearly pronounced nonlinearity. The coefficient γ becomes negative in the temperature range of 4.2–200 K, and the dependence $\gamma(T)$) has an extremum. However, the dependence $E_g(T)$ for this temperature range varies steadily, which is indicative of an insignificant contribution of the lattice distortion to the decrease in E_g with increasing T. According to the data of various sources, the contribution of vibration anharmonicity to variation E_gg with temperature ranges from 1 to 25% [6, 13, 14].

For QDs, in contrast with bulk crystals, it is necessary to take into account the influence of anharmonicity on the quantum-confinement energy, which depends on the QD radius, and the variation of the band gap, which is associated with varying the pressure of the matrix [15]. Thus, for example, for the CdSe QDs with r = 3.00 nm, the increase in the temperature from 200 to 300 K (in the range where the γ coefficient is large) causes an increase in the radius along the C axis by 0.02 %. If we take into account the size dependence of

Parameters of quantum dots and bulk crystals CdS_xSe_{1-x}

Parameter	$Cd_{0.13}Se_{0.87}$		$CdS_{0.32}Se_{0.68}$	
	Quantum dots	Bulk crystal	Quantum dots	Bulk crystal
$\bar{r}$, nm	7.63	–	2.90	–
a_B, nm	–	5.09	–	4.48
$\partial E_g/\partial T$, 10^{-4} eV/K	–4.40 ± 0.10	–4.64*	–2.80 ± 0.15	–4.73*
β, K	143	143	–	163
θ, K	–	240* [9]	–	258* [9]

* The data are obtained by interpolation between the parameters for CdS and CdSe.

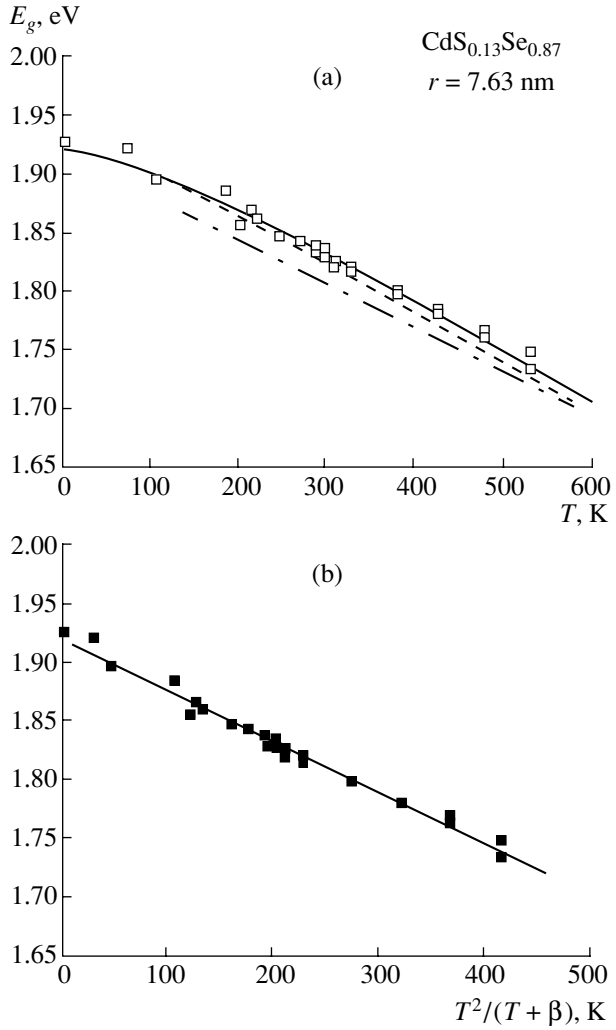

Fig. 2. Temperature dependences of the optical band gap for the $CdS_{0.13}Se_{0.87}$ quantum dots with $\bar{r} > a_B$. Points in (a, b) correspond to the experiment; solid lines in (a, b) represent the results of calculations with Varshni formula (1) for $\alpha = -4.40 \times 10^{-4}$ eV K^{-1} and β = 143 K; dashed line (a) was calculated using formula (1) for a single crystal; and dot-and-dash line (a) represents the same dependence with allowance made for the hydrostatic pressure of the glass matrix.

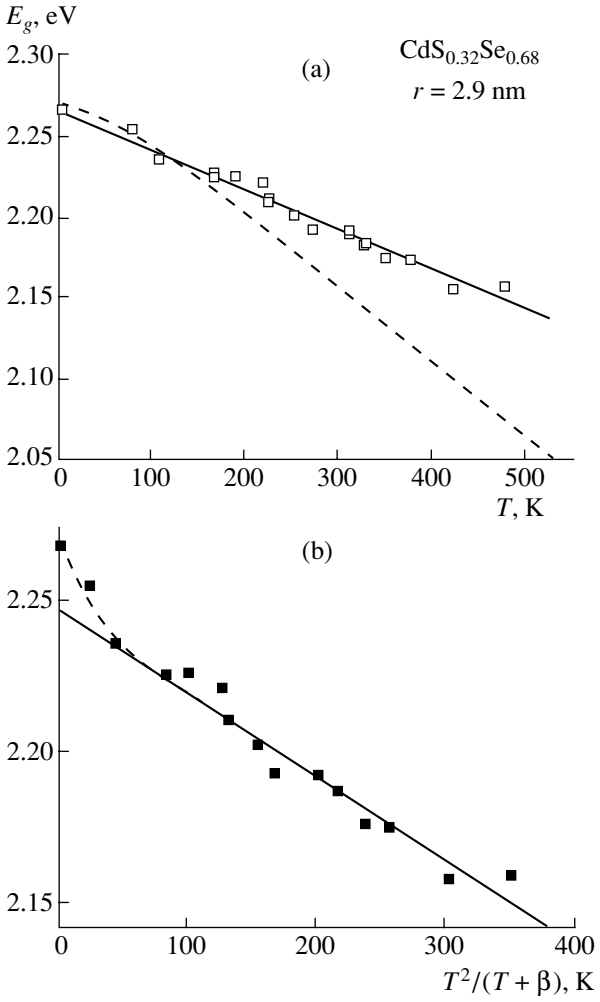

Fig. 3. Temperature dependences of the optical band gap for the $CdS_{0.32}Se_{0.68}$ quantum dots with $\bar{r} < a_B$. Squares (a, b) correspond to the experiment; solid line (a) was obtained after averaging by the least-squares method; dashed line (a) represents the calculation using Varshni formula (1) for a bulk crystal; and solid line (b) represents the calculation using the Varshni formula for quantum dots.

the lowest energy levels $(E_{01}^e)E_{01}^h$, this should lead to a decrease in E_g approximately by 0.0001 eV. In reality, for the temperature range mentioned, $\Delta E_g \approx 0.03$ eV; i.e., the relative contribution of the lattice distortion is 0.33 %, which correlates with the data for bulk crystals [13, 14]. Thus, we may assume that, similarly to bulk crystals, the electron–phonon interaction makes the major contribution to the dependence $E_g(T)$ for the CdS_xSe_{1-x} QDs in a borosilicate glass matrix.

In Fig. 2a, the dot-and-dash line also demonstrates the dependence $E_g(T)$ calculated with allowance made for the hydrostatic compression of QDs by the glass matrix [15]. In this case, the $\partial E_g/\partial T$ value is somewhat lower (-4.35×10^{-4} eV/K) compared to the value obtained with the pressure disregarded (-4.40×10^{-4} eV/K); i.e., the relative contribution of this effect is ~1.5 %.

Thus, as can be seen from Figs. 2 and 3, the coefficient $\partial E_g/\partial T$ decreases linearly with the transition from QDs with $\bar{r} > a_B$ to QDs with $\bar{r} < a_B$, whereas the dependence $E_g(T)$ becomes linear over a wide temperature range including low temperatures (4.2–100 K).

Basically, a decrease in the coefficient $\partial E_g/\partial T$ can be caused by weakening the electron–phonon interaction. However, by decreasing the radius of QDs to the polaron radius for a bulk crystal, the electron–phonon coupling constant increases [16], which contradicts the above assumption. On the other hand, it is evident that

a decrease in the QD volume reduces the total number of atoms (unit cells or oscillators) involved in vibrations (factor I) and leads to spatial limitation of the periodicity of elastic properties of the crystal lattice (factor II).

For sufficiently large crystals, boundary conditions (factor II) affect the vibration spectrum only slightly and can be neglected when analyzing the scattering processes. Such conditions can be realized easily even for macrocrystallites of diameter ~1 μm, whose vibration spectrum is identical to the spectrum of bulk crystals. For the QD with $r \approx a_B$, boundary conditions play an important role. If the surface atoms at opposite faces of the cubic QD oscillated in phase, this would be equivalent to the fulfilment of cyclic Born–Karman boundary conditions. In this case, no influence of the interface (size effects) on the vibration spectrum should be observed. However, even in this case, the spectrum could be modified under the effect of factor I, i.e., due to a decrease in the number of elementary oscillators.

For the actual situation, the condition for the cyclic recurrence of boundary conditions is not met and the phonon wave vector q is bounded from below; i.e.,

$$\frac{2\pi}{d} = \frac{\pi}{r} \le q \le \frac{\pi}{a}. \qquad (2)$$

Here, d is the QD diameter, and a is the lattice constant. It follows from condition (2) that, for a bulk crystal ($r \longrightarrow \infty$), $q_{min} \longrightarrow 0$. Thus, long elastic waves can be generated in such crystal. These waves are usually described in the continual approximation, in which case $q_{min} \longrightarrow \pi/a$; i.e., the phonon wave length in a solid is limited from the short-wave length side by the crystal lattice constant. The cutoff of the vibration spectrum of QDs from the long-wavelength side ($q_{min} > \pi/r$) is the reason why the acoustic waves with $\lambda \gg d$, for which $q \longrightarrow 0$, are not generated in QDs. The generation of such waves could be equivalent to the simple displacement of QDs, as a whole, in space. The reason is that, for $\lambda \gg d$, the displacement of atoms, which are located at a distance of the QD diameter, is negligible. Thus, the spatial restriction on periodicity of elastic properties of the crystal lattice for the QD (factor II) leads to the cutoff of the vibration spectrum from the side of small values of the wave vector, and to the accompanying restriction on the number of possible vibrational states for a given vibration mode. It is also necessary to remember that the phonon-state number for a crystal is governed by the unit cell number N and the atom number S per unit cell. Thus, the number of states is equal to $3SN$. For II–VI crystals, the unit cell contains two molecules (four atoms). For this reason, the total number of phonon states is equal to $12N$. As the QD radius decreases from ~7.6 to ~3.0 nm, the QD volume V (the number of unit cells of oscillators) decreases by 94%. This leads to a substantial decrease in the density of vibrational states ($\sim V/8\pi^3$).

The main phonon mechanism of carrier scattering in the CdS_xSe_{1-x} QDs is scattering by bulk longitudinal optical (LO) modes [16–18]. These modes manifest themselves in the first-order Raman spectra as rather intense peaks [19]. Scattering by surface optical modes, as well as by bulk and surface acoustic modes, is less efficient [18]. For QDs of smaller sizes ($\bar{r} < a_B$), a considerable decrease in the number of elementary oscillators (electrical dipoles in the case of LO modes, factor I) reduces the total electrical polarization of the lattice. As a consequence, the resulting macroscopic potential $V_j(\mathbf{r})$ decreases. This potential is a long-range one and appears in the total potential of the electron–phonon interaction along with the components which vary on the scale of the lattice constant. This leads to variation in the carrier energy. A decrease in $V_j(\mathbf{r})$ is equivalent to a decrease in the Lorenz field, which is proportional to $\mathbf{P}/3\varepsilon_0$, where $\mathbf{P}$ is the total polarization. The field at a specific point $\mathbf{r}_0$ is governed by the contribution from all other oscillators confined in the QD volume. On the other hand, the electrical polarization of the lattice is largest for the states with $q \longrightarrow 0$, whose number also decreases due to spatial-restriction effects (factor II).

Thus, we may assume that the main cause of a decrease in the coefficient $\partial E_g/\partial T$ for QDs with smaller size is a decrease in the QD volume and an associated decrease in the number of unit cells (oscillators). Variations in the vibration spectrum of QDs, with the spatial restriction on the periodicity of the elastic properties of their crystal lattice, also take place. Both factors decrease the resulting macroscopic potential, which governs the electron interaction with the lattice.

The linearity of the dependence $E_g(T)$ for glasses containing small-size quantum dots ($\bar{r} < a_B$) might be explained by a decrease in the Debye temperature in the context of the model described by the Varshni formula. In fact, setting $\beta = 0$ in formula (1), we obtain the linear calculated dependence. The assumption that the Debye temperature can decrease to zero ($\theta \longrightarrow 0$) was considered as far back as the 1950s [20, 21]. These papers were devoted to the theoretical consideration of decreasing the dimensionality of the solid; specifically, the chain and laminar crystals were considered. It was found that, if the interaction between the layers is weakened or is absent, the probability of propagation of elastic waves normally to the layers was lowered and tended toward zero. However, in this case, the statement that θ tends toward zero should be considered as an assumption only, which should be subjected to further experimental verification.

ACKNOWLEDGMENTS

This study was supported in part by the Soros International Foundation for the Support of Education in the Field of Exact Sciences (ISSEP), grant no. EPU 052023.

REFERENCES

1. H. Y. Fan, Phys. Rev. **82**, 900 (1951).
2. Ch. Keffer, T. M. Hayes, and A. Bienenstock, Phys. Rev. Lett. **21**, 1676 (1968).
3. Ph. Allen and V. Heine, J. Phys. C **9**, 2305 (1976).
4. B. Ridley, *Quantum Processes in Semiconductors* (Clarendon, Oxford, 1982; Mir, Moscow, 1986).
5. L. Brusaferri, S. Sanguinetti, E. Grilli, *et al.*, Appl. Phys. Lett. **69**, 3354 (1996).
6. Y. P. Varshni, Physica (Amsterdam) **34**, 149 (1967).
7. F. Adler, M. Geiger, A. Bauknecht, *et al.*, J. Appl. Phys. **83**, 1631 (1998).
8. N. R. Kulish, V. P. Kunets, and M. P. Lisitsa, Superlattices Microstruct. **22**, 341 (1997).
9. *Physicochemical Properties of Semiconducting Materials: A Handbook*, Ed. by S. A. Medvedev (Nauka, Moscow, 1979).
10. N. R. Kulish, V. P. Kuznets, M. P. Lisitsa, and N. I. Malysh, Ukr. Fiz. Zh. **37**, 1141 (1992).
11. V. P. Kunets, Semicond. Phys., Quantum Electron. Optoelectron. **2**, 23 (1999).
12. V. S. Oskotskiĭ, I. B. Kobyakov, and A. V. Solodukhin, Fiz. Tverd. Tela (Leningrad) **22**, 1478 (1980) [Sov. Phys. Solid State **22**, 861 (1980)].
13. N. V. Fomin, Fiz. Tekh. Poluprovodn. (Leningrad) **15**, 1625 (1981) [Sov. Phys. Semicond. **15**, 942 (1981)].
14. A. F. Revinskiĭ, Izv. Vyssh. Uchebn. Zaved., Fiz., No. 8, 3 (1996).
15. V. P. Kuznets, Ukr. Fiz. Zh. **43**, 64 (1998).
16. J. S. Marini, B. Stebe, and E. Kartheuser, Phys. Rev. B **50**, 14302 (1994).
17. E. Roca, C. Trallero-Giner, and M. Cardona, Phys. Rev. B **49**, 13 704 (1994).
18. Kasunori Oshiro, Koji Akai, and Mitsuru Matsuura, Phys. Rev. B **58**, 7986 (1998).
19. V. P. Kunets, N. R. Kulish, M. P. Lisitsa, *et al.*, Ukr. Phys. J. **45**, 164 (2000).
20. V. V. Tarasov, Zh. Fiz. Khim. **24**, 11 (1950).
21. L. M. Tarasova and V. V. Tarasov, Dokl. Akad. Nauk SSSR **107**, 719 (1956).

Translated by N. Korovin

Semiconductors, Vol. 36, No. 2, 2002, pp. 224–225. Translated from Fizika i Tekhnika Poluprovodnikov, Vol. 36, No. 2, 2002, pp. 232–233.
Original Russian Text Copyright © 2002 by Klimovskaya, Gule, Driga.

LOW-DIMENSIONAL SYSTEMS

The Dicke Superradiation in Quantum Heterostructures under Optical Pumping

A. I. Klimovskaya, E. G. Gule, and Yu. A. Driga

Institute of Semiconductor Physics, National Academy of Sciences of Ukraine, Kiev, 03028 Ukraine

Submitted December 5, 2000; accepted for publication July 11, 2001

1. INTRODUCTION

It is easy to produce a high density of exciton–dipoles in heterostructures with quantum wells by injection or optical pumping. Under conditions when the distance between dipoles becomes smaller than or comparable to the emission wavelength but considerably large to neglect the dipole–dipole interaction, their spontaneous phasing can occur in the field of the electromagnetic wave, which can result in the Dicke superradiation (SR) [1]. The SR was studied on many objects [2]. Recently, interest in SR has been associated with the development of long-wavelength lasers based on quantum InGaAs heterostructures. SR and its features in $In_{0.15}Ga_{0.85}As$-based structures was studied in [3–5] under pumping by current.

Results of SR studies in similar structures with various growth parameters (In concentration, quantum-well thickness, and doping level) are presented in this paper for conditions of optical pumping. It is shown that under excitation levels of <17 mW/mm^2, the spectra are satisfactorily described by a dependence which is characteristic of SR. A model is proposed on the effect of the δ-doping of a substrate on SR.

2. RESULTS AND DISCUSSION

We studied the spectra of spontaneous emission of heterostructures with a single $In_xGa_{1-x}As$ quantum well (QW) in GaAs grown by MOCVD (vapor-phase epitaxy from metal-organic compounds). The thicknesses of quantum layers were in the range d = 70–100 Å and In content x = 0.16–0.35. Several samples contained a d(Ge)-doped layer in the substrate at a distance of 300 Å from the QW. Optical pumping was produced by an He–Ne laser (wavelength 6328 Å), and the peak power of the beam was ~17 mW/mm^2. Photoluminescence (PL) spectra were recorded using a modified KSVU-23 system at a temperature of ~100 K. The excitation beam was attenuated by neutral filters. The spectra were measured from the sample surfaces; there were no special attempts at suppressing the lasing. However, a weak change of the external quantum efficiency and spectrum shape with the change of excitation intensity allows us to conclude that the lasing is absent.

Spectra of spontaneous emission $I(E)$ for various excitation levels are shown in the figure: for sample $S1$ with d = 84 Å and x = 0.16 and for sample $S2$ with d = 73 Å and x = 0.35 containing a δ-doped layer. The PL spectra for sample $S1$ and the low-energy wing of PL spectra for sample $S2$ are approximated in the figure by the following dependence:

$$I \approx A/\cosh\left(\pi\tau_N \frac{E - E_0}{\hbar}\right), \tag{1}$$

where $\hbar = h/2\pi$ is Planck's constant, E_0 is the spectral position of the PL peak (I_{max}), and τ_N is the time of the spontaneous cluster transition to an unexcited state. The time τ_N is expressed by the following formula [4]:

$$\tau_N = \tau_i/(N\mu + 1). \tag{2}$$

Here, N is the number of dipoles in a cluster, τ_i is the radiation time of a single cluster, and μ is the factor of the radiator shape. For the region of radiation of cylin-

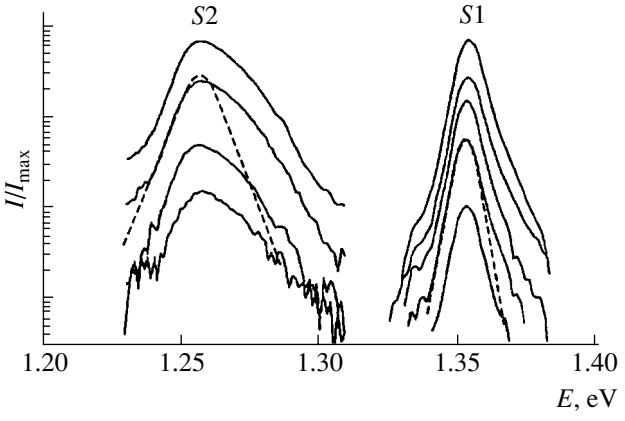

Photoluminescence spectra of heterostructures with a single quantum well under various excitation levels. Sample $S2$: $In_{0.35}Ga_{0.65}As$, d = 73 Å, δ(Ge)-doping, excitation level (from top to the bottom): 17, 6.8, 1.14, and 0.374 mW/mm^2; sample $S1$: $In_{0.16}Ga_{0.84}As$, d = 84 Å, excitation level (from top to the bottom): 17, 11.22, 5.61, 3.4, and 1.14 mW/mm^2. Dashed line is the approximation using expression (1).

1063-7826/02/3602-0224$22.00 © 2002 MAIK "Nauka/Interperiodica"

drical shape (the case under consideration), the form-factor is equal to [6]:

$$\mu = 3\lambda^2/8\pi S, \quad (3)$$

where λ is the emission wavelength, and S is the cylinder base.

The spectrum shape obtained experimentally is satisfactorily described by expression (1) (see figure, the dashed line), which is indicative of the fact that the main fraction of emission is caused by SR, though a fraction of incoherent radiation is present.

The dependence τ_N on the excitation intensity is plotted using the slope of the low-energy side of the spectra. The variation of power from 0.35 to 17 mW/mm^2 affects τ_N only slightly. Thus, we have $\langle\tau_N^{(1)}\rangle \approx (64.73 \pm 2.69)$ fs and $\lambda^{(1)} = 918$ nm for sample $S1$ and $\langle\tau_N^{(2)}\rangle \approx (38.39 \pm 3.92)$ fs and $\lambda^{(2)} = 992$ nm for sample $S2$.

Under conditions when the spectrum shape is mainly caused by superradiation, $N\mu \gg 1$ and $\tau_N = \tau_i/N\mu$. Using experimental values of τ_N and λ for $S1$ and $S2$ and taking into account a similar observation configuration, we find that τ_i/N for various samples differs by ~1.69 times. The causes of such a difference are the differences in τ_i and N. The difference in τ_i can be related to the type and number of defects, which are formed in structures of such type. As the defect concentration increases (formation of defects is caused by mismatch of lattice parameters and by the thickness of a quantum layer which exceeds the critical thickness [7]) in such a system, the carrier lifetime is abruptly reduced ($\tau_i^{(1)} \gg \tau_i^{(2)}$). However, proceeding from the line half-width, the lifetimes for these samples differ approximately by three times, whereas the ratios τ_i/N differ only by 1.69 times. This fact obviously indicates that the difference in N is important.

It is worthwhile to note that in the spectra of sample $S2$ (see figure), the high-energy wing of the spectrum is highly distorted. Obviously, this is caused by the filling of quantum subbands of the δ-layer. Proceeding from this fact, we may assume, as the explanation of the difference of the ratios τ_i/N, that, in the presence of a high concentration of free carriers caused by δ-doping in sample $S2$, interaction of dipoles with the electromagnetic field of the wave is weakened and the number of dipoles N, which form the cluster, is reduced. In the limiting case, when the free carrier concentration $n \longrightarrow \infty$, we have $N \longrightarrow 0$ and $\tau_N \longrightarrow \tau_i$; in this case, SR transforms into a normal spontaneous emission of independent dipoles.

The excess of free carriers weakens, to a significant extent, the coupling between dipoles. As a result, the emission fraction formed by SR is reduced, and the fraction of conventional spontaneous emission increases.

ACKNOWLEDGMENTS

We thank professor V.G. Litovchenko and professor P.M. Tomchuk for their fruitful participation in discussions of the results.

REFERENCES

1. R. H. Dicke, Phys. Rev. **93**, 99 (1954).
2. A. V. Andreev, V. I. Emel'yanov, and Yu. A. Il'inskiĭ, Usp. Fiz. Nauk **131** (4), 653 (1980) [Sov. Phys. Usp. **23**, 493 (1980)].
3. S. V. Zaĭtsev and A. M. Georgievskiĭ, Fiz. Tekh. Poluprovodn. (St. Petersburg) **32** (3), 366 (1998) [Semiconductors **32**, 332 (1998)].
4. A. M. Georgievskiĭ, S. V. Zaĭtsev, N. Yu. Gordeev, *et al.*, Fiz. Tekh. Poluprovodn. (St. Petersburg) **33** (7), 847 (1999) [Semiconductors **33**, 779 (1999)].
5. S. V. Zaĭsev, N. Yu. Gordeev, Z. A. Graham, *et al.*, Fiz. Tekh. Poluprovodn. (St. Petersburg) **33** (12), 1456 (1999) [Semiconductors **33**, 1309 (1999)].
6. R. Friedberg and S. R. Hartmann, Phys. Lett. A **37**, 285 (1971).
7. N. N. Grigor'ev, E. G. Gule, A. I. Klimovskaya, *et al.*, Ukr. Phys. J. **45** (7), 853 (2000).

Translated by T. Galkina

Semiconductors, Vol. 36, No. 2, 2002, pp. 226–229. Translated from Fizika i Tekhnika Poluprovodnikov, Vol. 36, No. 2, 2002, pp. 234–237.
Original Russian Text Copyright © 2002 by Zinov'ev, Andrianov, Nekrasov, Belyakov, Sreseli, Hill, Chamberlain.

LOW-DIMENSIONAL SYSTEMS

Electroluminescence from AlGaAs/GaAs Quantum-Cascade Structures in the Terahertz Range

N. N. Zinov'ev[1, 3], A.V. Andrianov[1], V. Yu. Nekrasov[1], L. V. Belyakov[1], O. M. Sreseli[1]^, G. Hill[2], and J. M. Chamberlain[3]

[1] *Ioffe Physicotechnical Institute, Russian Academy of Sciences, St. Petersburg, 194021 Russia*

[2] *Department of Electronic and Electrical Engineering, University of Sheffield, Sheffield, S10 2TN, United Kingdom*

[3] *IMP, School of Electronic and Electrical Engineering, University of Leeds, Leeds LS2 9JT, United Kingdom*

^e-mail: Olga.Sreseli@pop.ioffe.rssi.ru

Submitted August 21, 2001; accepted for publication August 29, 2001

Abstract—Electroluminescence from a quantum-cascade structure comprising 40 periods of GaAs/$Al_{0.15}Ga_{0.85}As$ tunnel-coupled quantum wells (QW) was studied. A terahertz emission band in the range 1.0–1.8 THz is observed under bias exceeding 1.5–2.0 V. The emission band peak shifts linearly to higher frequency with the increasing bias. The effect is accounted for by spatially indirect electron transitions between states in the neighboring QWs. © *2002 MAIK "Nauka/Interperiodica".*

1. INTRODUCTION

Currently, much attention is being given to studies of electromagnetic waves in the terahertz (or far-infrared) range. Terahertz radiation finds applications in tomographic systems, introscopy, microscopy, and image scanning systems in medicine, biology, communication, and monitoring systems. The available set of emission sources has been mainly limited to systems based on black-body radiation. Other available sources of the terahertz range, such as free-electron lasers, gas lasers optically pumped with a CO_2 laser, and *p*-Ge semiconductor lasers, have essential drawbacks, such as large dimensions, the impossibility of continuous tuning, or the necessity of using ultralow temperatures and strong magnetic fields. The lack of compact and wide-range sources for the terahertz range gave rise to the specific phenomenon of the "terahertz gap" (the range of electromagnetic waves ≈0.1–30 THz, access to which is difficult).

However, recently, it became rather probable that terahertz range emitters could be created on the basis of multi-period quantum-confinement semiconductor structures with electrical monopolar injection of charge carriers and intersubband radiative transitions. The original idea for this kind of emitter was put forward by Kazarinov and Suris in their pioneering work [1], soon after the discovery of superlattices by Esaki and Tsu [2]. The concept [1] presented a new principle of a monopolar semiconductor emitter, later named a quantum-cascade laser. The system of energy levels and the electronic kinetics in this emitter can be tailored purposefully by the appropriate selection of layer and barrier thicknesses in a quantum-cascade structure (QCS). The practical implementation of the idea [1] became possible only relatively recently (in the first half of the 1990s) and was accomplished for the mid-IR range [3, 4].

The approach developed in designing quantum-cascade lasers and QCSs for the mid-IR range will possibly enable the fabrication of far-IR range devices. Obtaining far-IR emission in radiative relaxation of quantum-confined electrons in QWs is complicated by the competing processes of phonon emission and electron–electron scattering [5]. However, far-IR electroluminescence (EL) from parabolic QWs was observed in several studies [6, 7]. Recently, spontaneous terahertz emission excited by an injection current has also been observed in a QCS in the temperature range 4–120 K [8, 9]. The emission efficiency achieved remains low, $\approx 10^{-12}$ W, at a current density of ≈10 A/cm^2 [8]. Therefore, a more detailed study of structures of this kind, with the structure parameters varied, is necessary for creating QCSs with optimal tunneling conditions.

The present study is concerned with EL from AlGaAs/GaAs QCSs based on tunnel-coupled QWs.

2. EXPERIMENTAL

The structures were grown by MBE on semi-insulating (100) GaAs substrates at the MBE EPSRC, University of Sheffield, UK. The structure comprises 40 periods, each containing four GaAs QWs separated by $Al_{0.15}Ga_{0.85}As$ tunneling barriers. The parameters of wells and barriers are presented in Figure 1. The structure terminates on each side in a n^+-GaAs layer ($n \approx 2 \times 10^{18}$ cm^{-3}) and a spacer of undoped GaAs, which make up a two-dimensional (2D) injection contact (Fig. 1). The active region of the structure is formed by 280-Å and 180-Å QWs separated by a 25-Å tunneling barrier. The neighboring QWs and barriers serve as, respec-

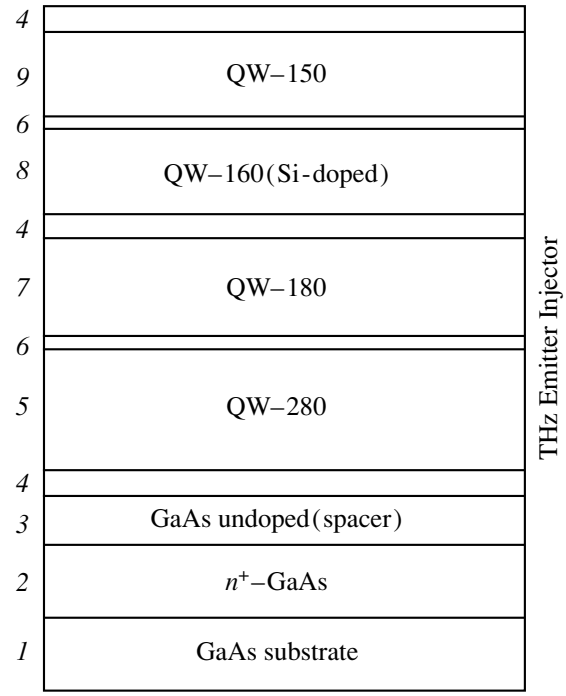

Fig. 1. First (bottom) of the 40 cascades of the emitting structure: (*1*) substrate, (*2*) low-resistivity GaAs layer (2 μm thick), (*3*) GaAs spacer, (*4*, *6*) $Al_{0.15}Ga_{0.85}As$ barriers, (*5*, *7*, *9*) GaAs QWs, and (*8*) GaAs:Si QW. The QW widths (Å) are given in the figure; barrier widths: (*4*) 40 and (*6*) 25 Å.

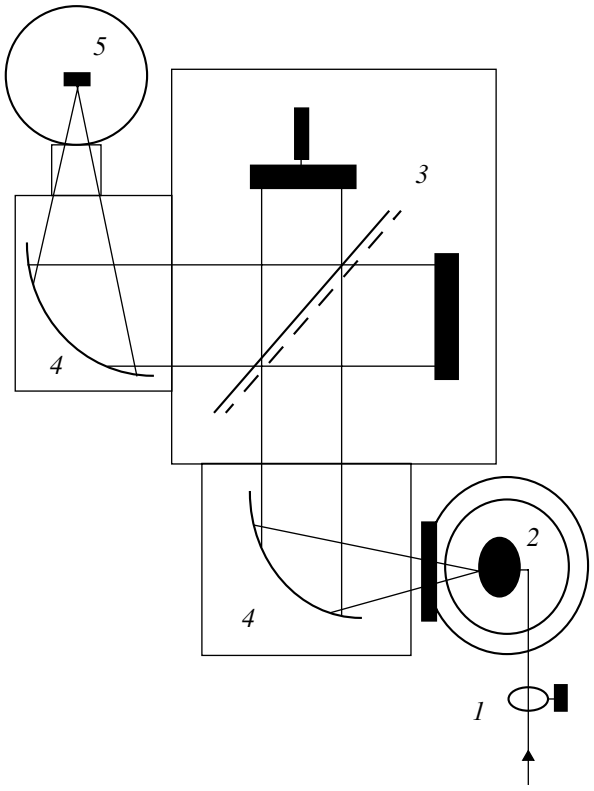

Fig. 2. Special-purpose Fourier spectrometer: (*1*) input for electric pulses, (*2*) liquid helium cryostat with the emitting structure, (*3*) Michelson interferometer, (*4*) parabolic mirrors, and (*5*) bolometer.

tively, an ejector of nonequilibrium electrons injected from the contact and their injector into the next active period of the structure. To suppress the influence of the space charge in the injection of nonequilibrium electrons, the 150-Å QWs were doped with silicon to $\approx 8 \times 10^{15}$ cm^{-3}.

Mesa structures ≈400 μm in diameter were formed on the samples. To extract the emission in the direction normal to the structure surface (perpendicularly to the QW plane), a metallic (Cr/Au) coupling grating with a 20-μm period was deposited onto the top contact layer and also served as the top electrical contact.

The samples under study were fixed on a copper cold finger of a liquid helium optical cryostat whose "warm" window was made of polyethylene. The bias was applied to the samples in the form of square pulses with 500-kHz repetition frequency (off-duty ratio of 2), modulated with low-frequency square pulses (80 Hz, off-duty ratio 2, modulation coefficient 1). This kind of bias was chosen to minimize the sample heating during measurements.

The EL was recorded with a Fourier spectrometer based on a Grubbs–Parsons instrument (Fig. 2). The emission from a sample was collected with an off-axis 90-degree paraboloid with relative aperture of 1 : 2. At the spectrometer output, the emission was focused onto the detector, also by an off-axis 90-degree paraboloid with relative aperture of 1: 6. The internal volume of the spectrometer and paraboloid units was evacuated to prevent the influence of water vapor absorption on the measurement results. The far-IR radiation was detected with a QMS Si-detector cooled with liquid helium, with an input optical band filter ensuring the detector operation in the spectral range 2–400 cm^{-1}. The detected signal was recorded at a frequency of 80 Hz by means of a lock-in amplifier. The movable mirror of the Fourier spectrometer was shifted by a precision step motor. The step motor control, recording of the lock-in amplifier signal, control of the amplitude of electrical bias pulses applied to the structures, and fast Fourier transform of the interference patterns were computerized.

The equipment sensitivity to the far-IR radiation was checked by recording EL spectra of test samples in the form of parabolic QWs, which were studied in detail, e.g., in [6]. Figure 3 shows the EL spectrum of a 140-nm-wide parabolic well. A narrow single line is observed with a peak at 78.9 cm^{-1} (2.368 THz), which is in close agreement with the data reported in [6]. The line half-width is about 5.6 cm^{-1}, which, in fact, corresponds to the spectral resolution of the employed instrument.

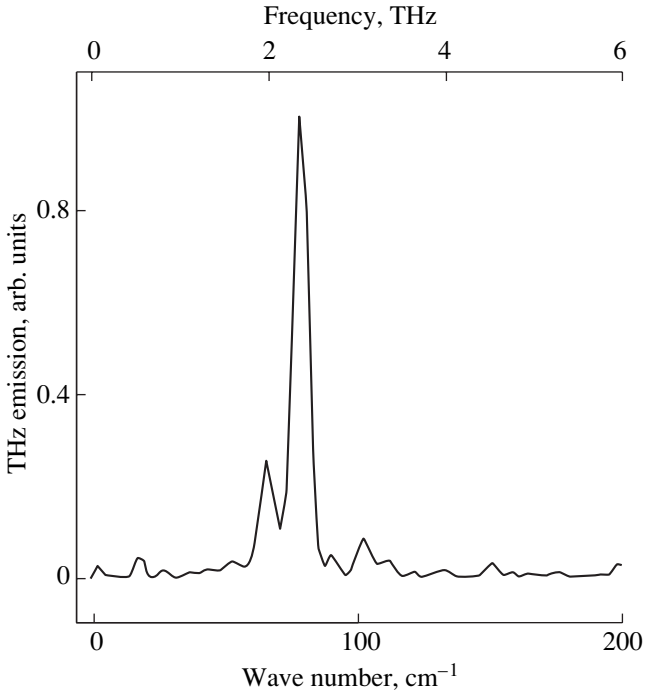

Fig. 3. Emission spectrum of a GaAs/AlGaAs test structure with parabolic QW.

3. RESULTS AND DISCUSSION

With forward bias applied to the QCS studied (with top contact positive and substrate negative) and zero path-length difference between the interferometer arms, an integral terahertz emission was detected, with the spectral range limited by the filter at the bolometer entrance (2–400 cm^{-1}). The detected signal vanished if the exit window of the cryostat was blocked with a metal plate or appropriate filters. Figure 4 shows the integral signal as a function of the bias applied across the structure. At low bias (<1 V), the signal is obscured by noise. With bias raised to 4–9 V, the signal-to-noise ratio is considerably improved, reaching 10 or more (Fig. 4).

Figure 5 presents the terahertz emission spectra recorded under forward and reverse bias of 5.5 V. As seen, the principal contribution to the EL spectrum is made by the band peaked at 48.8 cm^{-1} (6.05 meV or 1.46 THz), with a half-width of about 30 cm^{-1}. This kind of spectrum differs significantly from that reported in [8], where a QCS with similar parameters was studied, but the obtained emission line was narrow, with a peak at 113.6 cm^{-1}. This line was attributed in [8] to transitions between the first and second quantum-confinement subbands in a 280-Å-wide QW.

To improve the injection efficiency, the thickness of the tunneling barriers in our structures was reduced to 40 Å (compared with 60 Å in [8]). Making the injection barrier thinner should have also allowed the observation of not only direct but also indirect (in real space) optical transitions between the lower states in neighboring wells.

To discriminate among the transition types, we studied the dependence of the emission peak position on the applied bias (Fig. 6). This dependence can be approxi-

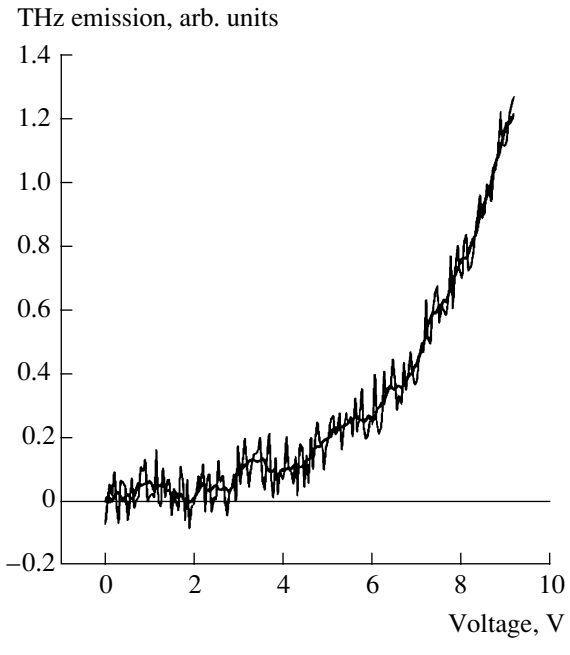

Fig. 4. Terahertz emission intensity vs. the bias V across the structure. Transmission window of the input filter 2–400 cm^{-1}, T = 7–13 K.

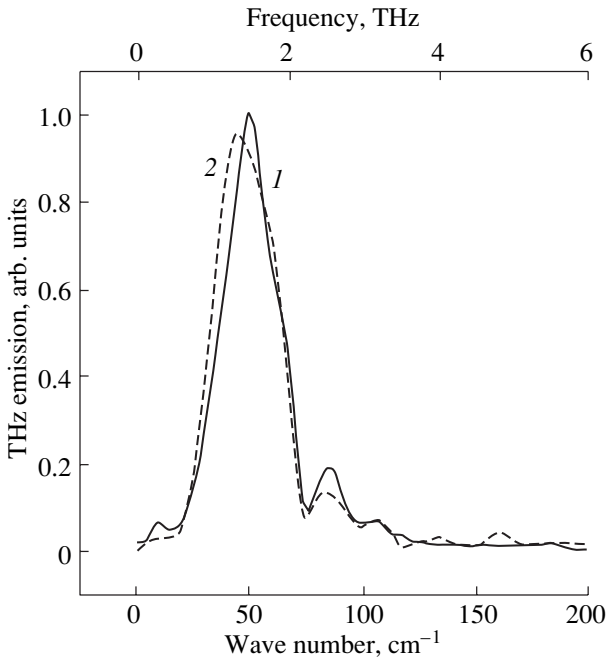

Fig. 5. Terahertz emission spectra of a QCS, V = 5.5 V, T = 7 K: (*1*) forward bias (with the structure positive), (*2*) reverse bias.

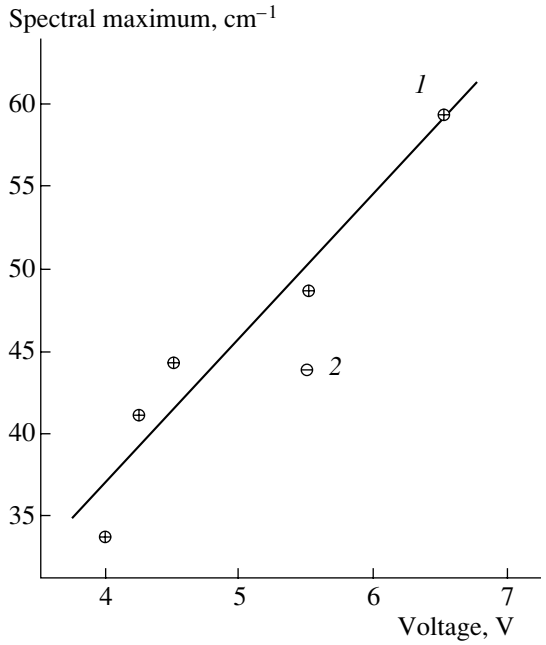

Fig. 6. Spectral position of the terahertz emission peak ν_{max} vs. the applied bias *V*.

mated by a linear function with ~8.9 cm^{-1}/V rate of peak frequency rise. The linear dependence of the emission peak position on the applied bias indicates that the observed band originates from emission in indirect (in real space) electron transitions in the QCSs. These may be transitions between the ground state in the 280-Å well and ground states in the neighboring wells. With account of the 0.5–1 V voltage drop across the contacts, an external voltage of 1.5–2 V should be applied across a 40-cascade structure to level the lowest states in the neighboring wells of the QCS' active region. It is noteworthy that the EL intensity starts to rise at biases close to this value (Fig. 4).

The integral power of the terahertz emission from the QCSs under study, estimated with account of the emission collection efficiency, is about 2 nW at a 5.5 V bias across the structure and a supplied electric power of 700 mW, which corresponds to a quantum efficiency of emission of about 3×10^{-9}. The higher emission power, compared with that in [8], may be the result of the use of 2D-injection contacts to QCSs and thinner injection barriers.

4. CONCLUSION

A band of terahertz EL, peaked at 48.8 cm^{-1} (1.46 THz), was observed in quantum-cascade structures containing GaAs/AlGaAs tunnel-coupled QWs at a 5.5 V bias across the structure. The band shifts nearly linearly to higher frequencies with increasing bias. The observed effects are attributed to spatially indirect electron transitions between the ground state in the wide well and ground states in the neighboring wells.

ACKNOWLEDGMENTS

This study was supported in part by INTAS (grant no. 97-0856); the Russian Foundation for Basic Research within the "Scientific School" Program (project no. 00-15-96750); and the Program "Quantum-Well Nanostructures." N.N. Zinov'ev is grateful to EPSRC for supporting his stay in the UK.

REFERENCES

1. R. F. Kazarinov and R. A. Suris, Fiz. Tekh. Poluprovodn. (Leningrad) **5**, 797 (1971) [Sov. Phys. Semicond. **5**, 707 (1971)]; Fiz. Tekh. Poluprovodn. (Leningrad) **6**, 148 (1972) [Sov. Phys. Semicond. **6**, 179 (1972)].
2. L. Esaki and R. Tsu, IBM J. Res. Dev. **14**, 61 (1970).
3. J. Faist, F. Capasso, D. L. Sivco, *et al.*, Science **264**, 553 (1994).
4. F. Capasso, J. Faist, S. Sirtori, and A. Y. Cho, Solid State Commun. **102**, 231 (1997).
5. P. Hyldgaard and J. W. Wilkins, Phys. Rev. B **53**, 6889 (1996).
6. K. D. Maranovski, A. C. Gossard, K. Unterrainer, and E. Gornik, Appl. Phys. Lett. **69**, 3522 (1996).
7. J. Ulrich, R. Zobl, K. Unterrainer, *et al.*, Appl. Phys. Lett. **74**, 3158 (1999).
8. M. Rochat, J. Faist, M. Beck, *et al.*, Appl. Phys. Lett. **73**, 3724 (1998).
9. M. Rochat, J. Faist, M. Beck, and U. Oesterle, Physica E (Amsterdam) **7**, 44 (2000).

Translated by D. Mashovets

Semiconductors, Vol. 36, No. 2, 2002, pp. 230–234. Translated from Fizika i Tekhnika Poluprovodnikov, Vol. 36, No. 2, 2002, pp. 238–243.
Original Russian Text Copyright © 2002 by Afanas'ev, Gudovskikh, Nevedomskiĭ, Sazanov, Sitnikova, Trapeznikova, Terukov.

AMORPHOUS, VITREOUS, AND POROUS SEMICONDUCTORS

Effect of Thermal Treatment on Structure and Properties of *a*-Si:H Films Obtained by Cyclic Deposition

V. P. Afanas'ev*, A. S. Gudovskikh*, V. N. Nevedomskiĭ, A. P. Sazanov*, A. A. Sitnikova**, I. N. Trapeznikova**^, and E. I. Terukov****

** St. Petersburg State University of Electrical Engineering, St. Petersburg, 197376 Russia*

*** Ioffe Physicotechnical Institute, Russian Academy of Sciences, St. Petersburg, 194021 Russia*

^e-mail: trapez@pop.ioffe.rssi.ru

Submitted May 11, 2001; accepted for publication May 31, 2001

Abstract—The effect of thermal treatment in a vacuum on the structure and properties of amorphous hydrogenated silicon (*a*-Si:H) films obtained by cyclic deposition with intermediate annealing in hydrogen plasma was studied. *a*-Si:H films deposited under optimal conditions are characterized by the nonuniform distribution of the nanocrystalline phase (<1 vol %) across the film thickness and have the optical gap E_g = 1.85 eV, the activation energy of conductivity E_a = 0.91 eV, and a high photosensitivity ($\sigma_{ph}/\sigma_d \approx 10^7$ under illumination of 100 mW/cm^2 in the visible spectral range). Transmission electron microscopy studies demonstrated that thermal treatment in a vacuum leads to blurring of the initial layered structure of *a*-Si:H films and to a somewhat higher amount of nanocrystalline inclusions in the amorphous phase matrix. Thermal treatment above 350°C causes a dramatic increase in the dark conductivity, as well as the resulting decrease in the photosensitivity, of *a*-Si:H films. © *2002 MAIK "Nauka/Interperiodica".*

1. INTRODUCTION

The wide diversity of applied problems of optoelectronics requires that the number of materials used, which are frequently of an unconventional nature, should be steadily increased. Amorphous hydrogenated silicon (*a*-Si:H), which possesses high photoconductivity, can be effectively doped, is characterized by low temperature of deposition onto virtually any substrate, and can be easily deposited in the form of large-area films [1], belongs to materials of this kind. However, problems of obtaining *a*-Si:H films with stable characteristics have not been solved, and specific features of their behavior in relation to deposition modes and subsequent treatment are unclear.

One of the ways to obtain high-quality *i*-type *a*-Si:H layers at comparatively low substrate temperatures (200–280°C) consists in the use of an intermittent (cyclic) deposition mode in which plasma chemical deposition of an *a*-Si:H film of thickness 1–10 nm from a gas mixture with monosilane alternates with its treatment in hydrogen plasma [2]. It has been noted that optimization of the deposition time to treatment duration ratio allows a significant improvement of the photosensitivity of *i*-type layers [2–4]. It was shown in our previous studies [5] that the use of intermediate annealing in hydrogen plasma in cyclic deposition of *a*-Si:H films leads to their enrichment in hydrogen and is accompanied by an increase in photosensitivity, the optical gap, and activation energy of dark conductivity. The optimal thicknesses of layers exhibiting the maximum sensitivity, optical gap, and activation energy of dark conductivity on being subjected to hydrogen plasma treatment were determined to be 14–16 nm [6]. As shown by transmission electron microscopy (TEM) studies [7], the obtained *a*-Si:H films were characterized by a clearly pronounced layered structure associated with the nonuniform distribution of nanocrystallites across the film thickness. High-temperature annealing in a vacuum (at temperatures exceeding 350°C) substantially changes both the structure and the conductivity of *a*-Si:H films [8].

However, a number of phenomena, such as the high photosensitivity of *a*-Si:H films with nanocrystalline phase [9, 10], the specific behavior of their spectral characteristics [5, 6, 9], and structural changes upon thermal treatment, have not been explained satisfactorily so far. The performed investigations of the effect of thermal treatment on the structure and properties of amorphous hydrogenated silicon films obtained by cyclic deposition give new insight into their specific behavior.

2. SAMPLE PREPARATION TECHNOLOGY AND MEASUREMENT TECHNIQUE

Undoped *a*-Si:H films were obtained on glass-ceramic, quartz, and silicon substrates by cyclic plasma chemical deposition in an rf diode system (13.56 MHz). *a*-Si:H layers of nanometer thickness were deposited in the previously chosen optimal technological mode of cyclic deposition in a fixed gas mixture (80% Ar + 20% SiH_4) [5]: substrate temperature 250°C, rf dis-

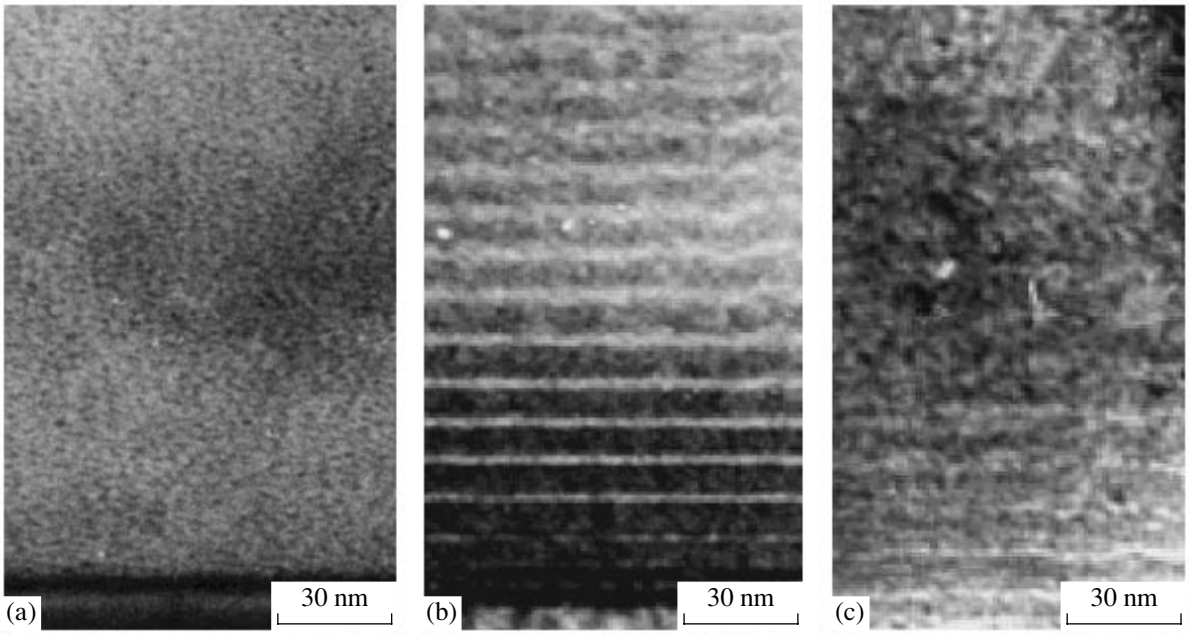

Fig. 1. Cross-sectional TEM images of *a*-Si:H films: (a) film deposited in a gas mixture with fixed composition, (b) film deposited by the cyclic method with annealing in hydrogen plasma, and (c) film deposited by the cyclic method and then annealed in a vacuum at 450°C for 1 h.

charge power 40 W, rotation speed of substrate holder drum 4 rpm, and gas mixture pressure 25 Pa.

In the course of cyclic deposition, leak valves were used to vary the composition of the gas mixture, which predetermined the times of deposition (t_{dep}) and thermal treatment (t_{tr}). In the experiment, the thickness of *a*-Si:H layers deposited in a cycle was varied between 6 and 26 nm, whereas the annealing time was fixed at 2 min. A steady-state composition was attained in several tens of seconds, i.e., in a time comparable with the times of deposition and annealing. This circumstance created fundamentally nonequilibrium conditions of film formation.

To determine the dark conductivity σ_d and photoconductivity σ_{ph} of *a*-Si:H films, thin-film resistors were formed on glass-ceramic substrates with the use of aluminum electrodes with an interelectrode spacing of 0.2 mm and form factor of 0.018. The photoconductivity was studied in the visible spectral range under an incident radiation power of 100 mW/cm^2 [8]. The activation energies of conductivity were found from temperature dependences of dark conductivity. Normalized photoconductivity spectra were measured with an MDR-3 monochromator.

Structural features of the films were studied by TEM.

3. EXPERIMENTAL RESULTS AND DISCUSSION

Figure 1 presents cross-sectional TEM images of different *a*-Si:H films. It can be seen that the film deposited in the continuous mode (Fig. 1a) is structurally uniform across the thickness. The structural uniformity of such films is also indicated by high-energy electron diffraction. The radial distribution function clearly shows the first and second coordination spheres for the Si–Si bond, whereas the third coordination shell for Si–Si with a bond length of 0.45 nm is poorly pronounced.

Films deposited in the cyclic mode with annealing of 16-nm-thick layers in hydrogen plasma show a clearly pronounced layered structure with a step corresponding to the thickness of the *a*-Si:H layer deposited in a single cycle (Fig. 1b). It is noteworthy that films deposited by the cyclic method with a layer thickness of 16 nm per cycle are optimal as regards their electrical parameters [6]. The observed contrast is due to the presence of a crystalline phase at interfaces between the layers, which is presumably formed during intermediate annealing in hydrogen plasma. Upon annealing in a vacuum at 450°C for 1 h, the layered structure of *a*-Si:H films obtained in the cyclic mode is markedly blurred (Fig. 1c), and annealing at 550°C for 1 h makes the film virtually uniform across its thickness.

The presence of crystalline inclusions in the amorphous *a*-Si:H matrix is confirmed by plan-view TEM images of films (Fig. 2). Analysis of the micrographs makes it possible not only to determine the size of nanocrystalline Si inclusions in the amorphous matrix, but also to plot histograms of the size distribution of these inclusions (Fig. 2) and evaluate the volume fraction of the nanocrystalline phase. For example, for an *a*-Si:H film obtained in the cyclic mode with the use of intermediate annealing in hydrogen plasma of 16-nm-

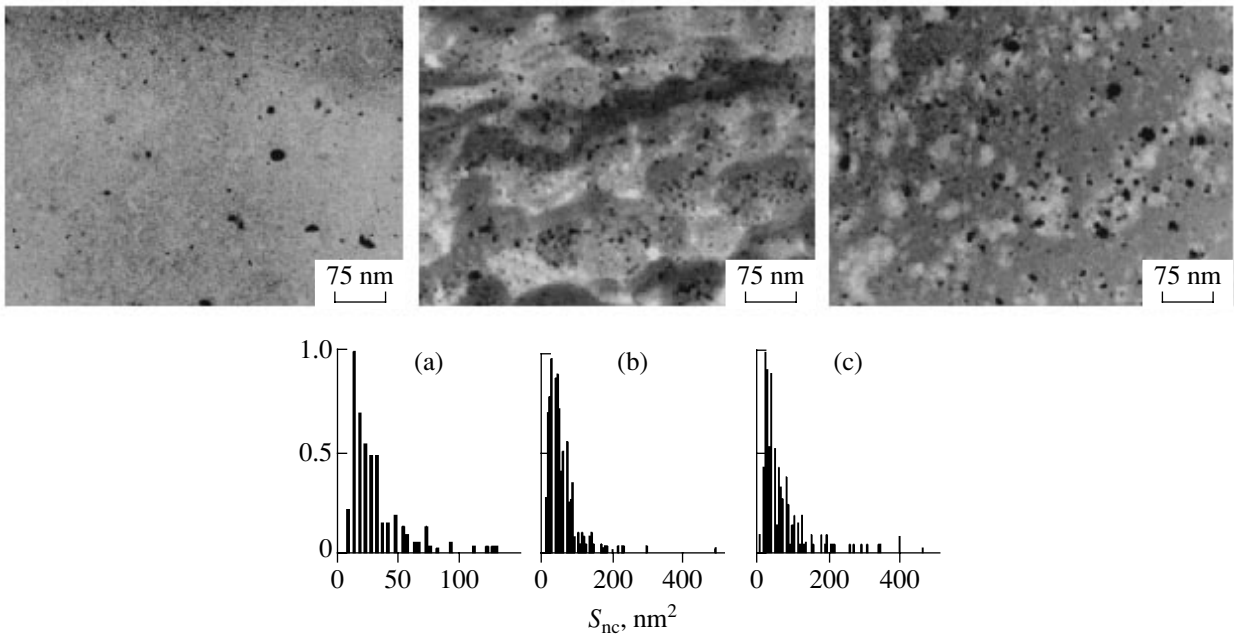

Fig. 2. Plan-view TEM images and the corresponding histograms of the cross-section area (S_{nc}) distribution of nanocrystallites for *a*-Si:H films: (a) immediately after deposition by the cyclic method and after subsequent annealing in a vacuum for 1 h at (b) 450 and (c) 550°C.

thick layers, the average cross-section area of nanocrystallites immediately after deposition is ~20 nm^2 and their average diameter is 4.5 nm (Fig. 2a). The volume fraction of the nanocrystalline inclusions in such a film is less than 1%. Because of such a small volume fraction, the nanocrystalline phase cannot be revealed in Raman spectra.

For *a*-Si:H films annealed at 450 and 550°C (Figs. 2b and 2c), the size and number of nanocrystalline inclusions increase somewhat. For example, the average cross-section area of nanocrystallites grows from 20 to 60 nm^2 upon annealing at 450°C and to 75 nm^2 upon annealing at 550°C. This corresponds to an increase in the average diameter from 4–5 to approximately 8–9 nm. It should be noted that crystallization in the films is strongly hindered, which is indicated by the small change in the volume fraction of the nanocrystalline phase upon high-temperature treatment. Even upon annealing at 550°C, this fraction increases approximately twofold and does not exceed 2% (Fig. 2c), which, as in the above case, gives no way of detecting the presence of the nanophase by Raman spectroscopy. It should be noted that at a nearly twofold increase in the volume fraction of nanocrystals, their size distribution represented by the histograms changes only slightly and no significant shift of the distribution density to larger sizes is observed. This indicates that, upon annealing at 550°C, the volume fraction of nanocrystals grows because of their increasing number, rather than growing size. Therefore, the blurring of the layered structure after thermal treatment in a vacuum can be accounted for by the disappearance of a part of the nanocrystallites at interfaces between layers and their nucleation across the entire film thickness.

With increasing temperature of thermal treatment, effusion of hydrogen occurs, with its content in a *a*-Si:H film decreasing from 15–17 at. % in the initial film to 12 and 6.5 at. % after thermal treatment at, respectively, 350 and 450°C. At thermal treatment temperatures exceeding 500°C, the content of hydrogen in a film becomes less than 1 at. % [8]. The hydrogen effusion is accompanied by a decrease in the activation energy of conductivity from 0.89 to 0.75 eV. Annealing at temperatures higher than 350°C leads to a dramatic increase in dark conductivity, a decrease in photoconductivity, and the resulting drop in the photosensitivity of *a*-Si:H films (Fig. 3). Apparently, such a small volume fraction of the nanocrystalline phase cannot lead to an increase in conductivity in terms of the percolation theory [11]. Therefore, the rise in the dark conductivity σ_d is presumably due to an increase in the density of states in the *a*-Si:H film.

An interesting feature of *a*-Si:H films obtained by cyclic deposition is the presence of two peaks in the spectral characteristic of photoconductivity (Fig. 4). It should be noted that the short-wavelength peak is shifted to shorter wavelengths with decreasing thickness of the *a*-Si:H layer deposited in a single cycle. Such behavior of the spectral dependence can be accounted for by the increasing content of hydrogen at interfaces between layers, which may lead to a local rise in the energy gap in the *a*-Si:H film. As noted in [12], changing the content of hydrogen leads to an

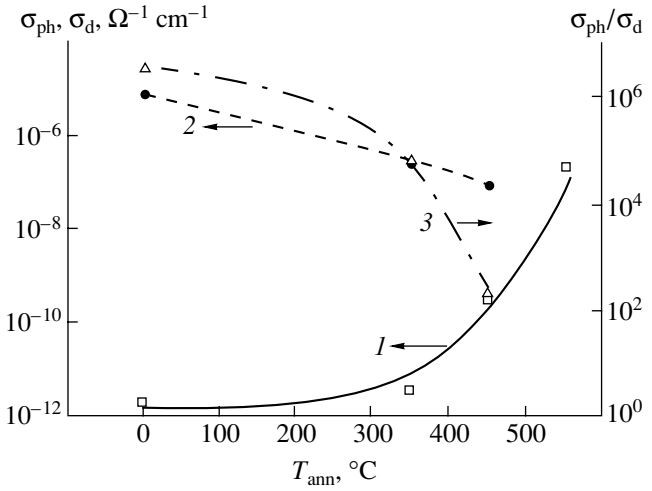

Fig. 3. (*1*) Dark conductivity σ_d; (*2*) photoconductivity σ_{ph}; and (*3*) ratio of these, σ_{ph}/σ_d, vs. temperature T_{ann} of annealing in a vacuum of *a*-Si:H films deposited in the 16-nm-per-cycle mode.

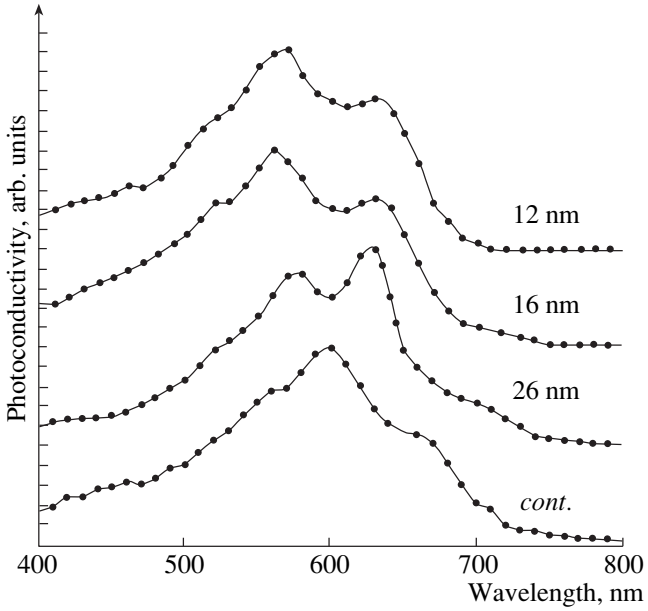

Fig. 4. Photoconductivity spectra of *a*-Si:H films obtained in a gas mixture with fixed composition (curve denoted by *cont.*) and by cyclic deposition with 26-, 16-, and 12-nm-thick layers deposited in a cycle.

increase in the energy gap to 2.1 eV. It may be assumed that an envelope with a high content of hydrogen (up to 20 at. %) [13] is formed around each nanocrystallite, creating a kind of cluster with a size markedly exceeding that of the nanocrystalline phase. Thus, the contribution to short-wavelength photosensitivity may be significantly enhanced. Such an explanation eliminates the contradiction between the small volume fraction of the nanocrystalline phase and its contribution to photoconductivity via photogeneration of carriers in the nanocrystalline phase whose energy gap is around 2.3 eV [9].

The proposed model is confirmed by a study of the photoconductivity spectra of *a*-Si:H films subjected to thermal treatment in a vacuum at different temperatures (Fig. 5). It can be seen that the photosensitivity peaks are shifted to longer wavelengths with increasing temperature of thermal treatment, which can be accounted for by effusion of hydrogen from the *a*-Si:H film.

One more result of importance obtained in the performed investigations is that the use of the cycling method improves the stability of *a*-Si:H films. Figure 6 shows the kinetics of photoinduced degradation of the normalized photoconductivity under illumination of 90 mW/cm^2 for *a*-Si:H films obtained in the continuous and cyclic modes. For the *a*-Si:H films grown using the cycling deposition technique with annealing in hydrogen plasma, the Staebler–Wronski effect is much less pronounced. A similar result was reported in [14], where virtually no Staebler–Wronski effect was observed in nanostructured *a*-Si:H films. It should be noted that, as regards the time stability, the optimal case is represented by *a*-Si:H films with 16-nm-thick layers deposited in a cycle. A specific feature of such films is that, retaining high photosensitivity, the density of states of these films in the mobility gap is about 30% higher than that in films obtained in the continuous mode. Annealing in a vacuum at 350°C for 1 h makes the photoinduced degradation of *a*-Si:H films even less

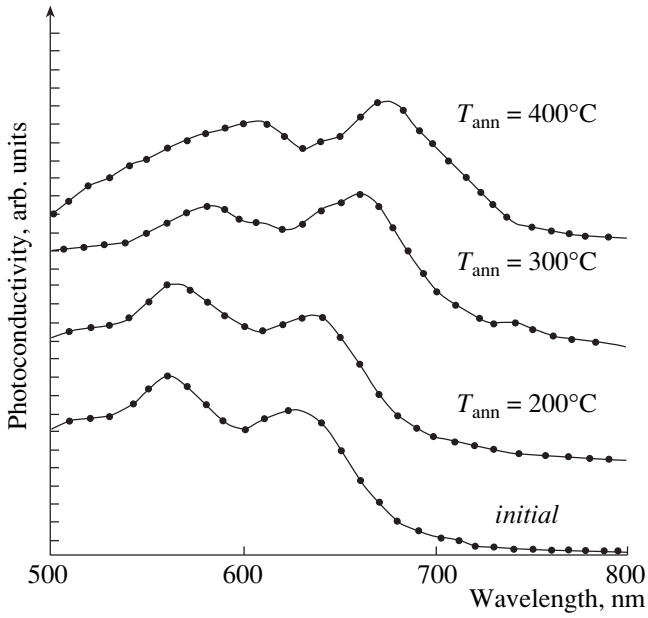

Fig. 5. Photoconductivity spectra of *a*-Si:H film obtained by cyclic deposition with 16-nm-thick layer deposited in a cycle, immediately after deposition (*initial*), and after annealing in a vacuum at temperatures T_{ann} indicated in the figure.

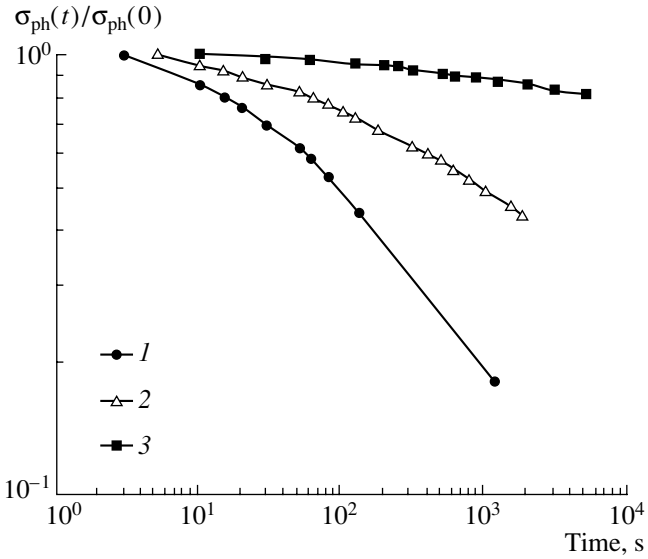

Fig. 6. Photoconductivity degradation under illumination of 90 mW/cm^2 for films obtained (*1*) in gas mixture of fixed composition and those grown by the cyclic deposition method (with 16-nm-thick layer deposited in a cycle), (*2*) immediately after deposition, and (*3*) after annealing in a vacuum at 350°C for 1 h.

pronounced, with the σ_{ph}/σ_d ratio remaining equal to 8×10^4 (Fig. 6).

4. CONCLUSION

Thermal treatment of *a*-Si:H films with a layered structure in a vacuum at 450°C leads to blurring of the initial structure, and at 550°C the film becomes virtually uniform across its thickness. It may be assumed that, in the course of thermal treatment, crystallites are redistributed over the film volume, with part of the nanocrystallites at layer boundaries collapsing and new nanocrystallites nucleating within the layers. It should be noted that upon thermal treatment at 550°C the crystallite size and the volume fraction of the nanocrystalline phase change by no more than a factor of 2, whereas the content of hydrogen in a film decreases from 17 to less than 1 at. %.

The presence of two peaks in the spectral dependence of photoconductivity is due to the nonuniform distribution of hydrogen in the *a*-Si:H film. This conclusion is confirmed by the shift of the short-wavelength peak to shorter wavelengths with decreasing thickness of layers deposited in a cycle, associated with the increasing fraction of hydrogen at interfaces. In addition, with the annealing temperature raised to 400°C, thermal treatment in a vacuum leads to a steady shift of the peaks of spectral characteristics to longer wavelengths, which is unambiguously due to a decrease in the hydrogen content of *a*-Si:H films. When annealed at 550°C, an *a*-Si:H film entirely loses its photosensitivity and its dark conductivity increases by more than 5 orders of magnitude.

It was established that *a*-Si:H films obtained using the cyclic deposition method possess higher stability under prolonged illumination; i.e., the Staebler–Wronski effect is less pronounced in these films, compared with those deposited in the continuous mode. In our opinion, this is due to the presence of the nanocrystalline phase in layered *a*-Si:H films.

ACKNOWLEDGMENTS

This study was supported by the Ministry of Education of the Russian Federation (grant no. TOO-2.2-2259).

REFERENCES

1. *Amorphous Semiconductor Technologies and Devices*, Ed. by Y. Hamakawa (Ohmsha, Tokyo, 1981; Metallurgiya, Moscow, 1986).
2. A. Asano, Appl. Phys. Lett. **56** (6), 533 (1990).
3. S. Okamoto, Y. Hishikawa, S. Tsuge, *et al.*, Jpn. J. Appl. Phys. **33** (4A), 1773 (1994).
4. S. Koynov, Jpn. J. Appl. Phys. **33** (8), 4534 (1994).
5. V. P. Afanas'ev, A. S. Gudovskikh, A. P. Sazanov, *et al.*, Mater. Élektron. Tekh., No. 4, 29 (1999).
6. V. P. Afanas'ev, A. S. Gudovskikh, O. I. Kon'kov, *et al.*, Fiz. Tekh. Poluprovodn. (St. Petersburg) **34**, 495 (2000) [Semiconductors **34**, 477 (2000)].
7. V. N. Nevedomskiĭ, A. A. Sitnikova, I. N. Trapeznikova, *et al.*, in *Proceedings of the II International Conference "Amorphous and Microcrystalline Semiconductors", St. Petersburg, 2000* (S-Peterb. Gos. Tekh. Univ., St. Petersburg, 2000), p. 40.
8. I. A. Kurova, N. N. Ormont, E. I. Terukov, *et al.*, Fiz. Tekh. Poluprovodn. (St. Petersburg) **35**, 367 (2001) [Semiconductors **35**, 353 (2001)].
9. O. A. Golikova and M. M. Kazanin, Fiz. Tekh. Poluprovodn. (Leningrad) **33**, 110 (1999) [Semiconductors **33**, 97 (1999)].
10. C. Longeaud, J. P. Kleider, P. Roca i Cabarrocas, *et al.*, J. Non-Cryst. Solids **227-230**, 96 (1998).
11. V. G. Golubev, L. E. Morozova, A. B. Pevtsov, and N. A. Feoktistov, Fiz. Tekh. Poluprovodn. (St. Petersburg) **33**, 75 (1999) [Semiconductors **33**, 66 (1999)].
12. O. A. Golikova, E. V. Bogdanova, M. M. Kazanin, *et al.*, Fiz. Tekh. Poluprovodn. (St. Petersburg) **35**, 600 (2001) [Semiconductors **35**, 579 (2001)].
13. Yu. He, Ch. Yin, G. Cheng, *et al.*, J. Appl. Phys. **75**, 797 (1994).
14. O. A. Golikova, M. M. Kazanin, A. N. Kuznetsov, and E. V. Bogdanova, Fiz. Tekh. Poluprovodn. (St. Petersburg) **34**, 1125 (2000) [Semiconductors **34**, 1085 (2000)].

Translated by M. Tagirdzhanov

Semiconductors, Vol. 36, No. 2, 2002, pp. 235–238. Translated from Fizika i Tekhnika Poluprovodnikov, Vol. 36, No. 2, 2002, pp. 244–247.
Original Russian Text Copyright © 2002 by Kyuregyan.

PHYSICS OF SEMICONDUCTOR DEVICES

Optimal Doping of the Drift Region in Unipolar Diodes and Transistors

A. S. Kyuregyan

All-Russia Power Institute, Krasnokazarmennaya ul. 12, Moscow, 111250 Russia

e-mail: kyureg@vei.ru

Submitted March 20, 2001; accepted for publication May 10, 2001

Abstract—An exact analytical solution to the problem of minimizing the drift-region resistance in high-power unipolar devices was obtained. It is shown that the optimal dopant profile $N(x)$ features a minimum in the central part of the drift region and increases without restriction when either of the boundaries of this region are approached. © *2002 MAIK "Nauka/Interperiodica".*

The high-power unipolar devices (the Schottky diodes and the vertical drift transistors) have a number of obvious advantages over the bipolar devices for relatively low breakdown voltages U_B. However, for high U_B, the efficiency of unipolar devices decreases drastically owing to a rapid increase in the resistance R of the layer with relatively high resistivity; almost the entire voltage in the blocking state drops across this layer [1].[1] If this layer with a thickness of d is doped uniformly with donors with concentration N and coincides completely with the space-charge region (SCR) only at a voltage $U = U_B$, the field distribution $E(x)$ in the SCR is triangular (see Fig. 1a, curve *1*); in this situation, the following obvious identities are valid for a given U_B:

$$d = w_{BS} \equiv 2U_B/E_{BS}, \quad N = N_S \equiv \varepsilon E_{BS}^2/2qU_B. \quad (1)$$

Here, ε is the dielectric constant of the semiconductor, q is the elementary charge, and E_{BS} is the highest field strength in the SCR of such a device under the conditions of breakdown. Strictly speaking, E_{BS} decreases logarithmically with increasing U_B [2, 3]. However, in order to facilitate the analytical calculation, the function

$$E_{BS} = \tilde{E}(\tilde{U}/U_B)^{1/(m-1)} \quad (2)$$

is often used [4, 5]; this function follows from the simplified breakdown criterion

$$\int_0^d \alpha[E(x)]dx = 1 \quad (3)$$

if the following power-law approximation for the dependence of effective impact-ionization coefficient on E is used:

$$\alpha(E) = a(E/\tilde{E})^m. \quad (4)$$

Here, a, $\tilde{E}$, and m are the parameters of the material; and $\tilde{U} = (m+2)\tilde{E}/2a$. In this study, we will also use this approximation. The following well-known [1] formula for the drift-region resistance stems from relations (1) and (2):

$$RA = r_S \equiv \frac{4\tilde{U}^2}{\varepsilon\mu\tilde{E}^3}\left(\frac{U_B}{\tilde{U}}\right)^{(2m+1)/(m-1)}. \quad (5)$$

Here, μ is the electron mobility and A is the device area. As can be seen, semiconductors with a large value of the product $\varepsilon\mu\tilde{E}^3$ should be used in production of unipolar devices; the wide-gap semiconductors (SiC, GaN, AlN, and diamond) are especially well-suited in this respect [6, 7]. However, when choosing a specific material, it is important to minimize r while optimizing the dopant profile $N(x)$ in the drift region.

An attempt at optimization for the simplest and most important case of the areally uniform drift region was undertaken by Hu [8], who solved the variational problem using equality (2) as the criterion of breakdown. Strictly speaking, this cannot be done even when optimizing a uniformly doped drift region. Actually, in this case, the following obvious inequalities should be satisfied: $d < w_{BS}$ and $N < N_S$ (see Fig. 1, curves *2*); therefore, E_B is governed only by the concentration of impurities,[2] but is independent of either U_B or d. Thus, using approximation (4), we obtain

$$E_B = \tilde{E}[N(d)/\tilde{N}]^{1/(m+1)}. \quad (6)$$

Using (6) and the known expression $U_B = E_B d - qNd^2/2\varepsilon$, we can easily show that, for a given U_B, the

[1] Henceforth, when referring to the high-resistivity layer, we will use the term "drift region."

[2] This follows directly from breakdown criterion (3) and the Poisson equation under the condition that N is constant within the effective-multiplication layer, the thickness of which should be smaller than d. At the same time, for $d \geq w_{BS}$, the quantities U_B, E_{BS}, and N are uniquely interrelated by formula (1); therefore, equalities (2) and (6) are equivalent.

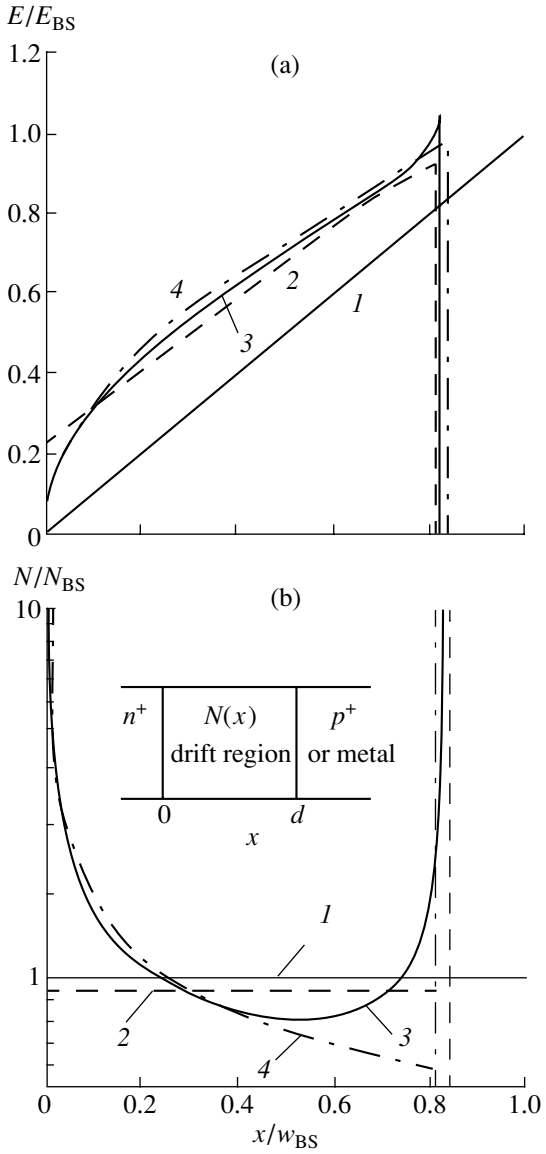

Distributions of (a) the field strength and (b) the dopant in the drift region for various methods for optimization: (*1*) uniformly doped drift region without the SCR restriction ($d = w_{BS}$); (*2*) an optimal uniformly doped drift region ($d < w_{BS}$); (*3*) an optimal nonuniformly doped drift region; and (*4*) an optimization in the limiting case of the critical field. Schematic representation of the diode's cross section is shown schematically in the inset.

smallest value of resistance of the uniformly doped base is given by

$$r = r_0 \equiv r_S\left(\frac{3}{2}\frac{m+1}{m+2}\right)^{(m+2)/(m-1)}\left(\frac{3}{2}\frac{m+1}{2m+1}\right)^{(2m+1)/(m-1)} \quad (7)$$

and is attained for

$$N = N_S\left[\frac{4}{9}\frac{(2m+1)(m+2)}{(m+1)^2}\right]^{(m+1)/(m-1)}, \quad (8)$$

$$d = w_{BS}\left(\frac{2m+1}{m+2}\right)^{1/(m-1)}\left(\frac{3}{2}\frac{m+1}{2m+1}\right)^{(m+1)/(m-1)}. \quad (9)$$

For typical [2–5] values of m = 5–7, quantitative discrepancies between (7)–(9) and the results obtained [8] for a uniformly doped drift region are insignificant. However, in the general case, the mathematically correct solution yields a radically new result.

For an arbitrary dopant profile $N(x)$, the drift-region resistance of a unit-area device is given by

$$r = \frac{1}{q\mu}\int_0^d \frac{dx}{N(x)}. \quad (10)$$

Since, in the blocking state, the field strength is related to the ionized-impurity concentration by the Poisson equation

$$\frac{dE}{dx} = \frac{q}{\varepsilon}N(x), \quad (11)$$

formula (10) can be rewritten as

$$r = \frac{1}{\varepsilon\mu}\int_0^d \frac{dx}{E'}, \quad (12)$$

where $E' \equiv dE/dx$. We must find a function $E(x)$, which ensures the minimization of the integral in (12) for a given breakdown voltage

$$U_B = \int_0^d E(x)dx; \quad (13)$$

the breakdown occurs when equality (3) holds. This is a classical isoperimetric problem in variational calculus [9], the solution of which should satisfy the following Euler equation for the function $F(x, E, E') = 1/E' - \lambda_1 E + \lambda_2\alpha(E)$:

$$2\frac{E''}{(E')^3} + \lambda_1 - \lambda_2\frac{d\alpha}{dE} = 0. \quad (14)$$

Here, $\lambda_{1,2}$ are the undetermined Lagrangian multiplers. The bounadary values of the field $E_0 = E(0)$ and $E_B = E(d)$ and the boundary position $x = d$ are not known beforehand. Therefore, we should assume the "natural" boundary condition at the boundary $\partial F/\partial E'|_{x=0} = 0$ and the transversability conditions $\partial F/\partial E'|_{x=d} = 0$ and $F(d, E, E') = 0$ [9] at the boundary $x = d$. In the case under consideration, these conditions yield

$$\frac{1}{E'(0)} = \frac{1}{E'(d)} = 0, \quad (15)$$

$$\lambda_1 E_B = \lambda_2\alpha(E_B). \quad (16)$$

It follows from (11) and (15) that, in the case of optimal doping, the concentration of impurities at both boundaries should tend toward infinity; therefore, the ques-

tion arises as to whether the assumption about the constancy of the mobility we used is valid. However, analysis shows the following:

(i) boundary conditions (15) remain to be valid for any dependence $\mu(N)$ only if the electrical conductivity increases steadily with increasing concentration; and

(ii) for typical values of U_B, the optimal concentration attains the values for which it is necessary to consider the dependence $\mu(N)$ only in infinitesimally thin boundary layers, the effect of which may be disregarded on the drift-region resistance.

Therefore, the consideration of the variability of $\mu(N)$ appreciably complicates the calculations but does not yield either significant quantitative or qualitative changes in the results.

In view of (15), the first integral of Eq. (14) has the form of

$$\frac{2}{E'} = \lambda_1 E - \lambda_2 \alpha(E). \tag{17}$$

It follows from (15) and (17) that $\lambda_1 E_0 = \lambda_2 \alpha(E_0)$; i.e., the boundary fields are solutions to the same equation. Since any dependence $\alpha(E)$ should be monotonic and superlinear, with $\alpha(0) = 0$ [2–5], Eq. (16) has only two solutions, one of which is $E_0 = 0$. This result, which is completely unobvious beforehand,[3] has been accepted without verification in [8] as one of the boundary-problem values of the variational problems.

In view of equality $E_0 = 0$, the second integral of Eq. (14) takes the form of

$$x = \lambda_1 \frac{E^2}{4} - \frac{\lambda_2}{2}\int_0^E \alpha(E)dE, \tag{18}$$

from which the following formula for the optimal drift-region width can be obtained:

$$d = \lambda_1 \frac{E_B^2}{4} - \frac{\lambda_2}{2}\int_0^{E_B} \alpha(E)dE. \tag{19}$$

Equations for $\lambda_{1,2}$ are derived from (3) and (13) taking into account (11) and (17). Solutions to these equations have the form

$$\lambda_1 = \frac{\Phi_2 U_B - \Phi_1 E_B}{\Phi_2/3 - \Phi_1^2} E_B^{-3}, \quad \lambda_2 = \frac{\Phi_1 U_B - E_B/3}{\Phi_2/3 - \Phi_1^2} E_B^{-2}, \tag{20}$$

where $\Phi_k = \int_0^1 t^{2-k} \alpha^k(E_B t)dt$. Substitution of (20) into (16) yields the following equation for the highest field strength during the breakdown:

$$(\Phi_2 U_B - \Phi_1 E_B) = (\Phi_1 U_B - E_B/3)\alpha(E_B); \tag{21}$$

this equation can be solved numerically for any dependence $\alpha(E)$ and, in view of the above formulas, can be used to calculate all characteristics of the optimal drift region, in particular, the resistance:

$$r = r_a \equiv \frac{1}{4\varepsilon\mu E_B^3}\left(\frac{\Phi_2 U_B - \Phi_1 E_B}{\Phi_2/3 - \Phi_1^2}\right)^2 \times\left(\frac{1}{3} + \frac{\Phi_2}{\alpha^2(E_B)} - 2\frac{\Phi_1}{\alpha(E_B)}\right). \tag{22}$$

The analytical solution, which is possible when using approximation (3), is representable in the parametric form as

$$E = E_B t, \tag{23}$$

$$x = d\frac{m+1}{m-1}\left[t^2 - \frac{2t^{(m+1)}}{m+1}\right], \tag{24}$$

$$N = N_S \frac{2}{3}\frac{m-1}{m+2}\left(\frac{2}{3}\frac{2m+1}{m+1}\right)^{2/(m-1)}(t - t^m)^{-1}, \tag{25}$$

$$E_B = E_{BS}\left(\frac{2}{3}\frac{2m+1}{m+1}\right)^{1/(m-1)}, \tag{26}$$

$$d = w_{BS}\frac{m+2}{2}\left[\left(\frac{3}{2}\right)^m \frac{(m+1)^{(2-m)}}{2m+1}\right]^{1/(m-1)}, \tag{27}$$

$$r_a = r_S \frac{m+2}{m+1}\left(\frac{3}{2}\frac{m+2}{2m+1}\right)^{(m+2)/(m-1)}. \tag{28}$$

The results of calculations using the above formulas for $m = 6$ are represented in Figs. 1a and 1b (curves *3*). Beyond the range of effective multiplication (i.e., for $t^{(m-1)} \ll 1$), the optimal dopant profile $N(x)$ can be readily obtained explicitly from expressions (24) and (25) as

$$N(x) = N_S \frac{2}{3}\frac{m-1}{m+2}\left(\frac{2}{3}\frac{2m+1}{m+1}\right)^{2/(m-1)}\sqrt{\frac{m+1}{m-1}\frac{d}{x}}. \tag{29}$$

As might be expected, this profile differs from that reported in [8] only in the numerical coefficient. However, in the range of effective multiplication, the results are radically different. According to [8], a dependence like (29) should be observed in the entire drift region so that the lowest concentration $N_{min} = \varepsilon E_B^2/3qU_B$ is attained at the boundary $x = d$ (see Figs. 1a, 1b, curves *4*). This (like all the results reported in [8]) follows also from (24) and (25) in the limiting case of $m \longrightarrow \infty$, which corresponds to the "critical field" approximation. However, for finite values of m, the profile in the vicinity of the boundary $x = d$ (for $(m+1)(1-t) \ll 1$) is given by

$$N(x) = N_S \frac{2}{3}\frac{1}{m+2}\left(\frac{2}{3}\frac{2m+1}{m+1}\right)^{2/(m-1)}\sqrt{(m+1)\frac{d}{d-x}}; \tag{30}$$

[3] For example, $E_0 \neq 0$ in the case of an optimally and uniformly doped drift region described above; furthermore, we can prove that $E_0 \neq 0$ if we use the dependence $\mu^{-1}(N) = \mu^{-1}(0)(1 + \text{const}N)$, which results in the levelling off of electrical conductivity with increasing N as a result of scattering by impurities.

i.e., the boundary concentration $N(d)$ should also be unlimited in accordance with (15).

In conclusion, we report the results of calculating the resistance of the drift region for $m = 6$ and for the following aforementioned variants of optimization:

(i) optimized uniform drift region (7), in which case $r = r_0 = 0.887 r_S$;

(ii) optimization in the critical-field limit [8], in which case $r = r_c = 0.957 r_S$; and

(iii) optimal nonuniform drift region, in which case we use (28) to obtain $r = r_a = 0.812 r_S$.

The value of the quantity r_c was calculated using the formula $r_c = \frac{r_S}{2}\left(\frac{3}{2}\right)^{(m+2)/(m-1)}$. In this formula, it is taken into account that the breakdown of the drift region with the dopant profile (29) occurs for the highest field value defined by formula (6), rather than by formula (2) suggested by Hu [8], in which case the value of r_c was underestimated. As can be seen, the dopant profile suggested in [8] yields a resistance even larger than r_0. The resistance of the actually optimal drift region was found to be only 10% lower than r_0. However, the latter result, strictly speaking, can be applied only to devices with planar electrodes that are uniform in area (for example, to the Schottky diodes). In vertical field-effect transistors, the resistance can be much higher owing to the spreading of current from the source, the area of which is typically several times smaller than the entire device area [1]. This resistance component is especially sensitive to the electrical conductivity of the material in close proximity to the source; therefore, the formation of the "optimal" dopant-concentration profile in transistors should give rise to a much more profound effect than in the aforementioned case.

REFERENCES

1. B. J. Baliga, *Modern Power Devices* (Singapore, 1987), p. 154.
2. I. V. Grekhov and Yu. N. Serezhkin, *Avalanche Breakdown of p-n Junctions in Semiconductors* (Leningrad, 1980).
3. A. S. Kyuregyan and S. N. Yurkov, Fiz. Tekh. Poluprovodn. (Leningrad) **23**, 1819 (1989) [Sov. Phys. Semicond. **23**, 1126 (1989)].
4. A. S. Tager and V. M. Val'-Perlov, *Avalanche-Transit Diodes and Their Application in Microwave Engineering* (Sov. Radio, Moscow, 1968).
5. S. M. Sze, *Physics of Semiconductor Devices* (Wiley, New York, 1981; Mir, Moscow, 1984).
6. A. A. Lebedev and V. E. Chelnokov, Fiz. Tekh. Poluprovodn. (St. Petersburg) **33**, 1096 (1999) [Semiconductors **33**, 999 (1999)].
7. K. Shenai, R. S. Scott, and B. J. Baliga, IEEE Trans. Electron Devices **ED-36**, 1811 (1989).
8. C. Hu, IEEE Trans. Electron Devices **ED-26**, 243 (1979).
9. G. A. Korn and T. M. Korn, *Mathematical Handbook for Scientists and Engineers* (McGraw-Hill, New York, 1961; Nauka, Moscow, 1968).

Translated by A. Spitsyn